

# Stochastic Disturbance Models A Next Generation of Model-Based Control

**Thilker, Christian Ankerstjerne**

*Publication date:*
2023

*Document Version*
Publisher's PDF, also known as Version of record

**DTU Compute**
Department of Applied Mathematics and Computer Science

# Stochastic Disturbance Models
# A Next Generation of Model-Based Control

PhD Thesis

**Christian Ankerstjerne Thilker**

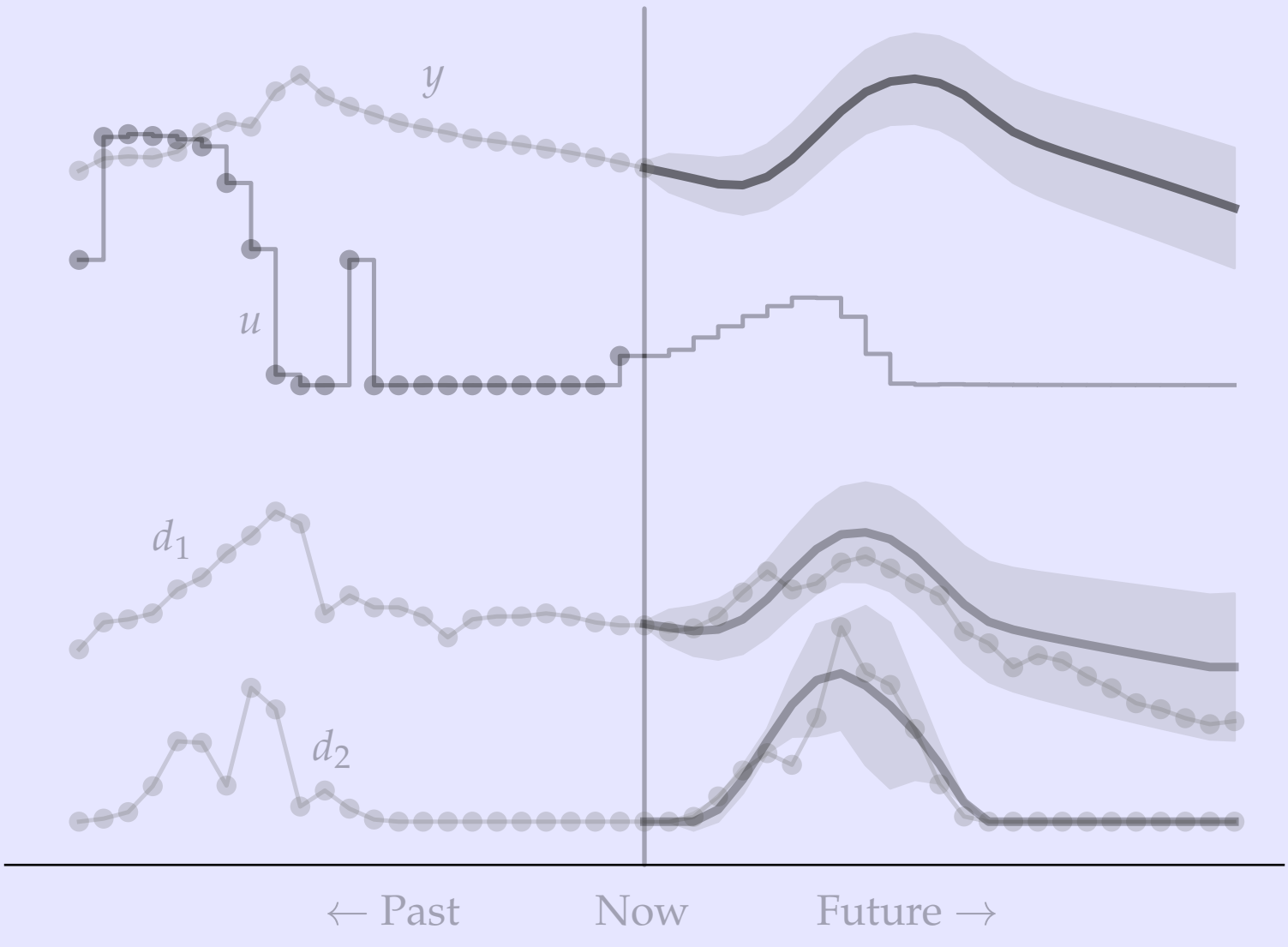

**Stochastic Disturbance Models**
A Next Generation of Model-Based Control

PhD Thesis
April, 2023


By: Christian Ankerstjerne Thilker (DTU Compute)
Main-supervisor: Henrik Madsen (DTU Compute)
Co-supervisor: John Bagterp Jørgensen (DTU Compute)





Cover photo: Christian Ankerstjerne Thilker, 2023
Published by: DTU, Department of Applied Mathematics and Computer Science, Asmussens Allé, Building 303b, 2800 Kgs. Lyngby Denmark
www.compute.dtu.dk
ISSN: [0000-0000] (electronic version)
ISBN: [000-00-0000-000-0] (electronic version)

ISSN: [0000-0000] (printed version)
ISBN: [000-00-0000-000-0] (printed version)

## Preface

This PhD thesis was prepared at the Department of Applied Mathematics and Computer Science at the Technical University of Denmark in fulfilment of the requirements for aquiring a PhD degree in Applied Mathematics.

Christian Ankerstjerne Thilker

.....

*Signature*

.....

*Date*

## Abstract (in English)

The future energy system will rely on the production of renewable and low-carbon energy sources, many of which are weather-dependent, such as wind and solar energy. To effectively implement this weather-driven energy system, there is a need to control energy demand in a manner that aligns with the fluctuating supply. This requires flexibility in various systems, such as adjusting indoor air temperatures in buildings, reactor temperatures in biogas production plants, and energy usage in wastewater treatment plants, among others, such as power-to-X, district heating, and electric vehicles. Scheduling energy usage optimally, however, poses a significant challenge. Model predictive control (MPC) is a control method that accounts for future inputs, disturbances, and system dynamics, allowing for optimal scheduling of energy usage. This dissertation investigates modelling techniques for various energy systems and applies predictive control methods to quantify and improve control and flexibility concepts. A significant contribution of this research is the proposal of embedded disturbance models for optimal control problems, which provide the controller with continuous-time disturbance forecasts and potentially more filtering information.

This dissertation considers various models for flexible control of the indoor climate in buildings. Paper A introduces a non-linear model describing the aggregated indoor air temperature of a building. Non-linearities come from the radiator thermostats and the energy usage, which are difficult to consider as linear phenomenons. Paper B presents the results and findings of a control experiment carried out using the continuous-time model in Paper A. The results successfully showed that the building was able to shift its heat load in time and react to varying prices. Paper C is a simulation study of online control of the same building using the model in A. The paper reaches the same conclusion that the building is suited for control and that significant economic and energy savings are available. Paper D considers non-linear ARX-models describing the indoor air temperature in single rooms. These take various inputs and disturbances into account and are simple and fast to estimate and use—and are thus useful for control.

The present dissertation also focus on modelling and forecasting of disturbances in control. Paper E introduces the concept of embedding a disturbance model in continuous-time into the formulation of the optimal control problem. This technique has the advantage of being able to describe the disturbances' influence on the system in continuous-time (instead of e.g. zero-order hold discretisations) and supply more information for the filtering of the system. Paper F uses this technique in a linear-quadratic controller used to control the indoor air climate of a building. It demonstrates the potential improvements of this forecasting technique used in a quadratic controller compared to standard disturbance mitigation techniques and the trade-offs between variation in inputs and the controlled system.

Choatic systems are dynamical systems governed by positive Lyapunov-exponents. This means that the predictability is lost exponentially if the initial state is not known exactly (which is rarely the case). Paper G introduces a method for controlling a chaotic system into an arbitrary point on a Poincaré section. The proposed method consists in two steps: first of solving an optimal control problem to obtain a periodically applied control signal and afterwards applying an additional adaptive control.

## Abstract (in Danish)

Fremtidens energisystem vil være baseret på produktion af vedvarende energikilder med lav $CO_2$-udledning, hvoraf mange er vejrafhængige, f.eks. vind- og solenergi. For at gennemføre en virkningsfuld implementering af det vejrbestemte energisystem, er der behov for at styre energiefterspørgslen på en måde, der er i overensstemmelse med det svingende udbud. Dette kræver fleksibilitet i forskellige systemer, f.eks. justering af indendørs lufttemperaturer i bygninger, reaktortemperaturer i biogasproduktionsanlæg og energiforbrug i spildevandsbehandlingsanlæg. Andre eksempler er power-to-X, fjernvarme og elbiler. Det er imidlertid en stor udfordring at planlægge energiforbruget optimalt. Model prædektiv regulering er en kontrolmetode, der tager højde for fremtidige input, forstyrrelser og systemdynamik, hvilket giver mulighed for optimal planlægning af energiforbruget. Denne afhandling undersøger modellleringsteknikker til brug i energisystemer og anvender prædiktive reguleringsteknikker med disse for at kvantificere og bevise kontrol- og fleksibilitetsteknikker.

Denne afhandling betragter flere modeller til optimal styring af indendørsklimaet i bygninger. Artikel A introducerer en ikke-lineær model, der beskriver den aggregerede indendørstemperatur (i alle rum) i bygningen. Ikke-linearitet stammer fra radiatortermostaterne og energiforbruget, som er svære at betragte som lineære fenomener. Artikel B præsenterer resultaterne og fundene fra et styringseksperiment udført med brugen af kontinuerttidsmodellen fra Artikel A. Resultaterne viser at bygningen var i stand til at flytte sit varmeforbrug og reagere på varierende priser. Artikel C præsenterer et simulationsstudie af online styring af den samme bygning med brug af modellen i A. Artiklen når til samme konklusion; at bygningen er egnet til optimal kontrol, og at der er potentiale for signifikante energimæssige- og økonomiske besparelser. Artikel D betragter ikke-lineære autoregressive modeller med eksterne inputs, der beskriver indendørstemperaturen i et enkelt rum i en bygning. Disse tager forskellige input og forstyrrelser i betragtning og er simple og hurtige at identificere og bruge—og er derfor sandsynligvis velegnede i kontrolsammenhænge.

Den foreliggende afhandling fokuserer også på modelling og fremskrivning af forstyrrelser til brug i kontrol. Artikel E introducerer konceptet at indlejre forstyrrelsesmodeller i kontinuert tid i formuleringen af optimal kontrol-problemer. Denne fremskrivningsteknik har fordelen at være i stand til at beskrive forstyrrelsernes påvirkning af systemet i kontinuert tid (i stedet for f.eks. nul'te ordens "hold" diskretisering) og giver mere information til filtreringsproblemet af systemet. Artikel F bruger den samme teknik i en lineær-kvadratisk regulator, der bruges til at styre indendørsklimaet i en bygning. Den demonstrerer de potentielle forbedringer fra den brugte fremskrivningsteknik i den lineære-kvadratiske regulator sammelignet med standard forstyrrelsesbehandlingsteknikker og de afvejninger, der er mellem variationen af input og det regulerede system.

Kaotiske system er dynamiske systemer, der er karakteriseret ved at have positive Lyapunov-eksponenter. Dette betyder, at systemets forudsigelighed tabes eksponentielt hvis systemets begyndelsestilstand ikke er kendt eksakt (hvilket sjældent er tilfældet). Artikel G introducerer en metode til at styre et kaotisk system ind på et vilkårligt punkt på et Poincaré-plan. Den forslåede metode består i to trin; først at løse et optimalt kontrolproblem for at beregne et periodisk anvendt styringssignal og derefter yderligere at anvende en adaptivt regulering.

## Acknowledgements

First, I would like to express my sincere gratitude towards my main supervisor, Henrik Madsen. Thank you for giving me the opportunity to start a PhD-study in the first place. A special thanks for being supportive in all regards of our collaboration and giving me the large amount of responsibility in tasks. And lastly, thank you for always being open for discussing any professional (and even private) matter—it has been a great help. This has made my time at DTU an invaluable experience. I would also like to thank my co-supervisor, John Bagterp Jørgensen, for always having an open door to discuss different matters and for the valuable feedback on the joint work.

Second, I would like to thank all of my colleagues for making the work environment inspiring and the section a nice place to be. I have always looked forward to going come to work and be with you. And a special thanks to all of my office mates (for most of the time), Rune Grønborg Junker, Christoffer Rasmussen, Dominik Franjo Dominković, Jaume Palmer Real, and Hjörleifur Bergsteinsson. I really enjoyed working with you and to do social things outside of work. I hope to get to work with you again in the future.

I would like to thank Lars Imsland, Brage Knudsen, and Kiet Hoang for hosting me at NTNU in Trondheim and for making the stay a pleasant time. I also hope to get the chance to collaborate with you again in the future.

Finally, a very special thanks goes to Peder Bacher with whom I have shared many (in my opinion) fun, motivational, instructive, and exciting experiences. Together, we spent many hours building and setting up a more or less home made indoor climate optimal control setup: Thank you for all the great and memorable times and late hours we worked together.

*"Love is patient, love is kind. It does not envy, it does not boast, it is not proud. It is not rude, it is not self-seeking, it is not easily angered, it keeps no record of wrongs. Love does not delight in evil but rejoices with the truth. It always protects, always trusts, always hopes, always perseveres. Love never fails."*

– Paulus' first letter to the Corinthians.

# Contents

# Part I

## Summary Report

# 1 Introduction

The so-called planetary boundaries must be respected to ensure an inhabitable planet for mankind (Steffen et al., 2015). One of these is climate change. In Denmark, it has been politically decided to reduce $CO_2$ emissions in 2030 by 70% compared to 1990 (Klimarådet, 2020). Production of energy from renewable sources such as solar and wind is therefore expected to grow in the coming years to meet the current energy demand solely from renewable sources (Klimarådet, 2019).

An arising challenge from the transition from fossil fuels to low carbon density energy sources is the unstable energy production from wind and solar. Historically, common practice has been to adjust the production to meet the demand at all times. With energy sources as wind and solar, we are however no longer in control of the production. We are, however, in control of the demand. This implies that the energy sector needs to move from a production-regulating-scheme to a consumption-regulating-scheme. The concept known as *energy flexibility* addresses this issue by utilising the ability of devices to shift their energy usage in time to utilise the energy when it is available (Junker, Kallesøe, et al., 2020; Dominković et al., 2020). Examples of such devices/units include regular batteries (found in electric vehicles fx), thermal storage of buildings, Power-to-X production, biogas production, district heating- and wastewater aeration operations, and sector coupling units in general. All the above devices/units are able to regulate their energy usage up and/or down to shift their energy usage to advantageous times while meeting local constraints (such as a minimum temperature in buildings, the EV battery needs to be fully charged at 17.00 o'clock, etc.). To align the energy consumption and demand, it is believed that all flexible units should be controlled and regulated according to a varying price signal (De Zotti, Pourmousavi Kani, et al., 2018; De Zotti, Kani, et al., 2020; Madsen, Parvizi, et al., 2015; Santos and B. N. Jørgensen, 2019) to incentivise usage of energy when it is available. This price signal has the purpose of making sure that the total consumption aligns with the production at all times. Multiple proposes to change the current market and tariffs as such has been made (Ma, B. N. Jørgensen, and Parker, 2019; Lund and Münster, 2006). Varying price signals can also be used to supply grid services (Parvizi, John B. Jørgensen, and Madsen, 2018)

This dissertation includes applications of modelling, forecasting, and control for such flexible energy systems (both simulation- and real-life cases). The results contribute to the literature on flexibility and optimal control and support the generally accepted hypothesis that energy flexibility via optimal control offers significant operational improvements while at the same time saving energy and/or carbon emissions. This is done by including better and more accurate disturbance forecasts in the optimal control problem while operating the system closer to the given constraints (e.g. temperature bounds in buildings). Some of the applications included in this dissertation are:

- Modelling of heat dynamics of buildings: This dissertation presents modelling methods for building heat dynamics based on stochastic grey-box models. These capture both the deterministic dynamics and the stochastic properties of the system.
- Control of heat dynamics of buildings: Using non-linear model predictive control, we demonstrate (in simulation and real-life) the buildings' abilities to be flexible.
- Stochastic disturbance modelling and forecasting techniques: Chapter 3, Paper E, and F present a formalism for including stochastic disturbance forecasts directly

into the optimal control problem.

- Control of chaotic systems: Chapter 4 and Paper G describes and introduces a method for stabilising chaotic systems using optimal control techniques.

All the applications above can be used to optimise the operation of the given dynamical systems. Better forecasts and system models makes it possible for the controller to better predict the system behaviour and thus is able to operate the system closer to its constraints. In the end, this may increase performance and enable the controller to better monetise and utilise the flexibility embedded in the system.

The rest of the introduction briefly introduces the reader to key concepts of modelling, forecasting, and controlling for stochastic, dynamical systems.

## 1.1 Stochastic differential equations

For modelling time-varying stochastic systems, this dissertation focuses on stochastic differential equations (SDEs). These generalises the ordinary differential equations by adding a stochastic process to the dynamical forces of the dynamical system in the following way:

$$x_t = x_0 + \int_0^t f(x_\tau, u_\tau, d_\tau, \tau; \theta)\mathrm{d}\tau + \int_0^t g(x_\tau, \tau; \theta)\mathrm{d}\omega_\tau \,, \tag{1.1}$$

where $x$ is the state vector, $u$ is the input vector, $d$ is the disturbance vector, $\theta$ is a parameter vector, and $\omega$ is Brownian motion. In this dissertation, we shall use an Itô integral as the last integral in (1.1). A brief introduction to SDEs and small examples are given in Chapter 2. Iacus, 2008; Jazwinski, 1970; Thygesen, 2022 give more theoretical introductions.

## 1.2 Control of dynamic systems under influence by stochastic inputs

This dissertation deals with control and forecasting for stochastic dynamical systems that undergo inputs from (stochastic) disturbances and inputs. In (1.1), we shall distinguish between the following three types of inputs of the dynamical system:

- Deterministic, controllable input, $u$: This is the type of input that the controller is able to manipulate in order to control the system and is assumed to be deterministic in this dissertation. We refer to $u$ as an *input*.
- Stochastic non-controllable input, $d$: This is the type of force/input that the controller has no control over and is referred to as a *disturbance*. It is, however, not a white-noise process and is (to some extend) forecast-able.
- Stochastic diffusion input, $\omega$: This is the type of force that is based on a white noise process (and often scaled by some function $g$) and is thus completely random and non-predictable.

This dissertation includes publications that focus their attention towards the disturbances, $d$, and how to deal with these in optimal control problems. E.g., for controlling energy systems (like the indoor air temperature), disregarding the solar radiation gain may cause severe discomfort due to overheating since the sun delivers significant amounts of energy in short time intervals (Candanedo and Athienitis, 2011). Typically, forecasts for these disturbances are needed in the numerical optimisation of the optimal control problem. If not provided, it may affect the control performance significantly. Otherwise, if "clever" forecasts are not available, simple and alternative methods like persistent forecasts may improve control performance.

As a different kind of "stochastic" systems, this dissertation briefly discusses chaotic dynamical systems and different control schemes for these. Such systems are characterised by differential equation models that have positive Lyapunov exponents and therefore exponentially diverges away from solutions starting infinitesimally close to each other. Stabilising these require special treatment, which Paper G discusses.

## 1.3 Model predictive control

A model of a system gives the possibilities to predict its future states. The model predictive control principle in short exploits the predictability of the system to find an optimal future input sequence to optimise its operations according to some objective. In the general case, when the model is non-linear, the optimal control problem posed to find the optimal input sequence can be written as

$$u^* = \arg\min_u \quad \left\{ \phi_k = \int_{t_k}^{t_k+T} q(x_\tau, u_\tau, d_\tau)\mathrm{d}\tau + q_b(x_{t_k+T}) \right\}, \tag{1.2a}$$

$$\text{s.t.} \quad x_t = \hat{x}_{k|k} + \int_{t_k}^{t} f(x_\tau, u_\tau, d_\tau; \theta)\mathrm{d}\tau\,, \qquad t \in [t_k, t_k + T[\,, \tag{1.2b}$$

$$u_t \in \mathcal{U}_t \qquad t \in [t_k, t_k + T[\,, \tag{1.2c}$$

$$x_t \in \mathcal{X}_t \qquad t \in [t_k, t_k + T[\,, \tag{1.2d}$$

where $u^*$ is the optimal input sequence that minimises the objective $\phi_k$. The objective has the role of making solutions comparable and should thus incentivise the desired behaviour of the system. This dissertation includes examples of linear-, quadratic-, and non-linear objectives. The linear objective is common if it is related to some economic cost, the quadratic is popular for reference tracking, and the non-linear if other incentives is embedded into the objective.

## 1.4 Applications

This dissertation includes two publications related to modelling of dynamical systems, both of which are models for predicting the indoor air temperature of buildings (and in fact the same building). The two papers approach the problem differently and both have pros and cons.

- Paper A: The first paper presents a model for predicting the indoor air temperature and heat usage of a Danish school building. The building gets heat from the local district heating network and uses radiators to distribute the heat in the rooms. Prior to the identification experiment, all radiators were equipped with smart Danfoss thermostats and all rooms were equipped with temperature sensors. To be able to predict the heat usage of the single rooms requires the supply- and return temperature of the water of the radiators and the water flow. The supply temperature is known (since it is set by the building managers). However, to measure the return temperature requires installation of addition heat sensors and the water flow is expensive to measure since it requires hypersonic equipment. Therefore, instead of modelling each room of the building, the paper presents an aggregated model of the building based on SDEs where the arithmetic average of all room temperatures was used as an estimate of the indoor air temperature of the entire building. The model includes non-linearities from the thermostats (modelled by a sigmoid function) and the heat usage. Based on the identification experiment, the model seems to perform well.

- Paper D: The conclusion from the results of a control experiment of a Danish school building (presented in Paper B) is that some individual room control is needed. In Paper D, the authors present an automated modelling technique for identifying autoregressive models for predicting the indoor air temperature in single rooms. These are readily used for predictive control.

The present dissertation also includes 4 (plus control of chaos and energy-planning articles) articles on predictive control of various dynamical systems.

- Paper D: During the winter of 2020/2021, the authors carried out a control experiment of the same school as modelled in Paper A and tested various control objectives including a flexibility experiment. The aim was to illustrate that the building was able to shift its heat load away from the peak hours (the morning and evening hours). The building performed well in terms of controlling the mean temperature of all the rooms inside the given temperature bounds. But further investigations showed that there was a significant spread in the individual room temperatures. The conclusion of the paper is that sufficient comfort cannot be reached or guaranteed by controlling the building on an aggregated level without taking the individual rooms difference in size and/or heating capacity into account.

- Paper C presents the results of a control simulation of the building model in presented in A. The simulation compares a non-linear MPC to the performance of a fixed heating schedule (that includes nightly set-backs). Results suggests that the MPC improves performance by up to 10-15%.

- Paper E presents a method for embedding disturbance forecasts into the formulation of a MPC. By modelling the disturbances and including these in the model formulation, the model predictions automatically include the disturbances and their forces on the system. The paper demonstrated the method in an example of controlling the indoor air temperature of a building. Results suggest electricity savings and comfort improvements of up to 10% and 90%, respectively, compared to standard forecasting schemes.

- Paper F presents the linear-quadratic control scheme for stochastic differential equation models and motivates and discusses how to deal with disturbances. It derives a discretisation of the system and the optimal control problem and applies this to a building thermal optimal control problem. The results emphasise the trade-off that linear-quadratic optimal control problems offer: minimisation of the variation in the input signal versus minimisation of the variation of the system around the reference trajectory.

- Paper G presents an optimal control problem for stabilising and controlling chaotic systems. Such a system is characterised by lacking predictability in uncertain settings. State-of-the-art methods for stabilising a chaotic system relies on stabilising the system around an already existing unstable periodic orbit (UPO). But if a certain path for the system is desired by the operator, and an UPO does not exists for this path, existing methods do not suffice. In this paper, the authors present a method for introducing an UPO at the desired path by solving an optimal control problem. Next, after the introduction of the UPO, existing methods for stabilising the chaotic system can be utilised.

## 1.5 Notation

Throughout this dissertation, $\mathbb{R}$ and $\mathbb{N}$ are the real and natural numbers, respectively. $\mathbb{R}^+$ and $\mathbb{R}^-$ means all non-negative and non-positive real numbers, respectively.

All time dependence is written as a subscript on the variable, e.g. $x_t$ instead of $x(t)$. This is however only the case for time dependence. If a variable depends on e.g. a set of parameters, $\theta$, it is written in parenthesis as $x_t(\theta)$. To avoid confusions with indexes, if a subscript is written with a $\tau$ or $t$, it refers to a continuous dependence, whereas if the subscript is an $i$, $k$, $m$, or $n$, it refers to a discrete index. Consequently, in the rest of the thesis, $\tau, t \in \mathbb{R}$ and $i, k, n, m \in \mathbb{N}$.

Let $f : \mathbb{R}^n \mapsto \mathbb{R}^m$ be a function. Then, in this dissertation,

$$\frac{\partial f}{\partial x} : \mathbb{R}^n \mapsto \mathbb{R}^m \tag{1.3}$$

shall be the matrix representation of the linear transformation that constitute the total derivative of $f$ w.r.t. $x \in \mathbb{R}^n$ (given that it exists) in the usual basis for $\mathbb{R}^n$.

## 1.6 Outline

This dissertation is structured in the following way:

- Chapter 2 briefly presents the background of stochastic differential equations and the filtering principle. Stochastic differential equations form the basis of the models used throughout the dissertation. The filtering principle is an important key for state estimation and for estimation of parameters embedded in stochastic differential equation models. It also briefly touches upon discrete-time models and semi-parametric models. The chapter includes short and simple examples underway to illustrate some of the theory in practice.
- Chapter 3 introduces the model predictive control principle and presents two common ways of discretising and solve such problems.
- Chapter 4 presents the applications of the background and theory priorly presented. All applications are based on the publications included in this dissertation.
- Chapter 5 sums up the findings of the dissertation and supplies opinions on what the future brings for this field of research.

# 2 Stochastic Differential Equations and Filtering

Stochastic differential equations (SDEs) are a useful and powerful tool for modelling and representing stochastic processes. It can be shown that under certain conditions, all stochastic processes with continuous trajectories can be written as a SDE (Bjork, 2009). Thus, SDEs are a general class of stochastic models. This section briefly introduces the theory of SDEs and filtering that is necessary to read the rest of the thesis. Further introductions to SDEs and their applications can be found in e.g. (Oksendal, 1992; Mikosch, 1998).

## 2.1 Stochastic differential equations

Let $\{x_t, t \geq 0\}$, $x_t \in \mathbb{R}^n$ be a continuous-time stochastic process governed by the following equation

$$x_t = x_0 + \int_0^t f(x_\tau, \tau; \theta)\mathrm{d}\tau + \int_0^t g(x_\tau, \tau; \theta)\mathrm{d}\omega_\tau \tag{2.1}$$

where $f : \mathbb{R}^n \times \mathbb{R}^+ \times \mathbb{R}^m \mapsto \mathbb{R}^n$ and $g : \mathbb{R}^n \times \mathbb{R}^+ \times \mathbb{R}^m \mapsto \mathbb{R}^n$ are the drift and diffusion functions, respectively, $\theta \in \mathbb{R}^m$ is a set of parameters, and $x_0 \in \mathrm{R}^{n_x}$ is the initial state. $\omega : \mathbb{R}^+ \mapsto \mathbb{R}^n$ is standard Brownian motion with the property $\omega_t - \omega_s \sim N(0, t-s)$ for $t > s$. Since the Brownian motion is not differentiable, (2.1) does not have a differentiable form. However, in short, we typically write (2.1) as

$$\mathrm{d}x_t = f(x_t, t; \theta)\mathrm{d}t + g(x_t, t; \theta)\mathrm{d}\omega_t \tag{2.2}$$

We shall use the Itô interpretation of the SDE, i.e. the integral in 2.1 is an Itô integral.

**Example**
A simple example of an SDE is the Cox-Ingersoll-Ross (CIR) diffusion, $x : \mathbb{R}^+ \mapsto \mathbb{R}$ having the form

$$\mathrm{d}x_t = \lambda(\mu - x_t)\mathrm{d}t + \sigma\sqrt{x_t}\mathrm{d}\omega_t\,, \tag{2.3}$$

where $\theta = (\lambda, \mu, \sigma) \in \mathbb{R}^+ \times \mathbb{R} \times \mathbb{R}^+$ are parameters in the SDE. We will use this SDE throughout this dissertation for examples.

### 2.1.1 Itô's lemma

The chain rule in deterministic calculus applies as long as the function at hand is smooth. However, due to the non-vanishing quadratic variation of Brownian motion, the deterministic chain rule does not hold. The chain rule in stochastic calculus is an important tool to analytically find a governing SDE of a transformed process. Let $x$ be an Itô-process governed by (2.1) and $z_t = \psi(x_t, t)$, $z_t : \mathbb{R} \mapsto \mathbb{R}^{n_z}$, $\psi : \mathbb{R}^{n_x} \times \mathbb{R} \mapsto \mathbb{R}^{n_z}$, be some transformation of $x$. The question is then: Given $\psi$, what SDE governs $z$? Itô's lemma tells us just that and is

$$\mathrm{d}z_t^{(i)} = \frac{\partial \psi_i}{\partial t}\mathrm{d}t + \frac{\partial \psi_i}{\partial x}\mathrm{d}x_t + \frac{1}{2}\mathrm{d}x_t^\intercal \frac{\partial^2 \psi_i}{\partial x^2}\mathrm{d}x_t\,, \tag{2.4a}$$

$$= \left(\frac{\partial \psi_i}{\partial t} + \frac{\partial \psi_i}{\partial x}f + \frac{1}{2}\mathrm{tr}\, g^\intercal \frac{\partial^2 \psi_i}{\partial x^2} g\right)\mathrm{d}t + \frac{\partial \psi_i}{\partial x} g \mathrm{d}\omega_t\,, \tag{2.4b}$$

where $z_t^{(i)}$ and $\psi_i$ is the $i$'th coordinate of $z_t$ and $\psi$, respectively, and tr is the matrix trace. From a modelling perspective, it is sometimes difficult to deal with processes with

state-dependent diffusion terms. But Itô's lemma supplies us with a tool to transform the process into an equivalent process that has state-independent diffusion. Consequently, we can answer the question: What transformation $\psi$ should we use to make the diffusion function of $z_t = \psi(x_t, t)$ be state-independent? The tool for this is also known as the Lamperti transformation (Møller and Madsen, 2010).

**The Lamperti-transformation**
Choose

$$\psi(x) = \int^x \frac{1}{g(s)} \mathrm{d}s \,. \tag{2.5}$$

Then $z_t = \psi(x_t)$ is governed by an Itô's process with state-independent diffusion term.

**Example**
Consider the CIR-process in (2.3). The diffusion function is $g(x_t; \theta) = \sigma\sqrt{x_t}$. The Lamperti transformation is then (leaving a constant on the diffusion of the Lamperti-transformed process)

$$\psi(x) = \int^x \frac{1}{\sqrt{s}} \mathrm{d}s = 2\sqrt{x} \,. \tag{2.6}$$

Inserting this into Itô's formula in (2.4), we get the process:

$$\mathrm{d}z_t = \frac{\lambda(4\mu - z_t^2) - \sigma^2}{2z_t} \mathrm{d}t + \sigma \mathrm{d}\omega_t \,. \tag{2.7}$$

(2.3) describes the same input-output relation as (2.7) and uses the exact same parameters, but the latter considers a transformed state space.

### 2.1.2 Partially observed stochastic differential equation models

For modelling stochastic and dynamical systems, it can be shown that (under certain regularity conditions) all continuous stochastic processes can be written as an SDE. This is a powerful statement and solidifies the applicability of SDEs for modelling stochastic time varying systems.

For a stochastic system, it may be the case that it is only partially observed—i.e. some states are hidden. This principle is also known as hidden Markov processes where the underlying system is observed through some function. Furthermore, observations are often taken at discrete points in time. The underlying system evolves according to some dynamics and the system is then observed through a function. Using SDEs to represent the underlying model, we can write the framework as

$$\mathrm{d}x_t = f(x_t, t; \theta)\mathrm{d}t + g(x_t, t; \theta)\mathrm{d}\omega_t \tag{2.8a}$$
$$y_k = h(x_{t_k}, v_k; \theta) \tag{2.8b}$$

where $y_k : \mathbb{N} \mapsto \mathbb{R}^{n_y}$ is the observation variable, $v_k : \mathbb{N} \mapsto \mathbb{R}^{n_v}$ is i.i.d. random variables and $h : \mathbb{R}^{n_x} \times \mathbb{R}^{n_v} \times \mathbb{R}^{n_\theta} \mapsto \mathbb{R}^{n_y}$ is the observation function. In engineering, the modelling framework in (2.8) is often referred to as grey-box modelling or continuous-discrete time modelling (Kristensen, Madsen, and S. B. Jørgensen, 2004; Juhl et al., 2016; Boiroux et al., 2016). It is widely applicable to all continuous-time processes where observations are taken discretely. This is a large class of processes and examples such as diabetes, refrigerators, district heating systems, and bacterial growth can be found in e.g. (Duun-Henriksen et al., 2013; Costanzo et al., 2013; Nielsen and Madsen, 2006; Møller et al., 2012).

## 2.2 Filtering

Assume we are dealing with a partially observed system with a hidden/latent process $x_t$ in continuous (or in general also discrete) time. Ultimately, the filtering principle is to associate and compute conditional distributions for the underlying stochastic process $x_t$ given observations $y_{t_k}$, $k \in \mathbb{N}$, by using the accumulated information as new observations become available. This is useful for state- and parameter estimation in stochastic models. The present section introduces the filtering principle and a practical approximation to the exact filtering principle. In model predictive control, it may be critical to compute and apply the optimal control in due time—therefore, approximations to the exact filtering may be useful since the exact filter equations may be computationally difficult to solve.

Let us first consider generalised state space models, and consider a sequence of state variables:

$$\{x_k; k \geq 1\}$$

and a sequence of observations:

$$\{y_k; k \geq 1\}$$

Here, we shall consider the so-called parameter-driven state-space models where the model evolve independently of the past history of the observation process. Let the history of $\{x_k\}$ and $\{y_k\}$ be denoted $\mathcal{X}^{k-1}$ and $\mathcal{Y}^{k-1}$:

$$\begin{aligned}\mathcal{X}^{(k-1)} &= (x_{k-1}, x_{k-2}, \ldots)\\ \mathcal{Y}^{(k-1)} &= (y_{k-1}, y_{k-2}, \ldots)\end{aligned}$$

Furthermore, we will assume that $y_k$ given $(x_k, \mathcal{X}^{(k-1)}, \mathcal{Y}^{(k-1)})$ is independent of $(\mathcal{X}^{(k-1)}, \mathcal{Y}^{(k-1)})$ (the Markov property) with conditional probability density:

$$p_{\text{obs}}(y_k|x_k) = p_{\text{obs}}(y_k \mid x_k, \mathcal{X}^{(k-1)}, \mathcal{Y}^{(k-1)}) \tag{2.9}$$

where the subscript "obs" is short for "observation" since this is the conditional density of the observation variables. And similarly the prior conditional density of $x_{k+1}$ given information up till time $t_k$ is

$$p_{\text{prior}}(x_{k+1}|x_k) = p_{\text{prior}}(x_{k+1}|x_k, \mathcal{X}^{(k-1)}, \mathcal{Y}^{(k-1)})\,. \qquad \text{(state eq.)}$$

The objective is then to reconstruct (filter) the hidden process $\{x_k\}$ based on the observations $\{y_k\}$ using Bayes' theorem. Recursive formulas for the filter densities exists and has the following form (Bayes' theorem)

$$p_{\text{post}}(x_k|\mathcal{Y}_k) = \frac{p_{\text{obs}}(y_k|x_k)p_{\text{prior}}(x_k|\mathcal{Y}_{k-1})}{\int p_{\text{obs}}(y_k|x_k)p_{\text{prior}}(x_k|\mathcal{Y}_{k-1})\mathrm{d}x_k} \tag{2.10}$$

where $\mathcal{Y}_k = \{y_1, y_2, \ldots, y_k\}$ is all observations up till time $t_k$. Note that the denominator is constant w.r.t. $x_k$ and is usually replaced by a normalisation constant $c_k$ such that the right-hand side integrates to unity. The density $p(x_k|\mathcal{Y}_{k-1})$ is given by:

$$p_{\text{prior}}(x_k|\mathcal{Y}_{k-1}) = \int p_{\text{prior}}(x_k|x_{k-1})p_{\text{post}}(x_{k-1}|\mathcal{Y}_{k-1})\mathrm{d}x_{k-1} \tag{2.11}$$

The prior conditional density can be computed as the solution to the forward Kolmogorov equation:

$$\dot{\rho} = -\nabla \cdot (v\rho - D\nabla\rho) \tag{2.12}$$

where $D(x,t) = \frac{1}{2}g(x,t)g^\top(x,t)$ is the diffusivity matrix and $v(x,t) = f(x,t) - \nabla D(x,t)$ is the advective flow vector field.

In general, the observation-, posterior- and prior distribution, $p_{\text{obs}}$, $p_{\text{post}}$, and $p_{\text{prior}}$, may be any valid probability distribution function (non-negative and integrating to 1). Given an underlying model, $f$, $g$, $h$, and the probability distribution of $v$, an exact filtering algorithm (in the sense that it uses the exact equations) can be summarised by the following:

1. Initialise with $t_0 = 0$, $p_{\text{post},0}(x|\mathcal{Y}_0)$, and $k = 0$.
2. *Compute prior density:* Solve the forward Kolmogorov equations with initial condition $\rho(x,t_k) = p_{\text{post},k}(x|\mathcal{Y}_k)$ on $[t_k, t_{k+1}]$. Set the prior density as the solution $p_{\text{prior},k+1}(x|\mathcal{Y}_k) = \rho(x,t_{k+1})$.
3. *Compute posterior density:* Compute $p_{\text{post},k+1}$ using Bayes' rule in (2.10).
4. Put $k := k+1$ and go to step 2 until finished.

The above algorithm computes the prior and posterior densities for each observation time, $\{p_{\text{prior},k}\}_{k=1}^N$ and $\{p_{\text{post},k}\}_{k=1}^N$, that in general may attain arbitrary distributions.

An example of a generalized state-space model and filtering using analytical expressions for the densities is shown in (Peter Thyregod et al., 1998). The paper illustrates the use of a Gamma-process for the dynamics, while the observations are Poisson distributed. In practice, however, it may be cumbersome to compute the conditional transition densities using the forward Kolmogorov equations, since numerical methods are needed. Especially if the system is high dimensional, the solution to (2.12) is practically infeasible to compute. Therefore, approximations to the analytical filtering equations can be useful in order to make filtering numerically tractable.

### 2.2.1 Maximum a posteriori estimation

The so-called maximum a posteriori estimation (MAP) is a filtering technique based on Bayes' formula in (2.10) and does not necessarily make any simplifications to the filtering equations. From Bayes' formula in (2.10), it is clear that the denominator is constant w.r.t. the underlying state $x_k$, hence

$$p_{\text{post}}(x_k|\mathcal{Y}_k) \propto p_{\text{obs}}(y_k|x_k)p_{\text{prior}}(x_k|\mathcal{Y}_{k-1})\,. \tag{2.13}$$

The filtered estimate given by the maximum a posteriori estimation is the state that maximises the posterior distribution

$$\hat{x}_{k|k} = \arg\max_x \left\{p_{\text{obs}}(y_k|x)p_{\text{prior}}(x|\mathcal{Y}_{k-1})\right\}\,. \tag{2.14}$$

In general, to solve (2.14) requires numerical optimisation techniques since it is usually non-linear. This might be numerically expensive to perform in each filtering step in an optimal control setup.

The continuous-discrete extended Kalman filter (CDEKF) is a very applicable tool for filtering in continuous-discrete models as the one in (2.8). It does, however, make critical assumptions on the distributions involved. But as a consequence, the filtering equations are given in closed form and are fast to compute. And one can show that under certain conditions, the assumptions are often reasonable.

### 2.2.2 The continuous-discrete extended Kalman filter

The CDEKF is a filtering technique for systems in continuous time with observations taken discretely as in (2.8). Its filtering procedures are simplifications of the exact filtering equations and thus supplies approximate estimates of the conditional transition densities (Kulikov and Kulikova, 2017). It makes the following assumptions to simplify the computations:

1. The conditional transition probabilities are Gaussian,

$$\varphi(x;\mu,\Sigma) = \frac{1}{(2\pi)^{n_x/2}\det(\Sigma)^{1/2}} \exp\left(-\frac{1}{2}(\mu-x)^\top \Sigma^{-1}(\mu-x)\right).$$

   where $\varphi : \mathbb{R}^{n_x} \times \mathbb{R}^{n_x} \times \mathbb{R}^{n_x \times n_x} \mapsto \mathbb{R}$ is the Gaussian density.

2. The observation noise is Gaussian and additive, i.e. $y_k = h(x_{t_k};\theta) + v_k$, $v_k \sim N(0,R)$, $R \in \mathbb{R}^{n_y \times n_y}$.

3. The observation function is well approximated by its linearisation, $h(x_t;\theta) \approx C(x_t - x_0) + h(x_0;\theta)$, where $C : \mathbb{R}^{n_x} \mapsto \mathbb{R}^{n_y}$ is the linearisation of $h$ around $x_0$.

*Remark.* Since the standard deviation of Brownian motion scales with the square root of time (compared to the advective scale, which is linear), the dynamics of Brownian motion dominates the deterministic dynamics for small transition times. Thus, as the transition time goes to zero, the conditional transition density approaches a Gaussian distribution. Assumption 1 is therefore good for small enough transition times. Assumption 2 might not hold directly if either the observation noise is non-Gaussian or the domain is bounded. In the latter case, transformations are usually useful. Assumption 3 also holds well if either the observation function is close to linear or if the transition times are sufficiently small. These assumptions can also be checked for a given model to see how well it resembles the assumptions of Gaussianity.

The CDEKF follows the algorithmic structure of the exact filtering having a prediction step and an update step. The two schemes are given below and uses the notation as in N. L. Brok, Madsen, and John Bagterp Jørgensen, 2018.

**The prediction scheme**

In the prediction step, the prior expectation of the state and its associated covariance is predicted at time $t_k$ based on the posterior estimates at time $t_{k-1}$. The estimates are obtained by solving the coupled system of moment differential equations

$$\dot{\hat{x}}_{k-1}(t) = f(\hat{x}_{k-1}(t), t;\theta), \tag{2.15a}$$

$$\dot{\hat{\Sigma}}_{k-1}(t) = A(t)\hat{\Sigma}_{k-1}(t) + \hat{\Sigma}_{k-1}(t)A(t)' + G(t)G(t)', \tag{2.15b}$$

with

$$A(t) = \frac{\partial f}{\partial x}(\hat{x}_{k-1}(t), t;\theta), \qquad G(t) = g\left(\hat{x}_{k-1}(t), t;\theta\right), \tag{2.16}$$

subject to the initial conditions $\hat{x}_{k-1}(t_{k-1}) = \hat{x}_{k-1|k-1}$ and $\hat{\Sigma}_{k-1}(t_{k-1}) = \hat{\Sigma}_{k-1|k-1}$, being the posterior estimates at the previous time $t_{k-1}$. The prior estimates at time $t_k$ are then the solution to (2.15) at $t_k$, $\hat{x}_{k|k-1} = \hat{x}_{k-1}(t_k)$ and $\hat{\Sigma}_{k-1}(t_k)$, respectively. The prior conditional density is given by the Gaussian density $\varphi(x;\hat{x}_{k|k-1},\hat{\Sigma}_{k|k-1})$.

**The update scheme**
In the update step, the observation $y_k$ and the prior density are used to compute the posterior density. The innovation gain is

$$e_k = y_k - h(\hat{x}_{k|k-1})\,. \tag{2.17}$$

The Kalman gain is

$$C_k = \frac{\partial h}{\partial x}(\hat{x}_{k|k-1};\theta)\,, \tag{2.18a}$$

$$R_{k|k-1} = C_k \hat{\Sigma}_{k|k-1} C_k' + R_k\,, \tag{2.18b}$$

$$K_k = \hat{\Sigma}_{k|k-1} C_k' R_{k|k-1}^{-1}\,. \tag{2.18c}$$

The updated posterior Gaussian conditional density is given by the mean and covariance

$$\hat{x}_{k|k} = \hat{x}_{k|k-1} + K_k e_k\,, \tag{2.19a}$$

$$\hat{\Sigma}_{k|k} = (I - K_k C_k)\,\hat{\Sigma}_{k|k-1}\,(I - K_k C_k)' + K_k R_k K_k'\,. \tag{2.19b}$$

The posterior conditional density is given by the Gaussian density $\varphi(x; \hat{x}_{k|k}, \hat{\Sigma}_{k|k})$.

**Example**
We return to the CIR-process in (2.3) to demonstrate the CDEKF. First, to see how the diffusion term of the CIR-process affects the conditional transition density, Figure 2.1 shows the conditional transition densities for the CIR-process starting at $x_{t_0} = 1$ for various values of $\sigma$ for two different transition times. One can show that these are Gamma distributions. For the small transition time, the transition densities look approximately Gaussian, even for large diffusion parameters. For longer transition times, the densities lose their Gaussian shapes fast, even for small diffusion parameters.

To illustrate the prediction and update scheme of the CDEKF, we apply it to the CIR-process. Figure 2.2 shows the conditional densities of the CIR process generated by the CDEKF (which are Gaussian approximations to the Gamma distributions). The process state is initially given by the density $p_{\text{post},k-1}(x) = \delta(x-1)$ at time $t_{k-1}$ (where $\delta$ is the Dirac delta function). The CDEKF then combines the predicted transition density and the observation to compute the posterior distribution that maximises the joint density function $p_{\text{post},k}$ at time $t_k$—assumed all densities are Gaussian.

## 2.3 Parameter estimation in stochastic differential equation models

A fundamental problem in modelling using stochastic differential equations is the identification and estimation of parameters. For such models, different estimation methods exists, e.g. maximum likelihood- and least squares methods. The maximum likelihood method is popular and relies on estimating the conditional probability densities. It is, however, often difficult (or impossible) to compute the analytical likelihood if the model does not satisfy the conditions for having Gaussian transition density functions (which requires linear drift- and state-independent diffusion functions). Instead, it is common to use the CDEKF to supply the transition densities and assume Gaussianity even though the requirements are not fulfilled. It is believed that this approximation is often sufficient to supply reliable parameter estimates and it also has the advantage of being fast to evaluate.

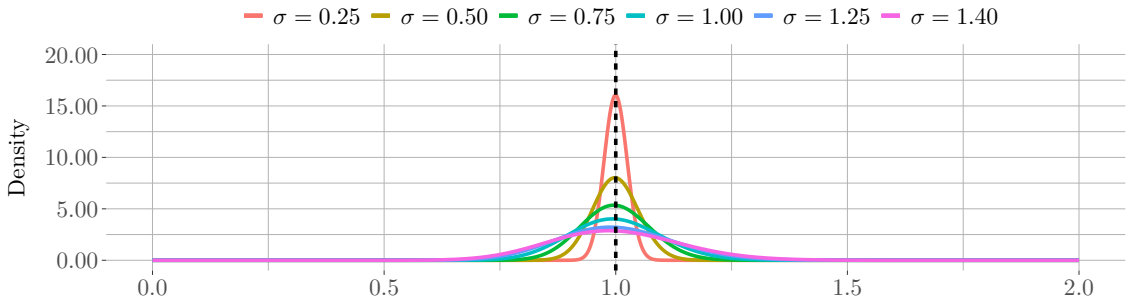


(a) Transition time $\Delta t = 0.01$.

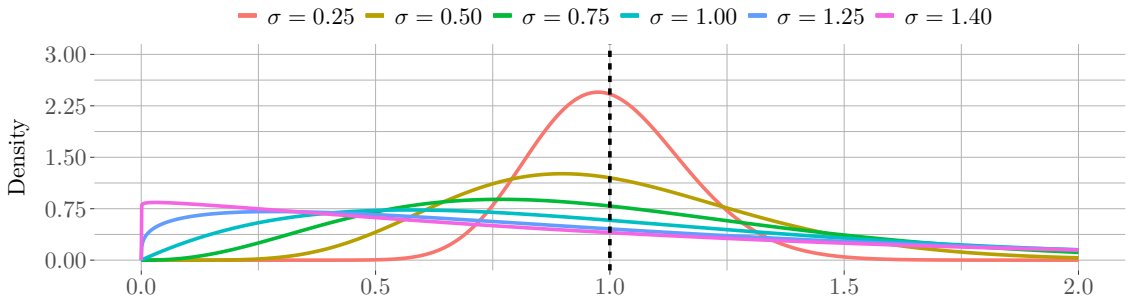


(b) Transition time $\Delta t = 1$.

Figure 2.1: The conditional transition densities for the CIR-process with $\lambda = 1$, $\mu = 1$, and varying $\sigma$. For the small transition time, the transition densities look pretty Gaussian, even for large diffusion parameters. For larger transition times, the densities lose their Gaussian shapes fast, even for small diffusion parameters.

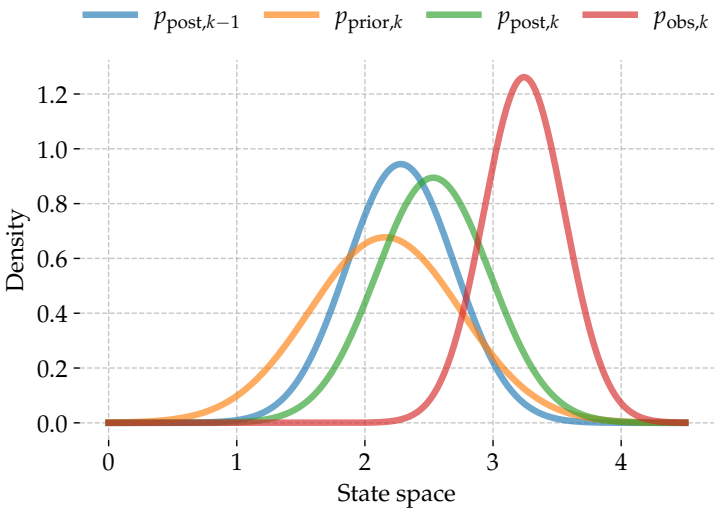


Figure 2.2: The conditional densities of the CIR process (with $\lambda = \mu = \sigma = 1$) computed with the CDEKF. I.e., assuming all densities are Gaussian.

The aim of this section is to introduce the maximum likelihood method for parameter estimation in stochastic differential equation models and show how to approximate the likelihood function using conditional densities supplied by the CDEKF.

### 2.3.1 The maximum likelihood method

One way of estimating parameters in SDE models is the widely used maximum likelihood method. This is based on maximising the joint probability density function of the observation variables evaluated at the observed values w.r.t. a set of parameters in the drift, diffusion, and/or in the observation function.

Formally, $f$, $g$, and $h$ as in (2.8) depends on a set of unknown parameters $\theta$. Now, the likelihood function $L(\theta; \mathcal{Y}_N)$, $L : \mathbb{R}^{n_\theta} \times \mathbb{R}^{n_y \times N} \mapsto \mathbb{R}^+$, is defined as the joint probability density function of the observation variables evaluated at the observed values but considered as a function of the parameters $\theta$,

$$L(\theta; \mathcal{Y}_N) = p_{Y_1, Y_2, \ldots, Y_N}(\mathcal{Y}_N; \theta)\,. \tag{2.20}$$

For time series data, the joint probability density function, $p_{Y_1, Y_2, \ldots, Y_N}$, can be written as a product of one-step ahead conditional transition densities. To do this, we single out the observations one at a time, starting with the last and proceeding all the way through the first

$$\begin{aligned} L(\theta; \mathcal{Y}_N) = p_{Y_1, Y_2, \ldots, Y_N}(\mathcal{Y}_N; \theta) &= p_{Y_N | Y_{N-1}, \ldots, Y_1}(y_N; \theta) p_{Y_1, \ldots, Y_{N-1}}(\mathcal{Y}_{N-1}; \theta)\,, && \text{(2.21a)} \\ &= \prod_{k=1}^{N} p_{Y_k | \mathcal{Y}_{k-1}}(y_1, \ldots, y_k; \theta)\,. && \text{(2.21b)} \end{aligned}$$

For numerical reasons, it is often advantageous to take the log of the likelihood function $\ell : \mathbb{R}^{n_\theta} \times \mathbb{R}^{n_y \times N} \mapsto \mathbb{R}$:

$$\ell(\theta; \mathcal{Y}_N) = \log L(\theta; \mathcal{Y}_N) = \sum_{k=1}^{N} \log p_{Y_k | \mathcal{Y}_{k-1}}(y_1, \ldots, y_k; \theta) \tag{2.22}$$

The maximum likelihood estimate of $\theta$ is then the value of $\theta$ that maximises the likelihood function

$$\hat{\theta}^* = \arg\max_{\theta} L(\theta; \mathcal{Y}_N)\,. \tag{2.23}$$

Thus, to evaluate the likelihood function (and then be able to perform some kind of optimisation), the problem ultimately comes down to estimating the one-step conditional transition densities. Two well-known and used methods for this estimating these are based on the CDEKF and the so-called Laplace approximation (Madsen and Poul Thyregod, 2011). The following section briefly introduces the method based on the CDEKF.

### 2.3.2 Parameter estimation using the CDEKF

The CDEKF as introduced in Section 2.2.2 makes the assumptions that the conditional transition densities are Gaussian. And the log-likelihood function in (2.22) *is the joint density function* of the observation variables (evaluated in the observed values) as a function of the parameters. Consequently, using the conditional transition densities supplied by the CDEKF, the log-likelihood function can be written

$$\begin{aligned} \ell(\theta; \mathcal{Y}) &= \sum_{k=1}^{N} \log \varphi(e_k; 0, R_{k|k-1})\,, && \text{(2.24a)} \\ &= \sum_{k=1}^{N} \log \left( \frac{1}{(2\pi)^{n_y/2} \det(R_{k|k-1})^{1/2}} \exp\left( -\frac{1}{2} e_k^\top R_{k|k-1}^{-1} e_k \right) \right)\,. && \text{(2.24b)} \end{aligned}$$

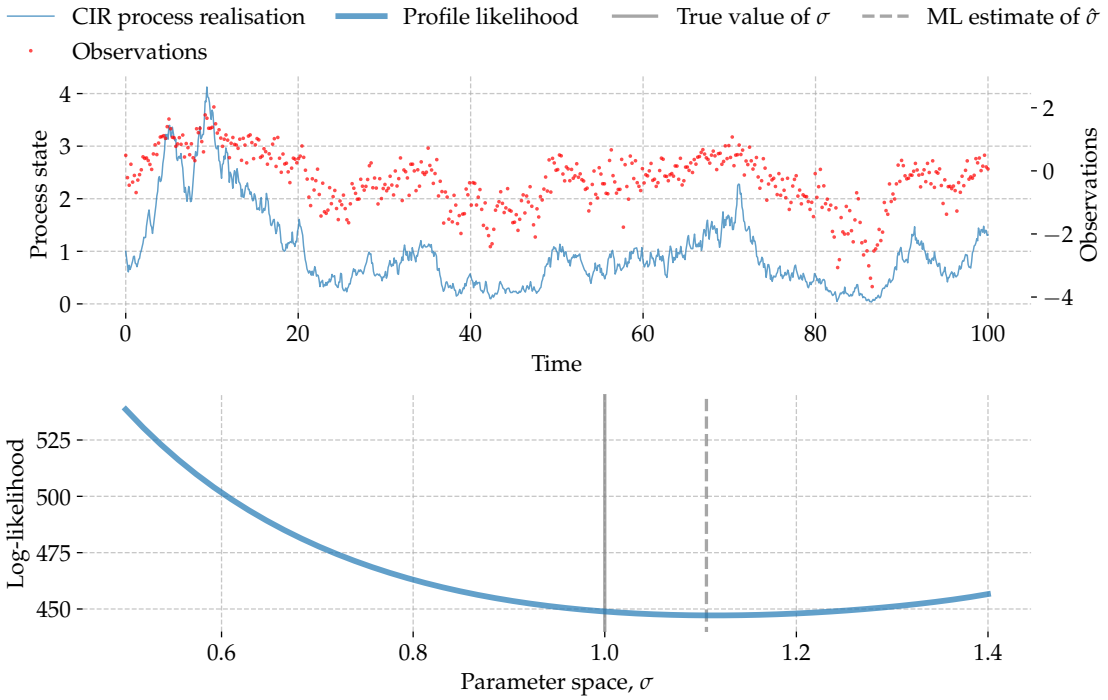


Figure 2.3: Upper plot: A realisation of the CIR process (with $\lambda = \mu = \sigma = 1$) and the observed values. Lower plot: The profile likelihood of $\sigma$ computed using the conditional transition densities supplied by the CDEKF. The solid grey line is the actual value of $\sigma$ while the dashed line is the ML-estimate.

where $e_k$ and $R_{k|k-1}$ are supplied by the CDEKF. The evaluation of the log-likelihood function using the CDEKF is thus recursive since the values $e_k$ and $R_{k|k-1}$ depends on the history up till time $t_k$ of the system.

**Example**

To illustrate the CDEKF for estimating the joint density function of the observation variables, we again consider the CIR-process in (2.3) with $\lambda = \mu = \sigma = 1$ with the observation equation:

$$y_k = \log(x_{t_k}) + v_k\,, \quad v_k \sim N(0, R)\,, \tag{2.25}$$

with $R = 0.1$. The purpose of the log-transformation of $x_t$ is to make the observation space $\mathbb{R}$ (and hopefully the observations are more Gaussian). Figure 2.3 shows a realisation of the process on the time interval $[0, 100]$ with $x_{t_0} = 1$ together with the discrete-time observations with $\Delta t = t_{k+1} - t_k = 0.02$. The observations are evidently noisy as seen from the significant scattering. The lower plot in Figure 2.3 shows the profile likelihood function w.r.t. $\sigma$ together with the true value of $\sigma$ and the maximum likelihood estimate $\hat{\sigma}$. The estimate is a bit off compared to the true value. This could be due to too few data points, too large transition times between observations, the observation function being too non-linear etc.

It is important to emphasise that the likelihood function is based on one-step ahead transition densities. This is important for parameter estimation since for small enough transition times, the transition densities are close to Gaussians. This is despite the underlying system being significantly non-linear.

## 2.4 Discretisation of stochastic differential equation models

SDEs describe continuous state-space models in continuous-time. However, for MPC, some discretisation or expansion of the system or the input variables are needed to make the optimal control problem numerically tractable. For linear SDE models with zero-order hold input and disturbances, closed form time-transition operators exists. If the system is non-linear, other discretisation methods are needed, some of which are introduced and discussed in Chapter 3.

Another problem, which is present for both linear and non-linear systems is how to describe the influence of disturbances on the system. The disturbances are often continuous (and maybe even smooth) functions of time. The often applied discretisations of the disturbances usually assume that they are constant between control points to make the discretisations easier to apply. This section discusses the zero-order hold discretisation scheme and use the arising linear discrete-time model as a motivation for autoregessive models.

Consider the following linear SDE model

$$\mathrm{d}x_t = (Ax_t + Bu_t + Ed_t)\mathrm{d}t + G\mathrm{d}\omega_t \tag{2.26}$$

where $A : \mathbb{R}^{n_x} \mapsto \mathbb{R}^{n_x}$, $B : \mathbb{R}^{n_u} \mapsto \mathbb{R}^{n_x}$, $E : \mathbb{R}^{n_d} \mapsto \mathbb{R}^{n_x}$, $G : \mathbb{R}^{n_x} \mapsto \mathbb{R}^{n_x}$. In the following, let

$$\mathcal{T} \,:\, 0 = t_0 < t_1 < \cdots < t_k < \ldots\,, \tag{2.27}$$

be a set of discrete time points. Given $x_{t_k}$, $u_t$, $d_t$, and $\omega_t$ in $t \in [t_k, t_{k+1}]$, the value of $x_{t_{k+1}}$ is given by

$$x_{t_{k+1}} = x_{t_k} \exp(AT_s) + \int_0^{T_s} \exp(A\tau)Bu_\tau \mathrm{d}\tau + \int_{t_k}^{t_{k+1}} \exp(A\tau)Ed_\tau \mathrm{d}\tau + w_k\,, \tag{2.28}$$

where $w_k = \int_{t_k}^{t_{k+1}} \exp(A(t_{k+1} - \tau))G\mathrm{d}\omega_\tau$ and is characterised by the distribution $w_k \sim N(0, Q)$ with $Q = \int_0^{T_s} \exp(A\tau)GG^\top \exp(A^\top\tau)\mathrm{d}\tau$ Hagdrup et al., 2016. Since $u_t$ is the input variable, we can choose it be constant between each time sample (known as zero-order hold). In the following, let the input be given by the zero-order hold scheme

$$u_t = \sum_{k=0}^{N-1} \chi_{[t_k, t_{k+1}[}(t) u_k\,, \quad \nu = \{u_k\}_{k=0}^{N-1}\,, \tag{2.29}$$

where $\chi_I(t)$ is the characteristic function that attains 1 if $t \in I$ and 0 otherwise. We cannot make the same zero-order hold assumption with the disturbances directly without error terms appearing—but let us try anyway: Define the variable

$$d_t = \sum_{k=0}^{N-1} \chi_{[t_k, t_{k+1}[}(t) d_k\,, \quad \eta = \{d_k\}_{k=0}^{N-1}\,. \tag{2.30}$$

where $\eta = \{d_k\}_{k=0}^{N-1}$ is the *true mean values* of the disturbance process in the time intervals $[t_k, t_{k+1}[$. Then the so-called *zero-order hold discretisation* of the linear diffusion process in (2.26) is

$$x_{t_{k+1}} = A_d x_{t_k} + B_d u_k + E_d d_k + w_k + \xi_k\,, \tag{2.31}$$

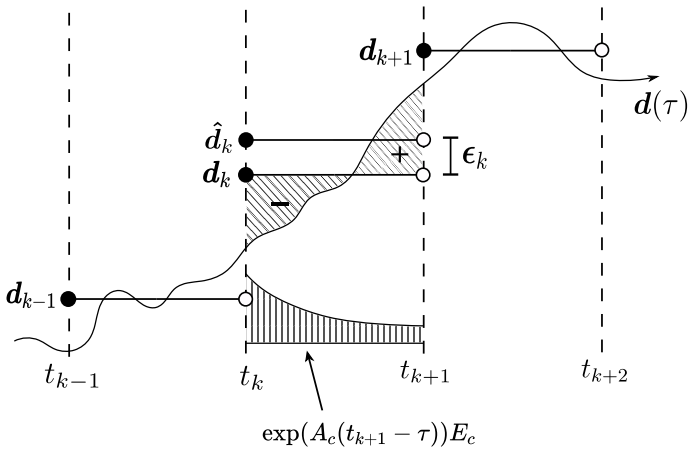

Figure 2.4: The discretisation related to the disturbances.

where

$$A_d = \exp(AT_s)\,, \tag{2.32a}$$

$$B_d = \int_0^{T_s} \exp(A\tau)B\mathrm{d}\tau\,, \tag{2.32b}$$

$$E_d = \int_0^{T_s} \exp(A\tau)E\mathrm{d}\tau\,. \tag{2.32c}$$

$\xi_k = \int_{t_k}^{t_{k+1}} \exp(A(t_{k+1}-\tau))E(d_\tau - d_k)\mathrm{d}\tau$ is an error term from the zero-order hold assumption on the disturbances. If the true mean value is further replaced by an estimate, $d_k = \hat{d}_k + \epsilon_k$, an additional term appears:

$$x_{t_{k+1}} = A_d x_{t_k} + B_d u_k + E_d \hat{d}_k + E_d \epsilon_k + w_k + \xi_k\,. \tag{2.33}$$

Figure 2.4 illustrates the zero-order hold scheme of the disturbances and depicts the error terms appearing. As discussed in Paper F, it is not trivial how to further describe and predict the error terms $E\epsilon_k$, $\xi_k$, and thus, it is easier to leave them out and assume they equal zero. Another possibility may be to include them in the process $w_k$ such that the filtering takes the increased uncertainty into account (which is not considered in this dissertation).

For simplicity, we disregard the error terms $E\epsilon_k$ and $\xi_k$ in the discretisation in (2.33). I.e., the system ends up having the form:

$$\hat{x}_{t_{k+1}} = A_d \hat{x}_{t_k} + B_d u_k + E_d \hat{d}_k + w_k\,. \tag{2.34}$$

The hat on $\hat{x}$ indicates that it is an estimate of $x$ since the formulation is no longer exact and is driven by the estimated disturbances, $\hat{d}$. This is the starting point for the motivation of discrete-time Markov models in this dissertation. A special class of discrete-time models are the AutoRegressive with eXogenous input (ARX) models.

### 2.4.1 Autoregressive Models with Exogenous Inputs

This section very briefly introduces the ARX model class. Paper D supplies a more thorough and contextual introduction to the model class and its applications and how to estimate embedded parameters. Let $\{Y_k; k \in \mathbb{N}\}$, $Y_k \in \mathbb{R}$, be a stochastic process, then an ARX model of order $m$ is

$$\alpha(\mathrm{B})Y_k = \beta(\mathrm{B})u_k + \varepsilon_k\,, \tag{2.35}$$

where $\alpha$ and $\beta$ are polynomials in the backshift operator B, $\mathrm{B}^i Y_k = Y_{k-i}$, such that $\alpha(\mathrm{B}) = \alpha_1 B + \alpha_2 B^2 + \cdots + \alpha_m B^m$. $u_k \in \mathbb{R}^{n_u+n_d}$ is the input vector containing all the inputs that drives the system (including disturbances), and $\{\varepsilon_k; k \in \mathbb{N}\}$, $\varepsilon_k \in \mathbb{R}$ is a white noise process s.t. $\varepsilon_k \sim N_{\text{iid}}(0, \sigma_\varepsilon^2)$. It relates to the discrete-time model in (2.34) by being a linear map from the state space and input space to the state space, predicting the next state of the system. Also, all autoregressive models can also be written as state models Madsen, 1985.

Given a series of observations of $Y_k$ separated equally in time, $\mathcal{Y}^n = (y_1, y_2, \ldots, y_n)^\top$, the parameters in (2.35) ($\alpha_i$ and $\beta_i$) are given in closed form. Maximum likelihood estimation or least squares estimation ends up with the same estimator for the parameters $\theta = (\alpha_1, \ldots, \alpha_m, \beta_1, \ldots, \beta_m)^\top$,

$$\hat{\theta}^* = (X_n^\top X_n)^{-1} X_n^\top \mathcal{Y}^n \,, \tag{2.36}$$

where $X_n \in \mathbb{R}^{n \times m(1+n_u+n_d)}$ is the so-called *design matrix* (Madsen and Poul Thyregod, 2011).

For a more theoretical introduction to regression models and more details, see (Madsen, 2007).

This kind of model is less related to physics in the sense that it is not as easy to induce physical constraints and features in its structure. One could call it less grey and more black. The parameters are simply chosen such that the past $m$ observations and inputs fit the next observation best in the least-squares sense. On the other hand, it has the advantage of being fast and easy to perform parameter estimation from the closed-form solution in (2.36). Due to its more black nature, one does not need to worry as much about the physical interpretation. Another problem is that the parameters depend on the sampling rate (the model is only valid for the given sampling rate), and we typically need much more parameters to form state-space models compared to continuous-time equivalents.

A limitation of the model is its linear structure: It is not directly possible to estimate parameters that appear non-linearly in the model. But some times one needs to estimate non-linearities in the model, fx where a parameter is expanded into a new basis such that it can vary in either time or space. Paper D presents an extended ARX-model type where parameters are split into linear- and non-linear sets, where they two sets are estimated iteratively and in parallel. This extension makes it possible to estimate non-linear dependencies of parameters in ARX-models and does it in a computationally efficient and robust manner.

# 3 Model Predictive Control

The difference between predictive and non-predictive control is the framework of being able to decide the control signal based on future predictions. What makes this possible, is the model of the system, which is able to predict the system behaviour as a function of a system input.

This chapter outlines the model predictive control framework and introduces linear- and non-linear model predictive control frameworks.

## 3.1 The Model Predictive Control Principle

In the following, let the following

$$\mathcal{T} : 0 = t_0 \leq t_1 \leq t_2 \leq \cdots \leq t_k \leq \ldots \tag{3.1}$$

be a sequence of time points where the controller computes and applies a new control signal to the controlled system.

The model predictive control principle is based on an algorithm constituting the following steps that run in a recursive manner (closed loop)

1. Initialise $t_0 = 0$, $\hat{x}_{0|0} = x_0$, and $k = 1$.
2. Filtering: When the next observation $y_k$ becomes available, filter the mean and covariance of the system state, $\hat{x}_{k|k}$ and $\hat{P}_{k|k}$ using an appropriate filter.
3. Optimal control: Given the filtered state, solve the optimal control problem and apply the optimal control until the next control time $\hat{u}^*(t)$, $t \in [t_k, t_{k+1}[$.
4. Go to step 2 and repeat until finished.

The framework is also displayed in Fig 3.1.z As information becomes available, the filter estimates the underlying system states. Based on the new information and state estimate, the controller updates its optimal control trajectory. Many real life systems are stochastic and models are not exact representations of the real life system, therefore closed loop operation is necessary to update the input signal to mitigate stochasticity and model errors. The following two subsections briefly introduce the filtering and optimal control steps.

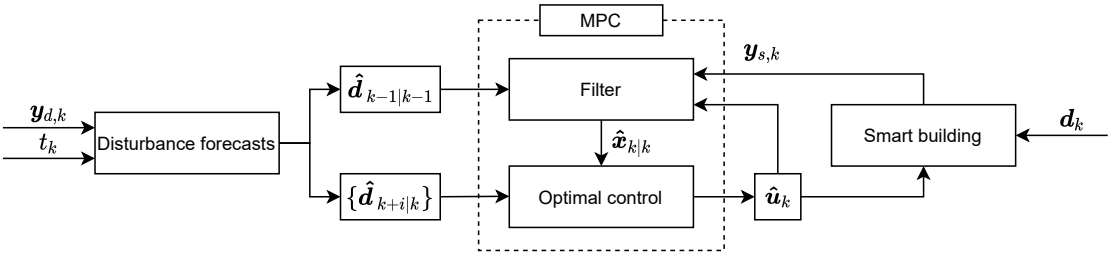


Figure 3.1: The MPC framework. The MPC-part with the filter and optimal control steps is highlighted by the dashed box. It takes as input future disturbances, the current input, and the observed system.

### 3.1.1 Filtering

The filtering principle was introduced in Sec. 2.2. Briefly, filtering accumulates information and estimates the most likely underlying system state (given the underlying system model) to generate the observed information. Fx, a very popular filtering method based on the Kalman filter takes in prior information $\{\hat{x}_{k|k-1}, \hat{P}_{k|k-1}, y_k\}$ at time $t_k$ and returns the posterior estimates of the mean and covariance of the system state. In many real life cases, however, it is significantly wrong to use only the mean and variance if the objective function (e.g.) is sufficiently asymmetric (Haessig et al., 2015). Still, the mean- and variance filtering is by far the most popular filtering technique in practice (Mantovani and Ferrarini, 2015; C. Thilker, Bacher, and Madsen, 2022; Vukov et al., 2015; N. Brok et al., 2022).

### 3.1.2 Optimal control

Optimal control—as indicated by its name—is the art of controlling a dynamical system in an optimal manner w.r.t. an objective, $q$. An infinite-horizon optimal control problem has the form:

$$\min_{u_t} \quad \int_{t_k}^{\infty} q(x_\tau, u_\tau, d_\tau)\mathrm{d}\tau\,, \tag{3.2a}$$

$$\text{s.t.} \quad x_t = \hat{x}_{k|k} + \int_{t_k}^{t} f(x_\tau, u_\tau, d_\tau; \theta)\mathrm{d}\tau + \int_{t_k}^{t} g(x_\tau; \theta)\mathrm{d}\omega_\tau\,, \qquad t \geq t_k\,, \tag{3.2b}$$

$$u_t \in \mathcal{U}(t) \qquad t \geq t_k\,, \tag{3.2c}$$

$$x_t \in \mathcal{X}(t) \qquad t \geq t_k\,, \tag{3.2d}$$

where $q : \mathbb{R}^{n_x} \times \mathbb{R}^{n_u} \times \mathbb{R}^{n_d} \mapsto \mathbb{R}$ is the infinitesimal objective (or cost), $\mathcal{U}(t)$ is the set of feasible inputs $u_t$ at time $t$, and $\mathcal{X}$ is the set of constraints imposed on the system states.

There are, however, two problems with the above formulation with regards to solving the optimal control problem. First, the integral in (3.2a) is numerically intractable since $q$ is not $L^1$-integrable in general (due to the infinite limit in time and in general $q \not\to 0$). Second, the stochastic differential equation in (3.2b) is on strong form, which cannot be solved without knowledge of the Brownian motion's trajectory.

To overcome the first problem, instead of considering an infinite horizon optimal control problem, consider instead the following finite horizon objective function:

$$\phi_k(u) = \int_{t_k}^{t_k+T} q(x_\tau, u_\tau, d_\tau)\mathrm{d}\tau + q_b(x_{t_k+T}) \tag{3.3}$$

where $\phi_k : \mathbb{R}^{n_u} \mapsto \mathbb{R}$ is the objective function and $q_b : \mathbb{R}^{n_x} \mapsto \mathbb{R}$ is the end-point cost (sometimes called cost-to-go) term. The integral in (3.3) is convergent assuming $|q| < \infty$, $\forall x, u, d$ or attains infinite only at a finite number of points. Instead of extending the integral to infinity, the cost-to-go term should reflect the cost of the system state at the final time $t_k + T$. This is of course an approximation to infinite horizon control problem. However, in closed loop, if $T$ is large enough and $q_b$ is chosen properly, an optimal control problem using (3.3) should perform close to that of a the infinite horizon control problem (Schlüter et al., 2019).

To overcome the second problem, it is common to use the expectation of $x_t$. And since the Itô integral is a martingale, it disappears in the expression of the expectation of $x_t$. This is also called the *certainty equivalent* optimal control problem. This corresponds to considering the first order Taylor expansion of the SDE. Likewise, higher order Taylor

expansions can be used and may supply more accurate predictions. Other methods are to include the variance in the objective function (as to minimise the variance) (Capolei et al., 2015) and stochastic programming (Prékopa, 2013).

The two simplifications applied to the optimal control problem turns it into a numerically tractable problem on the so-called Bolza form (Clarke, 1976)

$$\min_{u_t} \quad \left\{ \phi_k(u; \hat{x}_{k|k}, d) = \int_{t_k}^{t_k+T} q(x_\tau, u_\tau, d_\tau) \mathrm{d}\tau + q_b(x_{t_k+T}) \right\} , \tag{3.4a}$$

$$\text{s.t.} \quad x_t = \hat{x}_{k|k} + \int_{t_k}^{t} f(x_\tau, u_\tau, d_\tau; \theta) \mathrm{d}\tau , \qquad t \in [t_k, \infty[ , \tag{3.4b}$$

$$u_t \in \mathcal{U}(t) \qquad t \in [t_k, \infty[ , \tag{3.4c}$$

$$x_t \in \mathcal{X}(t) \qquad t \in [t_k, \infty[ , \tag{3.4d}$$

where the notation $\phi_k(u; \hat{x}_{k|k}, d)$ emphasises the dependence of the optimal control problem on the initial value and disturbance sequence.

## 3.2 Linear (Quadratic) Model Predictive Control

In the case where the model equations are linear, the objective function is linear or quadratic, and the constraints are linear, the optimal control problem becomes convex, which enables fast solvers to be used to perform the numerical optimisation (Boyd and Vandenberghe, 2004). And if only equality constraints are present and the objective is quadratic, the optimisation problem has a closed form solution (Åström, 2012).

This section briefly introduces the linear quadratic optimal control problem and its solution including the discretisation of the objective function. It is necessary to discretise both the system and objective function in order to make the problem numerically tractable. The rest of this section gives a simple method for doing this.

In the following, let

$$\mathcal{T}_k \, : \, t_k = \tau_0^k < \tau_1^k < \cdots < \tau_N^k = t_k + T , \tag{3.5}$$

be a discretised grid of time points in which we split the control horizon. Consider the following optimal control problem

$$\min_{u_t} \quad \int_{t_k}^{t_k+T} \frac{1}{2}(x_\tau - r_\tau^{(x)})^\top Q (x_\tau - r_\tau^{(x)}) + \tag{3.6a}$$

$$\frac{1}{2}(u_\tau - r_\tau^{(u)})^\top R (u_\tau - r_\tau^{(u)}) + c_\tau^\top u_\tau \mathrm{d}\tau , \tag{3.6b}$$

$$\text{s.t.} \quad x_t = \hat{x}_{k|k} + \int_{t_k}^{t} A x_\tau + B u_\tau + E d_\tau \mathrm{d}\tau + \int_{t_k}^{t} G \mathrm{d}\omega_\tau , \qquad t \in [t_k, t_k + T[ , \tag{3.6c}$$

$$H_u u_t \leq b_t^{(u)} , \qquad t \in [t_k, t_k + T[ , \tag{3.6d}$$

$$H_x x_t \leq b_t^{(x)} , \qquad t \in [t_k, t_k + T[ . \tag{3.6e}$$

where $r_t^{(x)} : \mathbb{R} \mapsto \mathbb{R}^{n_x}$ and $r_t^{(u)} : \mathbb{R} \mapsto \mathbb{R}^{n_u}$ are the desired reference trajectory of the system and the input, respectively. We assume that these are also piecewise constant (as with the input and disturbances):

$$r_t^{(u)} = r_i^{(u)} \quad \text{and} \quad r_t^{(x)} = r_i^{(x)} , \quad t \in [\tau_i^k, \tau_{i+1}^k[ . \tag{3.7}$$

$H_u : \mathbb{R}^{n_u} \mapsto \mathbb{R}^{n_{c_u}}$ and $H_x : \mathbb{R}^{n_x} \mapsto \mathbb{R}^{n_{c_x}}$ are the linear operators defining the constraints on the input and system states together with $b_t^{(u)} : \mathbb{R} \mapsto \mathbb{R}^{n_{c_u}}$ and $b_t^{(x)} : \mathbb{R} \mapsto \mathbb{R}^{n_{c_x}}$, respectively. $c_t : \mathbb{R} \mapsto \mathbb{R}^{n_u}$ is the economic cost related to the input. When the system is linear (and the diffusion function is state-independent), the zero-order hold discretisation derived in Section 2.4 is a commonly used discretisation scheme. We have carefully treated the errors that arise from the discretisation and we hence know the consequences and risks associated with it. Therefore, we write the approximated discrete-time system model as:

$$x_{k+1} = A_d x_k + B_d u_k + E_d \hat{d}_k + w_k \,. \tag{3.8}$$

The objective function can be discretised in different ways. In the linear quadratic case as in (3.6a), exact discretisation methods exists based on the matrix exponential. However, if the time sample $T_s$ is sufficiently small, approximative discretisations may be simpler — e.g. the Euler discretisation: Consider the first part of the objective in (3.6a) where we use the left end point in each time interval as the approximating function value, $x_{\tau_i^k}$:

$$\int_{t_k}^{t_k+T} \frac{1}{2}(x_\tau - r_\tau^{(x)})^\top Q (x_\tau - r_\tau^{(x)}) \mathrm{d}\tau \approx \sum_{i=0}^{N-1} \frac{1}{2} x_{\tau_i^k}^\top Q x_{\tau_i^k} + s_{\tau_i^k}^\top x_{\tau_i^k} + \frac{1}{2} {r_{\tau_i^k}^{(x)}}^\top Q r_{\tau_i^k}^{(x)} \,, \tag{3.9}$$

where $s_{\tau_i^k}^\top = -{r_{\tau_i^k}^{(x)}}^\top Q$. Analogously, the second part of the objective function becomes

$$\int_{t_k}^{t_k+T} \frac{1}{2}(u_\tau - r_\tau^{(u)})^\top R (u_\tau - r_\tau^{(u)}) \mathrm{d}\tau \approx \sum_{i=0}^{N-1} \frac{1}{2} u_i^\top R u_i + {r_i^{(u)}}^\top R u_i + \frac{1}{2} {r_i^{(u)}}^\top R r_i^{(u)} \,. \tag{3.10}$$

Assuming that $c_t$ is also piecewise constant such that $c_t = c_i$ for $t \in [\tau_i^k, \tau_{i+1}^k[$, the objective function can be written as sum (disregarding terms that does not depend on either $x$ or $u$)

$$\phi_d = \sum_{i=k}^{k+N-1} \frac{1}{2} x_{\tau_i^k}^\top Q x_{\tau_i^k} + s_{\tau_i^k}^\top x_{\tau_i^k} + \frac{1}{2} u_i^\top R u_i + {r_i^{(u)}}^\top R u_i \,. \tag{3.11}$$

With the discretised model, (3.8), and objective function, (3.11), it is straight forward to evaluate the objective function and compute gradients. Using the closed form of the discretised dynamics, the objective function can be written

$$U_k^*(x_0, \{\hat{d}_{k+i|k}\}_{i=0}^{N-1}) = \arg\min_{U_k} \quad \frac{1}{2} U_k^\top P U_k + q^\top U_k \,, \tag{3.12a}$$

$$\text{s.t.} \quad u_{k+i} \in \mathcal{U}_i \,, \tag{3.12b}$$

$$x_{k+i+1} \in \mathcal{X}_i \,, \tag{3.12c}$$

$$i = 0, \ldots, N-1 \,, \tag{3.12d}$$

where $U_k = [u_k^\top, u_{k+1}^\top, \ldots, u_{k+N-1}^\top]^\top$ is the vectorised input and $U_k^*$ is the optimal control solution. The matrix $P$ and vector $q$ are given by the following:

$$P = (\Gamma_u^\top \bar{Q} \Gamma_u + \bar{R}) \,, \tag{3.13a}$$

$$q = (\Gamma_u^\top \bar{Q} \Phi x_0 + \Gamma_u^\top \bar{Q} \Gamma_d \hat{D}_k + \Gamma_u^\top S_k + C_k - \bar{R} \bar{U}_k) \,, \tag{3.13b}$$

where

$$\hat{D}_k = \left[\hat{d}_{k|k}^\top, \ldots, \hat{d}_{k+N-1|k}^\top\right]^\top \tag{3.14a}$$

$$S_k = \left[s_k^\top, s_{k+1}^\top, \ldots, s_{k+N-1}^\top\right]^\top \tag{3.14b}$$

$$\Phi = \left[A^\top, (A^2)^\top, \ldots, (A^N)^\top\right]^\top \tag{3.14c}$$

$$\Gamma_u = \begin{bmatrix} B & 0 & \ldots & 0 \\ AB & B & \ldots & 0 \\ A^2B & AB & \ddots & \vdots \\ \vdots & \vdots & \ddots & 0 \\ A^{N-1}B & A^{N-2}B & \ldots & B \end{bmatrix} \tag{3.14d}$$

$$\Gamma_d = \begin{bmatrix} E & 0 & \ldots & 0 \\ AE & E & \ldots & 0 \\ A^2E & AE & \ddots & \vdots \\ \vdots & \vdots & \ddots & 0 \\ A^{N-1}E & A^{N-2}E & \ldots & E \end{bmatrix} \tag{3.14e}$$

$$\bar{Q} = \operatorname{diag}(Q, \ldots, Q) \tag{3.14f}$$

$$\bar{R} = \operatorname{diag}(R, \ldots, R) \tag{3.14g}$$

$$\bar{U}_k = \left[r_k^{(u)}, \ldots, r_{k+N-1}^{(u)}\right]^\top \tag{3.14h}$$

$$C_k = [c_k^\top, c_{k+1}^\top, \ldots, c_{k+N-1}^\top]^\top \tag{3.14i}$$

If $Q \neq 0_{n_x \times n_x}$ or $Q \neq 0_{n_u \times n_u}$ ($0_{n\times m}$ is the zero matrix of dimension $n \times m$) and $\mathcal{U}$ and $\mathcal{X}$ are only equality constraints, (3.12) has a closed form solution. Otherwise, numerical solvers are needed. The `CVXOPT` library (Andersen, Dahl, and Vandenberghe, 2022), available through Python, can be readily used for this purpose.

## 3.3 Non-linear Model Predictive Control

If the model $f$ is non-linear, a closed-form solution of the system predictions does not exists in general. A possibility to overcome this is to linearise the system around the predicted point $\hat{x}_{k|k-1}$ and solve the arising linear optimal control problem. However, if the system is sufficiently non-linear, this solution may produce suboptimal performance. Instead, methods such as single- and multiple shooting can be used. This section introduces these methods and how they work while giving illustrative examples.

**Representation of the input**
To numerically solve optimal control problems, it is necessary to formulate the input in terms of optimisation variables. So far, we have seen the zero-order hold scheme where each zero-order value is an optimisation variable. We could also have chosen a continuous representation in terms of series expansions. E.g., a Fourier expansion or a polynomial expansion:

$$u_{\text{Fourier},t}^N = \frac{a_0}{2} + \sum_{k=1}^{N} \left( a_k \cos \frac{2\pi}{T} kt + b_k \sin \frac{2\pi}{T} kt \right), \tag{3.15a}$$

$$u_{\text{Poly},t}^N = \sum_{k=0}^{N} p_k t^k, \tag{3.15b}$$

where $a_k \in \mathbb{R}$ $b_k \in \mathbb{R}$, $p_k \in \mathbb{R}$ are parameters of the expansions and $T$ is the time horizon of the optimal control problem. In practice, however, it is often easier to implement zero-order hold inputs instead of continuous signals. But series expansions have the advantage of some times reducing the amount of optimisation variables. Then afterwards, a zero-order hold of the optimal continuous input can be implemented in the system. Nonetheless, the system operator needs to decide how to best represent the input.

### 3.3.1 The adjoint method

To efficiently minimise a function requires the gradients of the function. The adjoint method provides a way to evaluate gradients of the objective function in (3.4). The goal of the following derivation is to end up with a set of ODEs that can be solved to compute the gradients of the objective function w.r.t. the input variables. To derive the adjoint equations, consider the objective function:

$$\phi_k(u) = \int_{t_k}^{t_k+T} q(x_\tau, u_\tau)\mathrm{d}\tau + q_b(x_{t_k+T})\,. \tag{3.16}$$

We now introduce the Lagrange multiplier $\lambda_t^k : \mathbb{R} \mapsto \mathbb{R}^{n_x}$ and add zero to the equation

$$\phi_k(u) = \phi_k(u) - \int_{t_k}^{t_k+T} \lambda_\tau^\top(\dot{x}_\tau - f(x_\tau, u_\tau, d_\tau))\mathrm{d}\tau\,, \tag{3.17}$$

where the integral equals zero since $\dot{x}_\tau = f(x_\tau, u_\tau, d_\tau)$. In the rest of the derivation, the dependences of functions will be omitted. Taking the derivative on both sides yields

$$\frac{\partial \phi_k}{\partial u} = \int_{t_k}^{t_k+T} \frac{\partial q}{\partial u} + \frac{\partial q}{\partial x} s \mathrm{d}\tau - \int_{t_k}^{t_k+T} \lambda^\top \left(\frac{\partial s}{\partial t} - \frac{\partial f}{\partial x} s - \frac{\partial f}{\partial u}\right)\mathrm{d}\tau + B_{t_k+T}\,, \tag{3.18}$$

where $s = \frac{\partial x}{\partial u}$ is the sensitivity of $x$ and $B = \frac{\partial q_b}{\partial x}(x_{t_k+T})\frac{\mathrm{d}x}{\mathrm{d}u}(u_{t_k+T})$ is the derivative of the boundary term evaluated at time $t_k + T$. By splitting the second integral and applying integration by parts to the term $\lambda^\top \frac{\mathrm{d}s}{\mathrm{d}t}$, we get

$$\begin{aligned}\int_{t_k}^{t_k+T} \lambda^\top \left(\frac{\partial s}{\partial u} - \frac{\partial f}{\partial x} s - \frac{\partial f}{\partial u}\right)\mathrm{d}\tau &= \int_{t_k}^{t_k+T} \lambda^\top \frac{\partial s}{\partial t}\mathrm{d}\tau - \int_{t_k}^{t_k+T} \lambda^\top \left(\frac{\partial f}{\partial x} s + \frac{\partial f}{\partial u}\right)\mathrm{d}\tau\,,\\ &= \left[\lambda_\tau^\top s_\tau\right]_{\tau=t_k}^{t_k+T} - \int_{t_k}^{t_k+T} \frac{\partial \lambda^\top}{\partial t} s \mathrm{d}\tau - \int_{t_k}^{t_k+T} \lambda^\top \left(\frac{\partial f}{\partial x} s + \frac{\partial f}{\partial u}\right)\mathrm{d}\tau\,.\end{aligned} \tag{3.19}$$

Inserting this into (3.18) yields

$$\frac{\partial \phi}{\partial u} = \int_{t_k}^{t_k+T} \frac{\partial q}{\partial u} + \frac{\partial q}{\partial x} s \mathrm{d}\tau - \left[\lambda_\tau^\top s_\tau\right]_{\tau=t_k}^{t_k+T} + \int_{t_k}^{t_k+T} \frac{\partial \lambda^\top}{\partial t} s \mathrm{d}\tau + \int_{t_k}^{t_k+T} \lambda^\top \left(\frac{\partial f}{\partial x} s + \frac{\partial f}{\partial u}\right)\mathrm{d}\tau + B_{t_k+T}\,. \tag{3.20}$$

Re-arranging the terms

$$\frac{\partial \phi}{\partial u} = \int_{t_k}^{t_k+T} \frac{\partial q}{\partial u} + \lambda^\top \frac{\partial f}{\partial u}\mathrm{d}\tau - \left[\lambda_\tau^\top s_\tau\right]_{\tau=t_k}^{t_k+T} - \int_{t_k}^{t_k+T} \left(\lambda^\top \frac{\partial f}{\partial x} + \frac{\partial \lambda^\top}{\partial t} + \frac{\partial q}{\partial x}\right) s \mathrm{d}\tau + B_{t_k+T}\,. \tag{3.21}$$

Let's now require that $\lambda^\top$ satisfies the following differential equation backwards in time

$$-\frac{\partial \lambda^\top}{\partial t} = \lambda^\top \frac{\partial f}{\partial x} + \frac{\partial q}{\partial x}\,, \quad \text{with} \quad \lambda_{t_k+T}^\top = \frac{\partial q_b}{\partial x}(x_{t_k+T})\,. \tag{3.22}$$

But then the last integral in (3.21) vanishes! And even better; the boundary term at $\tau = t_k + T$ in integration by parts cancels out the cost-to-go term, $B_{t_k+T} = \frac{\partial q_b}{\partial x}(x_{t_k+T})\frac{\mathrm{d}x}{\mathrm{d}u}(u_{t_k+T})$. And since the sensitivity, $\frac{\partial x}{\partial u}$, is initialised to zero, the other boundary term of $[\lambda_\tau^\top s_\tau]_{\tau=t_k}^{t_k+T}$ at $\tau = t_k$ is also zero. Thus, if $\lambda$ satisfies (3.22), the derivative of the objective function in (3.21) w.r.t. the input $u$ simplifies to solving the integral

$$J = \frac{\partial \phi}{\partial u} = \int_{t_k}^{t_k+T} \frac{\partial q}{\partial u} + \lambda^\top \frac{\partial f}{\partial u} \mathrm{d}\tau \,, \tag{3.23}$$

where $J \in \mathbb{R}^{n_u}$. Since ODEs are solved by integration, we can couple the equations in (3.23), (3.22), and the system dynamics such that computing the derivative is equivalent to solving the following system of ODEs:

$$\frac{\partial x}{\partial t} = f \,, \qquad x_{t_k} = \hat{x}_{k|k} \,, \tag{3.24a}$$

$$-\frac{\partial \lambda^\top}{\partial t} = \lambda^\top \frac{\partial f}{\partial x} + \frac{\partial q}{\partial x} \,, \qquad \lambda_{t_k+T}^\top = \frac{\partial q_b}{\partial x}(x_{t_k+T}) \,, \tag{3.24b}$$

$$\frac{\partial J}{\partial t} = \frac{\partial q}{\partial u} + \lambda^\top \frac{\partial f}{\partial u} \,, \qquad J_{t_k+T} = 0 \,. \tag{3.24c}$$

where $\frac{\partial \phi}{\partial u} = J_{t_k}$ is the solution of $J$ at the initial time. This is in perfect analogy to the first order optimality conditions to an equality constrained optimisation problem. For a deeper discussion on the derivation, see John Bagterp Jørgensen, 2007.

**On solving the adjoint equations**
Solving the adjoint equations in (3.22) (to compute the Jacobian of the optimal control problem) requires the values of $x_t$—but the dynamics of $x$, $\dot{x} = f$, are defined forward in time (in contrast to (3.22) which is backwards in time). Solving the system in (3.24) can be done in different ways:

1. Solve $\dot{x} = f$ forward in time to retrieve $x_{t_k+T}$. Then, using $x_{t_k+T}$ as initial condition, solve the entire system (3.24) backwards in time. Numerically, this method might be unstable (since we solve $f$ backwards in time), and it might not produce the same result as if it was solved forward in time.

2. Solve $\dot{x} = f$ forward in time and interpolate between the saved points to retrieve the solution at any given time when solving for $\lambda$ and $\frac{\mathrm{d}\phi}{\mathrm{d}u}$ backwards. This is fast but memory-intensive.

3. Every time a value of $x$ is needed, re-solve $\dot{x} = f$ forward (expensive!). Alternatively, save *checkpoints* of the solution of $x_t$ in a grid $t \in \{\tau_0, \tau_1, \ldots, \tau_N\}$ and instead solve $\dot{x} = f$ from the nearest point when needed.

Independently of the approach, implementational care needs to be given to solving (3.24). The next section introduces the single shooting method, which suffers from the issues raised above. Multiple shooting, partly, gets around the instability issues (Morrison, Riley, and Zancanaro, 1962).

**Example**
This example demonstrates the adjoint method for a small example to illustrate how it works and is used to solve optimal control problems. For this example, we use again the CIR-process, but this time modified such that it includes a disturbance and input:

$$\mathrm{d}x_t = \lambda(\mu - x_t + x_t^2 d_t + u_t)\mathrm{d}t + \sigma\sqrt{x_t}\mathrm{d}\omega_t \tag{3.25}$$

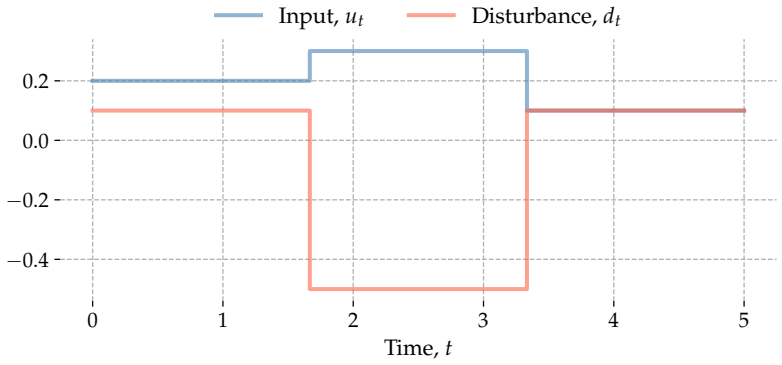


Figure 3.2: The solution to the adjoint system equations in (3.24) of the system in (3.26).

where $d_t : \mathbb{R} \mapsto \mathbb{R}$ is the disturbance process and $u_t : \mathbb{R} \mapsto \mathbb{R}$ is the controllable input. The factor $x_t^2$ on the disturbance process makes sure that the disturbances goes to zero as the process goes to zero (while adding non-linearities to the system). For numerical purposes, we consider the Lamperti-transformed process in the optimal control problem:

$$\mathrm{d}z_t = \left( \frac{\lambda \left( 4(\mu + u_t) - z_t^2 + \frac{z_t^4}{4} d_t \right) - \sigma^2}{2z_t} \right) \mathrm{d}t + \sigma \mathrm{d}\omega_t \,, \tag{3.26}$$

with $z_t$ being the Lamperti-transformed variable. Consider now the optimal control problem

$$\min_{u_i} \qquad \left\{ \phi = \int_0^{T=5} (z_\tau - r_\tau)^2 + \alpha u_\tau^2 \mathrm{d}\tau \right\} \,, \tag{3.27a}$$

$$\text{s.t.} \qquad \dot{z}_t = \frac{\lambda \left( 4(\mu + u_t) - z_t^2 + \frac{z_t^4}{4} d_t \right) - \sigma^2}{2z_t} \,, \qquad t \geq t_k \,, \tag{3.27b}$$

where $r_t$ is a reference signal that we wish to steer the system along and $\alpha u_t^2$ (with $\alpha = 0.001$) is a regularisation term on the input to ensure uniqueness. We use the following discretisation of the input and disturbance:

$$u_t = \sum_{i=0}^{2} u_i \chi_{[i \cdot T/3, (i+1) \cdot T/3[}(t), \quad d_t = \sum_{i=0}^{2} d_i \chi_{[i \cdot T/3, (i+1) \cdot T/3[}(t) \tag{3.28}$$

The inputs used in this example are $\{u_i\}_{i=0}^2 = (0.1, 0.2, 0.1)$ and $\{d_i\}_{i=0}^2 = (0.4, -0.2, -0.1)$ and are depicted in Fig. 3.2. Consequently, there are three input variables in this optimal control problem. Using these value for the input and disturbances together with the reference trajectory $r_t = 1.9$, the solution to the adjoint system in (3.24) is depicted in Fig. 3.3. The derivative of the objective function w.r.t. the input is values of $J_t^{(i)}$, $i = 1, 2, 3$ at time $t = 0$. Notice that the derivative variables for each input only change within the time interval in which it influences the system variable.

### 3.3.2 Single Shooting

The class of direct optimal control methods requires a discretisation of the input $u$ before performing the optimisation—known as *first discretise, then optimise*. Therefore, in the following, it is assumed that the input and disturbance have the form as in (2.29).

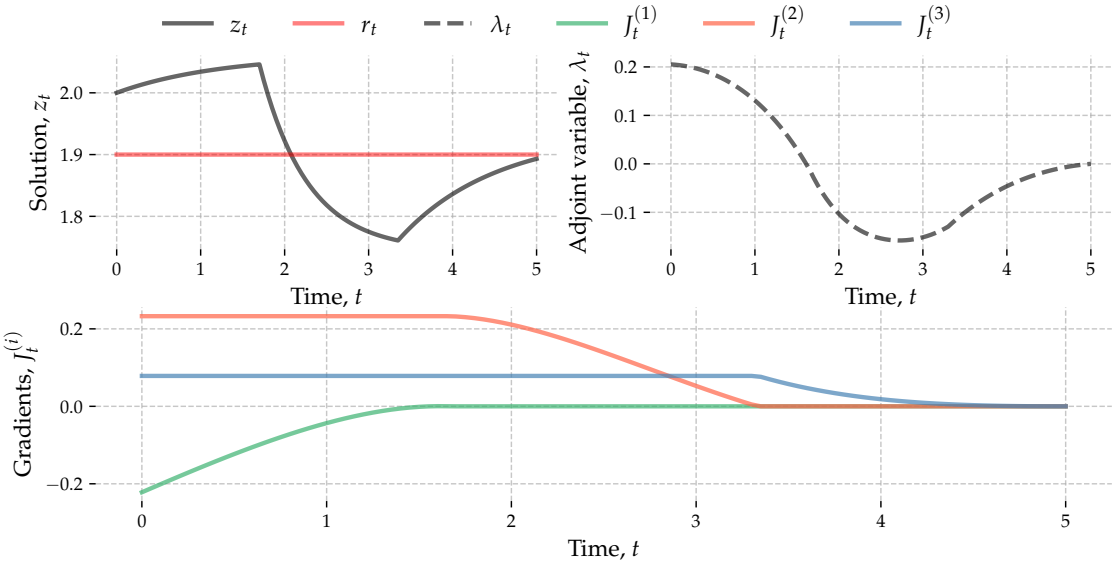


Figure 3.3: The solution to the adjoint system equations in (3.24) of the system in (3.27).

Direct methods rely on the consideration that given an initial condition, $\hat{x}_{k|k}$, the input $u$, and the disturbances, $d$, the entire trajectory of $x$ is uniquely determined in (3.4) by the solution to the differential equation. In this way, one is "shooting" the system, which then ends up somewhere at the boundary of the time domain at time $t_N$. And by changing $u$, the shooting trajectory of $x$ changes. The optimal control problem can be written in the following way

$$\min_{u_i} \quad \left\{ \phi_k(u; \hat{x}_{k|k}, d) = q_b(x_{t_k+T}(u, \hat{x}_{k|k}, d)) \right. \tag{3.29a}$$

$$\left. + \sum_{i=0}^{N-1} \int_{\tau_i^k}^{\tau_{i+1}^k} q(x_\tau(u, \hat{x}_{k|k}, d), u_i) \mathrm{d}\tau \right\},$$

$$\text{s.t.} \quad x_t(u, \hat{x}_{k|k}, d) = \hat{x}_{k|k} + \int_{t_k}^{t} f(x_\tau, u_\tau, d_\tau; \theta) \mathrm{d}\tau\,, \qquad t \in [t_k, t_k + T[\,, \tag{3.29b}$$

$$u_i \in \mathcal{U}(\tau_i^k) \qquad \text{for } i = 0, 1, \ldots, N-1\,, \tag{3.29c}$$

$$x_t \in \mathcal{X}(t) \qquad t \in [t_k, t_k + T[\,, \tag{3.29d}$$

The summation of the integrals of each interval $[\tau_i^k, \tau_{i+1}^k[$ stresses the fact that the input and disturbances are constant in each interval. The notation $x_t(u, \hat{x}_{k|k}, d)$ indicates the solution's dependence on the input, initial condition, and the disturbance.

The adjoint method supplies the gradient of $\phi_k(u, \hat{x}_{k|k}, d)$ directly by solving $x$ forward in time and saving the result (as in one of the proposals in 3.3.1), and afterwards solving

the boundary value problem for all $u_i$, $i \in \mathcal{N}$ simultaneously,

$$\frac{\partial \lambda^\top}{\partial t} = -\lambda_t^\top \frac{\partial f}{\partial x}(x_t, u_t, d_t) - \frac{\partial q}{\partial x}(x_t, u_t)\,, \tag{3.30a}$$

$$\lambda_{t_k+T}^\top = \frac{\partial q_b}{\partial x}(x_{t_k+T})\,, \tag{3.30b}$$

$$\frac{\partial J_i^k}{\partial t} = \frac{\partial q}{\partial u}(x_t, u_t) + \lambda_t^\top \frac{\partial f}{\partial u}(x_t, u_t, d_t)\,, \tag{3.30c}$$

$$J_{i,t_k+T}^k = 0\,, \tag{3.30d}$$

from time $t_k + T$ to $t_k$ for $i = 0, 1, \ldots, N-1$. The gradient of the objective function w.r.t. the $i$'th input is then

$$\frac{\partial \phi_k}{\partial u_i} = J_{i,t_k}^k\,. \tag{3.31}$$

### 3.3.3 Multiple Shooting

A downside of the single shooting method is that shooting far into the future can give massive gradients since all inputs might affect the future state trajectory $x$. An alternative method is to divide the prediction horizon into smaller subintervals and solve many smaller single shooting intervals: Since the input $u_k$ only affects the integration in a single time step $[t_k, t_{k+1}[$, the integration becomes more robust compared to integrating the entire prediction horizon. Of course, one will not know the "initial conditions of the future", but one can instead make each initial condition a parameter in the optimal control problem. By doing so, each subinterval in the optimal control problem can be solved independently. One can then add to the optimisation problem that the end of each interval must match up with the beginning of the next. To formulate this, divide the prediction horizon $[t_k, t_k + T[$ into subintervals of $\mathcal{T}$ as in (3.1). Let $\{x_t^i, t \in [\tau_i, \tau_{i+1}]\}$ be the trajectory of the system in the $i$'th time interval given by the initial value problem:

$$\frac{\partial x_t^i}{\partial t} = f(x_t^i, u_i, d_i; \theta) \quad \text{with} \quad x_{\tau_i^k}^i = x_{\tau_i^k}^{i-1} \quad \text{on the interval} \quad t \in [\tau_i^k, \tau_{i+1}^k[\,. \tag{3.32}$$

The requirement $x_{\tau_i^k}^i = x_{\tau_i^k}^{i-1}$ means that the $i$'th trajectory starts where the $i-1$'th trajectory ends—thereby "gluing" the trajectories together. To formalise this, define the so-called *flow map*, $\Phi_t(s, \zeta, u_i, d_i)$, as the solution to the initial value problem

$$\frac{\partial x_\tau}{\partial \tau} = f(x_\tau, u_i, d_i)\,, \quad \text{with} \quad x_s = \zeta\,, \tag{3.33}$$

at time $t$ for $t > s$. The flow map thus *flows* the system from one point $\zeta$ at time $s$ forward in time till time $t$. With this notation, the multiple shooting discretisation of the optimal control problem in (3.4) becomes

$$\min_{u_i, z_i} \quad \left\{ \phi_k(u, \{z_i\}; \hat{x}_{k|k}, d) = q_b(z_N) + \sum_{i=0}^{N-1} \int_{\tau_i^k}^{\tau_{i+1}^k} q(x_\tau^i(z_i, u_i, d_i), u_i) \mathrm{d}\tau \right\}\,, \tag{3.34a}$$

$$\text{s.t.} \quad z_{i+1} = \Phi_{\tau_{i+1}^k}(\tau_i^k, z_i, u_i, d_i)\,, \qquad i \in \mathcal{N}\,, \tag{3.34b}$$

$$z_0 = \hat{x}_{k|k}\,, \tag{3.34c}$$

$$u_i \in \mathcal{U}_k(\tau_i^k) \qquad i \in \mathcal{N}\,, \tag{3.34d}$$

$$z_i \in \mathcal{Z}_k(\tau_i^k) \qquad i \in \mathcal{N}\,. \tag{3.34e}$$

To solve (3.34), the procedure is the exact same as for the single shooting problem, except here, there are $N$ shooting problems to solve. Let $\lambda_{i,t} : \mathbb{R} \mapsto \mathbb{R}^{n_x}$ be the adjoint variable for the $i$'th shooting trajectory in the optimisation problem in (3.34). Then the gradient of $\frac{\partial \phi_k}{\partial u_i}$ w.r.t. the $i$'th input variable is the solution to John Bagterp Jørgensen, 2007

$$\frac{\partial \lambda_i^\top}{\partial t} = -\lambda_{i,t}^\top \frac{\partial f}{\partial x}(x_t, u_i, d_i) - \frac{\partial q}{\partial x}(x_t, u_i)\,, \tag{3.35a}$$

$$\lambda_{i,\tau_{i+1}}^\top = 0\,, \tag{3.35b}$$

$$\frac{\partial J^k}{\partial t} = \frac{\partial q}{\partial u}(x_t, u_i) + \lambda_{i,t}^\top \frac{\partial f}{\partial u}(x_t, u_i, d_i)\,, \tag{3.35c}$$

$$J_{\tau_{i+1}}^k = 0\,, \tag{3.35d}$$

at time $\tau_i^k$ for $i = 0, 1, \ldots, N-2$. For the boundary $i = N-1$, the terminal value (3.35b) changes to $\lambda_{i,\tau_N}^\top = \frac{\partial q_b}{\partial x}(z_N)$.

The procedures to compute all the required gradients for solving the optimal control problem in (3.34) can be found in e.g. (Aydogmus and TOR, 2021) or (Grimm and Markl, 1997).

## 3.4 Embedded Stochastic Disturbance Models

Consider the following model

$$\mathrm{d}x_t = f_x(x_t, u_t, d_t, t; \theta_x)\mathrm{d}t + g_x(x_t, t; \theta_x)\mathrm{d}\omega_t^{(x)}\,, \tag{3.36a}$$

$$\mathrm{d}d_t = f_d(d_t, t; \theta_d)\mathrm{d}t + g_d(d_t, t; \theta_d)\mathrm{d}\omega_t^{(d)}\,, \tag{3.36b}$$

$$y_{x,k} = h_x(x_{t_k}, v_k; \theta_x)\,, \tag{3.36c}$$

$$y_{d,k} = h_d(d_{t_k}, w_k; \theta_d)\,, \tag{3.36d}$$

where $f_x : \mathbb{R}^{n_x} \times \mathbb{R}^{n_u} \times \mathbb{R}^{n_d} \times \mathbb{R} \times \mathbb{R}^{n_{\theta_x}} \mapsto \mathbb{R}^{n_x}$ is the system drift function, $f_d : \mathbb{R}^{n_d} \times \mathbb{R} \times \mathbb{R}^{n_{\theta_d}} \mapsto \mathbb{R}^{n_d}$ is the function governing the drift of the disturbances of $x$, and $g_x : \mathbb{R}^{n_x} \times \mathbb{R} \times \mathbb{R}^{n_{\theta_x}} \mapsto \mathbb{R}^{n_x}$ and $g_d : \mathbb{R}^{n_d} \times \mathbb{R} \times \mathbb{R}^{n_{\theta_d}} \mapsto \mathbb{R}^{n_d}$ are likewise the diffusion functions of the system and the disturbances, respectively. $h_x : \mathbb{R}^{n_x} \times \mathbb{R}^{n_x} \times \mathbb{R}^{n_{\theta_x}} \mapsto \mathbb{R}^{n_{y_x}}$ and $h_d : \mathbb{R}^{n_d} \times \mathbb{R}^{n_d} \times \mathbb{R}^{n_{\theta_d}} \mapsto \mathbb{R}^{n_{y_d}}$ are the observation equations with $v_k \sim N_{\text{iid}}(0, R_k^x)$ and $w_k \sim N_{\text{iid}}(0, R_k^d)$.

The above formulation indicates the nature of disturbances: They are influential elements that the operator has no control over but must (or should, at least) include to sufficiently describe the process $x$.

This formulation has multiple consequences and benefits for optimal control problems. First, embedded SDE models of the disturbances provide knowledge about the uncertainty of the disturbances. This can be utilised in the filtering-step of the MPC to improve the updated system (and disturbance) estimates. Furthermore, the uncertainty may be used in a stochastic model predictive controller to better respect constraints (e.g. change-constrained MPC). Secondly, a continuous-time description of the disturbances gets rid of the zero-order hold discretisation. The latter is typically a wrongful approximation, which is imposed for simplistic reasons. The formulation can also be used for more advanced control/decision problems as in (Blanco et al., 2018; Guericke et al., 2020).

### 3.4.1 Current practices and stochastic disturbance models

This section briefly shows and demonstrates (via an example) how stochastic disturbance models are useful in forecasting and control. Ultimately, forecasting is typically used for some kind of control or decision making. E.g.,

- forecasting of solar radiation can be utilised for estimating the electricity production from PV cells (Iversen et al., 2014),
- forecasting of the covid-19 related infection and hospitalisation rates can help decision makers choose how closed/open the society should be in order to avoid too occupied hospitals (Johnsen, Christiansen, and Græsbøll, 2022),
- forecasting of district heating loads can be used by the district heating companies to decide the correct forward temperature in order to minimise the energy usage of district heating (Hjörleifur G. Bergsteinsson et al., 2021).

Forecasting is thus a central part of MPC since the underlying model is integrated forward in time. Thus, system disturbances are important to incorporate in the MPC formulation. One *currently standard* way for dealing with unknown disturbances in the literature is to use offset-free regulation (i.e. persistent forecasts, $d_{t+\tau} = d_t$, $\tau > 0$). For systems with significant influence of fast changing disturbances, this method tends to be insufficient for optimal control. We will show this by an example in the next section.

Instead, having stochastic models describing the disturbances in the model has multiple advantages. First and foremost, the mean value is supplied and can be readily used in certainty equivalent MPC. But, the knowledge of the stochasticity of the disturbances can bu utilised in some kind of stochastic MPC (e.g. chance-constrained MPC). E.g. any quantile may be extracted from the density that can be used to compute back-off values to use in the MPC constraints.

**Example**
This example shows simulations of the transition probability densities of the advanced disturbance model in articles E and F. For a more thorough introduction and walk through of the model, the reader is referred to (C. A. Thilker, 2020). The model forecasts the values of the following four climatic processes; *cloud cover*, *global solar radiation*, *net radiation*, and *air temperature*. The purpose is to demonstrate the models' abilities to forecast the weather variables characterised as densities.

We use a Monte Carlo-based approach for illustrating the transition densities. Figures 3.4, 3.5, 3.6, and 3.7 are computed using the following steps:

1. Given the history up till time $t_0$, (that is all data from time $t = 0$ till $t = t_0$) use the model given in E to simulate a realisation of all the climatic processes. Do this $N = 1000$ times.
2. Given $N$ simulations of the climatic processes, we can compute properties of the transition densities. In this example, we compute the mean and the 5-, 50-, and 95% quantiles. Additionally, the following plots illustrate the transition densities by colouring small vertical columns. Warmer colours mean higher density.

Figure 3.4a shows 10 simulations of the cloud cover process 24 hours into the future. On top is the actual observed realisation. By using all 1000 simulations and computing the amount of simulation trajectories that lie in each small square at a given time, we can form a density evolving in time shown in Figure 3.4b. Some quantiles and the mean value in time are also indicated.

Figure 3.5 shows similar simulations and a realisation for the solar radiation. Here, the distribution is more uniform in space (of course varying in time) compared to the cloud cover process. The net radiation is shown in Figure 3.6 and the air temperature in Figure 3.7. The air temperature is described by a linear stochastic process, but depends on the

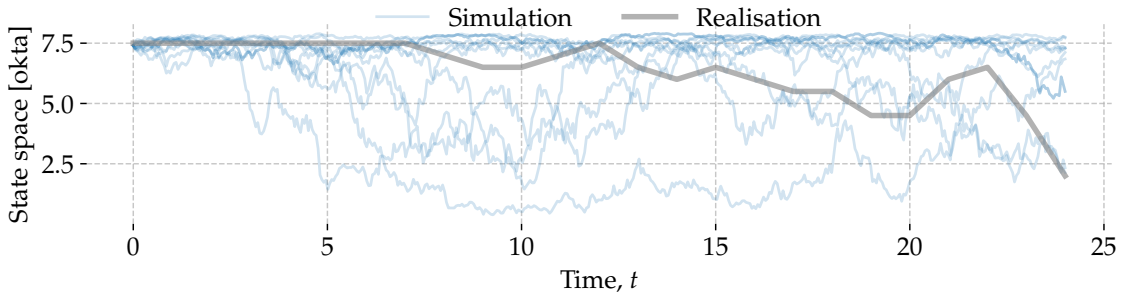


(a) Simulation of the cloud cover and the actual realisation.

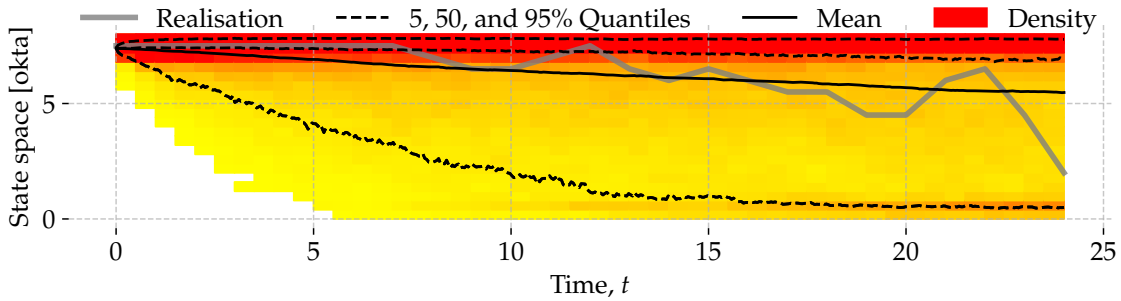


(b) Density forecast of the cloud cover state and the actual realisation.

Figure 3.4: A Monte Carlo simulation of the density of the cloud cover process given the initial condition at time $t = 0$, $\kappa_0 = 7.5$ (see Appendix E or F or (C. A. Thilker, 2020) for more details). The upper plot shows 10 simulations (computed using the Euler-Maruyama scheme) together with the actual realisation. The lower plot shows the a Monte Carlo simulation of the forward density of the cloud cover state in time (using 1000 simulations). Red is higher density while yellow is lower.

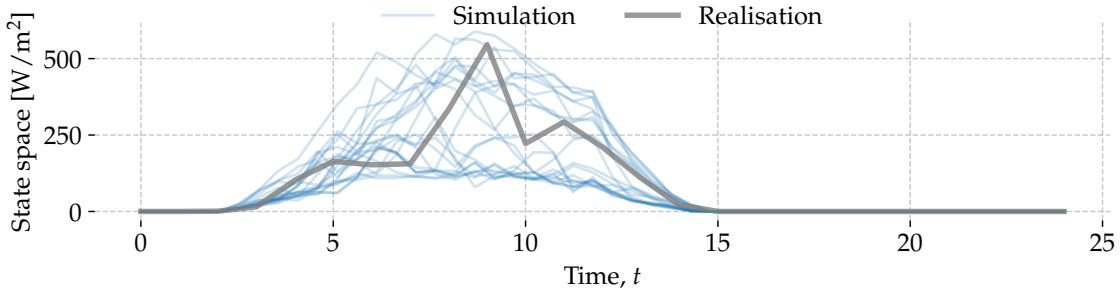


(a) Simulation of the cloud cover and the actual realisation.

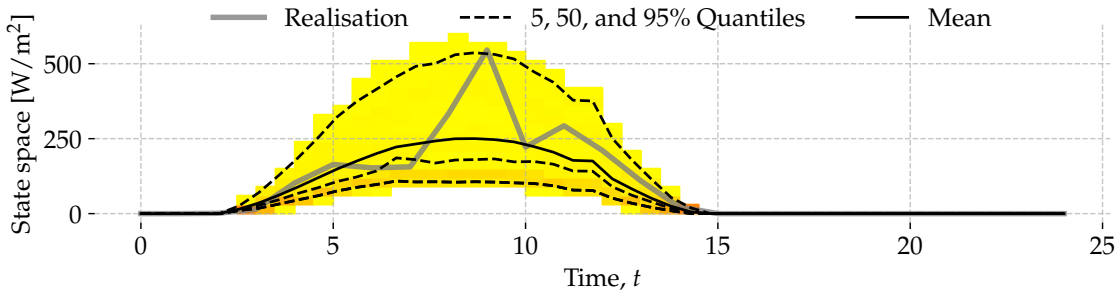


(b) Density forecast of the cloud cover state and the actual realisation.

Figure 3.5: A Monte Carlo simulation of the transition density of the solar radiation (see Appendix E or F or (C. A. Thilker, 2020) for more details). The upper plot shows the actual realisation together with 10 simulations. The simulations are based on simulated values of the cloud cover in Figure 3.4). The lower plot shows the density given by colours where warmer colours mean higher density. The model is able to capture the very non-linear dynamics with zero radiation during night and positive radiation during day time.

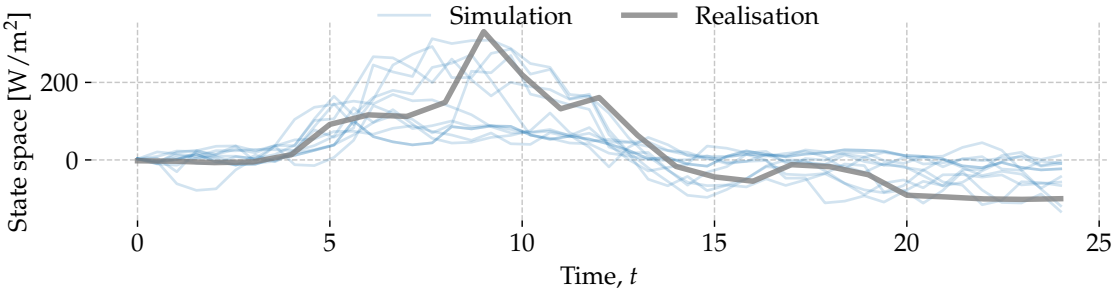


(a) Simulation of the cloud cover and the actual realisation.

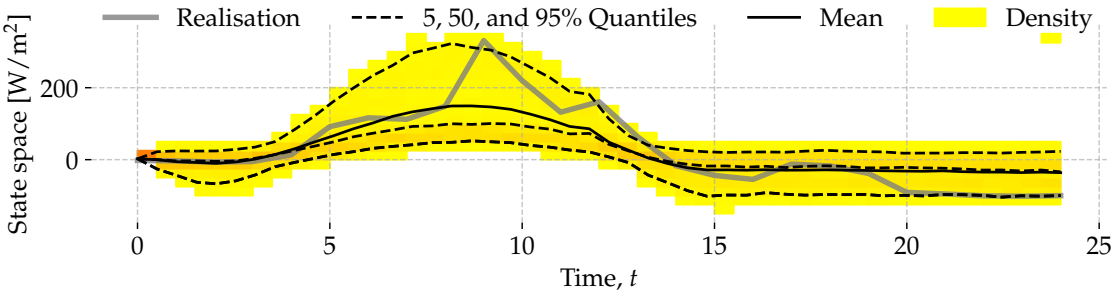


(b) Density forecast of the cloud cover state and the actual realisation.

Figure 3.6: A Monte Carlo simulation of the transition density of the net radiation (see Appendix E or F or (C. A. Thilker, 2020) for more details). The upper plot shows the actual realisation together with 10 simulations. The net radiation depends non-linearly on the cloud cover and solar radiation and the simulations are based on the simulated values of the cloud cover in Figure 3.4 and solar radiation in Figure 3.5). The lower plot shows the density given by colours where warmer colours mean higher density.

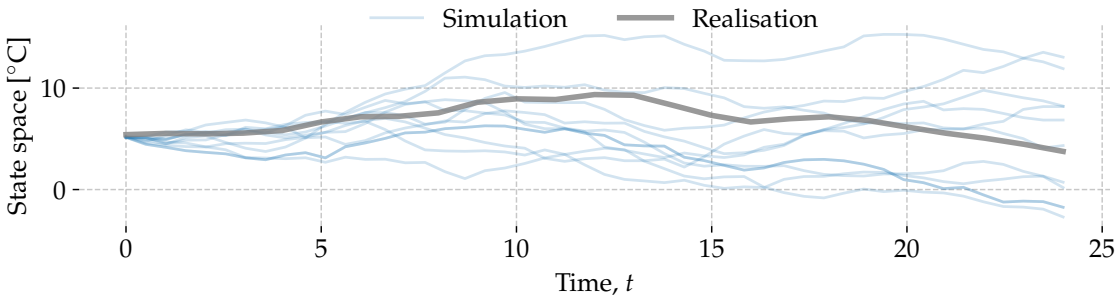


(a) Simulation of the cloud cover and the actual realisation.

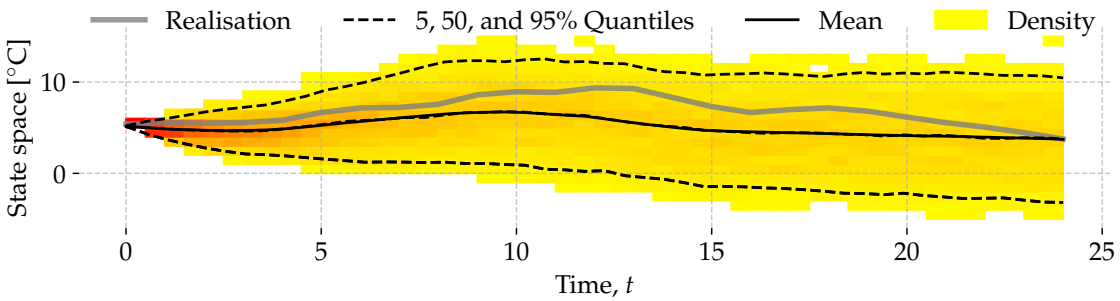


(b) Density forecast of the cloud cover state and the actual realisation.

Figure 3.7: A Monte Carlo simulation of the transition density of the air temperature process (see Appendix E or F or (C. A. Thilker, 2020) for more details). The upper plot shows the actual realisation together with 10 simulations. The air temperature is described by a set of linear stochastic differential equations and depends on the net radiation depicted in Figure 3.6. The lower plot shows the density given by colours where warmer colours mean higher density. Due to the linearity of the process, the transition density is Gaussian, which is also visible by the collapsing mean and median in time.

net radiation, which depends on the cloud cover- and solar radiation processes (all of which are non-linear processes). The transition density is thus not Gaussian.

### 3.4.2 Embedded disturbance model in MPC

The following example showcases the idea of having an embedded disturbance model using the previously introduced modified CIR-process with an embedded disturbance model.

**Example**

This example demonstrates the multiple shooting method for closed-loop control of the modified CIR-process introduced in the previous example but with two states added; one for the disturbance and one for the input. The integrated input adds delay to the effect on the system state. The example also illustrates the MPC framework with embedded disturbance forecasts. To do this, we here consider the following model

$$\mathrm{d}x_t = \lambda_1(\mu - x_t + I_t + x_t^2 d_t)\mathrm{d}t + \sigma_t\sqrt{x_t}\mathrm{d}\omega_t^{(x)}\,, \tag{3.37a}$$

$$\mathrm{d}d_t = \lambda_2(\bar{d}_t - d_t)\mathrm{d}t + \sigma_d\mathrm{d}\omega_t^{(d)}\,, \tag{3.37b}$$

$$\mathrm{d}I_t = u_t\mathrm{d}t + \sigma_u\mathrm{d}\omega_t^{(u)}\,, \tag{3.37c}$$

$$y_{x,k} = \log x_t + v_k\,, \tag{3.37d}$$

$$y_{d,k} = d_t + w_k\,, \tag{3.37e}$$

where $u_t : \mathbb{R} \mapsto \mathbb{R}$ is the controllable input that affects a state, which in turn controls $x$. $d_t : \mathbb{R} \mapsto \mathbb{R}$ is the disturbance, $v_k \sim N(0, R_v)$ and $w_k \sim N(0, R_w)$ are the observation noises. The disturbance process in (3.37) is governed by a stochastic differential equation itself—a mean reverting process that follows the signal $\bar{d}_t : \mathbb{R} \mapsto \mathbb{R}$. The system state is observed in the log-domain to ensure that the Kalman filter does not update the state illegally (i.e. if $x$ should end up as a negative number).

In the present control simulation, we use the following optimal control problem to compute the optimal input at each time step:

$$\min_{\{u_i\}_{i=0}^{19}} \quad \left\{\phi_k(\hat{x}_{k|k}, \{u_i\}_{i=0}^{19}) = \int_{t_k}^{t_k+T} (x_\tau - r_\tau)^2 + \alpha u_\tau^2 \mathrm{d}\tau\right\}\,, \tag{3.38a}$$

$$\text{s.t.} \quad \text{Eq. (3.37)}\,, \tag{3.38b}$$

$$u_t = u_i\,, \qquad t \in [t_{k+i}, t_{k+i+1}[\,, \tag{3.38c}$$

$$u_i \in [-1, 1]\,, \qquad i = 0, \ldots, 19\,, \tag{3.38d}$$

$$0 \leq x_t\,, \qquad t \in [t_k, t_k + T[\,. \tag{3.38e}$$

where $\alpha = 0.001$, the prediction horizon is $T = 2$, and the time step is $t_{k+1} - t_k = 0.1$ such that the number of optimisation variables in the optimal control problem is $N = 20$. Note that the disturbance model is embedded in the system model and description. Consequently, the disturbances are continuous in the model and in the model description. The current practice is usually to supply disturbances from external sources and assume they are constant between time points as in Section 2.4 (see Paper E).

Figure 3.8 depicts the results of controlling (3.37) using the optimal control problem in (3.38) with the multiple shooting scheme. In the optimal control algorithm, we use the CDEKF to filter the system and disturbance state at every time point $t_k$. As a comparison, we make the same control experiment of (3.37) (considering the optimal control problem in (3.38)) but using persistent forecasts instead of embedded forecasts in the optimal control problem to supply disturbance forecasts. The system does therefore not include knowledge about the disturbance dynamics and, consequently, the considered system

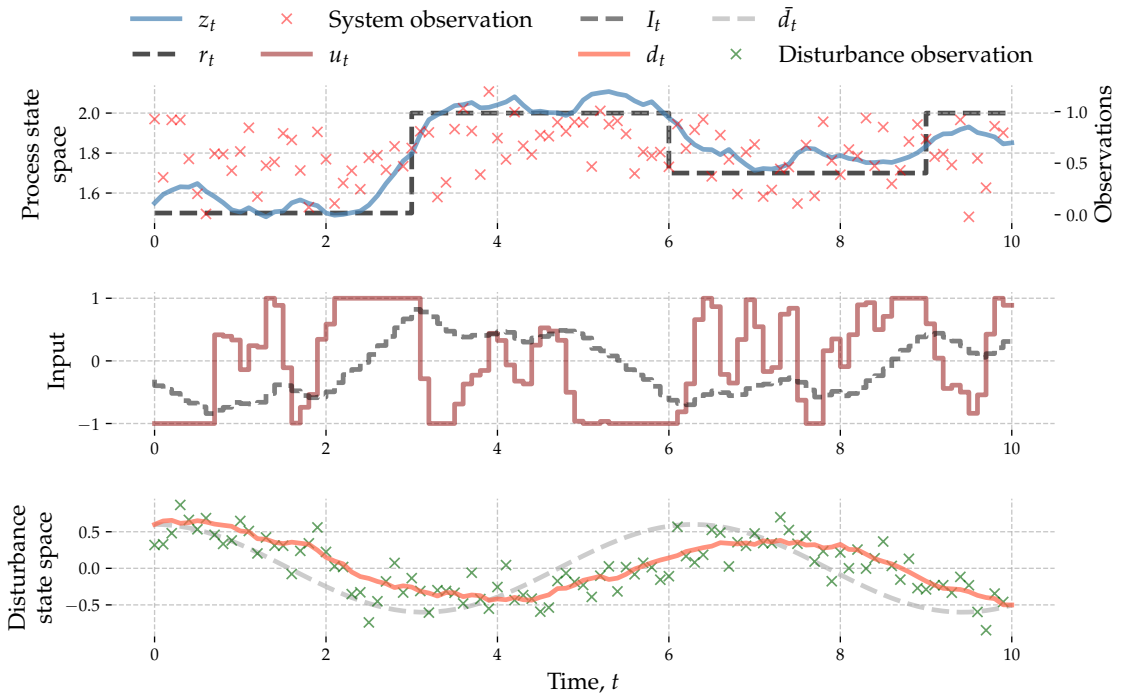


Figure 3.8: A control example of the model in (3.38) WITH an embedded disturbance model. The upper plot is the controlled process $x_t$ and the tracked reference signal $r_t$. The middle plot is the integrated input $I_t$ and the input signal $u_t$. The lower plot is the disturbance process $d_t$ and the reference trajectory $\bar{d}_t$.

gets the simpler form:

$$\mathrm{d}x_t = \lambda_1(\mu - x_t + I_t + x_t^2 d_t)\mathrm{d}t + \sigma_t\sqrt{x_t}\mathrm{d}\omega_t^{(x)}\,, \tag{3.39a}$$

$$\mathrm{d}I_t = u_t\mathrm{d}t + \sigma_u\mathrm{d}\omega_t^{(u)}\,, \tag{3.39b}$$

$$y_{x,k} = \log x_t + v_k\,, \tag{3.39c}$$

$$y_{d,k} = d_t + w_k\,, \tag{3.39d}$$

where the disturbance forecasts are given by $\hat{d}_{t+\tau} = d_t$ for $\tau > 0$. The results of the controlled system using persistent forecasts is shown in Fig. (3.9). It is visible (compared to the results using an embedded disturbance model) that this controller performs worse. The state of $x$ persistently deviates from the set point at certain times. Compared to Figure 3.8, the controller does a better job especially when transitioning to different reference points (e.g. in the intervals [2,4] and [5,7]). The objective function (given in (3.38a)) integrated over the simulated time interval $[0, 10]$ is 0.95 for the embedded disturbance forecast controller versus 1.33 for the persistent forecasts. I.e. an improvement of around 29%. This is allegedly due to 1) better state updates due to more information and 2) better predictive performance from the extra disturbance equation in the model in (3.38).

To see the influence of the additional (and more accurate) information supplied by the stochastic disturbance model on the Kalman filter update of the system state, Figure 3.10 shows the updated/filtered state deviation from the true state in time. It is visible that the controller using persistent forecasts deviates significantly more from the true state. Especially during the time interval $[4, 8]$, the state deviates up to 0.3 from the true state. The error done by the filter using the embedded disturbance model makes less errors and deviates a maximum of 0.1 by the end of the simulation.

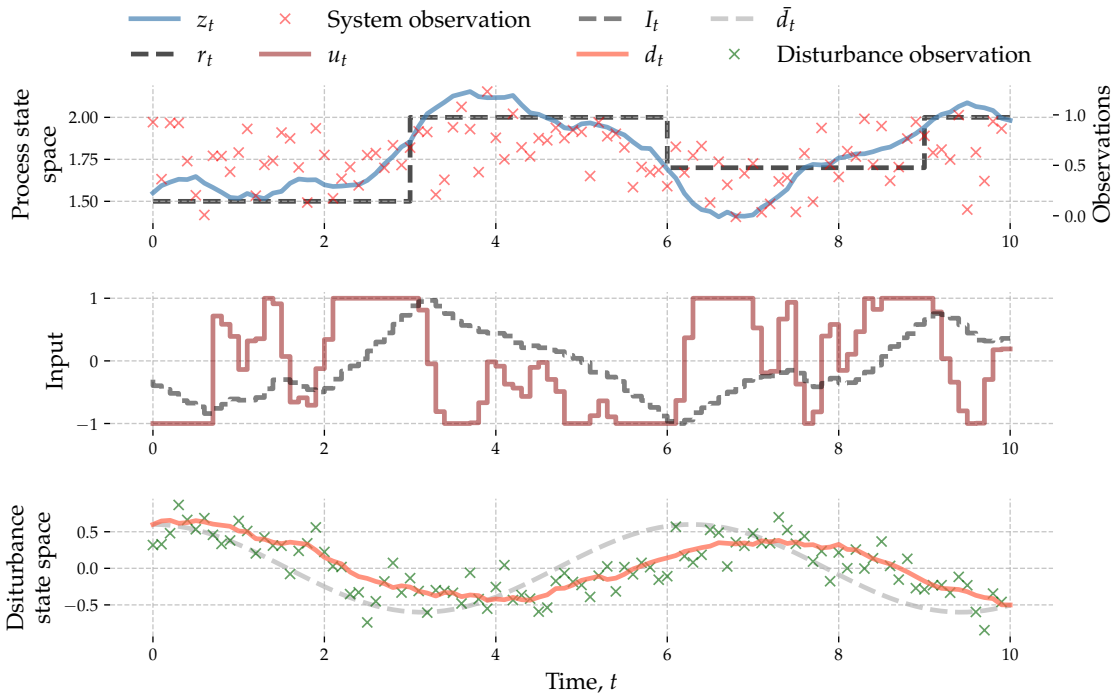


Figure 3.9: A control example of the model in (3.38) WITHOUT an embedded disturbance model. The upper plot is the controlled process $x_t$ and the tracked reference signal $r_t$. The middle plot is the integrated input $I_t$ and the input signal $u_t$. The lower plot is the disturbance process $d_t$ and the reference trajectory $\bar{d}_t$. In general, the controller using persistent forecasts performs significantly worse compared to the one using the embedded disturbance model.

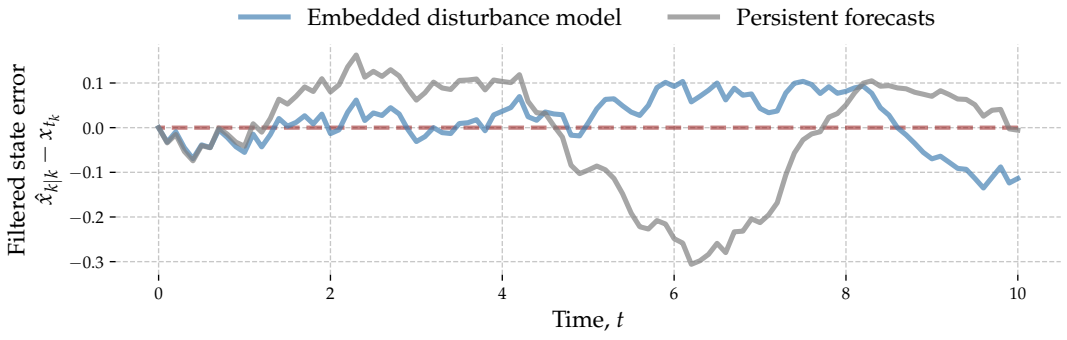


Figure 3.10: The state update deviation from the true state for the two control simulation results, $\|x_{t_k} - \hat{x}_{t_k}\|$.

*Remark.* Since the observation equation of the system and the system dynamics are non-linear, the CDEKF is not exact and the Gaussian densities are only approximative. Especially in the filter update where the observation equation is linearised, the posterior system estimate may be significantly biased. In the case of the logarithm, this may occur when the system in the natural domain is close to zero. Figure 3.11 illustrates this: It shows the observation equation ($\log x$) and three linearisations around different points, $x_0$. For large $x_0$, the linearisation is better compared to smaller $x_0$. When $x_0$ is close to zero, the linearisation becomes worse even for small deviations from $x_0$ due to the stronger

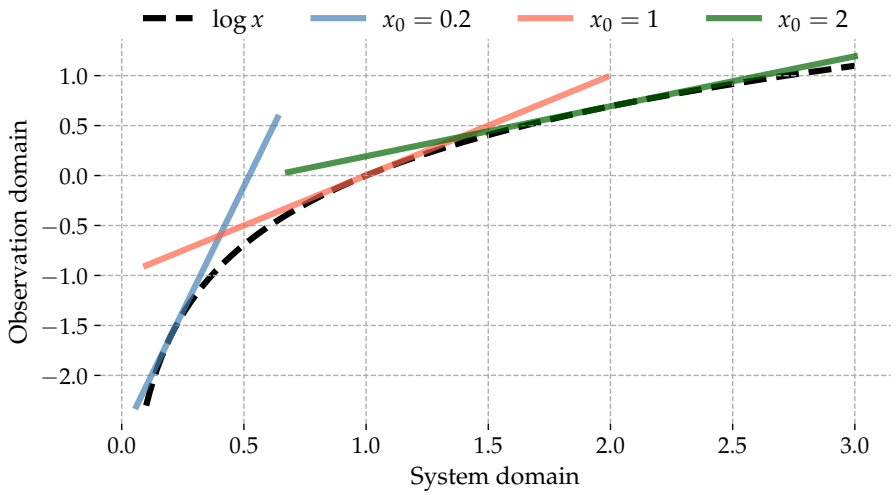


Figure 3.11: Linearisations of the function $\log x$ at different points. The linearisations become worse as $x \to 0$ since the curvature gets large.

non-linearities. This may affect the system, if it is operated close to zero—or in general, if it is operated in areas of the observation space or system space with significant non-linearities. However, seen from Figure 3.8, it does not seem to be a significant problem in the given case. This is likely due to the time step being small enough compared to the system dynamics.

# 4 Applications

The previous sections introduced important concepts for modelling, forecasting, and controlling stochastic dynamical systems. These are all based on SDE models, which have proved very useful for these aspects. They provide the modeller with a tool for stochastically model and predict/forecast the system's state and also for controlling the system while taking the stochasticity into account using some form of MPC. This could be accounted for in e.g. the objective function (by penalising a certain quantile of the system) or in the constraints (by tightening a constraint according to the uncertainty).

This chapter goes over some applications of the theory and concepts introduced in the former chapters. These include stochastic modelling of buildings' thermal dynamics with the aim of controlling these. This has been done in both discrete and continuous time. Real-life- and simulation based control of the buildings thermal dynamics are also presented. Next, application of embedding a short-term disturbance model for MPC are presented. The chapter ends with a small presentation of controlling a chaotic dynamical system.

## 4.1 Temperature Modelling for Large Buildings

Paper A presents a modelling procedure for identifying a non-linear grey-box model for the heat dynamics of large-scale buildings. It is commonly stated that buildings in the western countries take up 40% of the total energy usage. Optimal operation of buildings therefore constitute a great opportunity for delivering flexibility. Around 70% of Danish buildings are heated by district heating, where the buildings use hydraulic systems to distribute (using e.g. radiators or floor heating) the heat into every room.

Some of the modelling challenges arise from the many rooms of the building. Since the water flow and return water temperature in each radiator is not known, the heat load of the individual rooms is not known. However, on a building level, we measure these variables and are able to predict them. Therefore, to simplify the air temperature modelling of the building, we choose to aggregate the temperature of all the rooms of the building using an average of all the room air temperatures. Likewise, we send the same set-point to all radiator thermostats in the building, thus, controlling the aggregated building.

Other modelling challenges include non-linearities of the system. One of these is the thermostatic control of the water flow of the radiators. These are controlled by a temperature set-point where the thermostatic valve opens according to the current air temperature. Paper A suggests to use a sigmoid curve to approximate the behaviour of the thermostatic valve state as a function of the indoor air- and set-point temperatures.

Another non-linearity comes from the heat load of the building. The heat load rate is given by

$$\phi_{\mathrm{h}} = \Phi_{\mathrm{water}}(T_{\mathrm{forward}} - T_{\mathrm{return}}) \tag{4.1}$$

where $\phi_{\mathrm{h}}$ is the heat load rate of the building, $\Phi_{\mathrm{water}}$ is mass flow rate of the water of the heating system, and $T_{\mathrm{forward}}$ and $T_{\mathrm{return}}$ are the forward- and return water temperature, respectively. Evaluating (4.1) (i.e. to predict the heat load) requires the modeller to be able to predict all three variables on the right-hand side. The future heat load is essential to predict in order to enable flexibility.

Figure 4.1 depicts the results of the model's ability to predict the data: It shows a simulation of the system variables given only the initial conditions at time $t_0$ and the inputs and disturbance time series's. It indicate good capabilities of the model to predict the needed variables with sufficient accuracy. Paper B and Paper C present real-life and simulation control experiments, respectively, of the modelled school where this model was used.

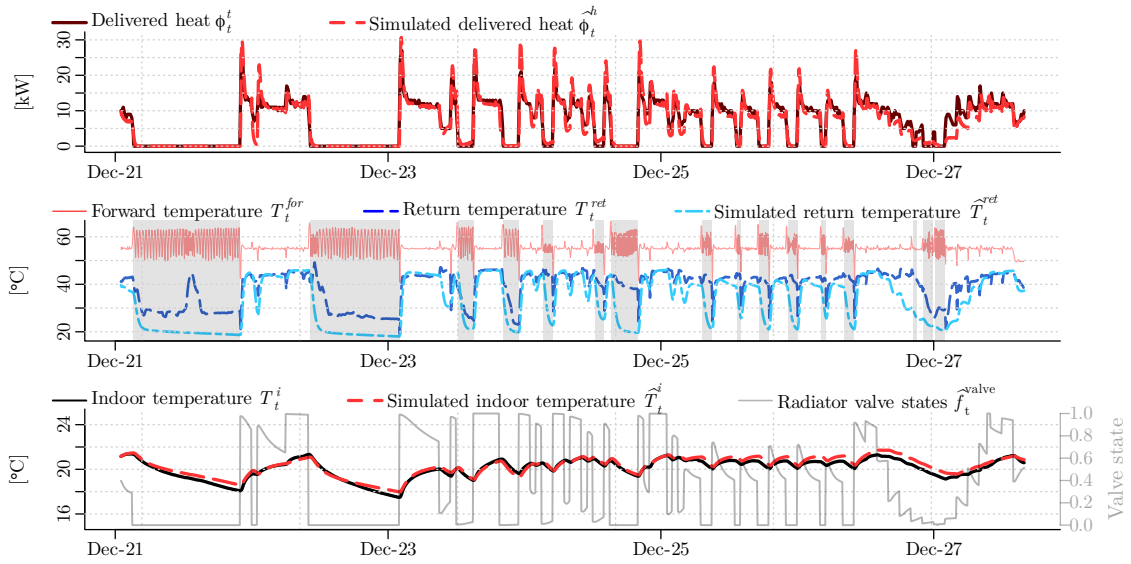


Figure 4.1: This plot is taken from Paper A. The identification experiment in December 2019 is used to form the state-space model of the indoor air temperature of Borgerskolen. It shows the measured values together with the simulated ones (given only the initial conditions). The upper plot shows the heat load of the building: The spikes in the heat load when the heat is turned on is due to aggregated cold water in the system that is heated up. The middle plot shows the return water temperature. The greyed-out periods depicts the time periods where the heat load is zero (and where the return temperature is not predictable). The lower graph shows the mean indoor air temperature and the estimated thermostatic valve state.

## 4.2 Optimal Control for Indoor Air Temperature in large Buildings

Paper B presents the results of optimal control of the indoor air temperature applied to a large school building in Denmark (the same as in Paper A). The school is located in Høje Taastrup and was build in 1929, and is not insulated according to modern standards. Prior to the control experiment, the school had wireless air temperature sensors installed in all rooms and all radiators had smart thermostats installed as well. The rooms are of different sizes and have different radiator capacities.

To control the indoor air temperature of the building, the controller used the building model presented in Paper A. Therefore, the controller considered only the mean indoor air temperature for the optimal control problem. The set-point computed by the controller was sent to all rooms, which means all rooms were controlled identically. This aggregation makes the optimal control problem much simpler compared to the case where rooms are considered individually. To display the flexibility of the building, we used a variable

price for the heat such that the heat was expensive in the morning and evening (and cheap outside these hours). An introduction to flexibility concepts for buildings can be found in (Junker, Azar, et al., 2018). ENFOR supplied the weather forecasts (air temperature and global solar radiation).

Figure 4.2 shows the entire control experiment results: The indoor air temperature of all the rooms, the mean indoor temperature, and the temperature bounds. Evidently, the controller successfully keeps the mean air temperature inside the bounds and lowers the heat usage in the hours with expensive heat. However, the spread of the individual room air temperatures is big. Nearly all rooms violate the temperature bounds frequently and are hence not steered well. This is not surprising since all rooms are different in size and heating capacity. It shows that such a simple control setup (with an aggregated model and an identical control signal for all rooms) is not sufficient to keep each room comfortably heated while making the building flexible. The conclusion is that some kind of room-based control is needed. Suggestions for this could be:

- Static room temperature models: A simple set-point offset is learned for each room to figure out how much the aggregated control signal should be altered for the individual rooms.
- Dynamic room temperature models: The different dynamical behaviour of each room is taken into account by considering individual dynamical models for each room. Paper D addresses this problem and proposes ARX models to model each room temperature and have an individual MPC for each room as well.

It is difficult to determine the savings of applying an optimal controller in terms of money and comfort compared to standard operations since it is very dependent on the current weather. Instead, Paper C carries out a simulation study to determine an estimate of the advantages of the optimal control operation of the indoor climate. The paper uses historical weather data and the model presented in Paper A to perform the simulations. A simulation based on a month of data suggests energy savings of 2.5% and economic savings of 10%. The small energy savings is due to the building being poorly insulated making the heat usage difficult to reduce. The economic savings come from the ability of the controller to reduce the return temperature (since high return temperatures are penalised by the district heating companies).

## 4.3 Temperature Modelling for Individual Rooms

Paper D presents a modelling technique for identifying parameters that appear non-linearly in Auto-Regressive models with Exogenous inputs (ARX) models models—dubbed ”non-linear ARX models”. The application of the modelling procedure is temperature modelling for individual rooms in a large-scale building. The aggregated model presented by Paper A predicts the *mean* temperature of the buildings' rooms. But, as the result of the real-life control experiment of the indoor air temperature in Paper B shows, the control performance is not sufficient in terms of each room's performance. This is due to the significant individual behaviour of the rooms. This indicates that a room-level control is necessary to conduct to obtain sufficient control performance on room-level.

A fundamental problem arises, though, when choosing a model for the individual rooms. Grey-box models are well suited for control compared to black-box models due to the regularisation of the physics that are usually imposed. Black-box models on the other hand tend to have unknown behaviour outside of the training data. For this reason, grey-box models may be preferred over black-box models for real-time control. However, on room level in many large-scale Danish buildings, the heat load is not known (since neither

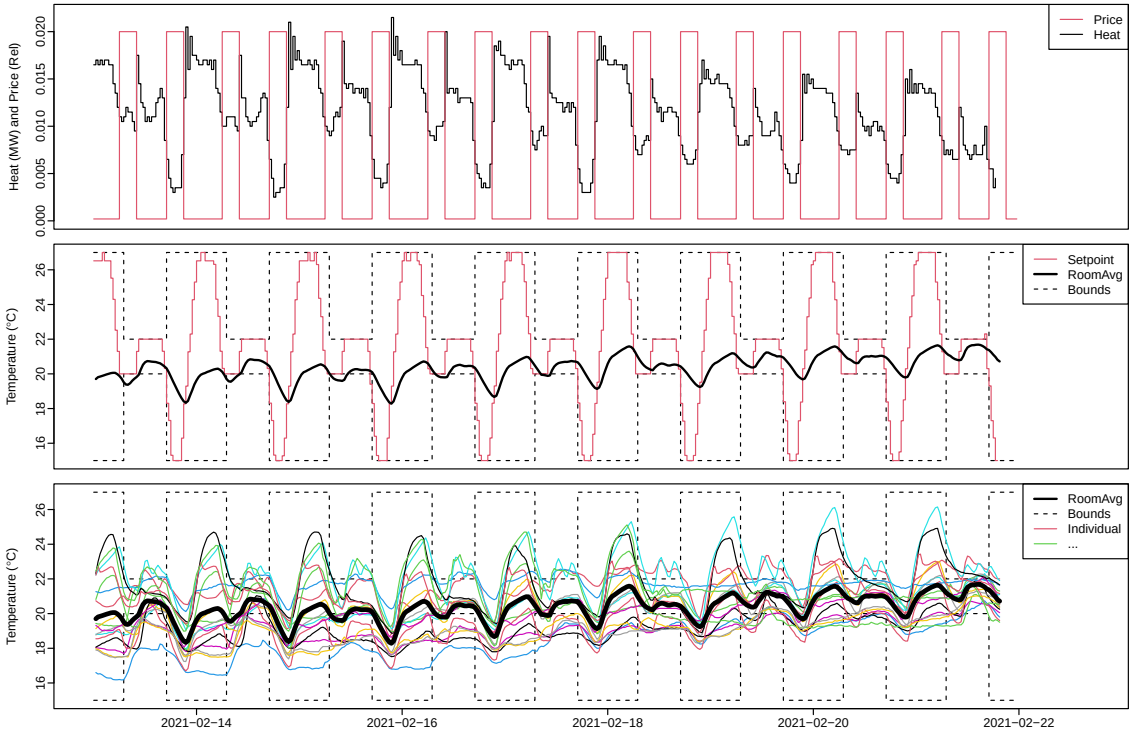


Figure 4.2: This plot is taken from Paper B. It displays a part of the results of the control experiment of Borgerskolen where all rooms were controlled in an identical manner. The upper plot shows the variable heat load price together with the heat load. The controller successfully moved the main heat load away from the expensive periods, however, since we did not control all rooms, the heat load did not go to zero. Middle plot: The mean indoor air temperature and the temperature bounds together with the set-point sent to all the rooms. The lower plot shows all the room air temperatures and reveals the large spread in the indoor air temperatures.

the mass-flow rate nor the return temperature of the individual rooms are known)! This rules out the possibility of using the popular RC-based models for modelling the heat dynamics. In paper D, the authors instead use ARX models where they include the non-linearities that appear in the grey-box model presented in Paper A. Furthermore, they use B-spline (Christensen, 2010) and Hermite (Fritsch and Carlson, 1980) basis expansions to model the solar radiation gain and thermostatic valve functions for each room.

Figure 4.3 shows the modelling results of a single room. The upper graph shows the multi-step ahead predictions of the time series given only the initial conditions and the actual inputs. The model is able to sufficiently predict the overall trend of the data in all parts of the domain–without diverging. Stability is not guaranteed with this kind of model, so this result is good. The solar radiation gain also seems to make sense from a physical point of view since the particular room has windows to the east (and thus sun is present only during the morning hours). The histogram of the residuals reveal a larger spread compared to the corresponding Gaussian distribution. This may indicates that the variance is varying in time and/or space. Model extensions to capture this exists, such as GARCH-models (Lamoureux and Lastrapes, 1990) or variable transformations.

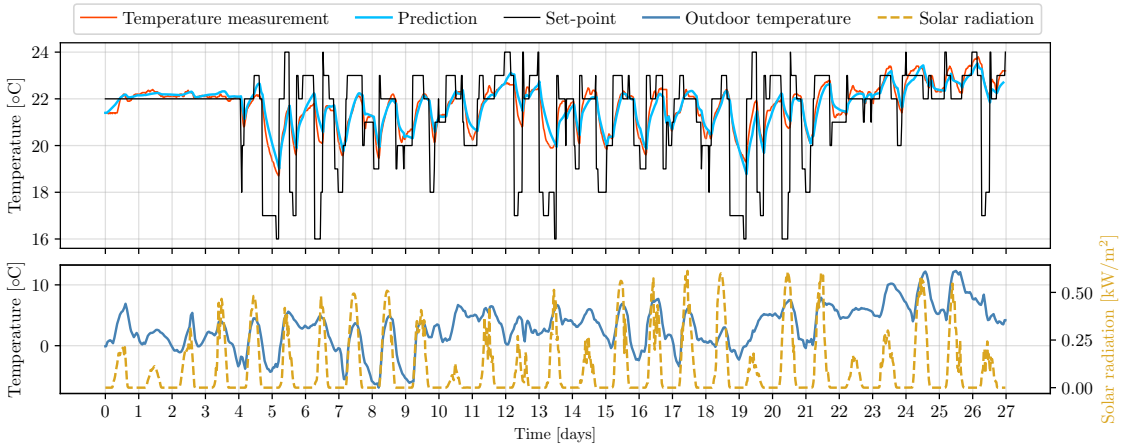


(a) Multi-step prediction given only the initial conditions and the inputs.

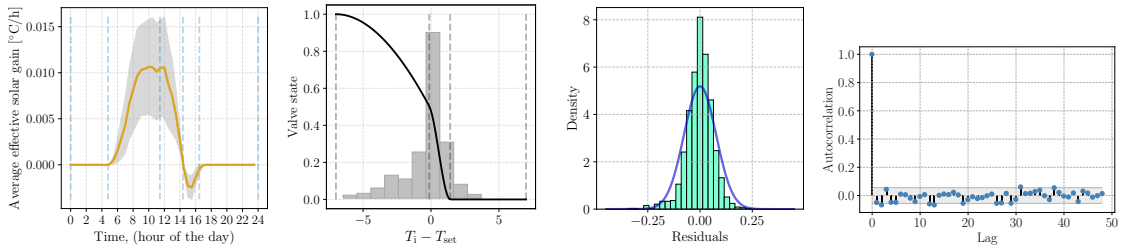


(b) Solar gain throughout the day. The vertical dashed lines indicates the placement of the knots.

(c) Thermostatic valve function. The vertical dashed lines indicates the placement of the knots. The histogram shows the distribution of the data points.

(d) Histogram of residuals and the associated Gaussian distribution.

(e) Autocorrelation function of the one-step ahead residuals.

Figure 4.3: This figure is taken from Paper D. It shows the modelling results of room C1.09 together with its statistical properties.

## 4.4 Embedded Stochastic Disturbance Models for Optimal Control Problems

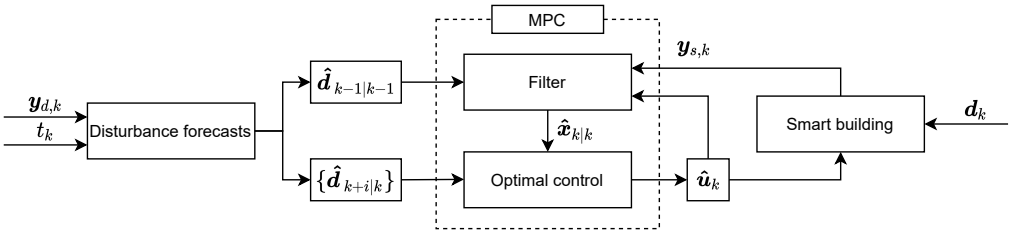


Figure 4.4: This plot is taken from Paper E. It depicts the MPC framework with an embedded disturbance model.

Paper E presents a method for embedding a disturbance model into a controller such that disturbance forecasts are supplied on the fly in continuous time. The paper considers SDE models for both the system and disturbances and demonstrates the method via thermal control of the indoor air in a building. For such a system, the outdoor air temperature and solar radiation are considered the significant disturbances. The former acts through a low-

pass filter (the walls) and does not influence the dynamics much—instead, it determines a base line heat load needed to keep a constant temperature at steady state. In contrast, the solar radiation fluctuates significantly and delivers a lot of energy in short time intervals and is the number one source of discomfort due to overheating inside buildings.

Figure 4.4 shows the control framework using the embedded disturbance model. Just as with the system, the controller applies the filtering principle on the disturbances as new information becomes available. It then uses the disturbance model to compute new forecasts for each time an optimal control problem is being solved. It then computes the expected disturbances forward in time. Figure 4.5 shows an example of the expected and true disturbances: The accuracy decays with time since the forecasts are based only on historical data and requires no inputs. Therefore, for forecasts beyond 5-8 hours, meteorological forecasts might be preferred.

Results suggests, compared to current standards for mitigating disturbances, that using the embedded disturbance model offers significant improvements. In a simulation study where the indoor air climate in buildings is controlled, the paper compares the embedded disturbance forecasts to perfect forecasts and finds that their performance is almost identical. The simulation study compares different heating devices (and heating strategies) since the dynamics may differ significantly for different heating devices. These are

- Electrical heater (fast dynamics, coefficient of performance equal to 1)
- heat pump (slow dynamics, coefficient of performance between 3 and 6)
- heat pump plus electrical heater (can heat with both the slow/fast and efficient/inefficient device)
- heat pump plus electrical heater AND cooler (as the above setup but is able to cool as well)

Results suggest electricity savings between 5-10% and reduction in comfort violations of up to 90% compared to standard forecasting strategies. Paper F carries out a simulation study using LQG control and finds that operational improvements of up to 25% percent is available. Figure 4.6 shows a simulation of two weeks where the three forecasting schemes (perfect, advanced, and persistent) are presented.

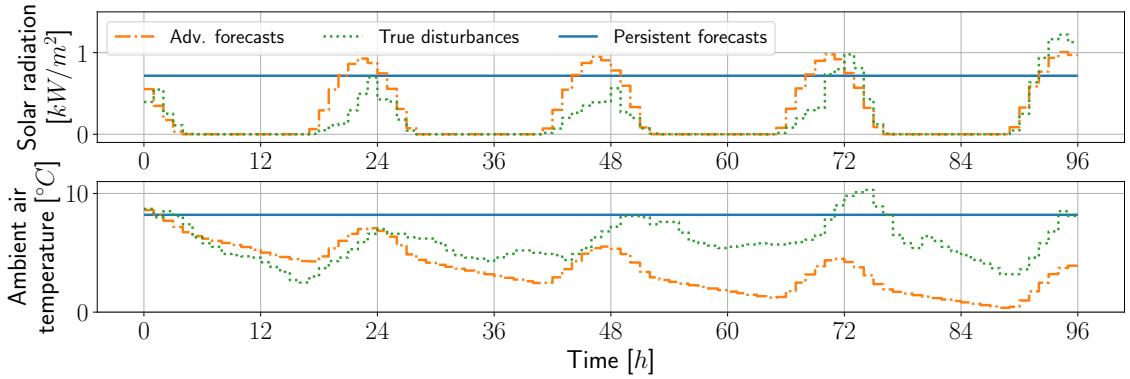


Figure 4.5: This plot is taken from Paper E. It shows the conditional mean value forecasts of the disturbances (ambient air temperature and global solar radiation) against persistent forecasts. It also shows that the model reaches some steady state while the disturbances of course continues its fluctuations.

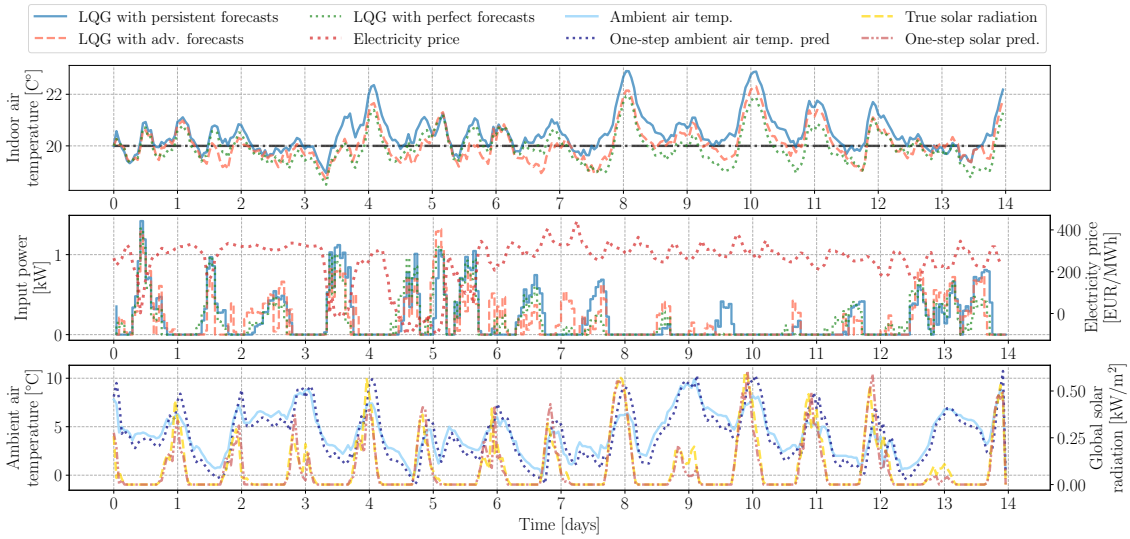


Figure 4.6: This figure is taken from Paper F. It displays a 14-day sample of the operation of the different forecasting strategies carried out to compare the LQG control methods. It shows the indoor air temperature as well as the heating inputs at the same point in the time series of disturbances.

## 4.5 Optimal Control for Chaotic Systems

Paper G introduces a method for controlling chaotic dynamical systems. Chaotic systems are characterised by having positive Lyapunov exponents. That is, given two infinitesimally separated points at time $t_0$, integrating the chaotic system forward will lead to exponentially increasing separation of the two points. This implies that the dynamical system loses its predictability exponential in time. For predictive control, this is an issue since it is difficult to stabilise the system.

Current state of the art relies on stabilising the system around an already existing unstable periodic orbit. This is done by pushing the system onto the stable manifold of the unstable periodic orbit with small perturbations.

But what if an unstable periodic orbit does not exist for the place in the state space we wish to stabilise the system? In that case, current methods does not suffice. Paper G introduces a method for altering the chaotic system such that an unstable periodic orbit appears at the exact place we want. This is done by solving an optimal control problem. The solution to the altered system now embeds the desired unstable periodic orbit. Now, current methods for stabilising the system around the unstable periodic orbit can be utilised to finish the job.

Paper G focuses on the driven Josephson junction governed by the equation

$$\ddot{\phi} + \alpha\dot{\phi} + \sin\phi = \eta + A\sin(\omega t) + u_1 + u_2\,, \tag{4.2}$$

where $u_1$ and $u_2$ are the control inputs. We apply $u_1$ such that the system is altered to make the desired unstable periodic orbit appear. $u_2$ is then the small perturbations to stabilise the system around the newly introduced unstable periodic orbit. Figure 4.7a shows the Josephson junction *before* the input $u_1$ is applied and all the period-1, -2, and -3 solutions on the Poincaré map defined by $\phi(2\pi n)$, $n \in \mathbb{N}$. The plot in 4.7b shows the chaotic attractor *after* $u_1$ is applied and the desired unstable periodic orbit appears. The plot in 4.7c shows a time series of $\phi(2\pi n)$, $n \in \mathbb{N}$ where the arrows indicate when the

control signals $u_1$ and $u_2$ are applied. It clearly shows how the system is stabilised by the end of the time series. This solution was not obtainable without the newly introduced method.

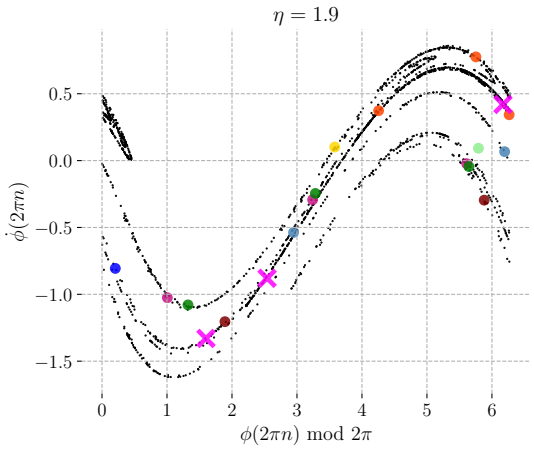


(a) The chaotic attractor of the Josephson junction together with all the period-1, -2, and -3 solutions of the system (colored dots). Each color is a periodic solution. The pink crosses are the desired unstable periodic orbit that we wish to stabilise the system around (which does not exists for this chaotic attractor).

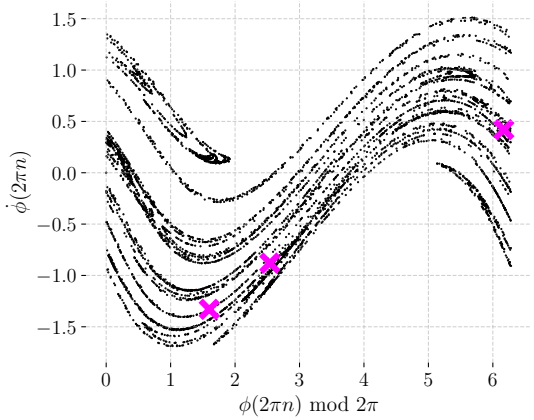


(b) The chaotic attractor after the system has been altered—it now embeds the desired unstable periodic orbit marked with purple crosses.

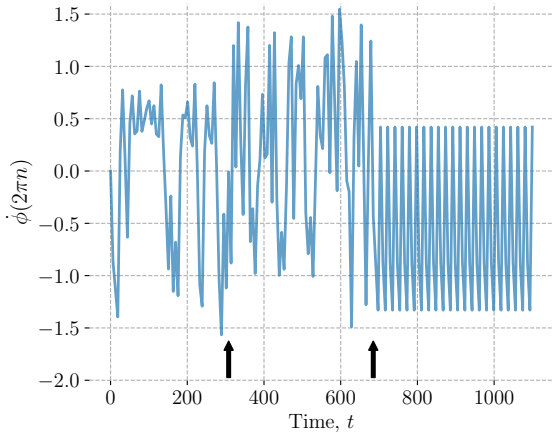


(c) The controlled Josephson junction. The black arrows indicates the points in time where the two control signals are applied. The first arrow is the altering control signal (such that the system embeds the desired periodic orbit). The second is the adaptive control to stabilise the system around this orbit.

Figure 4.7: These plots are taken from Paper G. It shows the chaotic attractor of the Josephson junction together with the altered system (where the desired unstable periodic orbit exists). The lower plot shows the Josephson junction when both of the controls are turned on and stabilises the system.

# 5 Conclusion, outlook, and future perspectives

The main focus of this dissertation has been many-fold. However, the research has primarily been centred around the following

- non-linear modelling based on stochastic differential equations,
- embedded disturbance modelling and optimal control based on such,
- optimal control of indoor air climate and energy usage of buildings (smart buildings, if you will),

The main findings are, among many things, that non-linearities and disturbances are crucial to include in system models for obtaining sufficient optimal control performance.

One focus has been on the description, modelling, and inclusion of advanced disturbance models in optimal control problems. Paper E and F describe the principle of accurately modelling the system disturbances and then including them in the model description. This has the advantage of being readily used in optimal control and we have seen that this increased the control performance significantly compared to current standards.

The second focus was on identifying and modelling non-linearities of building thermal dynamics. The non-linearities become significant when using a centralised water-based heating system, which is common in Denmark. Modelling the non-linearities compared to using linear approximations increase the control performance drastically.

The last prime focus was on optimal control of building thermal dynamics. The non-linearities pose a challenge towards the identifiability of the underlying model. Consequently, in order to control the building's heat consumption, an aggregated building model is needed. Real life experiments suggest that such a control setup could work. However, problems still remain and needs further investigation to be solved.

## 5.1 Modelling and control of building thermal dynamics

Paper A and D dealt with identification and modelling of building thermal dynamics. Due to the water-based heating system of the building, the heat usage in each room is not known. Therefore, to model the heat demand of the building, an aggregated building model was needed (that used the average air temperature of the rooms as reference). The real-life optimal control quickly revealed that some room-based control is needed, since almost all rooms varied too much from the reference temperature because they need different treatment. The room-based control could be based on either a static or dynamic model:

- **A static model** could be an offset in the set-point temperature used in the thermostat. This would presumably elevate the air temperature in the room by the offset value. However, the rooms' placement in the heating system graph also determines how much water flows to each room, which requires more information to incorporate.
- **A dynamic model** could be an ARX-model as proposed in D (or even continuous-time models) where the solar radiation and thermostatic dynamics are incorporated. Additional information about the rooms' interaction with each other could also be included.

Both of these approaches could improve the applied optimal control performance and mitigate the evident variance of the room temperatures around the reference mean value. However—as mentioned multiple times already—room-level control cannot quantify the heat usage of the rooms. Therefore, a hierarchical control setup could be a solution to control the heat usage. The aggregated building model constitute the upper level controller, which computes a reference temperature forward in time. Each room then has its own (say) dynamic model and controller, which tries to track the reference temperature. The upper level thus optimises over the heat usage and tries to decide the building's overall heat load. The lower level controllers then make sure that each room is comfortably heated by following the reference by individually controlling each room.

This also resembles well with the fact that a multi-room building typically has a substation for the entire building and then individual controllers for each room. Today, the individual control is typically provided by thermostats, but in the future a different set point for each room might be advantageous. This also opens up for human-in-the-loop control.

Another promising avenue for future research could be derived from the temporal (and spatial) hierarchical forecasting literature (Athanasopoulos et al., 2017). A hierarchical forecasting example could be in the case of heat load forecasting (Nystrup et al., 2020), where models predicting the heat load during different time intervals need to align with each other. Specifically, the sum of the predictions made by two models forecasting the heat load during hours 1-6 and 7-12, respectively, must be equal to the prediction made by a single model forecasting the total heat load during hours 1-12. This idea of ensuring agreement across different scales could prove useful as a regularization technique for modelling individual rooms in a building. Specifically, the combined heat load on the building level could serve as a regularization constraint on the combined temperature increase across all rooms (somehow). This line of research could offer interesting directions for further exploration.

## 5.2 Disturbance modelling for optimal control

For systems described in continuous time, continuous-time disturbances gets rid of the zero-order hold assumption, which (as shown in this dissertation) gives rise to errors. Thus, by including accurate continuous-time disturbance forecasts, the discretisation errors disappear and may give more accurate control performance. Paper E and Paper F introduces embedded continuous-time disturbance forecasts for building thermal control and shows that significant improvements are available. More research is needed to quantify the improvements that continuous disturbance forecasts may supply over zero-order disturbances forecasts.

For building thermal control, the embedded forecasts has an addition advantage over, e.g., meteorological forecasts for short term purposes. The solar radiation and outdoor air temperature can vary significantly by location even for small geographical distances (Hjörleifur G. Bergsteinsson et al., 2022). The embedded disturbance model utilises local weather observation and thus eliminates local bias in the forecasts. Often, numerical meteorological forecasts are made for larger areas—e.g. 10-by-10 kilometres. An embedded disturbance model can correct for this local bias introduced by the numerical weather forecasts. It is suggested to look further into this line of research to investigate and quantify the benefits further and find the best use cases.

# Bibliography


Steffen, Will et al. (2015). "Planetary boundaries: Guiding human development on a changing planet". In: *Science* 347.6223, p. 1259855. DOI: 10.1126/science.1259855. eprint: https://www.science.org/doi/pdf/10.1126/science.1259855. URL: https://www.science.org/doi/abs/10.1126/science.1259855.

Klimarådet (Mar. 2020). *Kendte veje og nye spor til 70 procents reduktion*. Klimarådet.

– (Nov. 2019). *Status for Danmarks klimamålsætninger og -forpligtelser 2019*. Klimarådet.

Junker, Rune Grønborg, Carsten Skovmose Kallesøe, et al. (2020). "Stochastic nonlinear modelling and application of price-based energy flexibility". In: *Applied Energy* 275, p. 115096. ISSN: 0306-2619. DOI: https://doi.org/10.1016/j.apenergy.2020.115096. URL: https://www.sciencedirect.com/science/article/pii/S0306261920306085.

Dominković, Dominik Franjo et al. (2020). "Implementing flexibility into energy planning models: Soft-linking of a high-level energy planning model and a short-term operational model". In: *Applied Energy* 260, p. 114292. ISSN: 0306-2619. DOI: https://doi.org/10.1016/j.apenergy.2019.114292. URL: https://www.sciencedirect.com/science/article/pii/S0306261919319798.

De Zotti, Giulia, Seyyed Ali Pourmousavi Kani, et al. (2018). "Consumers' Flexibility Estimation at the TSO Level for Balancing Services". eng. In: *IEEE Transactions on Power Systems* 34.3, pp. 1918–1930. ISSN: 15580679, 08858950. DOI: 10.1109/TPWRS.2018.2885933.

De Zotti, Giulia, Seyyed Ali Pourmousavi Kani, et al. (2020). "A Control-based Method to Meet TSO and DSO Ancillary Services Needs by Flexible End-Users". eng. In: *IEEE Transactions on Power Systems* 35.3, pp. 1868–1880. ISSN: 15580679, 08858950. DOI: 10.1109/TPWRS.2019.2951623.

Madsen, Henrik, Jacopo Parvizi, et al. (2015). "Control of Electricity Loads in Future Electric Energy Systems". eng. In: *Handbook of Clean Energy Systems*. Ed. by Antonio J. Conejo, Erik Dahlquist, and Jinyue Yan.

Santos, Athila Quaresma and Bo Nørregaard Jørgensen (2019). *Control strategies and algorithms for obtaining Energy Flexibility in buildings*.

Ma, Zheng, Bo Nørregaard Jørgensen, and Jim Parker (2019). *Stakeholders' perceptiveson Energy Flexible Buildings*.

Lund, Henrik and Ebbe Münster (2006). "Integrated energy systems and local energy markets". In: *Energy Policy* 34.10, pp. 1152–1160.

Parvizi, Jacopo, John B. Jørgensen, and Henrik Madsen (2018). "Robust Model Predictive Control with Scenarios for Aggregators in Grids with High Penetration of Renewable Energy Sources". In: *2018 IEEE International Conference on Communications, Control, and Computing Technologies for Smart Grids (SmartGridComm)*, pp. 1–7. DOI: 10.1109/SmartGridComm.2018.8587603.

Iacus, Stefano M. (2008). *Simulation and Inference for Stochastic Differential Equations: With R Examples (Springer Series in Statistics)*. 1st ed. Springer Publishing Company, Incorporated. ISBN: 0387758380.

Jazwinski, Andrew (Jan. 1970). *Stochastic Processes and Filtering Theory*. Academic Press. ISBN: 9780080960906.

Thygesen, Uffe Høgsbro (2022). *Stochastic Differential Equations for science and engineering*. Accepted for publication by CRC Press / Taylor and Francis.

Candanedo, José and Andreas Athienitis (June 2011). "Predictive Control of Radiant Floor Heating and Transmitted Irradiance in a Room with High Solar Gains (ML-11-015)". In: *HVAC&R Research* 17, pp. 235–256.

Bjork, Tomas (2009). *Arbitrage Theory in Continuous Time*. 3rd ed. Oxford University Press. URL: https://EconPapers.repec.org/RePEc:oxp:obooks:9780199574742.

Oksendal, Bernt (1992). *Stochastic Differential Equations (3rd Ed.): An Introduction with Applications*. Berlin, Heidelberg: Springer-Verlag. ISBN: 3387533354.

Mikosch, T (1998). *Elementary Stochastic Calculus with Finance in View*. Dutch. World Scientific Publishing. ISBN: 981-02-3543-7.

Møller, Jan Kloppenborg and Henrik Madsen (2010). *From state dependent diffusion to constant diffusion in stochastic differential equations by the Lamperti transform*.

Kristensen, Niels Rode, Henrik Madsen, and Sten Bay Jørgensen (2004). "Parameter estimation in stochastic grey-box models". In: *Automatica* 40.2, pp. 225–237. ISSN: 0005-1098. DOI: https://doi.org/10.1016/j.automatica.2003.10.001. URL: https://www.sciencedirect.com/science/article/pii/S000510980300298X.

Juhl, Rune et al. (2016). "Modeling and Prediction Using Stochastic Differential Equations". In: *Prediction Methods for Blood Glucose Concentration: Design, Use and Evaluation*. Ed. by Harald Kirchsteiger et al. Cham: Springer International Publishing, pp. 183–209. ISBN: 978-3-319-25913-0. DOI: 10.1007/978-3-319-25913-0_10. URL: https://doi.org/10.1007/978-3-319-25913-0_10.

Boiroux, Dimitri et al. (2016). "Model Identification using Continuous Glucose Monitoring Data for Type 1 Diabetes**This work has been funded by the Danish Diabetes Academy supported by the Novo Nordisk Foundation." In: *IFAC-PapersOnLine* 49.7. 11th IFAC Symposium on Dynamics and Control of Process SystemsIncluding Biosystems DYCOPS-CAB 2016, pp. 759–764. ISSN: 2405-8963. DOI: https://doi.org/10.1016/j.ifacol.2016.07.279. URL: https://www.sciencedirect.com/science/article/pii/S2405896316304864.

Duun-Henriksen, Anne Katrine et al. (2013). "Model Identification Using Stochastic Differential Equation Grey-Box Models in Diabetes". In: *Journal of Diabetes Science and Technology* 7.2. PMID: 23567002, pp. 431–440. DOI: 10.1177/193229681300700220. eprint: https://doi.org/10.1177/193229681300700220. URL: https://doi.org/10.1177/193229681300700220.

Costanzo, Giuseppe Tommaso et al. (2013). "Grey-box modeling for system identification of household refrigerators: A step toward smart appliances". In: *2013 4th International Youth Conference on Energy (IYCE)*, pp. 1–5. DOI: 10.1109/IYCE.2013.6604197.

Nielsen, Henrik Aalborg and Henrik Madsen (2006). "Modelling the heat consumption in district heating systems using a grey-box approach". In: *Energy and Buildings* 38.1, pp. 63–71. ISSN: 0378-7788. DOI: https://doi.org/10.1016/j.enbuild.2005.05.002. URL: https://www.sciencedirect.com/science/article/pii/S0378778805000745.

Møller, Jan Kloppenborg et al. (2012). "Development of a restricted state space stochastic differential equation model for bacterial growth in rich media". In: *Journal of Theoretical Biology* 305, pp. 78–87. ISSN: 0022-5193. DOI: https://doi.org/10.1016/j.jtbi.2012.04.015. URL: https://www.sciencedirect.com/science/article/pii/S0022519312001968.

Thyregod, Peter et al. (1998). "Modelling the embedded rainfall process using tipping bucket data". eng. In: *Water Science and Technology* 37.11, pp. 57–64. ISSN: 02731223, 19969732. DOI: 10.2166/wst.1998.0435.

Kulikov, Gennady Yu. and Maria V. Kulikova (2017). In: *Russian Journal of Numerical Analysis and Mathematical Modelling* 32.1, pp. 27–38. DOI: doi:10.1515/rnam-2017-0003. URL: https://doi.org/10.1515/rnam-2017-0003.

Brok, Niclas Laursen, Henrik Madsen, and John Bagterp Jørgensen (2018). "Nonlinear Model Predictive Control for Stochastic Differential Equation Systems". In: *IFAC-PapersOnLine* 51.20. 6th IFAC Conference on Nonlinear Model Predictive Control NMPC 2018, pp. 430–435. ISSN: 2405-8963. DOI: https://doi.org/10.1016/j.ifacol.2018.11.071. URL: https://www.sciencedirect.com/science/article/pii/S2405896318327290.

Madsen, Henrik and Poul Thyregod (Jan. 2011). *Introduction to General and Generalized Linear Models*. ISBN: 978-1420091557. DOI: 10.1201/9781439891148.

Hagdrup, Morten et al. (2016). "On the significance of the noise model for the performance of a linear MPC in closed-loop operation". In: *IFAC-PapersOnLine* 49.7. 11th IFAC Symposium on Dynamics and Control of Process SystemsIncluding Biosystems DYCOPS-CAB 2016, pp. 171–176. ISSN: 2405-8963. DOI: https://doi.org/10.1016/j.ifacol.2016.07.241. URL: https://www.sciencedirect.com/science/article/pii/S2405896316304487.

Madsen, Henrik (1985). "Statistically determined dynamical models for climate processes". PhD thesis. Technical University of Denmark.

– (2007). *Time series analysis*. English. Chapman & Hall. ISBN: 9780429195839. DOI: 10.1201/9781420059687.

Haessig, Pierre et al. (2015). "Energy storage sizing for wind power: impact of the autocorrelation of day-ahead forecast errors". In: *Wind Energy* 18.1, pp. 43–57. DOI: https://doi.org/10.1002/we.1680. eprint: https://onlinelibrary.wiley.com/doi/pdf/10.1002/we.1680. URL: https://onlinelibrary.wiley.com/doi/abs/10.1002/we.1680.

Mantovani, Giancarlo and Luca Ferrarini (2015). "Temperature Control of a Commercial Building With Model Predictive Control Techniques". In: *IEEE Transactions on Industrial Electronics* 62.4, pp. 2651–2660. DOI: 10.1109/TIE.2014.2387095.

Thilker, Christian Ankerstjerne, Peder Bacher, and Henrik Madsen (2022). "Learnings from experiments with MPC for heating of older school building". English. In: vol. 362. BuildSim Nordic 2022 ; Conference date: 22-08-2022 Through 23-08-2022. E D P Sciences. DOI: 10.1051/e3sconf/202236212004.

Vukov, M. et al. (2015). "Real-time nonlinear MPC and MHE for a large-scale mechatronic application". In: *Control Engineering Practice* 45, pp. 64–78. ISSN: 0967-0661. DOI: https://doi.org/10.1016/j.conengprac.2015.08.012. URL: https://www.sciencedirect.com/science/article/pii/S0967066115300095.

Brok, Niclas et al. (2022). "Optimal operation of an ice-tank for a supermarket refrigeration system". In: *Control Engineering Practice* 119, p. 104973. ISSN: 0967-0661. DOI: https://doi.org/10.1016/j.conengprac.2021.104973. URL: https://www.sciencedirect.com/science/article/pii/S0967066121002501.

Schlüter, Hjørdis Amanda et al. (2019). "Economic Model Predictive Control for Energy Systems in Smart Homes". In: *2019 IEEE Conference on Control Technology and Applications (CCTA)*, pp. 598–604. DOI: 10.1109/CCTA.2019.8920663.

Capolei, Andrea et al. (2015). "A mean–variance objective for robust production optimization in uncertain geological scenarios". In: *Journal of Petroleum Science and Engineering* 125, pp. 23–37. ISSN: 0920-4105. DOI: https://doi.org/10.1016/j.petrol.2014.11.015. URL: https://www.sciencedirect.com/science/article/pii/S0920410514003751.

Prékopa, András (2013). *Stochastic programming*. Vol. 324. Springer Science & Business Media.

Clarke, Frank H. (1976). "The Generalized Problem of Bolza". In: *SIAM Journal on Control and Optimization* 14.4, pp. 682–699. DOI: 10.1137/0314044. eprint: https://doi.org/10.1137/0314044. URL: https://doi.org/10.1137/0314044.

Boyd, Stephen and Lieven Vandenberghe (2004). *Convex Optimization*. English. Cambridge University Press. ISBN: 9780521833783. DOI: 10.1017/CBO9780511804441.

Åström, Karl J (2012). *Introduction to stochastic control theory*. Courier Corporation.

Andersen, Martin, Joachim Dahl, and Lieven Vandenberghe (Mar. 2022). *CVXOPT*. https://cvxopt.org/.

Jørgensen, John Bagterp (2007). "Adjoint sensitivity results for predictive control, state- and parameter-estimation with nonlinear models". In: *2007 European Control Conference (ECC)*, pp. 3649–3656. DOI: 10.23919/ECC.2007.7068974.

Morrison, David D., James D. Riley, and John F. Zancanaro (Dec. 1962). "Multiple Shooting Method for Two-Point Boundary Value Problems". In: *Commun. ACM* 5.12, pp. 613–614. ISSN: 0001-0782. DOI: 10.1145/355580.369128. URL: https://doi.org/10.1145/355580.369128.

Aydogmus, Ozgur and Ali Hakan TOR (2021). "A Modified Multiple Shooting Algorithm for Parameter Estimation in ODEs Using Adjoint Sensitivity Analysis". In: *Applied Mathematics and Computation* 390, p. 125644. ISSN: 0096-3003. DOI: https://doi.org/10.1016/j.amc.2020.125644. URL: https://www.sciencedirect.com/science/article/pii/S0096300320305981.

Grimm, W. and A. Markl (1997). "Adjoint Estimation from a Direct Multiple Shooting Method". In: *Journal of Optimization Theory and Applications*, pp. 263–283. DOI: 10.1023/A:1022650928786.

Blanco, Ignacio et al. (2018). "Operational Planning and Bidding for District Heating Systems with Uncertain Renewable Energy Production". In: *Energies* 11.12. ISSN: 1996-1073. DOI: 10.3390/en11123310. URL: https://www.mdpi.com/1996-1073/11/12/3310.

Guericke, Daniela et al. (Dec. 2020). "A two-phase stochastic programming approach to biomass supply planning for combined heat and power plants". In: 42, pp. 863–900. DOI: 10.1007/s00291-020-00593-x.

Iversen, E. B. et al. (2014). "Probabilistic forecasts of solar irradiance using stochastic differential equations". In: *Environmetrics* 25.3, pp. 152–164. DOI: https://doi.org/10.1002/env.2267. eprint: https://onlinelibrary.wiley.com/doi/pdf/10.1002/env.2267. URL: https://onlinelibrary.wiley.com/doi/abs/10.1002/env.2267.

Johnsen, Morten Guldborg, Lasse Engbo Christiansen, and Kaare Græsbøll (2022). "Seasonal variation in the transmission rate of covid-19 in a temperate climate can be implemented in epidemic population models by using daily average temperature as a proxy for seasonal changes in transmission rate". In: *Microbial Risk Analysis* 22, p. 100235. ISSN: 2352-3522. DOI: https://doi.org/10.1016/j.mran.2022.100235. URL: https://www.sciencedirect.com/science/article/pii/S2352352222000329.

Bergsteinsson, Hjörleifur G. et al. (2021). "Heat load forecasting using adaptive temporal hierarchies". In: *Applied Energy* 292, p. 116872. ISSN: 0306-2619. DOI: https://doi.org/10.1016/j.apenergy.2021.116872. URL: https://www.sciencedirect.com/science/article/pii/S0306261921003603.

Thilker, Christian Ankerstjerne (2020). "Optimization for Smart Energy Systems". MA thesis. Department of Applied Mathematics and Computer Science.

Junker, Rune Grønborg, Armin Ghasem Azar, et al. (2018). "Characterizing the energy flexibility of buildings and districts". In: *Applied Energy* 225, pp. 175–182. ISSN: 0306-2619. DOI: https://doi.org/10.1016/j.apenergy.2018.05.037. URL: https://www.sciencedirect.com/science/article/pii/S030626191830730X.

Christensen, Ole (2010). *Functions, Spaces, and Expansions*. Birkhauser Basel. DOI: 10.1007/978-0-8176-4980-7.

Fritsch, F. N. and R. E. Carlson (1980). "Monotone Piecewise Cubic Interpolation". In: *SIAM Journal on Numerical Analysis* 17.2, pp. 238–246. ISSN: 00361429. URL: http://www.jstor.org/stable/2156610.

Lamoureux, Christopher G. and William D. Lastrapes (1990). "Persistence in Variance, Structural Change, and the GARCH Model". In: *Journal of Business & Economic Statistics* 8.2, pp. 225–234. DOI: 10.1080/07350015.1990.10509794. URL: https://www.tandfonline.com/doi/abs/10.1080/07350015.1990.10509794.

Athanasopoulos, George et al. (2017). "Forecasting with temporal hierarchies". In: *European Journal of Operational Research* 262.1, pp. 60–74. ISSN: 0377-2217. DOI: https://doi.org/10.1016/j.ejor.2017.02.046. URL: https://www.sciencedirect.com/science/article/pii/S0377221717301911.

Nystrup, Peter et al. (2020). "Temporal hierarchies with autocorrelation for load forecasting". In: *European Journal of Operational Research* 280.3, pp. 876–888. ISSN: 0377-2217. DOI: https://doi.org/10.1016/j.ejor.2019.07.061. URL: https://www.sciencedirect.com/science/article/pii/S037722171930640X.

Bergsteinsson, Hjörleifur G. et al. (2022). "Data-Driven Methods for Efficient Operation of District Heating Systems". In: *Handbook of Low Temperature District Heating*. Ed. by Roberto Garay-Martinez and Antonio Garrido-Marijuan. Cham: Springer International Publishing, pp. 129–163. DOI: 10.1007/978-3-031-10410-7_6. URL: https://doi.org/10.1007/978-3-031-10410-7_6.

# Part II

## Publications

# A Published - Non-linear grey-box modelling for heat dynamics of buildings

# Non-Linear Grey-Box Modelling for Heat Dynamics of Buildings

Christian Ankerstjerne Thilker, Peder Bacher, Hjörleifur G. Bergsteinsson, Rune Grønborg Junker, Davide Cali, Henrik Madsen

*Technical University of Denmark, Department of Applied Mathematics and Computer Science,*
*Asmussens Allé, Building 303B, DK-2800 Kgs. Lyngby, Denmark*

**Abstract**

This paper introduces a non-linear grey-box (GB) model based on stochastic differential equations that describes the heat dynamics of a school building in Denmark, equipped with a water-based heating system. The building is connected to a local district heating network through a heat exchanger. The heat is delivered to the rooms mainly through radiators and partially through a ventilation system. A monitoring system based on IoT sensors provides data on indoor climate in the rooms and on the heat load of the building. Using this data, we estimate unknown states and parameters of a model of the building's heating system using the maximum likelihood method. Important novelties of this paper include models of the water flow in the circuit and the state of the valves in the radiator thermostats. The non-linear model accurately predicts the indoor air temperature, return water temperature and heat load. The ideas behind the model lay a foundation for GB models of buildings that use different kinds of water-based heating systems such as air-to-water/water-to-water heat pumps. Such GB models enable model predictive control to control e.g. the indoor air climate or provide flexibility services.

*Keywords:* Grey-box models, Stochastic differential equations, Non-linear models, District heating, Smart energy systems

## 1. Introduction

The use of fossil-based energy sources does not belong in a sustainable future [1]. Society must shift to energy sources where $CO_2$-emissions lie within the planetary boundaries; i.e. we need to use resources that are renewable [2]. This future low-carbon society calls for fundamental changes of the energy system. Today the systems are operated such that the production follows the demand. However, an efficient implementation of a low-carbon society calls for a system where the demand follows the weather-driven energy production. Most importantly we need methods for unlocking the flexibility at all levels of the society; examples being buildings, supermarkets, wastewater treatment plants, industrial process facilities, districts, municipalities and cities. A lot of recent work, therefore, centres around the concept known as energy flexibility [3, 4]. The core idea is to control the energy consumption to align it with energy production. For this purpose, model-based predictive control is a very promising control framework [5]. This paper introduces a novel grey-box (GB) model based on stochastic differential equations (SDEs) that is designed for controller based optimisation of the heat load of buildings. The ultimate purpose of developing such a GB model is to intelligently control buildings in order to minimise the $CO_2$-emissions and unlock the flexibility. A reliable model (together with weather forecasts) is essential for a good performance of model predictive control (MPC) for buildings [6].

MPC for control of buildings' indoor climate requires reliable building models that describe the heat dynamics. Complex building energy performance models based exclusively on physical equations, known as white–box models, are often used for providing simulations. Occasionally, in white box building models, stochastic models are used to simulate occupants behaviour, as in [7, 8]. However, they are demanding to build, computationally heavy, and difficult or impossible to tune to real-world data, which makes them infeasible for control. Especially for the existing building stock. On the contrary, black–box models can be fast in terms of simulation time. But they do not include laws of physics, and thus may be hard to interpret and lack the ability to extrapolate and generalise beyond training data. GB models bridge the gap between white- and black-box models by leveraging both physical and statistical properties [9]. They are based on *simple* physical principles and considerations of the system, which make them computationally light and ideal for parameter calibration using available data. Linear GB models for buildings are widely seen in the literature [10]. Wang and Xu [11] use a genetic algorithm to estimate a linear heat dynamics model that describes the thermal conditions in the wall envelopes and internal mass for an office building. The goal is to predict the heat load and the indoor air temperature. Massano et al. [12] uses an unscented Kalman filter to estimate parameters in a linear RC-inspired model to predict the indoor air temperature. Bacher and Madsen [13] outlines a model development procedure for SDE-based GB models. However, it is a well known fact that *non-linear systems* exhibit vast richness in the solution structure, far beyond what is seen in linear systems [14]. For instance, non-linear models are necessary to sufficiently describe the heat dynamics of build-

*Email addresses:* chant@dtu.dk (Christian Ankerstjerne Thilker), pbac@dtu.dk (Peder Bacher), hgbe@dtu.dk (Hjörleifur G. Bergsteinsson), rung@dtu.dk (Rune Grønborg Junker), dcal@dtu.dk (Davide Cali), hmad@dtu.dk (Henrik Madsen)

ing integrated photo-voltaic modules [15, 16]. Non-linear GB models can also be found within industrial robotics [17] and in aquatic ecosystems modelling [18], just to mention a few areas. To the knowledge of the authors, the literature on non-linear GB models for radiator-based heating systems is scarce.

We propose SDEs as the modelling framework for the building model [19]. This has many advantages: First, SDEs provide a natural method to model physical phenomena as they are formulated in continuous-time. Second, they include probabilistic uncertainty that accounts for modelling approximations, unrecognised exogenous variables, and uncertainty related to the provided input variables. Last, they lay a solid foundation providing predictions of the system behaviour and for model-based optimal control, to predict system behaviour. It is well-know that solutions to Ordinary Differential Equations (ODEs) are functions of time, and this implies that an ODE modelling framework assumes that we are able to predict the exact evolution in time of the states. Solutions to SDEs are stochastic processes, which are characterised by the family of finite-dimensional densities, and this implies that the future evolution of the states is encumbered with uncertainty, and this uncertainty can be quantified. Optimal control theory based on SDEs is well-established in the literature with numerous examples of applications, e.g. for control of glucose concentration in humans [20], building thermal control [21], and operation of waste-water treatment plants [22].

### 1.1. Main contributions

The existing literature contains various examples of linear GB models of the heat dynamics of buildings. However, the literature seems to contain limited work on SDE-based non-linear GB models for water-based heating systems, especially related to district heating (DH). This paper presents and analyses the development of a non-linear GB model for a school building in Denmark with water-based heating. We base the analysis and estimation on a single week of data using meteorological weather observations as inputs, and we will demonstrate that one week of data is sufficient for identifying a good model. Due to the generality of the model, it is argued that the model is applicable to a wide range of buildings with water-based heating systems and different heat sources (including heat pumps).

An important contribution of this paper is the model of the thermostatic valves of the radiators. The radiator valves are mechanically adjusted by the thermostats that are configured with a set-point. The valves open and close proportionally to the difference between the set-point and actual air temperature. The valves naturally do not behave discontinuously when heat is or is not needed. Models for thermostatic valves exist in applications of white-box models [23]. Most are modelled as P, PI, or PID-based controllers for white-box building models [24]. Hansen [25] suggested detailed physical models of radiators and thermostats. However, the models end up being too large and detailed for grey-box purposes. To the knowledge of the authors, the literature contains no examples of models for thermostat valves formulated as GB-models. This paper presents a sigmoid-function to describe the continuous sensitivity of the valves due to changes in the indoor air temperature according to the set-point. Another important contribution is a model of the water flow in the building heating system.

### 1.2. Structure and outline of the paper

This paper has the following structure. Section 2 introduces the building and its engineering systems, together with the overall experiment. Here, we also describe the data and how it was gathered. Section 3 describes the model development process and the ideas behind the suggested model. Next, we present and discuss the results; the parameter estimates, a simulation of the variables compared to data, and a 1-step residual analysis. Lastly, Section 6 sums up the essential findings of the paper.

## 2. The building and the experimental setup

This section introduces the building and describes the experimental data and the generation process.

### 2.1. The building

The building, a school with three floors and a basement, is located in Høje Taastrup, Denmark. The uppermost floor is a part-refurbished roof attic. Bruun [26] provides all technical information about the building.

Being built in 1929, the building is not insulated according to modern standards. Figure 1 shows a digital reconstruction and a photo of the building. It includes 10 classrooms that are ventilated by mechanical ventilation using an air handling unit (AHU) for air circulation. The facade and internal walls consist of solid bricks (300 mm and 180 mm thickness, respectively). The windows have wooden frames and double-paned low-E glazings. Floors are made from wood joists and the roof is partly uninsulated and partly insulated slate roof. The building is connected to the local electricity and heat grid, where the ladder is a DH system. The building uses district heating for domestic hot water (DHW), the AHU, and space heating. The latter term governs the heating (and cooling) system of the indoor air. For this building, the space heating is a separate water-based circuit with dedicated pumps. Radiators of different types (cast-iron, panel convectors, plane conductors) with individual thermostats establish the space heating system in the individual rooms of the building. Individual thermostatic valves automatically regulate the water flow into the radiator units as to maintain a pre-defined *set-point*. The space heating system is separated from the DH system by a plate heat exchanger. Independent PI-controllers regulate the water flow on both the district heating and the building side of the heat exchanger.

### 2.2. The experiment

The experiment carried out was planned in advance and designed to generate data suitable for system identification purposes. The main focus was to change the control input, the thermostat set point, such that information about the essential dynamics of the system can be estimated. A sequence of the set point was designed with four different parts. First part contains a few long steps with set points set to a minimum (10 °C) and back again to a base level (21 °C) to get information about

Figure 1: Visual illustrations of the building site. The upper digital reconstruction is supplied by [26]

the dynamics governing the system. Second part is a multi-level signal, where the extremes (14 and 27 °C) are kept for the longest time and then shorter periods are kept for relatively shorter time. Third part contains short periods with drops to a minimum from the base temperature. Finally, a step sequence where the set point is stepped from 23 °C in two hours steps down to 17 °C and up again. The forward temperature of the space heating water is set constant to 55 °C at all times. The entire sequence was slightly shorter than 7 days and was executed during the Christmas vacation, where the building was unoccupied.

### 2.3. The data

Table 1 lists all the variables of the data. Figure 2 shows the experimental data in the period December 21 through December 27. The upper graph displays the heat load of the building. It seems to be characterised by a large peak whenever the heat turns on, before reverting to a lower and steady level. The second graph shows the forward- and return water temperature, which go to and from the space heating system. The forward temperature fluctuates a lot when the thermostat set point is set very low – because the thermostat valves are closed and thus the flow in the radiator circuit is nearly stopped, which results in poor control of the forward temperature since the control was not designed for this situation. The return temperature quickly becomes large when the space heating is turned on. In absence of heat load, the return temperature quickly decreases. But, the reversion and behaviour in absence of heat load seem to be rather inconsistent. The third graph shows the indoor temperature of each room (in grey) and the mean of all rooms (in black). Lastly, the bottom graph shows the exterior weather conditions, i.e. the ambient air temperature and the global solar radiation. The latter is relatively small throughout the period, which complicates the estimation of the solar radiation gain for the model. We return to this matter later in Section 5.

The variables of the building we wish to be able to predict are the following

- The mean indoor air temperature, $T_t^i$.
- The heat load of the building delivered by the DH system, $\phi_t^h$.
- The temperature of the returning water in the SH system of the building, $T_t^{\text{ret}}$.

The subscript $t$ indicates the dependence on time. These variables are of special interest when it comes to optimal control of the indoor climate. In Denmark, building operators pay for the amount of heat they consume. Additionally, the operators pay fees for too high return temperatures since it is a source of poor energy efficiency in the DH network. First, the DH operators have to increase the mass flow rate of the water, if the users do not cool the return water. Secondly, if the return water to the DH facilities is too hot, the efficiency of the central heat production plant decreases. This payment scheme makes it economically advantageous for the building operators to use heat when it is cheap and minimise the return temperature.

Table 1: Data interpretation.

| Name | Quantity | Unit |
|---|---|---|
| $T_t^{(i,j)}$ | Indoor air temperature in room $j$ | [°C] |
| $T_t^i$ | Mean indoor air temperature in the building | [°C] |
| $T_t^{\text{for}}$ | Forward temperature | [°C] |
| $T_t^{\text{ret}}$ | Return temperature | [°C] |
| $T_t^{\text{set}}$ | Temperature set-point | [°C] |
| $\phi_t^h$ | Delivered heat to the building | [kW] |
| $T_t^a$ | Ambient air temperature | [°C] |
| $\phi_t^s$ | Solar radiation on a horizontal surface | [kW/m$^2$] |

## 3. Model development

This section describes the model development process.

Due to the large parameter and state space, it is advantageous to perform the modelling in small steps. The main idea is to split up the modelling processes into two parts. To identify the steps, we need to realise that the building heat dynamics consist of two parts (as a first simple assumption). The delivered heat from the water in the radiator system operates independently and only interacts with the indoor air temperature of the building by the radiators themselves. This interaction involves only two parameters. Therefore, we split the modelling part into the following three steps:

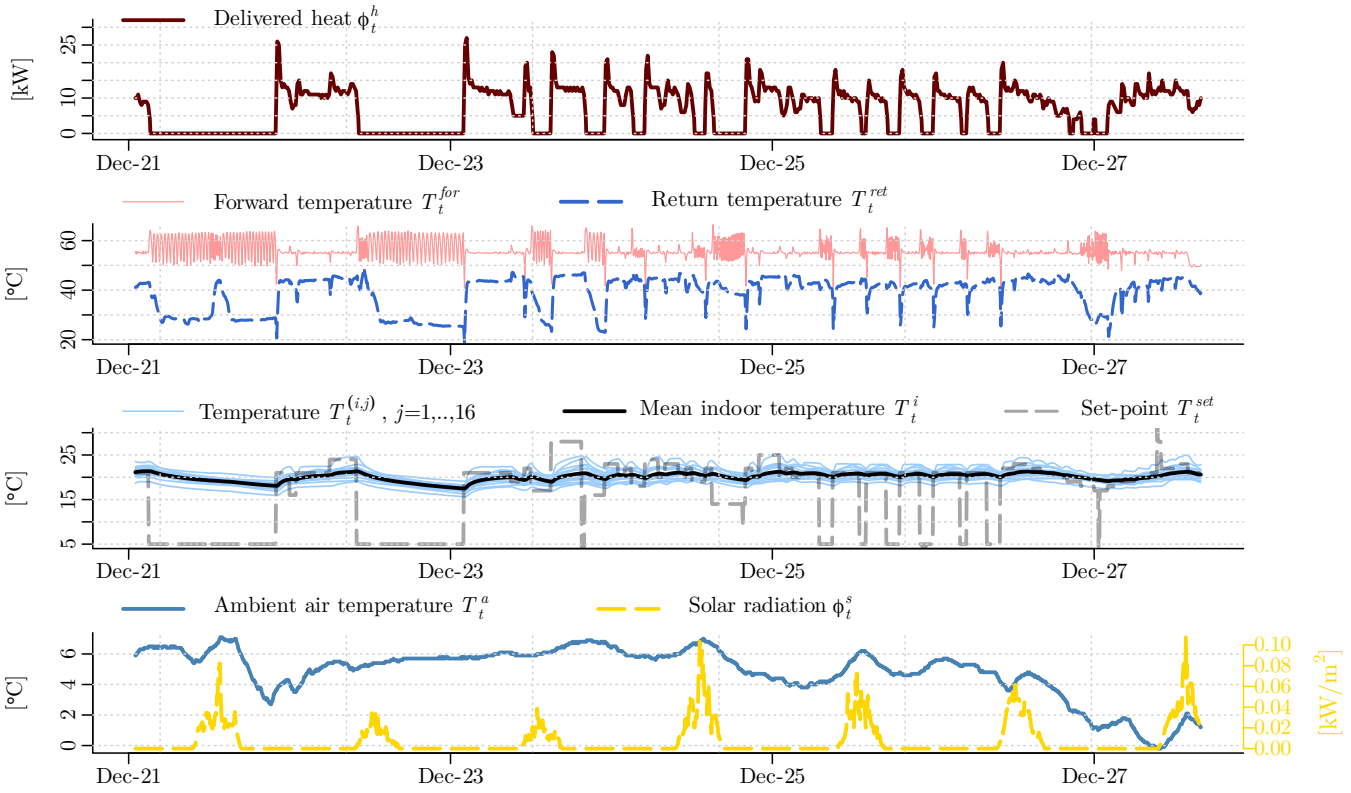


Figure 2: The data from the experiment performed in December 2019.

1. Given the observed time series of the delivered heat from the district heating system, we develop a model that predicts only the indoor air temperature of the building.
2. Given the observed time series of the indoor air temperature and set point, we develop a model that predicts only the heat load from the district heating system to the building. That is while keeping the parameters fixed, that concerns the indoor air temperature model obtained in step 1.
3. We combine the two models and start the parameter optimisation from the results of the two independently sufficient models to obtain a combined model structure.

By developing the two system models individually at first, it also becomes much easier to identify the necessary dynamical features that govern the systems.

### 3.1. Stochastic differential equations

The model will be formulated using SDEs. A SDE typically has the following form

$$\mathrm{d}\boldsymbol{X}_t = f(\boldsymbol{X}_t, t)\mathrm{d}t + g(\boldsymbol{X}_t, t)\mathrm{d}\boldsymbol{\omega}_t \tag{1}$$

where $f$ and $g$ are the drift and diffusion terms, respectively, and the subscript $t$ denotes the dependence on time. The diffusion term makes a SDE differ from an ordinary differential equation. $\omega_t$ is known as Brownian motion and is a fundamental process for stochastic calculus. It is governed by independent Gaussian increments; $\omega_t - \omega_s \sim N(0, t-s)$, for $s \leq t$. This has remarkable consequences and relates it to the physical diffusion equation. The purpose of the diffusion term is to describe chaotic phenomena that are too complex to include in the drift part of the model structure.

### 3.2. The building heat dynamics model

The literature contains numerous examples of developing heat dynamic models for buildings using continuous-time GB models, see e.g. [27–31]. We do not give the model identification steps explicitly for our case though but simply report the final result.

Figure 2 gives insights into what elements the building model should include. Inspections of the two long periods, where the heat is turned off, show that the mean indoor temperature seems to drop fast at first and then flatten to a certain decay rate. This indicates that we should include two time constants; one for the fast and initial drop and one for the slow long-term decay. We may interpret these fast and slow dynamics as the temperature

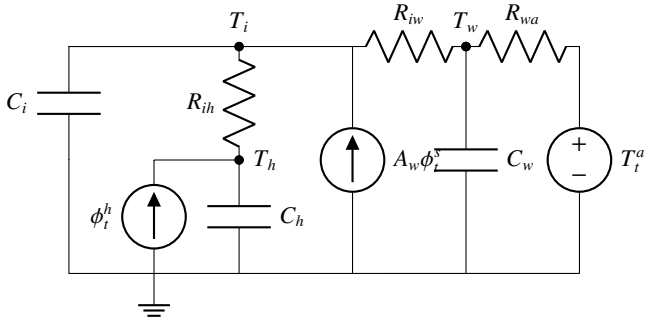


Figure 3: The model structure of the building heat dynamics. The model predicts the indoor air temperature, $\hat{T}_i$, given the delivered power $\phi_h$.

of the indoor air and the temperature of the building walls. For this reason, the wall temperature state exchanges heat with the ambient air temperature and acts as a low-pass filter between the interior and exterior. We also choose to model the radiators as an accumulating medium where the heat input enters directly. The solar radiation gain enters the room air directly through windows.

Figure 3 shows the heat dynamics structure for the building as an RC-diagram. The equivalent SDE model has the following form

$$\mathrm{d}T_t^i = \frac{1}{C_i}\left(\frac{1}{R_{ih}}\left(T_t^h - T_t^i\right) + \frac{1}{R_{iw}}\left(T_t^w - T_t^i\right) + A_w\phi_t^s\right)\mathrm{d}t + \sigma_1\mathrm{d}\omega_t^1\,, \tag{2a}$$

$$\mathrm{d}T_t^w = \frac{1}{C_w}\left(\frac{1}{R_{iw}}\left(T_t^i - T_t^w\right) + \frac{1}{R_{wa}}\left(T_t^a - T_t^w\right)\right)\mathrm{d}t + \sigma_2\mathrm{d}\omega_t^2\,, \tag{2b}$$

$$\mathrm{d}T_t^h = \frac{1}{C_h}\left(\frac{1}{R_{ih}}\left(T_t^i - T_t^h\right) + \phi_t^h\right)\mathrm{d}t + \sigma_3\mathrm{d}\omega_t^3\,. \tag{2c}$$

$$\tag{2d}$$

### 3.3. The radiator circuit dynamics model

The thermostatic valves regulate the water flow through the radiators. An important novelty of this paper is to model the thermostatic valves using the non-linear sigmoid function. The idea is that the vales open when it is too cold and close when it is too warm. Assuming that the valves react continuously to the indoor air temperature, the sigmoid function corresponds to some kind of proportional control (0 being closed and 1 being open).

#### 3.3.1. The thermostatic valve function

To describe the thermostatic control, i.e. the amount of heat that the heat exchanger delivers, we use a sigmoid function. To be specific, it describes the sensitivity of the heating system to deviations in the mean indoor temperature. We use the following formulation

$$f_t^{\text{valve}} = \frac{1}{1 + \exp\left(-\alpha(T_t^{\text{set}} + T_{\text{offset}} - T_t^i)\right)}\,. \tag{3}$$

$\alpha$ is the slope of the sigmoid function and determines how quickly the heating system turns on and off. $T_{\text{offset}}$ acts as an offset: since the observations of the indoor temperature typically is taken some place in the rooms (probably not right next to the radiators), the thermostats may respond to a temperature that is warmer or colder than the observed one.

The sigmoid function has the disadvantage that it cannot reach 1 nor 0. For the purpose of this paper, it means that even though the set-point is, say, 18 and the observed temperature is 20, the model predicts that the radiators still deliver some heat (depending on the slope and offset). Depending on the specific thermostats and the valves in the radiators, this prediction may be wrong. We address this problem further in Section 5.

#### 3.3.2. Derivation of the space heating model structure

The space heating system proved hard to model. It is difficult to describe all necessary dynamics in a simple manner. However, we found it fruitful to model the *water flow* in the radiator circuit as a dynamical equation governed by a time-delay. The governing physical equation of the net energy transferred to the radiator, $Q_t^h$, from the water is [24]

$$\mathrm{d}Q_t^h = \Phi_t c_{p,w}(T_t^{\text{for}} - T_t^{\text{ret}})\mathrm{d}t \tag{4}$$

where $\Phi_t$ is the flow of the water in the SH system, $c_{p,w}$ is the specific heat capacity of water.

As Section 2.1 describes, pumps that are controlled by some PI controllers regulate the water flow in the SH system to maintain a certain pressure. Therefore, there is a delay from when the valves open until the pumps increase the water accordingly. For this reason, it seems reasonable to model the water flow as a differential equation itself.

To model the return temperature, a few observations are important. It is obvious that when the space heating system delivers heat, the hot/cold water has been round in the radiator circuit and returns to the heat exchanger in a colder state. This is clearly visible in Figure 2 that the return temperature varies between 40-50 °C when heat is delivered. However, when the heat load equals zero, the return temperature acts rather inconsistently. At these times, the return temperature mostly responds with a quick decay to below 30 °C. But as Figure 2 shows, it sometimes drifts indescribably. Most times, when the water flow stops, the water in the return pipes quickly delivers its heat to the surroundings and arrives at some equilibrium. But when no heat is delivered, the building operators do not pay for larger return temperatures and gives no additional insights into the system. Therefore, we have no means to model the return temperature, when the heat load is zero. We thus disregard the return temperature observations when the flow is zero for simplicity. Section 5 explains how we implement this in the parameter estimation.

To recap the above thoughts; when heat is needed, the water flows into the radiators to deliver heat and afterward returns to the heat exchanger to be heated again. By combining (4) with a state for the flow and the return temperature, we arrive at the

following model

$$\mathrm{d}\Phi_t = \frac{1}{\lambda_1}\left(\Phi_{\max} f_{\text{valve}} - \Phi_t\right)\mathrm{d}t + \sigma_3 \mathrm{d}\omega_t^3\,, \tag{5a}$$

$$\mathrm{d}T_t^h = \frac{1}{C_h}\left(\Phi_t c_{p,w}\left(T_t^{\text{for}} - T_t^h\right) + \frac{1}{R_{ih}}\left(T_t^i - T_t^h\right)\right)\mathrm{d}t + \sigma_4 \mathrm{d}\omega_t^4\,, \tag{5b}$$

$$\mathrm{d}T_t^{\text{ret}} = \frac{1}{\lambda_2}\left(T_t^h - T_t^{\text{ret}}\right)\mathrm{d}t + \sigma_5 \mathrm{d}\omega_t^5\,. \tag{5c}$$

where $\Phi_{\max}$ the maximum attainable flow of the radiator circuit water. $\lambda_1$ is a time constant that describes the delay of the movement of the mass, since it needs to be accelerated in the heating circuit. $\lambda_2$ is a time constant that adds second order dynamics to the return temperature, which we found more accurate to include. We found these This model cannot be depicted as an electrical RC-diagram since there is no feedback from the return temperature.

### 3.4. Heat load estimation equation

From (4) we estimate the heat load, i.e. the power from the DH to the indoor air, as

$$\phi_t^h = \Phi_t c_{p,w}\left(T_t^{\text{for}} - T_t^{\text{ret}}\right)\,. \tag{6}$$

It should be natural to assume that the heat difference between the forward and return water is due only to the delivered heat by the space heating system. The temperature difference multiplied by the flow and the specific heat capacity of water is thus an estimate of the heat load. The flow state creates a time delay on the heat load. The term $\left(T_t^{\text{for}} - T_t^{\text{ret}}\right)$ is almost always large when the heat is turned off. Had there been no delay, e.g. for the equation $C_1 f_{\text{valve}}\left(T_t^{\text{for}} - T_t^{\text{ret}}\right)$, where $C_1$ is an arbitrary parameter, the heat load would immediately spike when the valves open. However, the heat load data is governed by delay which suggests that such time delay is needed.

### 3.5. The combined model

The combined model has the form

$$\mathrm{d}T_t^i = \frac{1}{C_i}\left(\frac{1}{R_{ih}}\left(T_t^h - T_t^i\right) + \frac{1}{R_{iw}}\left(T_t^w - T_t^i\right) + A_w\phi_t^s\right)\mathrm{d}t + \sigma_1 \mathrm{d}\omega_t^1\,, \tag{7a}$$

$$\mathrm{d}T_t^w = \frac{1}{C_w}\left(\frac{1}{R_{iw}}\left(T_t^i - T_t^w\right) + \frac{1}{R_{wa}}\left(T_t^a - T_t^w\right)\right)\mathrm{d}t + \sigma_2 \mathrm{d}\omega_2\,, \tag{7b}$$

$$\mathrm{d}\Phi_t = \frac{1}{\lambda_1}\left(\Phi_{\max} f_{\text{valve}} - \Phi_t\right)\mathrm{d}t + \sigma_3 \mathrm{d}\omega_t^3\,, \tag{7c}$$

$$\mathrm{d}T_t^h = \frac{1}{C_h}\left(\Phi_t c_{p,w}\left(T_t^{\text{for}} - T_t^h\right) + \frac{1}{R_{ih}}\left(T_t^i - T_t^h\right)\right)\mathrm{d}t + \sigma_4 \mathrm{d}\omega_t^4\,, \tag{7d}$$

$$\mathrm{d}T_t^{\text{ret}} = \frac{1}{\lambda_2}\left(T_t^h - T_t^{\text{ret}}\right)\mathrm{d}t + \sigma_t \mathrm{d}\omega_t^5\,. \tag{7e}$$

where $\Phi_{\max}$ are the flow speed of the water on the building site. The observation equations are

$$y_k^i = T_{t_k}^i + v_1\,, \qquad v_1 \sim N_{iid}(0, R_1)\,, \tag{8a}$$

$$y_k^h = \Phi_t c_{p,w}\left(T_t^{\text{for}} - T_t^{\text{ret}}\right) + v_2\,, \qquad v_2 \sim N_{iid}(0, R_2)\,, \tag{8b}$$

$$y_k^{\text{ret}} = T_{t_k}^{\text{ret}} + v_3\,, \qquad v_3 \sim N_{iid}(0, R_3)\,. \tag{8c}$$

## 4. Model identification and estimation

This section describes the identification method and the details governing the parameter estimation process. This paper proposes maximum likelihood inference for parameter estimation in stochastic differential due to its ability to estimate noise parameters. See e.g. Madsen [32] or Pawitan [33] for an introduction to maximum likelihood methods.

### 4.1. The maximum likelihood principle

Given the sequence of observations $\mathcal{Y}_N = \{\boldsymbol{Y}_i\}_{i=1}^N$, $\boldsymbol{Y}_k = [y_k^i, y_k^h, y_k^{\text{ret}}]^\intercal \in \mathbb{R}^{n_y}$, and set-points $\mathcal{U}_{N-1} = \{T_{\text{set},i}\}_{i=0}^{N-1}$, define the likelihood function as the product of the one-step ahead conditional densities:

$$\mathcal{L}(\boldsymbol{\theta}|\mathcal{Y}_N, \mathcal{U}_{N-1}) = p(\boldsymbol{X}_0)\prod_{k=1}^{N} p(\boldsymbol{Y}_k|\mathcal{Y}_{k-1}, \mathcal{U}_{k-1}, \boldsymbol{\theta})\,. \tag{9}$$

Here, $p$ is the probability of observing $\boldsymbol{Y}_k$ given the previous observations, set-points, and parameters $\boldsymbol{\theta}$. For linear stochastic differential equations, where the noise is state-independent and driven by Brownian motion, the conditional densities are also Gaussian. For non-linear systems though, this is not the case and the analytical density is in general hard (or impossible) to find. But when the time between observations are small, the Gaussian density approximates the analytical (unknown) density well. This motivates our choice of using the Gaussian density in the likelihood function. The Gaussian density is completely characterised by its conditional mean and variance; by introducing the one-step prediction error

$$\boldsymbol{\epsilon}_k = \boldsymbol{Y}_k - \hat{\boldsymbol{Y}}_{k|k-1}\,, \tag{10}$$

where $\hat{\boldsymbol{Y}}_{k|k-1} = \mathrm{E}[\boldsymbol{Y}_k|\mathcal{Y}_{k-1}, \mathcal{U}_{k-1}, \boldsymbol{\theta}]$, and the associated covariance $\boldsymbol{R}_{k|k-1} = \mathrm{Var}[\boldsymbol{Y}_k|\mathcal{Y}_{k-1}, \mathcal{U}_{k-1}, \boldsymbol{\theta}]$, we can write the likelihood function as

$$\mathcal{L}(\boldsymbol{\theta}|\mathcal{Y}_N, \mathcal{U}_{N-1}) = p(\boldsymbol{X}_0)\prod_{k=1}^{N}\frac{\exp\left(-\frac{1}{2}\boldsymbol{\epsilon}_{k|k-1}^\intercal \boldsymbol{R}_{k|k-1}^{-1}\boldsymbol{\epsilon}_{k|k-1}\right)}{\sqrt{\det(\boldsymbol{R}_{k|k-1})(2\pi)^{n_y}}}\,. \tag{11}$$

Taking the logarithm on both sides, we obtain the log-likelihood function

$$\begin{aligned}\ell(\boldsymbol{\theta}|\mathcal{Y}_N, \mathcal{U}_{N-1}) = \log\left(p(\boldsymbol{X}_0|\boldsymbol{\theta})\right) - \frac{1}{2}\sum_{k-1}^{N}\boldsymbol{\epsilon}_{k|k-1}^\intercal \boldsymbol{R}_{k|k-1}^{-1}\boldsymbol{\epsilon}_{k|k-1} \\ + \log\left(\det(\boldsymbol{R}_{k|k-1})(2\pi)^{\frac{n_y}{2}}\right)\end{aligned} \tag{12}$$

The log-likelihood has some attractive advantages over the ordinary likelihood when it comes to numerical properties, which

is why it is often preferred. The parameter estimates $\hat{\boldsymbol{\theta}}$ is found by maximising the log-likelihood function

$$\hat{\boldsymbol{\theta}} = \arg\max_{\boldsymbol{\theta}} \ell(\boldsymbol{\theta}|\mathcal{Y}_N, \mathcal{U}_{N-1}) \tag{13}$$

To evaluate the log-likelihood function, we need to compute the one-step prediction errors, $\boldsymbol{\epsilon}_k$, and the associated covariance $\boldsymbol{R}_{k|k-1}$ (due to our assumption of Gaussian densities). The continuous-discrete extended Kalman filter supplies exactly these.

### 4.2. The continuous-discrete extended Kalman filter

The continuous-discrete extended Kalman filter (CDEKF) is a variant of the celebrated Kalman filter [34]. It considers system models governed by continuous-time dynamics where the observer observers parts of the system at discrete times. In short, the CDEKF consists of a *prediction* step and an *update* step. The extended Kalman filter relies on a linearisation of the non-linear system (1), which causes troubles if $g$ is state-dependent. In such cases, the Lamperti-transformation is an important tool to transform (1) into a state-independent SDE [35, 36]. The literature contains many introductions and applications to Kalman filtering and the CDEKF, see e.g. [19, 37].

#### 4.2.1. The prediction scheme

In this step, the CDEKF predicts the state of the building $\hat{\boldsymbol{X}}_{k|k-1} = \mathrm{E}[\boldsymbol{X}_k|\mathcal{Y}_{k-1}, \mathcal{U}_{k-1}, \hat{\boldsymbol{\theta}}]$, $\boldsymbol{X}_k = \left[T^i_{t_k}, T^w_{t_k}, \Phi_{t_k}, T^h_{t_k}, T^{\mathrm{ret}}_{t_k}\right]^\mathsf{T}$, together with the state covariance $\hat{P}_{k|k-1} = \mathrm{Var}[\boldsymbol{X}_k|\mathcal{Y}_{k-1}, \mathcal{U}_{k-1}, \hat{\boldsymbol{\theta}}]$ at the next time step $t_k$ given the estimated state at time $t_{k-1}$, $\hat{\boldsymbol{X}}_{k|k-1}$. This involves solving a set of coupled ordinary differential equations (ODEs). Any ODE-solver is sufficient for this task.

#### 4.2.2. The update scheme

The updating scheme is about estimating the underlying state and its covariance, denoted $\hat{\boldsymbol{X}}_{k|k}$ and $\hat{P}_{k|k}$, at the next time instance $t_k$, given our predictions, $\hat{\boldsymbol{X}}_{k|k-1}$ and $\hat{P}_{k|k-1}$, and an observation $\boldsymbol{Y}_k$. Informally speaking, the updating scheme finds a weight $K$, typically called the *Kalman gain*, which "measures" how much weight the observation should have on the estimate $\hat{\boldsymbol{X}}_{k|k}$. Consider the update equations for the state estimate

$$\hat{\boldsymbol{X}}_{k|k} = \hat{\boldsymbol{X}}_{k|k-1} + K\boldsymbol{\epsilon}_k\,. \tag{14}$$

If $K$ is small, the prediction weights more compared to the observation in the estimate of the state. The covariance of the one-step prediction error, $\boldsymbol{R}_{k|k-1}$, is usually calculated in the updating scheme as well. With $\boldsymbol{\epsilon}_k$ and $\boldsymbol{R}_{k|k-1}$ at hand, we can evaluate the conditional density associated with the $k$'th observation. This recursion is applied to all observations in $\mathcal{Y}_N$, and with a given initial condition $\boldsymbol{X}_0$, the log-likelihood in (12) can be computed.

Table 2: The parameter estimates together with their statistical properties

| Parameter | Estimate | 95% confidence interval | Unit |
|---|---|---|---|
| $T_{\mathrm{offset}}$ | -0.101 | [-0.081, -0.121] | [°C] |
| $C_h$ | 0.134 | [0.128, 0.140] | [kJ/°C] |
| $\lambda_1$ | 0.198 | [0.194, 0.202] | [h] |
| $\lambda_2$ | 0.272 | [0.254, 0.290] | [h] |
| $C_i$ | 9.57 | [9.40, 9.742] | [kJ/°C] |
| $C_w$ | 45.36 | [42.80, 47.92] | [kJ/°C] |
| $R_{ih}$ | 2.151 | [2.121, 2.181] | [°C h / kJ] |
| $R_{iw}$ | 0.199 | [0.195, 0.203] | [°C h / kJ] |
| $R_{wa}$ | 2.251 | [1.775, 2.727] | [°C h / kJ] |
| $A_s$ | 7.600 | [-1.443, 16.64] | [$m^2$] |
| $\sigma_1$ | 8.6e-4 | [9.7e-5, 0.008] | [°C] |
| $\sigma_2$ | 0.429 | [0.419, 0.439] | [°C] |
| $\sigma_3$ | 111.6 | [107.6, 118.0] | [kg/h] |
| $\sigma_4$ | 1.647 | [1.144, 2.370] | [°C] |
| $\sigma_5$ | 6.469 | [6.327, 6.612] | [°C] |
| $R_1$ | 9.6e-7 | [1.1e-7, 8.5e-6] | [°C] |
| $R_2$ | 2.7e-4 | [5.2e-6, 0.014] | [kW] |
| $R_3$ | 5.4e-3 | [1.4e-3, 0.021] | [°C] |
| $\Phi_{\mathrm{max}}$ | 1145.3 | [1133.5, 1157.1] | [kg/h] |
| $\alpha$ | 1.592 | [1.550, 1.634] | [1/°C] |

### 4.3. Details in the parameter estimation

As previously described, the return temperature exhibits inconsistent behaviour when the heat load is zero. Also, at these times, the return temperature is not of interest for control purposes. For these reasons, we choose to disregard the return temperature in the parameter estimation at times where the heat load is zero. That is, we need to ensure that the return temperature for these times does not affect the likelihood function. We thus add a very large constant (say $10^{20}$) to the observation variance in the Kalman filter when the heat load is close to zero (say < 0.01 [kW]). As a result, the *observed* return temperature has negligible effect on the likelihood estimates during these times. Such actions are crucial to implement for applications in general, e.g. MPC, where indescribable dynamics occur or observations are not of interest and a Kalman filter is applied for state estimation. The larger variance on the observed return temperature ensures that it contributes very little to the state estimate at that point in time.

To evaluate the log-likelihood in Eq. (12), this paper uses the software CTSM-R [38]. To maximise Eq. (13), we use the `NLopt` optimisation library in `R` [39].

## 5. Results and discussion

This section presents the results in terms of parameter estimates, simulation of the model, and residual analysis. We compare a simulation of the model with the experiment data to see the model's performance over the entire data set given only the initial conditions. For the simulations, we use the same weather observations and set-points as inputs. Finally, we discuss the capabilities and strengths/weaknesses of the model.

### 5.1. Simulation results

Table 2 displays the parameter estimates for the model presented in Section 3. All parameters are strongly significant, except the solar radiation gain $A_s$. The explanation is likely that the data contains no significant solar radiation. The parameter thus becomes hard to determine without large uncertainty. But the solar radiation gain is an important disturbing factor for building climate control [40]. We thus intend to describe the solar radiation gain better in the future, when more experiments/data are available. The literature contains interesting approaches to model this, such as using B-splines to describe the varying solar gain during the day [41].

Figure 4 shows a simulation of the experiment given only the initial states. The model does a good job for all three variables. It predicts long into the future and still shows good accuracy without large drifts. That is, the model performs very well on long prediction horizons. This is crucial for the performance of MPC. This simulation, however, uses the same weather disturbances as the data. For practical purposes, weather forecasts are not perfect, which affects the prediction performance [42, 43].

The predicted heat was a challenge to model, but the simulation suggests that the model captures the most crucial dynamics. However, the simulation also indicates that the model is not able to "turn off" the delivered heat fast enough compared to data, as it seems to go slower to zero. This flaw comes from the fact that we model the flow as an SDE itself, $\Phi_t$. Thus, the flow goes exponentially towards the term $\Phi_{\max} f_t^{\text{valve}}$ (which never equals zero due to the sigmoid curve).

We found that the dynamics of the return temperature were hard to mimic and capture, especially when the heat is turned off. Figure 4 confirms that we are somewhat capable of predicting the return temperature whenever the heating system is turned on.

The indoor air temperature in Figure 4 seems to catch the overall dynamics of the data. The building model, however, does seem to be a bit too well insulated by the looks of the long periods where no heat is delivered. The simulated temperature decreases slower compared to data. Also, from around December 25th and onwards, the simulated indoor air temperature seems to drift a bit upwards compared to data. In this period, the estimated valve states are never fully opened, indicating that the set-point and observed temperatures are very close. Thus, the upwards drift of the simulation could come from the sigmoid curve of the valve function, since it never fully closes and is still open even when the observed temperature is above the set-point.

### 5.2. Residual analysis

Figure 6 shows the estimated autocorrelation function and the cumulated periodogram of the 1-step prediction errors for each of the variables. Both the autocorrelation function and the cumulated periodogram indicate that the residuals of the indoor air temperature and the return temperature can be classified as white noise. However, the heat load residuals are governed by some minor autocorrelation in the first few lags. Inspection of the spectral density and the residual plots confirms that non-uniformity of the spectrum primarily comes from the heater state's exponential decay towards zero when the heat is turned off. However, this is a minor autocorrelation that is not going to impact MPC performance significantly.

### 5.3. Future work

Since the experiment took place during the Christmas holiday, the building was not occupied at any time. However, human occupancy/behaviour is important to model and include in MPC [44]. Also, due to the lag of occupancy, we do not know how open windows affect the indoor air temperature. These are important topics to investigate further to accurately model the thermal dynamics of the building [45].

## 6. Conclusion

This paper introduced a physically inspired SDE-based nonlinear model to describe the complex heat dynamics of a school building with water-based heating. The purpose of the model is to predict the indoor air temperature, the heat load, and the return temperature of the water in the space heating (SH) system. We model the thermostats in the radiators using a Sigmoid function to describe the level of water flow through the radiators. We fitted the parameters in the model from time-series data using maximum likelihood estimation. To validate the estimated model, we compared a simulation of the model, only given the initial conditions and disturbances, to data. This showed great accuracy over an entire week. The residual analysis indicated that the model lacks some dynamical descriptions of the heat load. We believe the reason might be that the model does not shut down the heat load fast enough. Beside this, the model looks promising for enabling MPC and e.g. embedded forecasts.

## 7. Acknowledgement

The authors received funding from the following projects; *Sustainable plus energy neighbourhoods (syn.ikia)* (H2020 No. 869918), *Centre for IT-Intelligent Energy Systems (CITIES)* (DSF 1305-00027B), Top-Up (Innovation Fund Denmark 9045-00017B), SCA+ (Interreg Öresund-Kattegat-Skagerrak), *Research Centre on Zero Emission Neighbourhoods in Smart Cities (FME-ZEN)* (Research Council of Norway, No. 257660), and *Flexibile Energy Denmark (FED)* (IFD 8090-00069B).

## References

[1] M. Z. Hauschild, S. Kara, I. Røpke, Absolute sustainability: Challenges to life cycle engineering, CIRP Annals 69 (2020) 533 – 553. doi:https://doi.org/10.1016/j.cirp.2020.05.004.

[2] D. W. O'Neill, A. L. Fanning, W. F. Lamb, J. K. Steinberger, A good life for all within planetary boundaries, Nature Sustainability 1 (2018) 88–95. doi:10.1038/s41893-018-0021-4.

[3] N. O'Connell, P. Pinson, H. Madsen, M. O'Malley, Benefits and challenges of electrical demand response: A critical review, Renewable and Sustainable Energy Reviews 39 (2014) 686–699. doi:10.1016/j.rser.2014.07.098.

[4] S. Østergaard Jensen, J. Parker, P. Engelmann, A. Joanna, Examples of Energy Flexibility in Buildings, Technical Report, 2019.

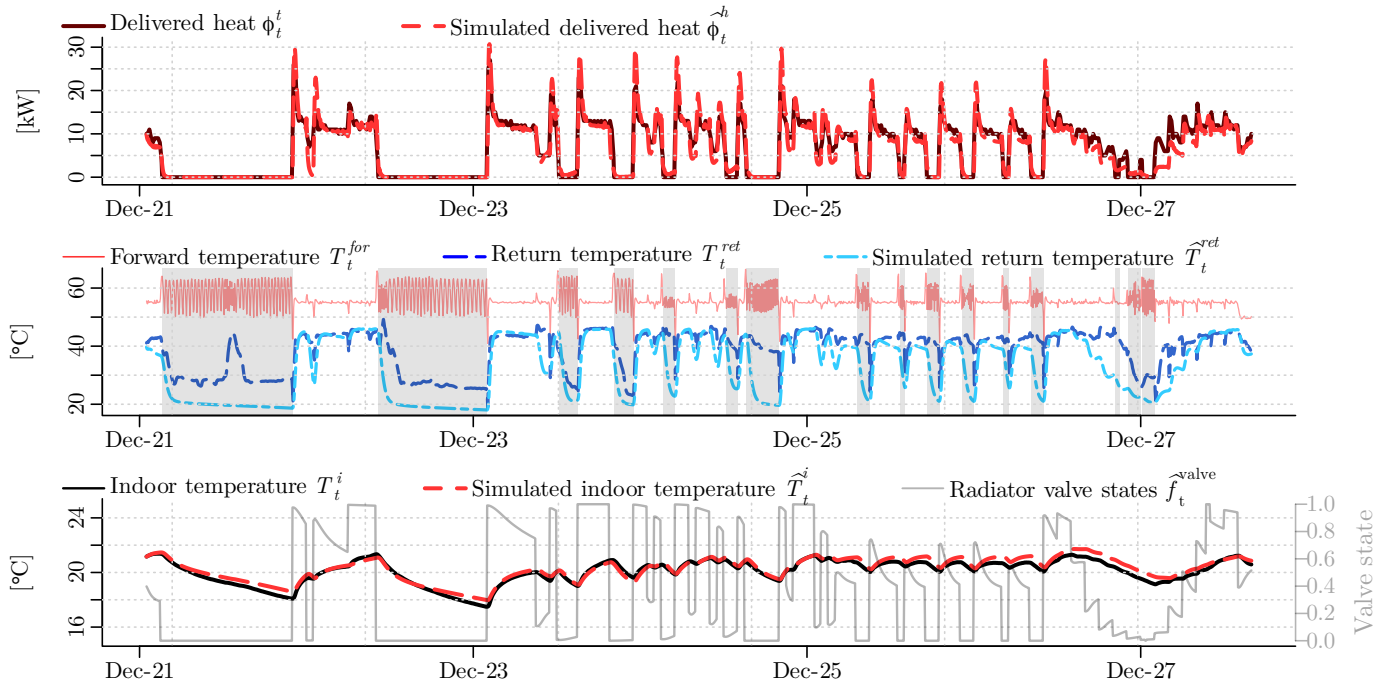


Figure 4: A simulation of the resulting model: given initial conditions, the model predicts the entire week. The model performs well given the long prediction horizon. The grey periods in the second plot depicts the periods where the observation variance on the return temperature is large.

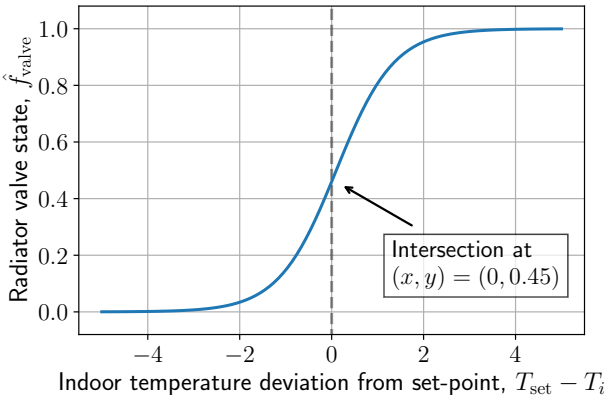


Figure 5: The estimated valve function


[5] G. Serale, M. Fiorentini, A. Capozzoli, D. Bernardini, A. Bemporad, Model predictive control (mpc) for enhancing building and hvac system energy efficiency: Problem formulation, applications and opportunities, Energies 11 (2018) 631. doi:10.3390/en11030631.

[6] J. Drgoňa, J. Arroyo, I. Cupeiro Figueroa, D. Blum, K. Arendt, D. Kim, E. P. Ollé, J. Oravec, M. Wetter, D. L. Vrabie, L. Helsen, All you need to know about model predictive control for buildings, Annual Reviews in Control (2020).

[7] D. Cali, D. Müller, H. Madsen, Benefits of the inclusion of occupant behaviour profiles in the simulation of the energy performance of buildings, in: Proceedings of 16th IBPSA International Conference & Exhibition Building Simulation 2019, 2019. URL: http://buildingsimulation2019.org, building Simulation 2019, BS 2019 ; Conference date: 02-09-2019 Through 04-09-2019.

[8] S. Wolf, D. Cali, M. Alonso, R. Li, R. Andersen, J. Krogstie, H. Madsen, Room-level occupancy simulation model for private households, volume 1343, IOP Publishing, 2019. URL: https://cisbat.epfl.ch/, cISBAT 2019 : Climate Resilient Cities - Energy Efficiency & Renewables in the Digital Era, CISBAT 2019 ; Conference date: 04-09-2019 Through 06-09-2019.

[9] A. Duun-Henriksen, S. Schmidt, R. Røge, J. Møller, K. Nørgaard, J. Jørgensen, H. Madsen, Model identification using stochastic differential equation grey-box models in diabetes, Journal of diabetes science and technology 7 (2013) 431–440. doi:10.1177/193229681300700220.

[10] A. Afram, F. Janabi-Sharifi, Gray-box modeling and validation of residential HVAC system for control system design, Applied Energy 137 (2015) 134 – 150. doi:https://doi.org/10.1016/j.apenergy.2014.10.026.

[11] S. Wang, X. Xu, Simplified building model for transient thermal performance estimation using ga-based parameter identification, International Journal of Thermal Sciences 45 (2006) 419 – 432. doi:https://doi.org/10.1016/j.ijthermalsci.2005.06.009.

[12] M. Massano, E. Macii, E. Patti, A. Acquaviva, L. Bottaccioli, A grey-box model based on unscented kalman filter to estimate thermal dynamics in buildings, in: 2019 IEEE International Conference on Environment and Electrical Engineering and 2019 IEEE Industrial and Commercial Power Systems Europe (EEEIC / I CPS Europe), 2019, pp. 1–6.

[13] P. Bacher, H. Madsen, Identifying suitable models for the heat dynamics of buildings, Energy and Buildings 43 (2011) 1511 – 1522. doi:https://doi.org/10.1016/j.enbuild.2011.02.005.

[14] A. Scott, The Nonlinear Universe, Springer, Berlin, Heidelberg, 2007.

[15] M. Jiménez, H. Madsen, J. Bloem, B. Dammann, Estimation of non-linear continuous time models for the heat exchange dynamics of building

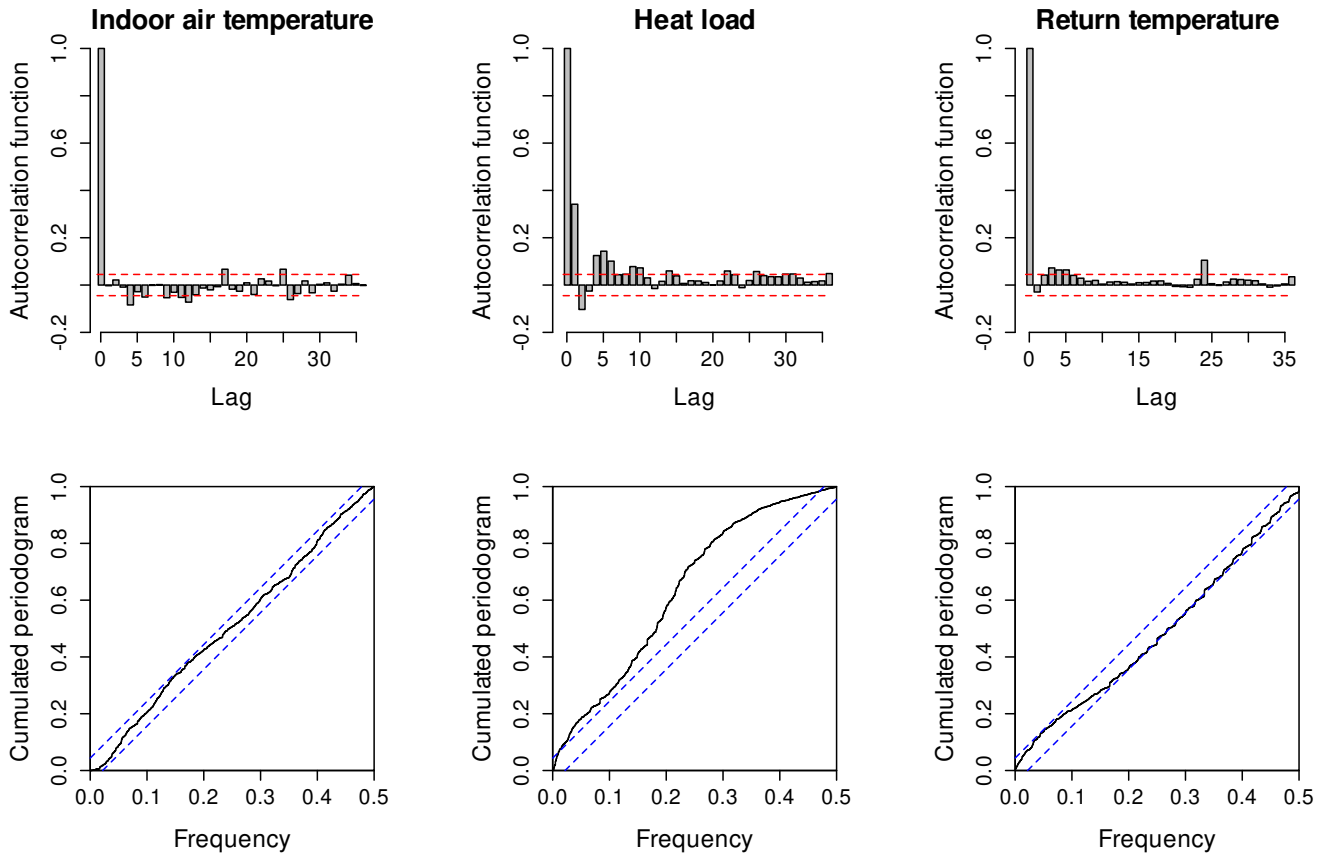


Figure 6: The estimated autocorrelation function and the cumulated periodogram of the 1-step prediction errors. Each column corresponds to a variable.

integrated photovoltaic modules, Energy and Buildings 40 (2008) 157 – 167. doi:https://doi.org/10.1016/j.enbuild.2007.02.026.

[16] C. Lodi, P. Bacher, J. Cipriano, H. Madsen, Modelling the heat dynamics of a monitored test reference environment for building integrated photovoltaic systems using stochastic differential equations, Energy and Buildings 50 (2012) 273 – 281. doi:https://doi.org/10.1016/j.enbuild.2012.03.046.

[17] E. Wernholt, S. Gunnarsson, Nonlinear grey-box identification of industrial robots containing flexibilities, IFAC Proceedings Volumes 38 (2005) 356 – 361. doi:https://doi.org/10.3182/20050703-6-CZ-1902.00060, 16th IFAC World Congress.

[18] J. K. Møller, H. Madsen, J. Carstensen, Parameter estimation in a simple stochastic differential equation for phytoplankton modelling, Ecological Modelling 222 (2011) 1793 – 1799. doi:https://doi.org/10.1016/j.ecolmodel.2011.03.025.

[19] B. Øksendal, Stochastic Differential Equations (3rd Ed.): An Introduction with Applications, Springer-Verlag, Berlin, Heidelberg, 1992.

[20] D. Boiroux, J. B. Jørgensen, A nonlinear model predictive control strategy for glucose control in people with type 1 diabetes, IFAC-PapersOnLine 51 (2018) 192 – 197.

[21] C. A. Thilker, R. G. Junker, P. Bacher, J. B. Jørgensen, H. Madsen, Model predictive control based on stochastic differential equations, in: C. Ghiaus, M. Amayri, S. Ploix (Eds.), Towards Energy Smart Homes: Algorithms, technologies, and applications, Springer, 2021. Publication expected in 2021.

[22] P. A. Stentoft, T. Munk-Nielsen, L. Vezzaro, H. Madsen, P. S. Mikkelsen, J. K. Møller, Towards model predictive control: online predictions of ammonium and nitrate removal by using a stochastic ASM, Water Science and Technology 79 (2018) 51–62.

[23] B. Xu, L. Fu, H. Di, Dynamic simulation of space heating systems with radiators controlled by trvs in buildings, Energy and Buildings 40 (2008) 1755 – 1764. doi:https://doi.org/10.1016/j.enbuild.2008.03.004.

[24] M. S. Mohseni, D. Gotthardsson, R. Hållbus, H. Vallmark, Analysis of the thermal performance of hydronic radiators and building envelop: Developing experimental (step response) and theoretical models and using simulink to investigate different control strategies, Civil Engineering Research Journal 2 (2017). doi:10.19080/CERJ.2017.02.555595.

[25] L. H. Hansen, Stochastic modelling of central heating systems, Ph.D. thesis, Technical University of Denmark, 1997. URL: http://www2.imm.dtu.dk/pubdb/pubs/2460-full.html.

[26] C. G. Bruun, Optimization of Building Operation Using High-resolution Sensor Data, Master's thesis, Technical University of Denmark, Department of Civil Engineering, 2019. Can be found at https://www.findit.dtu.dk.

[27] H. Madsen, J. Holst, Estimation of continuous-time models for the heat dynamics of a building, Energy and Building 22 (1995) 67–79.

[28] K. K. Andersen, H. Madsen, L. H. Hansen, Modelling the heat dynamics of a building using stochastic differential equations, Energy and Buildings 31 (2000) 13 – 24.

[29] B. Nielsen, H. Madsen, Identification of a linear continuous time stochastic model of the heat dynamics of a greenhouse, Journal of Agricultural Engineering Research 71 (1998) 249 – 256. doi:https://doi.org/10.1006/jaer.1998.0322.

[30] O. Brastein, D. Perera, C. Pfeifer, N.-O. Skeie, Parameter estimation for grey-box models of building thermal behaviour, Energy and Buildings 169 (2018) 58 – 68. doi:https://doi.org/10.1016/j.enbuild.2018.03.057.

[31] H. Harb, N. Boyanov, L. Hernandez, R. Streblow, D. Müller, Development and validation of grey-box models for forecasting the thermal response of occupied buildings, Energy and Buildings 117 (2016) 199 – 207. doi:https://doi.org/10.1016/j.enbuild.2016.02.021.

[32] H. Madsen, Time series analysis, Chapman & Hall, 2007.

[33] Y. Pawitan, In All Likelihood: Statistical Modelling and Inference Using Likelihood, Oxford: Clarendon Press, 2006.

[34] R. E. Kalman, A New Approach to Linear Filtering and Prediction Problems, Journal of Basic Engineering 82 (1960) 35–45.

[35] J. K. Møller, H. Madsen, From State Dependent Diffusion to Constant Diffusion in Stochastic Differential Equations by the Lamperti Transform, IMM-Technical Report-2010-16, Technical University of Denmark, DTU Informatics, Building 321, 2010.

[36] C. A. Thilker, Optimization for Smart Energy Systems, Master's thesis, Technical University of Denmark, Department of Applied Mathematics and Computer Science, 2020.

[37] P. Frogerais, J.-J. Bellanger, L. Senhadji, Various ways to compute the continuous-discrete extended kalman filter, IEEE Transactions on Automatic Control - IEEE TRANS AUTOMAT CONTR 57 (2012) 1000–1004. doi:10.1109/TAC.2011.2168129.

[38] R. Juhl, N. R. Kristensen, P. Bacher, J. Kloppenborg, H. Madsen, CTSM-R User Guide, 2013. Technical University of Denmark.

[39] S. G. Johnson, The nlopt nonlinear-optimization package, 2020. URL: http://github.com/stevengj/nlopt.

[40] T. Mingfang, Solar control for buildings, Building and Environment 37 (2002) 659 – 664. doi:https://doi.org/10.1016/S0360-1323(01)00063-4.

[41] C. Rasmussen, L. Frölke, P. Bacher, H. Madsen, C. Rode, Semi-parametric modelling of sun position dependent solar gain using b-splines in grey-box models, Solar Energy 195 (2020) 249 – 258.

[42] C. Thilker, H. Madsen, J. Jørgensen, Advanced forecasting and disturbance modelling for model predictive control of smart energy systems, Applied Energy 292 (2021). doi:10.1016/j.apenergy.2021.116889.

[43] F. Oldewurtel, A. Parisio, C. N. Jones, D. Gyalistras, M. Gwerder, V. Stauch, B. Lehmann, M. Morari, Use of model predictive control and weather forecasts for energy efficient building climate control, Energy and Buildings 45 (2012) 15 – 27. doi:https://doi.org/10.1016/j.enbuild.2011.09.022.

[44] F. Oldewurtel, D. Sturzenegger, M. Morari, Importance of occupancy information for building climate control, Applied Energy 101 (2013) 521 – 532. doi:https://doi.org/10.1016/j.apenergy.2012.06.014, sustainable Development of Energy, Water and Environment Systems.

[45] H. B. Rijal, P. Tuohy, F. Nicol, M. A. Humphreys, A. Samuel, J. Clarke, Development of an adaptive window-opening algorithm to predict the thermal comfort, energy use and overheating in buildings, Journal of Building Performance Simulation 1 (2008) 17–30. doi:10.1080/19401490701868448.

# B Published - Learnings from experiments with MPC for heating of older school building

**Learnings from experiments with MPC for heating of older school building**
**Building Simulation 2022 Conference, Copenhagen**

Christian Ankerstjerne Thilker[1]; Peder Bacher[1]; Henrik Madsen[1]
[1]Technical University of Denmark, Department of Applied Mathematics and Computer Science, DK-2800 Kgs. Lyngby, Denmark

## Abstract

The paper presents the learnings from designing and running a model predictive control (MPC) of the heating system in a school building. Several real-life applications of MPC controlled heating have been presented in the literature. Most of them work by controlling the room temperature usingn a heating system and thus need a reference measured temperature in the building. Some have a single-zone temperature as the reference, while others use some kind of mean temperature of multiple rooms. In the present experiment, the MPC used the mean temperature of all rooms as the reference and was able to keep it within a lower and upper comfort bound, while minimizing the heat costs by responding to a heat price signal. However, the analyses of the temperature in each room revealed that the temperature bounds were heavily violated: some rooms were too cold and some too warm, while the mean was within the bounds. The main conclusion from the study is that, at least for buildings with different sized rooms and room radiator capacities, it's not reliable to use a mean room temperature – rather, the control must consider individual rooms in order to guarantee comfort.

## Introduction

Control of HVAC systems in buildings is important for the green energy transition, both in order to decrease the heat demand and to increase flexibility for integration of variable renewables, like wind and solar. The level of activity in the field has been increasing over the last decades and focus has centered around the use of Model Predictive Control (MPC). The present paper describes an actual real-life experiment where MPC was applied to control the heating system in an older school building in a cold climate. The main focus of the paper is on the learnings achieved from the experiment, especially the way the room temperatures were taken into account in the MPC and the underlying model, and how they actually realized. In the MPC, a simple mean of all room temperatures was used, hence the control was carried out at a building level and this temperature was kept well within comfort temperature bounds. However at individual room level the temperatures violated the comfort bounds, some rooms got too cold and others too hot.

Recent overview papers provides a lot of insights into the techniques and challenges of MPC for HVAC in buildings. Killian and Kozek (2016) pose ten questions that should be considered for MPC in buildings, however of the questions none related to building vs. room level temperature. They emphasize that a main problem "is the high modeling efforts, where currently no commercial tools exist to derive easily a suitable model for MPC design". Drgoňa et al. (2020) provides a very comprehensive review and overview of MPC of energy systems in building. Not much on multi-zone temperature control is included, though Table 5 lists several studies of modelling for control with multi-zone models, however none of these are implemented in real-life experiments.

The the volume of literature on real-life experiments with MPC in buildings is increasing. Liao and Dexter (2004) identifies a single-zone model for a three storage building where they model the mean room temperature of the entire building. Each floor was similar in terms of the heating equipment, which made it easy to model. The results were good in terms of controlling the mean temperature to different levels, but no analysis on room-level is presented. Široký et al. (2011) present an experiment with MPC of heating in a five-floor building block on a university campus. The room temperature was measured in only two reference rooms and parameters in a linear RC-model was estimated using data from those rooms. An MPC ran in closed loop for two weeks and energy savings were achieved over a rule based control. However, the room temperatures are not evaluated in detail in the paper and there is no information about temperatures in other rooms than the reference rooms. West et al. (2014) present an MPC implemented in a large office building. They consider varying costs in the objective function, however it was implemented as constant in the demonstration period. Indoor comfort were evaluated via feedback from occupants, however no detailed evaluation of the measured temperatures is presented. Huang et al. (2015) developed an MPC for control of the indoor air temperature of an airport terminal in Australia. They carry out a simulation and an experiment to test the model and MPC both showing increased comfort and cost reductions. De Coninck and Helsen (2016) presents the results of implementing an MPC in a two-storey office building. They do room temperature averaging: "To obtain a single-zone model, all room temperature measurements are arithmetically averaged into TZon.". The objective was to minimize heat demand, not with a varying price. A comparison to rule based control is included, which showed 20% to 30% per-

cent reduction in heat demand. No evaluation of temperatures on room level is included. Finck et al. (2019) present and implement EMPC for a Dutch building. The models for the building heat dynamics and the weather forecasts are based on artificial neural networks. They tested the controller for flexibility optimisation and to regulate on-site power generation and grid-consumption and feed-in. The results showed that the EMPCs increased the flexibility of the heat demand while maintaining the same heat costs.

The existing literature presenting multi-zone control systems don't deal with flexible demand – only control of air temperatures. Scattolini (2009) explains and review hierarchical and distributed control. Moroşan et al. (2010) presents a simulation study demonstrating how different MPCs for multi-zone temperature control in a building perform. The focus is on the interaction between the rooms in form of heat exchange due to temperature differences. The results indicate, that either a centralized control, which has a full multi-zone model, or a distributed control, where the room models exchange information, is preferable over a fully decentralized control, which does not take the interactions into account. Elliott and Rasmussen (2013) present temperature control of multiple zones with a multi-evaporator vapor compression system. An architecture that is decentralized and modular, avoiding competing controllers and the practical difficulty of implementing a centralized controller, is presented. Eini and Abdelwahed (2019) presents a distributed control, which in a simulation study has a better performance over a centralized control. The model is a detailed multi-zone model, where the parameters are known in advance. Zong et al. (2019) present a case study of MPC-based BEMS for a multi-family residential building where a hierarchy controller design is applied. The performance of the decentralized controller strongly depends on the level of interactions between the subsystems: The distributed, as each controller knows about control actions of its neighbors, keeps the same performance as the centralized. Results are not presented in detail, only a plot for a single zone is presented.

In the modelling carried out for the present paper, a single-zone grey-box model was identified using the approach presented in Bacher and Madsen (2011) describes. The particular model used is the model presented by Thilker et al. (2021). Some development in terms of automatic model selection has been made, as presented by Andriamamonjy et al. (2019). Interesting multi-zone model identification studies have been carried out by Joe et al. (2020), who present a grey-box model of room temperature fitted for each room individually and compared to a model fitted to all at the same time. The total RMSE is smaller for the decentralized approach. Arroyo et al. (2020) presents a divide-and-conquer approach to grey-box multi-zone parameter estimation, where first the parameters are estimated on single-zone level and then used an initial guess in the multi-zone model parameter estimation.

*Figure 1: Photo of the building in question.*

From the literature, it's apparent that focus on MPC and the underlying data-driven modelling is increasing, however experimenting with MPC in real-life is in an early stage – especially the implementation and application of a price responsive control in real-life experiments is novel.

### Main contributions of the paper

The main contributions of the present paper are, first, the presention of a successful real-life experiment with a price responsive MPC, and second, to highlight some of the challenges encountered using a single-zone model. In particular, it's emphasized that by using the mean room temperature of all rooms as the reference, which must be kept inside a comfort bound, worked well on the single-zone (or building) level, but caused violations in the individual rooms: some rooms got too hot while others too cold, while the mean was still within the comfort bound.

First the building and data setup is described, and thereafter the two experiments carried out: the system identification and the MPC experiment. Second, the results are presented and discussed, and finally the conclusions are drawn.

## Building, systems and data

### The building

The building is located in Høje Taastrup, Denmark, and is a school with three floors. The uppermost floor is a part-refurbished roof attic.

Build in 1929, the building is not insulated up to modern standards. Figure 1 shows a photo of the building. It includes 10 classrooms that are ventilated by mechanical ventilation using an air handling unit for air circulation. The ventilation was not active during any of the experiments (due to absence of occupants). The facade and internal walls consist of solid bricks (300 mm and 180 mm thickness, respectively). The windows have wooden frames and double-paned low-E glazings. Floors are made from wood joists and the roof is a partly uninsulated and partly insulated slate roof. The building is connected to the district heating grid. The heating system is used for domestic hot water, air handling unit, and space heating. The space heating is a separate water-based circuit with dedicated pumps. Radiators of different types (cast-iron and plane conductors) with individual smart thermostats distribute the heat in the rooms. The thermostats work as

PI-controllers, which regulate the water flow into the radiator units to maintain a pre-defined *set point* by the user. See Bruun (2019) for further technical details about the building.

### Data

All main rooms are each equipped with a temperature sensor (uncertainty is $\pm 0.1°\text{C}$) to measure the indoor air temperature. All radiators in rooms with a temperature sensor are equipped with smart thermostats where a temperature set point can be set remotely. Each thermostat have their own temperature sensor, hence they are not controlled using the measured temperature included in the analysis. The supply and return temperature of the water of the building's heating system is measured together with the actual heat usage of the building.

Weather forecasts for the location are available with 6 hours delay and 48 hours ahead. The sampling time of the forecasts is 1 hour. The forecasts were available in real-time and were used in the filter update in the MPC. To see how the weather was during the period, Figure 2 shows the observed ambient temperature and global solar radiation. It can be seen that the weather conditions include both cold and mild days, as well as both sunny and cloudy days.

### System identification

The model used for the heat dynamics of the building is based on stochastic differential equations. The identification method is based on a maximum likelihood method using a variant of the Kalman filter to compute the transition densities. The modelling procedure is thoroughly described in Thilker et al. (2021). The model includes the following states

$$\boldsymbol{x} = [T_\text{i}, T_\text{w}, \Phi, T_\text{h}, T_\text{ret}]^\top ,$$

where $T_\text{i}$ is the indoor air temperature, $T_\text{w}$ is the temperature of the building's wall, $\Phi$ is the water flow of the heat system, $T_\text{h}$ is the temperature of the average surface temperature of the radiators in the building, and $T_\text{ret}$ is the return water temperature.

The model is a significant simplification of the heat dynamics of the building. We use the arithmetic mean of the air temperature of the rooms as a measure of the indoor air temperature in the building as a whole. Since we didn't have knowledge about the heat released in the individual rooms, we cannot easily employ a multi-zone RC-based model. Also, the dimensionality of the model increases drastically if multiple rooms were modelled, which complicates real-time MPC due to a bad scaling in computational requirements to solve the optimal control problem. For these reason, we used a single-zone model, well knowing that it might cause issues in the individual rooms.

### System identification experiment

The system identification experiment carried out was planned in advance and designed to generate data suitable for system identification. The main focus was to change the control input, the thermostat set point, such that information about the essential dynamics of the system can be estimated. A sequence of the set point was designed with four different parts. First part, contained a few long steps to get information about the slow dynamics governing the system. Second part, was a multilevel signal, where extremes were kept for longer periods than values closer to 20 °C. Third part, contained short periods with drops to a minimum from the base temperature. Finally, a step sequence where the set point was stepped down and back up again. The forward temperature of the space heating water was set constant to 55 °C at all times. The entire sequence was slightly shorter than 7 days and was executed during the Christmas vacation, where the building was unoccupied. The experiment is described in more details by Thilker et al. (2021).

## MPC experiment

The MPC experiment was carried out during January and February 2021. The building was no used in the period, due to the pandemic lockdown. This section introduces a direct multiple-shooting method for solving the particular non-linear MPC problem. It also discusses a method to discretise the optimisation problem to make it numerically tractable. The optimisation problem results in the set points applied for the radiator thermostats. However, solving the optimisation problem requires us to know the entire state of the system. For reconstructing the system states the continuous-discrete extended Kalman filter is used Kristensen et al. (2004).

The implemented optimal control problem has the following (Lagrange) form

$$\min_{\boldsymbol{x},u,\boldsymbol{s}} \quad \varphi_k = \int_{t_k}^{t_k+T} \ell(\boldsymbol{x}(t), u(t), \boldsymbol{d}(t), s(t))\mathrm{d}t, \tag{1a}$$

$$s.t. \quad \boldsymbol{x}(t_k) = \hat{\boldsymbol{x}}_{k|k}\,, \tag{1b}$$

$$\mathrm{d}\boldsymbol{x}(t) = f(\boldsymbol{x}(t), u(t), \boldsymbol{d}(t))\mathrm{d}t, \qquad t \in \mathcal{T}_k, \tag{1c}$$

$$u_\text{min}(t) \le u(t) \le u_\text{max}(t), \qquad t \in \mathcal{T}_k, \tag{1d}$$

$$\Delta u_\text{min}(t) \le \Delta u(t) \le \Delta u_\text{max}(t), \qquad t \in \mathcal{T}_k, \tag{1e}$$

$$T_\text{min}(t) \le T_\text{i}(t) + s(t) \le T_\text{max}(t), \qquad t \in \mathcal{T}_k, \tag{1f}$$

where $\hat{\boldsymbol{x}}_{k|k}$ is the reconstructed system state, $T$ is the prediction horizon, $\ell$ is the cost function, $L$ is the terminal cost, and $f$ is the model dynamics. The time set is $\mathcal{T}_k = [t_k, t_k + T[$. $s(\cdot)$ is a slack variable that softens the temperature constraints. In the next section, we describe how we penalise a non-zero slack.

### Optimal control problem

To make the optimal control problem in $(1)$ numerically tractable, we use a multiple shooting method to discretise the problem. The problem is discretised in the sense that the system considers $\boldsymbol{x}$ at discrete time points $t_k < t_{k+1} < \cdots < t_{k+N} = t_k + T$. Now, define a function $\phi(\boldsymbol{x}, u, \boldsymbol{d})$ that computes the solution at time $t_{k+1}$ to the following initial value problem

$$\dot{\boldsymbol{x}}(t) = f(\boldsymbol{x}(t), u(t), \boldsymbol{d}(t))\,, \tag{2a}$$

$$\boldsymbol{x}(t_k) = \boldsymbol{x}_k\,. \tag{2b}$$

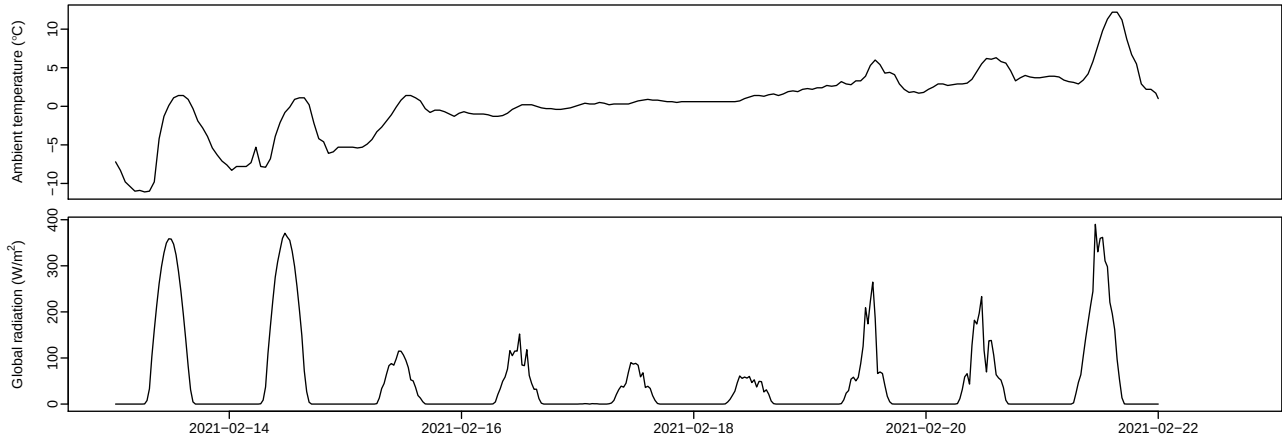


*Figure 2: Observed weather during the period.*

Thus, $\phi(\boldsymbol{x}, u, \boldsymbol{d}) = \boldsymbol{x}(t_{k+1})$ integrates the system forward to the next time instance. Furthermore, we assume the disturbances and input be constant between control points

$$u(t) = u_k \,,\; t \in [t_k, t_{k+1}[\,, \tag{3a}$$
$$\boldsymbol{d}(t) = \boldsymbol{d}_k \,,\; t \in [t_k, t_{k+1}[\,. \tag{3b}$$

The discretised optimal control problem can thus be written as

$$\min_{\boldsymbol{x}_i, u_i, \boldsymbol{s}_i} \quad \varphi_k = \sum_{i=k}^{k+N-1} L_i(\boldsymbol{x}_i, u_i, \boldsymbol{d}_i, s_i)\,, \tag{4a}$$
$$s.t. \quad \boldsymbol{x}_k = \hat{\boldsymbol{x}}_{k|k}\,, \tag{4b}$$
$$\boldsymbol{x}_{i+1} = \phi(\boldsymbol{x}_i, u_i, \boldsymbol{d}_i)\,, \qquad i \in \mathcal{N}, \tag{4c}$$
$$u_{\min,i} \le u_i \le u_{\max,i}\,, \qquad i \in \mathcal{N}, \tag{4d}$$
$$\Delta u_{\min,i} \le \Delta u_i \le \Delta u_{\max,i}, \qquad i \in \mathcal{N}, \tag{4e}$$
$$T_{\min,i} \le T_{\mathrm{i},i} + s_i \le T_{\min,i}, \qquad i \in \mathcal{N} \tag{4f}$$

where $L_i(\cdot) = \int_{t_{k+i}}^{t_{k+i+1}} \ell(\cdot)\mathrm{d}t$ and the index set is $\mathcal{N} = \{0, 1, \ldots, N-1\}$. To approximate $L_i$, we use a fourth-order Runge-Kutta method with fixed step size of 3 minutes. The sampling time between control points is fixed and is $T_s = t_{k+1} - t_k = 0.5$ h.

We implement the optimal control problem using CasADi, which offers easy numerical implementation and automatic differentiation for optimal control problems as the above.

### Objective functions

The objective function in an optimal control problem has the purpose of making solutions comparable. The objective function should thus reflect all considerations towards the desired behaviour of the controller. We use the following objective function

$$\ell = c \cdot P_h + \rho \cdot s^2, \tag{5}$$

where $c$ is the heat price, $P_h$ is the heat load, $\rho$ is slack penalty and $s$ is the slack. The objective function is non-linear due to the heat term, $P_h = \Phi c_w (T_{\text{for}} - T_{\text{ret}})$, which depends on the product of two states, $\Phi$ and $T_{\text{for}}$, and the quadratic slack.

In the experiment carried out, we wanted to shift the heat load away from peak hours (also known as peak shaving). Therefore, we constructed a price signal accordingly:

$$c(t) = \begin{cases} 1000 & \text{if } t \in \texttt{PEAKHOURS} \\ 10 & \text{otherwise} \end{cases} \tag{6}$$

where we define the peak hours to be

$$\texttt{PEAKHOURS} = [06\text{AM}, 10\text{AM}[ \cup [5\text{PM}, 9\text{PM}[ \quad . \tag{7}$$

The price for heating is thus expensive during the morning and evening hours where the district heating peak hours usually are.

### MPC tuning

During the experiment we tuned several parameters of the objective function in an iterative process as we learned how the MPC behaved. The objective function consists of two terms that need to be weighted such that the controller prioritises in an appropriate manner. We found $\rho = 10$ to be suitable together with the price in Equation (6). The reason for the quadratic slack penalty (instead of linear) is that it ensures a smooth objective function. We found that a linear slack penalty caused a more sensitive solution when it is close to the temperature bounds.

To avoid too large variations in the input signal, dampen oscillations and make the solution more robust, we choose to restrict the allowed variation between control points, furthermore, too large increases in the set point will cause large increases in the return temperature, which in general is not desired. We choose the maximum allowed absolute change to be 3 °C per hour. With $T_s = 0.5$, Equation (4e) becomes $-1.5 \le \Delta \boldsymbol{u}_i \le 1.5$.

We chose the maximum and minimum bounds of the input to be the maximum and minimum temperature bounds, $u_{\min,k} = T_{\min,k}$ and $u_{\max,k} = T_{\max,k}$. The rationale behind this, is to avoid overheating in some of the fast reacting

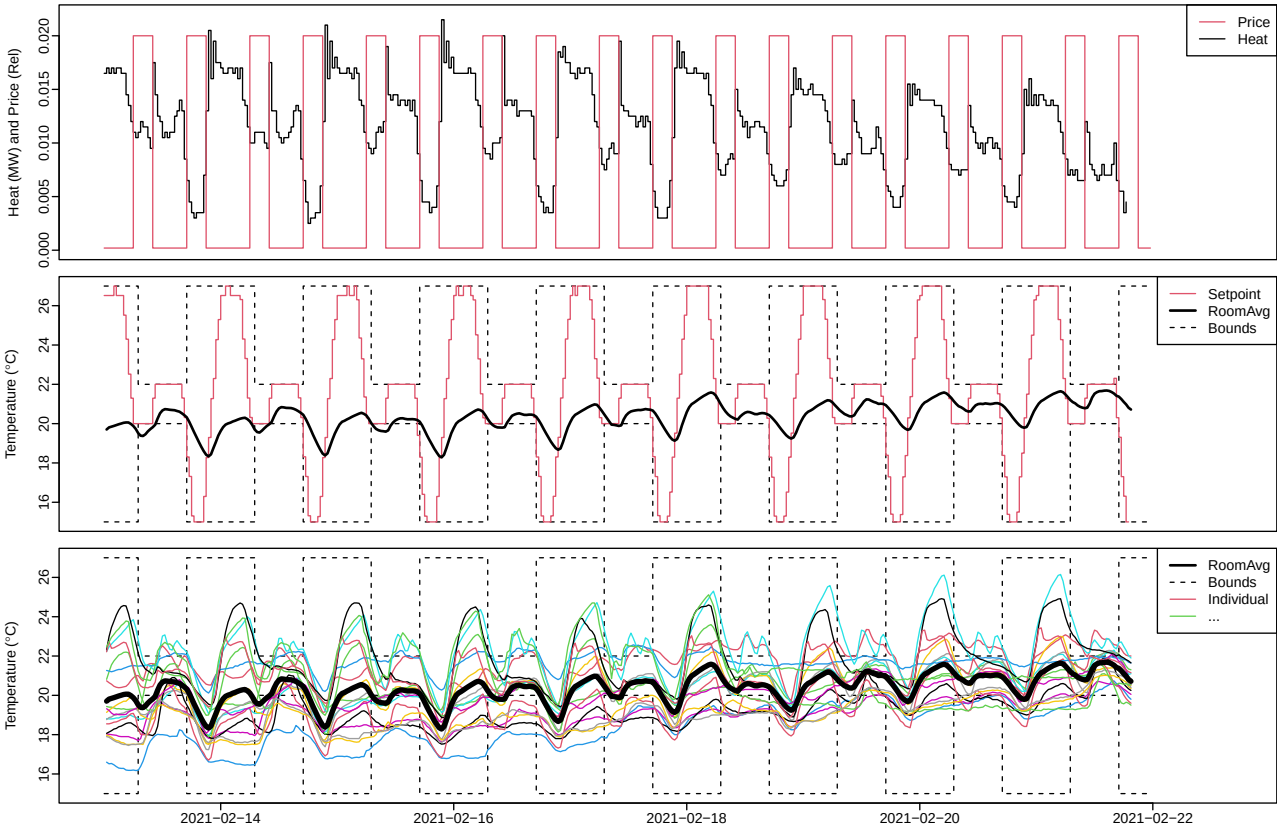


*Figure 3: Results from the period running with the tuned MPC. Upper plot is of the price and heat demand. Mid plot is of the temperatures considered by the MPC. Lower plot is of the individual room temperatures and the mean temperature. The latter plots also contain the temperature constraints.*

rooms to limit the chance that they violate the temperature bounds.

## Results

The MPC was tuned for a period and thereafter it was run for a period of nine days. The results from the nine days period is presented and analysed in the following. Selected variables recorded during the period are plotted in Figure 3. The upper-plot shows the price signal and the realized heat demand. It clearly shows that the MPC was able to lower the heat demand in the high price periods, although it was not decreased all the way to zero. The mid-plot shows the lower and upper temperature bounds, together with the set point and mean room temperature. It's clearly seen that the MPC managed to keep mean room temperature within the bounds, except during the first four days in the morning hours where the lower temperature bound is stepped up. The lower-plot shows the individual room temperatures. It's easy to see that there was a huge spread in the temperatures among the rooms. Some responded very fast and became very warm when the set point was increased, others responded slow and the coldest rooms didn't even to reach the set point – these issues will be discussed in detail later. Finally, it's noticed that there was an increasing trend in the mean temperature over the period, which was caused by the increase in outdoor air temperature over the period, as pointed out in previously. The pattern in the heat demand and temperature response to the price signal is very regular. In order to get more insight into the details, a zoom on the two first days is shown in Figure 4.

From the two presented plots of the results, it becomes clear that the MPC was capable of controlling the heat demand in response to the price signal. However, there is a potential for improvements. Firstly, the heat demand was not able to decrease fully to zero in the periods of high price, especially in the morning price peak. We identify the two main reasons for that as:

- Some hours before the price peak in the morning the set point was stepped down, which can seem to be too early to be optimal, however it's a compromise between decreasing the demand during the peak and the temperature lower bound violation. This could most likely be tuned to achieve a lower demand during the morning peak.

- Due to technical issues, not all the radiators were controlled, so there was a lower limit to the heat demand – probably around the heat level in the afternoon price peak.

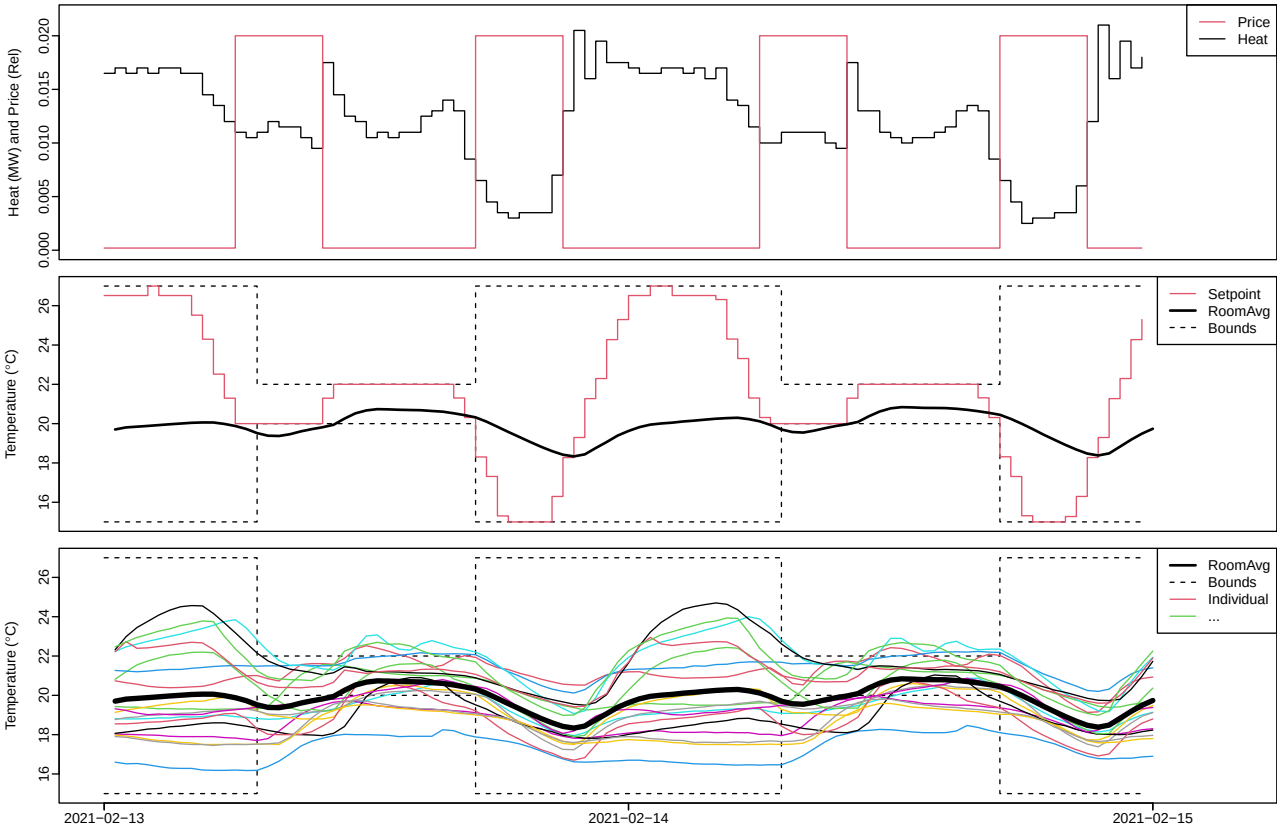


*Figure 4: Two days plot of the MPC results. Upper plot is of the price and heat demand. Mid plot is of the temperatures considered by the MPC. Lower plot is of the individual room temperatures.*

However, the biggest issue encountered with the implemented MPC is the resulting huge spread in room temperatures. As seen in the lower plots of Figure 3 and 4, the spread of the realized room temperatures was huge. This pose a real problem, since the comfort of occupants would have been compromised – essentially the temperature bounds in the individual rooms cannot be guaranteed when a mean temperature over multiple rooms is used as reference. It is noted here, that the thermostats were not controlling using the measure temperature, they had each a sensor. In order to see more details of the rooms temperature response a two days plot of the temperatures is presented in Figure 5. The rooms are divided between the types of rooms in order to see if there are any similarities because of the type of room.

The main findings from this plot are:

- Clearly, the temperature bounds are violated in nearly all rooms – some gets too hot and some gets too cold.
- Similarities due to the type of room is mainly seen for the hallways.
- The response to the temperature set point is very different among the rooms. Some rooms respond very fast, indicating that the radiators heating power is high relative to the room size and heat losses. Some rooms respond very slow, indicating that the radiator's power is not sufficient to heat the rooms under the conditions during the period.

## Discussion

From the presented results, it is clear that there are various trade-offs between controllability, stability, and performance. The MPC input was quite regularized, which resulted in higher heat usage during the morning peak hours (since the set point could not be lowered further). It overall affected the ability of the MPC to adjust demand when the price changes – and therefore affected the controllability. However, the regularisation was necessary for the MPC to increase stability of the solution. The slower-changing set point resulted in a lower return temperature, since the temperature in the rooms has more time to adapt to the increased set point.

The performance is of course also affected by the regularisation and the model's ability to predict the air temperature, which could be improved. This could be done using an adaptive parameter estimate update as observations become available.

From the presented room temperature plots, it is apparent that their individual properties, such as radiator capacities, dimensions, etc., have a huge impact in the rooms'

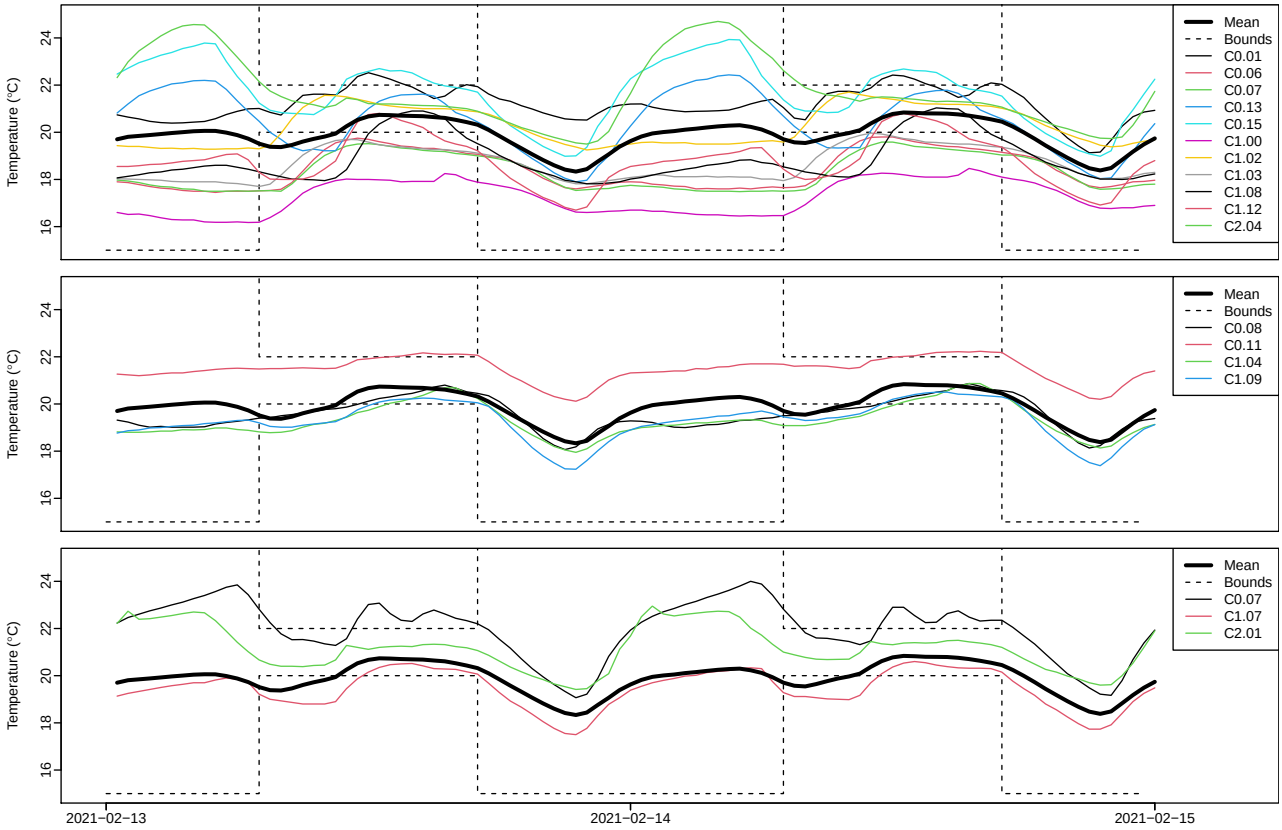


*Figure 5: Plot of the temperature set point, the mean room temperature and the individual room temperatures. The upper-plot contains the classrooms, the mid-plot the hallways and the lower-plot the smaller rooms.*

individual response to set point changes. Potentially, another interaction may be due to the thermostats opening and closing at about the same time in all rooms, which can create pressure losses, such that the radiators at the far end of the heating circuit cannot supply enough heat. This is a balancing issue, which may be fixed by tuning the max valve openings of each radiator and installing additional radiator capacity.

To which extend these results generalise to other buildings cannot be concluded from the present results. Newer and more well-insulated buildings are probably less likely to suffer from dimensioning issues since less heat is needed Knudsen et al. (2021).

### Further work

Regarding the significant room temperature differences, it's a real fundamental issue, which must be solved for MPC in buildings to be usable in practice. It's possible to make a few simple changes to the constraints, for example keeping the upper limit of the set point to e.g. 23 °C could avoid overheating rooms, however it also limits the control capabilities.

Another approach could be to introduce a hierarchical and distributed MPC (Scattolini, 2009; Moroşan et al., 2010):

- Constant room temperature model: Simply a room temperature set point offset can be learned for each room. This does not take the individual room dynamics into account.
- Dynamic room temperature model: The dynamics of the rooms taken into account by individual room temperature models. One idea is to use an ARX model (which are more black-box models compared to the resistor-capacitor model in this paper) for each room and have indivual MPCs run each room.

## Conclusion

An MPC for price flexible heat demand was demonstrated in an experiment. The results illustrate the ability of the MPC to respond to a varying price and lower the heat demand of the building in the high price periods, however, there was potential for improvements.

Using the arithmetic mean temperature as a representative for all rooms led to a high spread in room temperatures between rooms, thus violating the temperature comfort bounds. The rooms and radiator power in the building were not uniformly sized, hence this behaviour is not surprising, but pose a real problem for MPCs, which does not take individual room's dynamics into account. To which degree this phenomena can be generalized to other buildings can of course not be concluded with the present study. However, it is clear that when using temperature constraints on a mean temperature over multiple rooms, the

constraints cannot be guaranteed for the individual rooms.

## Acknowledgments

The work was carried with funding from the following projects; *Sustainable plus energy neighbourhoods (syn.ikia)* (H2020 No. 869918), FME-ZEN (Research Council of Norway - 257660), Top-up (Innovation Fund Denmark 9045-00017B), SCA+ (Interreg Öresund-Kattegat-Skagerrak) and *Flexibile Energy Denmark (FED)* (IFD 8090-00069B).

## References

Andriamamonjy, A., R. Klein, and D. Saelens (2019). Automated grey box model implementation using bim and modelica. *Energy and Buildings 188*, 209–225.

Arroyo, J., F. Spiessens, and L. Helsen (2020). Identification of multi-zone grey-box building models for use in model predictive control. *Journal of Building Performance Simulation 13*(4), 472–486.

Bacher, P. and H. Madsen (2011). Identifying suitable models for the heat dynamics of buildings. *Energy and Buildings 43*(7), 1511–1522.

Bruun, C. G. (2019). Optimization of Building Operation Using High-resolution Sensor Data.

De Coninck, R. and L. Helsen (2016). Practical implementation and evaluation of model predictive control for an office building in brussels. *Energy and Buildings 111*, 290–298.

Drgoňa, J., J. Arroyo, I. Cupeiro Figueroa, D. Blum, K. Arendt, D. Kim, E. P. Ollé, J. Oravec, M. Wetter, D. L. Vrabie, and L. Helsen (2020). All you need to know about model predictive control for buildings. *Annual Reviews in Control 50*, 190–232.

Eini, R. and S. Abdelwahed (2019). Distributed model predictive control based on goal coordination for multi-zone building temperature control. In *2019 IEEE Green Technologies Conference (GreenTech)*, pp. 1–6. IEEE.

Elliott, M. S. and B. P. Rasmussen (2013). Decentralized model predictive control of a multi-evaporator air conditioning system. *Control Engineering Practice 21*(12), 1665–1677.

Finck, C., R. Li, and W. Zeiler (2019). Economic model predictive control for demand flexibility of a residential building. *Energy 176*, 365 – 379.

Huang, H., L. Chen, and E. Hu (2015). A new model predictive control scheme for energy and cost savings in commercial buildings: An airport terminal building case study. *Building and Environment 89*, 203 – 216.

Oak Ridge National Lab.(ORNL), Oak Ridge, TN (United States) (2020). *DECENTRALIZED APPROACH TO MULTI-ZONE GREY-BOX MODELING FOR MODEL-BASED PREDICTIVE CONTROL.*

Killian, M. and M. Kozek (2016). Ten questions concerning model predictive control for energy efficient buildings. *Building and Environment 105*, 403–412.

Knudsen, M. D., L. Georges, K. S. Skeie, and S. Petersen (2021). Experimental test of a black-box economic model predictive control for residential space heating. *Applied Energy 298*, 117227.

Kristensen, N. R., H. Madsen, and S. B. Jørgensen (2004). Parameter estimation in stochastic grey-box models. *Automatica 40*(2), 225–237.

Liao, Z. and A. Dexter (2004). A simplified physical model for estimating the average air temperature in multi-zone heating systems. *Building and Environment 39*(9), 1013–1022.

Moroşan, P.-D., R. Bourdais, D. Dumur, and J. Buisson (2010). Building temperature regulation using a distributed model predictive control. *Energy and Buildings 42*(9), 1445–1452.

Scattolini, R. (2009). Architectures for distributed and hierarchical model predictive control–a review. *Journal of process control 19*(5), 723–731.

Thilker, C. A., P. Bacher, H. G. Bergsteinsson, R. G. Junker, D. Cali, and H. Madsen (2021). Non-linear grey-box modelling for heat dynamics of buildings. *Energy and Buildings 252*, 111457.

West, S. R., J. K. Ward, and J. Wall (2014). Trial results from a model predictive control and optimisation system for commercial building hvac. *Energy and Buildings 72*, 271–279.

Zong, Y., W. Su, J. Wang, J. K. Rodek, C. Jiang, M. H. Christensen, S. You, Y. Zhou, and S. Mu (2019). Model predictive control for smart buildings to provide the demand side flexibility in the multi-carrier energy context: Current status, pros and cons, feasibility and barriers. *Energy Procedia 158*, 3026–3031.

Široký, J., F. Oldewurtel, J. Cigler, and S. Prívara (2011). Experimental analysis of model predictive control for an energy efficient building heating system. *Applied Energy 88*(9), 3079–3087.

# C Published - Non-linear Model Predictive Control for Smart Heating of Buildings

# Non-linear Model Predictive Control for Smart Heating of Buildings

*Christian Ankerstjerne* Thilker[1*], *Hjörleifur G.* Bergsteinsson, *Peder* Bacher[1], *Henrik* Madsen[1], *Davide* Calì[1], and *Rune G.* Junker

[1]Department of Applied Mathematics and Computer Science, Technical University of Denmark, DK-2800 Kgs. Lyngby, Denmark

**Abstract.** Smart and flexible operation of components in district heating systems can play a crucial role in integrating larger shares of renewable energy sources in energy systems. Buildings are one of the crucial components that will enable flexibility in the district heating by using intelligent operation. Recent work suggests that such improved operation at the same time can increase thermal comfort and lower economic costs. We have digitalised the heating system in a Danish school by adding IoT devices, such as smart thermostats and temperature sensors to demonstrate the possibilities of making buildings smart. Based on experimental data, this paper introduces a non-linear grey-box model of the thermal dynamics of the building. A non-linear model predictive control method is presented for the thermostatic set-point control of the building's radiators. Based on the building model and the control algorithm, simulation studies are carried out to show the flexibility potential of the building. When used for lowering the return temperature the results suggest that operational costs can be lowered by around 10% using predictive control.

## 1 Introduction

Digitalisation of heating systems, i.e., through smart thermostats and indoor climate sensors, creates the possibility of making buildings smart by having data of the building heat dynamic. This, however, does not alone make the building (or the heating system) smart as it does not yet use the data to make the system efficient or flexible. Without smartness, the system is just data-rich. The system becomes smart when it uses the data to e.g. lower some cost functions, that could be to lower the heating costs without violating thermal comfort or reduce heat consumption during peak hours (known as peak shaving). The data can be used to formulate models that describe the dynamics of the building climate. Such models enable the system to become smart using e.g. Model Predictive Control (MPC) [1]. MPC is a control method that minimises some predefined cost function while satisfying a set of constraints. MPC has become very popular for the heating, ventilation, and air-conditioning sector in the past years as it makes the system smart by making it efficient and/or flexible [2] [3] [4]. The advantage of the MPC over other control methods is its ability to predict the future behaviour of the system. Thereby, the MPC can take weather predictions and future activities into account when optimising the manipulated variables (e.g., desire temperature in a room) of the system [5]. MPC setups usually run in a closed-loop where the controller gets feedback on how the system reacted to the latest input or disturbance. The MPC is based on a model (e.g. a set of differential equations) that describes the behaviour of the system and generates predictions of the system's future behaviour.

This article considers the heating system of an old Danish school building. The building has been "digitalised" with the use of smart thermostats and IoT sensing devices [6], to enable smart control of its heating system using MPC. For this building, a non-linear grey-box model, hence a model based on physics and monitoring data, is formulated, with the purpose to describe the behaviour of the building's heat dynamics. Grey-box modelling is a well-known procedure used for system identification and modelling dynamics of buildings [7] [8]. The parameters of the building model are estimated using the CTSM-R software [9]. The non-linear MPC (NMPC) uses the grey-box model to control the heating system according to some thermal comfort constraints. The MPC utilises weather predictions of the solar irradiance and outdoor temperature to compute the optimal radiator set-points, needed to obtain the desired indoor air temperature. The objective of the controller presented in this work is to lower the heating cost of the building. In order to demonstrate the flexibility potential of the model, we generated a fictive price signal for the energy delivered by the district heating (DH) network. The model developed here is able to use such a variable price signal and consequently minimise the heating costs (by heating when the energy price from the DH network is lower).

The methodology adopted in this work has already shown to be fruitful for lowering the electricity consumption of a smart solar tank for storing heat during sunny periods. The tank was modelled as a grey-box

* Corresponding author: chant@dtu.dk

model, and the MPC takes advantage of future disturbances (solar radiation and outdoor temperature) and its flexibility [10]. The methodology was also successfully adopted in controlling the heat pump of a residential house, by lower the electricity expenses with varying electricity prices [11].

The main contribution of this work is to demonstrate how to use a non-linear grey box model for MPC. We present a multiple shooting method to solve the optimal control problem related to the MPC [12] and incorporate numerical weather forecasts as future inputs. The second contribution of this work is to illustrate the effects of using the MPC through two different simulation studies. The first study shows how to make the building flexible by utilising the right price signal. The second study shows the potential for optimising the operations of the building in order to minimise the economic costs associated with heating a Danish building in a district heating network. The result of the MPC is compared to a simple fixed-schedule control strategy which is among the current standards in buildings.

### 1.1 Structure and outline of the paper

The article is organized as follows. Section 2 presents the building and the modelling scheme along with the parameter estimation method and its results from the estimation. Section 3 introduces the NMPC method that is used to control the building. The simulation results are presented and discussed in Section 4. The article is concluded in Section 5.

## 2 The building and the non-linear thermal model

This section introduces the building and the non-linear building model used in the present work. The model is thoroughly introduced and discussed in [13], where also further details on the building and the model can be found.

### 2.1 Building description and set-up

The building with an area of 1576 m$^2$ acts as a school and has 12 classrooms, 3 meeting/office rooms, and 7 corridors/stairs/open spaces distributed over three floors. Fig. 1 shows a picture and a detailed, digital simulation model of the building. The building was built in 1929 and is not insulated- to meet today's standards. The building is equipped with a hydronic heating system and is connected to the local district heating network. To deliver heat to the rooms, radiators are used; the radiators are connected through a two-pipe system to the building heat exchanger It should be noticed that steady-state analyses related to the heat load of the building indicated that the heating power of the radiators are under-sized in some rooms. As a result, in such rooms a comfortable temperature cannot always be maintained [14].

**Figure 1.** The building picture (top) and a screenshot of the digital model of the building (bottom) used as demo-case in this work.

To make the building smart and enable real-time control, sensors and actuators were installed. Accordingly, temperature sensors have been installed in each room (the sensors are also able to measure $CO_2$-levels and humidity), and each radiator was equipped with a smart thermostat. Moreover, heat-meters have been installed to monitor the energy use of the building. Furthermore, the temperature of the supply- and return water to the heat exchanger connected to the district heating is measured (on the building side) by sensors on both sides of the heat exchanger. All sensor data are collected through servers installed at DTU and the data readings are executed every 15 minutes.

### 2.2 Building model

We consider a non-linear model on the form of Eq. (1$a$) and (1$b$)

$$d\boldsymbol{x}(t) = f\big(\boldsymbol{x}(t), u(t), \boldsymbol{d}(t)\big)dt + g\big(\boldsymbol{x}(t), u(t), \boldsymbol{d}(t)\big)d\boldsymbol{\omega}(t) \quad (1a)$$

$$\mathbf{y}_{\mathrm{k}} = h\big(\boldsymbol{x}(t_k)\big) + \boldsymbol{w}_k, \qquad \boldsymbol{w}_k \sim N(0, \boldsymbol{R}) \quad (1b)$$

where $\boldsymbol{x}(t)$ is the state vector, $u(t)$ is the control input, $\boldsymbol{d}(t)$ is the disturbances, and $\boldsymbol{R}$ is the observation error covariance. $\boldsymbol{\omega}(t)$ is Brownian motion and reflects the uncertainty of the model. Eq. (1$a$) is structurally similar to ordinary differential equations except for the diffusion term. The use of the diffusion term has the advantages that it describes effects that are too complex and (nearly) impossible to model deterministically, and it predicts uncertainty as well, e.g. the variance of the estimates [15].

**Table 1.** The parameter estimates and their physical units

| Parameter | Estimate | Unit |
|---|---|---|
| $T_{\text{offset}}$ | -0.101 | [°C] |
| $C_h$ | 0.134 | [kJ/°C] |
| $C_f$ | 0.198 | |
| $R_{rf}$ | 2.030 | [°C h/kJ] |
| $C_i$ | 9.57 | [kJ/°C] |
| $C_w$ | 45.36 | [kJ/°C] |
| $R_{ih}$ | 2.151 | [°C h/kJ] |
| $R_{iw}$ | 0.199 | [°C h/kJ] |
| $R_{wa}$ | 2.251 | [°C h/kJ] |
| $A_s$ | 7.600 | [m$^2$] |
| $\sigma_1$ | 8.6e-4 | [°C] |
| $\sigma_2$ | 0.429 | [°C] |
| $\sigma_3$ | 111.6 | [kg/h] |
| $\sigma_4$ | 1.647 | [°C] |
| $\sigma_5$ | 6.469 | [°C] |
| $R_1$ | 9.6e-7 | [°C] |
| $R_2$ | 2.7e-4 | [kW] |
| $R_3$ | 5.4e-3 | [°C] |
| $\Phi_{\text{max}}$ | 1145.3 | [kg/h] |
| $\alpha$ | 1.592 | [°C$^{-1}$] |

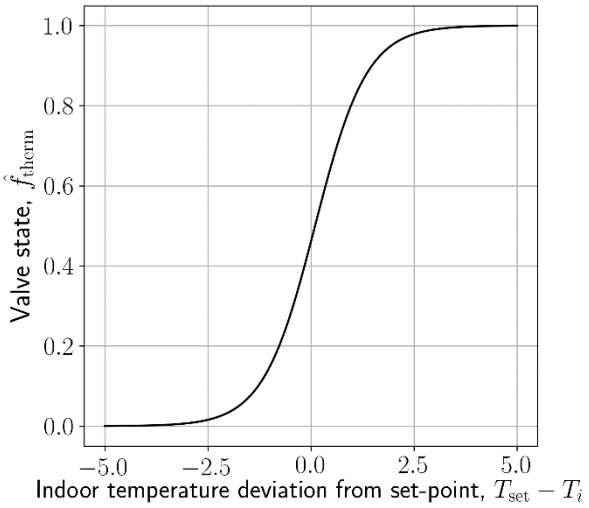


**Figure 2.** The estimated valve function of the thermostats, $\hat{f}_{\text{valve}}$, as a function of how much the room temperature deviates from the set-point. The sigmoid function is attractive for this model since it ranges from 0 to 1 and has an exponential transition. Also, it relies on only two parameters and makes the parameter estimation robust.

In order to simplify the control of the building, in this work we consider and model the building as a unique big room with uniform temperature, represented by the *average* of the measured temperature in all closed rooms (classrooms and meeting rooms)

$$T_i = \frac{1}{n}\sum_{k=1}^{n} T_k \,. \tag{2}$$

Since the heating system is not correctly balanced, and some of the rooms have under-dimensioned radiators, this modelling and control approach consequently implies that some rooms are going to be warmer or colder; however, this simplification is needed at this first stage, since the problem is simplified significantly in terms of dimensionality. It is important for real-time MPC that the model is small enough to compute the control input without too much delay. In the following, we consider a system with the states

$$\boldsymbol{x}(t) = [T_i(t), T_w(t), \Phi(t), T_h(t), T_{\text{ret}}(t)], \tag{3}$$

where $T_i$ is the average indoor air temperature, $T_w$ is the temperature of the building wall, $\Phi$ is the flow of the water in the radiator circuit, $T_h$ is the temperature of the radiators, and $T_{\text{ret}}$ is the temperature of the returning water (going to the heat exchanger of the building). The control input to the model, $u(t)$, is the set-points of the radiator thermostats. To estimate the valve-opening state of the thermostats, the following sigmoid function is used:

$$f_{\text{valve}}(t) = \frac{1}{1 + e^{-\alpha\left(u(t) - T_i(t) + T_{\text{offset}}(t)\right)}}, \tag{4}$$

where $u$ is the thermostat set-point, α determines the slope of the sigmoid function, and $T_{\text{offset}}(t)$ is an offset that models the physical distance between the temperature sensors in the room and the thermostats of the radiators. Fig. 2 shows the estimated $\hat{f}_{\text{valve}}$. The sigmoid function is attractive due to its fixed shape that fits the behaviour of thermostats and requires only two parameters, $\alpha$ and $T_{\text{offset}}$. The term $\hat{f}_{\text{valve}}$ therefore estimates how open the radiator valves are (1 being fully open and 0 being fully closed), i.e. how much water flows through the radiators. The disturbances include the ambient air temperature and solar irradiance $\boldsymbol{d}(t) = [T_a(t), \phi_s(t)]^{\text{T}}$.

The building dynamics model are the following [1]:

$$f\big(\boldsymbol{x}(t), u(t), \boldsymbol{d}(t)\big) = \begin{bmatrix} \frac{1}{C_i}\left(\frac{1}{R_{ih}}\left(T_t^h - T_t^i\right) + \frac{1}{R_{iw}}\left(T_t^w - T_t^i\right) + A_w\phi_t^s\right) \\ \frac{1}{C_w}\left(\frac{1}{R_{iw}}\left(T_t^i - T_t^w\right) + \frac{1}{R_{wa}}\left(T_t^a - T_t^w\right)\right) \\ \frac{1}{C_f}\left(\Phi_{\text{max}} f_t^{\text{valve}} - \Phi_t\right) \\ \frac{1}{C_h}\left(\Phi_t c_{p,w}\left(T_{\text{for}} - T_t^h\right) + \frac{1}{R_{ih}}\left(T_t^i - T_t^h\right)\right) \\ \frac{1}{C_h}\left(\frac{1}{R_{fr}}\left(T_t^h - T_t^{\text{ret}}\right)\right) \end{bmatrix}. \tag{5}$$

In Eq (5), to save space, we write time dependence as subscript, e.g. $T_a(t) = T_t^a$. $A_w$ is the effective area of the solar radiation gain, $c_{p,w}$ is the specific heat capacity of water, and $\Phi_{\text{max}}$ is the maximum water flow in the radiator circuit. $T_{\text{for}}$ is the supply temperature of the water on the building side of the heat exchanger and is

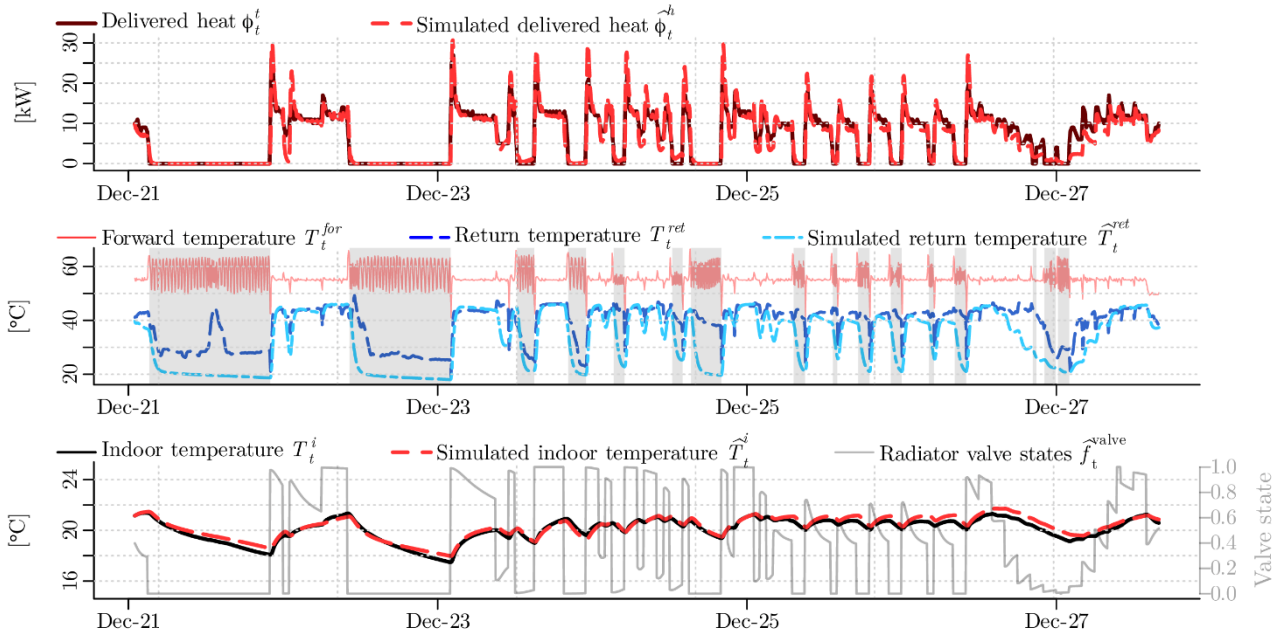


**Figure 3.** Experimental data together with the estimated heat load, air temperature, and return water temperature by the model. The greyed-out periods in the secondgraph indicates periods where the return temperature is disregarded, because the observations do not represent the actual return temperature

kept constant at 55 °C. The diffusion term in Eq. (1), $g$, has the simple form of Eq. (6):

$$g\big(\boldsymbol{x}(t), u(t), \boldsymbol{d}(t)\big) = \mathrm{diag}(\sigma_1, \sigma_2, \sigma_3, \sigma_4, \sigma_5) \qquad (6)$$

Naturally, not all states of the building are observed. Instead, we are limited to the information available in the non-linear observation equation

$$\boldsymbol{y}_k = h\big(\boldsymbol{x}(t_k)\big) = [T_i(t_k),\, \phi_h(t),\, T_{\mathrm{ret}}(t_k)]^{\mathrm{T}} \qquad (7)$$

That is, we observe the average indoor air temperature $T_i(t_k)$, the heat load $\phi_h(t_k) = \Phi(t_k)\big(T_{\mathrm{for}} - T_{\mathrm{ret}}(t_k)\big)$, and the return temperature $T_{\mathrm{ret}}(t_k)$. Recall that the supply temperature is known and is $T_{\mathrm{for}} = 55$ °C.

### 2.3 Model parameter estimation

We use the software CTSM-R [9] to estimate the parameters in the continuous-time stochastic model. The parameter estimation is based on the maximum likelihood principle [16]. That is, we maximise the likelihood function, which is a function of the parameters

$$\mathcal{L}(\boldsymbol{\theta}) = p(\boldsymbol{x}_0)\prod_{k=1}^{N} p(\boldsymbol{y}_k | \mathcal{Y}_{k-1}; \boldsymbol{\theta}) \qquad (8)$$

Where $\mathcal{Y}_{k-1} = \{y_{k-1}, y_{k-2}, \cdots, y_0\}$ is the information up till time $t_{k-1}$, $p$ is the probability of observing $\boldsymbol{y}_k$ with the model in Eq. (5) and Eq. (6) given the parameters $\theta$ and the information $\mathcal{Y}_{k-1}$. Given the model structure in Eq. (5) and Eq. (6), as well as appropriate informative data, any unknown parameters can be estimated.

Table 1 lists the parameter estimates from the estimation procedure. Fig. 3 compares the fit of the resulting model to the data and indicates a good match. It shall be noted that the return temperature measurements are not representative when the heat load is zero and the water flow in the building is zero. We thus put very low weight on the return temperature observations in the estimation procedure in these time intervals (indicated by the grey periods in the figure).

## 3 Non-linear model predictive control: a multiple shooting method

This section introduces a direct multiple-shooting method for solving the particular NMPC problem. It also discusses a method to discretise the optimisation problem to make it numerically tractable. The optimisation problem lies the basis for computing the set-points for the radiators. However, solving the optimisation problem requires us to know the entire state of the system, $\boldsymbol{x}$. For reconstructing the system states based on observation, $\boldsymbol{y}$, the continuous-discrete extended Kalman filter is used [17].

This paper considers an optimal control problem on the following form

$$\min_{x,u} \;\; \varphi = \int_{t_k}^{t_k+T} \ell\big(\boldsymbol{x}(t), u(t), \boldsymbol{d}(t)\big)\,\mathrm{d}t \qquad (9a)$$

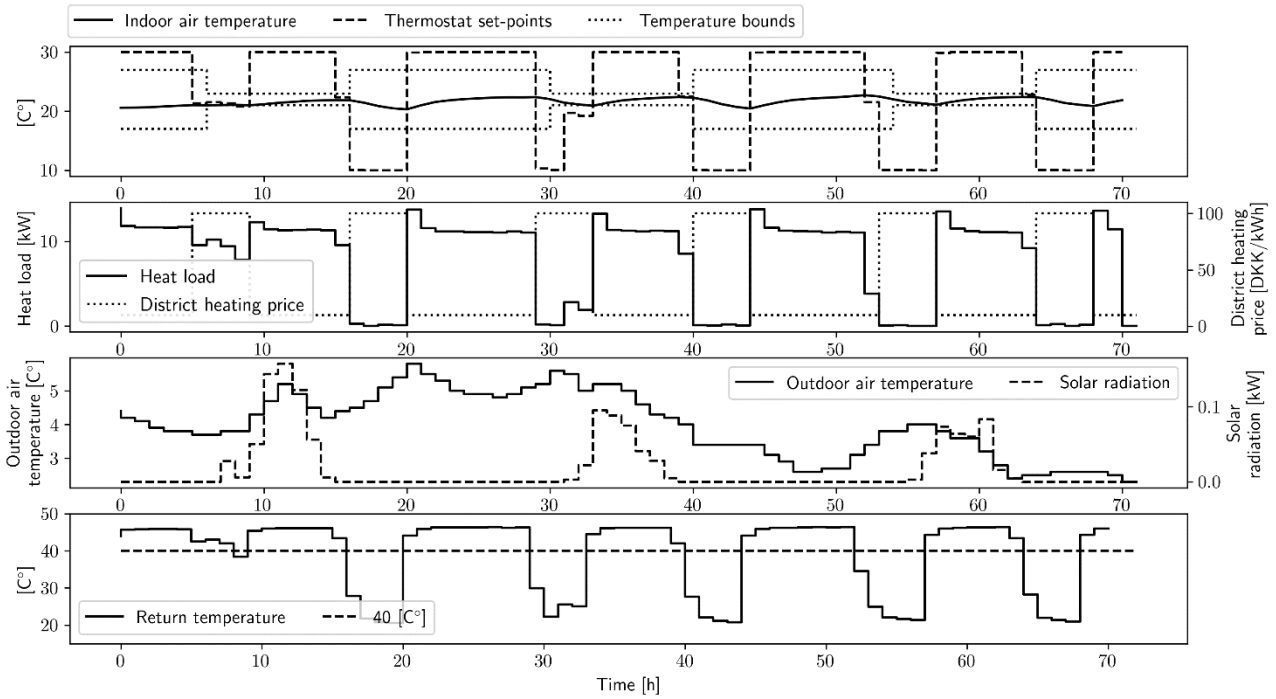


**Figure 4.** A small simulation of thermostatic set-point control of the building using a price signal that reflects peak hours and displays flexibility. The controller keeps the heat usage to a minimum during peak hours when the heat is expensive.

$$s.t. \quad \boldsymbol{x}(t_k) = \boldsymbol{x}(0) \tag{9b}$$
$$\dot{\boldsymbol{x}}(t) = f\big(\boldsymbol{x}(t), u(t), \boldsymbol{d}(t)\big) \tag{9c}$$
$$u_{min}(t) \le u(t) \le u_{\max}(t) \tag{9d}$$
$$T_{\min}(t) \le T_i(t) \le T_{\max}(t) \tag{9e}$$

where $T$ is the prediction and control horizon, $\ell$ is the cost function, and $f\big(\boldsymbol{x}(t), u(t), \boldsymbol{d}(t)\big)$ is the model equations in Eq. (5).

### 3.1 Discrete-time approximation of the optimal control problem

To make the optimal control problem in Eq. (9) numerically tractable, we propose a multiple shooting method to discretise the problem. Multiple shooting is a *simultaneous* method in the sense that the state variables also are a part of the optimisation problem.

The problem is discretised in the sense that the system consider $x$ at discrete time points $t_k$, $t_{k+1}$, ..., $t_{k+N}$ starting from the initial time $t_k$ till $t_k + T$. Now, define a function $\phi\big(\boldsymbol{x}(t), u(t), \boldsymbol{d}(t)\big)$ that computes the solution to the following initial value problem

$$\dot{\boldsymbol{x}}(t) = f\big(\boldsymbol{x}(t), u(t), \boldsymbol{d}(t)\big) \tag{10a}$$
$$\boldsymbol{x}(t_k) = \boldsymbol{x}_k\,, \qquad \text{(initial condition)} \tag{10b}$$

at time $t_{k+1}$. Hence, $\phi\big(\boldsymbol{x}(t_k), u(t), \boldsymbol{d}(t)\big) = \boldsymbol{x}(t_{k+1})$ is a function that integrates the system forward to the next time instance given the input and disturbances in the time interval $[t_k, t_{k+1}[$. To simplify the optimisation problem, we assume that the set-points, $u(t)$, and the disturbances, $d(t)$, are piece-wise constant in each time interval $[t_k, t_{k+1}[$

$$u(t) = u_k, \quad t \in [t_k, t_{k+1}[ \tag{11a}$$
$$\boldsymbol{d}(t) = \boldsymbol{d}_k, \quad t \in [t_k, t_{k+1}[ \tag{11b}$$

The optimal control problem therefore simplifies to

$$\min_{\{\boldsymbol{x}\}_{k=1}^{N}, \{\boldsymbol{u}\}_{k=0}^{N-1}} \ \varphi = \sum_{k=0}^{N-1} L_k(\boldsymbol{x}_k, u_k, \boldsymbol{d}_k) \tag{12a}$$
$$s.t. \quad \boldsymbol{x}_k = \boldsymbol{x}(0) \tag{12b}$$
$$\boldsymbol{x}_{k+1} = \phi(\boldsymbol{x}_k, u_k, \boldsymbol{d}_k) \tag{12c}$$
$$u_{min,k} \le u_k \le u_{\max,k} \tag{12d}$$
$$T_{\min,k} \le T_{i,k} \le T_{\max,k} \tag{12e}$$

In the above,

$$L_k = \int_{t_k}^{t_{k+1}} \ell(\boldsymbol{x}(t), u_k, \boldsymbol{d}_k)\mathrm{d}t \tag{13}$$

is the quadrature of $x(t)$ w.r.t $\ell$ in the time interval $[t_k, t_{k+1}]$.

For numerical computation of the minimisation problem in Eq. (12), we use CasADi [18], which offers easy numerical implementation and automatic differentiation for optimal control problems.

## 4 Simulation results

This section presents the results of two simulation studies. The first simulation investigates the flexibility of the building. The second simulation investigates the ability of the NMPC to minimise the economic operational costs of heating the building (here, the objective is related to the minimisation of return temperature to the district heating, hence to the minimisation of penalty fees due to high return temperature to the grid). We use the Euler-Maruyama simulation scheme to simulate from the SDE-model and

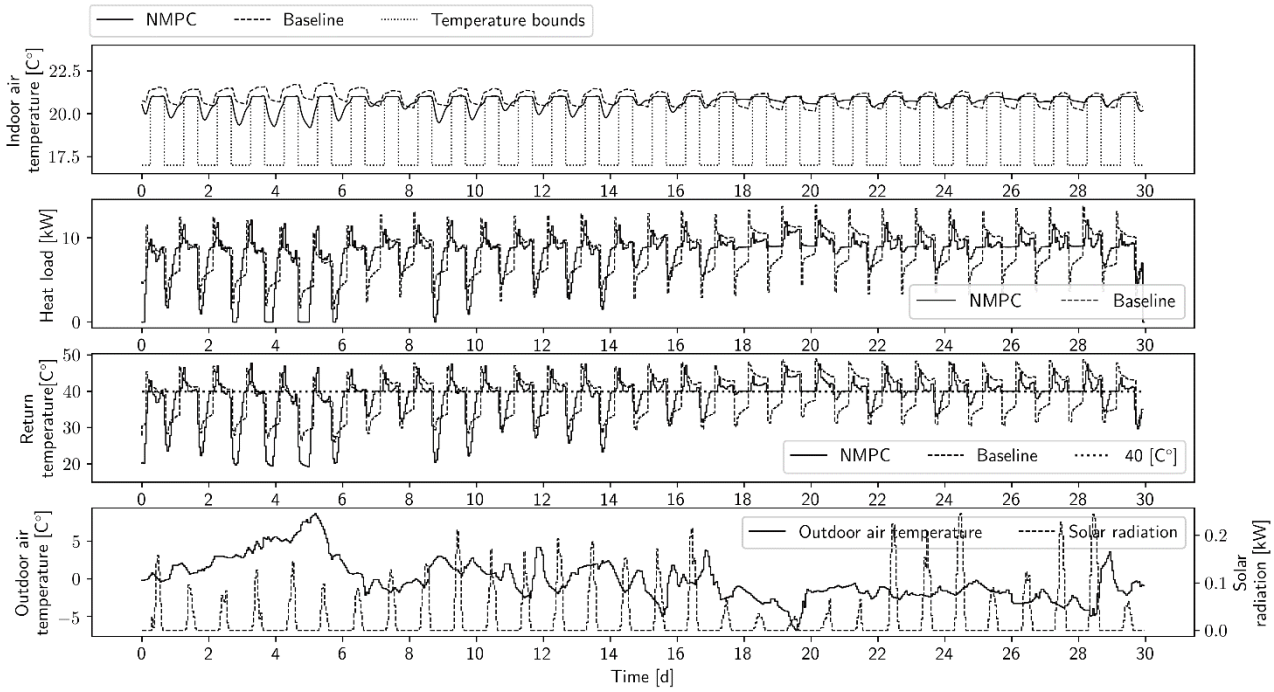


**Figure 5.** A simulation study that compares a current standard set-point control in today's buildings (Baseline) and the NMPC presented in this paper. The heat costs are constant at 0.71 DKK/kWh plus a penalty of 2% for each °C the return temperature is above 40 °C. Results suggest an economic reduction by around 10%.

the continuous-discrete extended Kalman filter to reconstruct the system state.

### 4.1 Simulation: Flexibility of the building

To investigate the flexibility of the building in a smart energy system, we use a cost function in the MPC that takes a price signal. In a flexibility setting, the price signal reflects how "expensive" it is to heat the building at any given time. We define the cost function as

$$\ell_1\big(\boldsymbol{x}(t), u(t), \boldsymbol{d}(t), s(t)\big) = c(t)\Phi(t)\big(T_{\text{for}} - T_{\text{ret}}(t)\big) + \rho s(t) \qquad (14)$$

where $c$ is the price signal, $s$ is a slack variable to soften the indoor air temperature constraints (to make the optimisation problem feasible outside of the constraints), and ρ is the slack penalty. Fig. 4 presents a simulation of the building model in Eq. (5) using the optimal control problem introduced in Section 3 with the cost function in Eq.(14). The control runs in a closed-loop setting with the time between control inputs and the prediction horizon equal to one hour and 24 hours, respectively. Furthermore, the controller has access to the future weather disturbances. In the simulation, the heating price is simply designed in order to see the effect of the MPC. It is expensive at 100 DKK per kWh during peak hours in the mornings and evenings. The heat price is otherwise low at 10 DKK per kWh. As a result, the controller mainly heats outside peak hours and only does so if the indoor temperature gets too low. Due to the under-dimensioned heating system and the building's poor insulation level, the controller still needs to supply some heat during the peak hours to maintain the desired temperature. The results suggest that the building can supply some flexibility under these circumstances. However, considering that the outdoor temperature in Denmark can become even lower than in the present simulation, the building will have less flexibility in such situations.

### 4.2 Simulation: Minimisation of operational costs by lowering return temperature

As a building owner in the Danish district heating, one pays an additional fee if the return temperature is high for two reasons. First, if the temperature difference is small, the mass flow rate needs to be higher. Second, high return temperature to the district heating sources decreases the production efficiency. The pricing scheme is very different between district heating areas. This holds for both the price of heat and the penalty for not cooling the return adequately. In the present analysis, we set it quite progressively, namely as follows: if the return temperature is above 40 °C, the heat price increases 2% per extra degree Kelvin of the return temperature. The cost-function where this is accounted for is

$$\ell_2\big(\boldsymbol{x}(t), u(t), \boldsymbol{d}(t), s(t), v(t)\big) = c(t)\Phi(t)\big(T_{\text{for}} - T_{\text{ret}}(t)\big)\big(1 + 0.02v(t)\big) + \rho s(t) \qquad (15)$$

where $v$ is a slack variable that softens the upper constraint at 40 °C on the return temperature and the scalar 0.02 is the percent-wise increase in heat cost.

Fig. 5 displays a simulation study of the building model in Eq. (5) using the cost function in Eq. (14). The figure also depicts a baseline, which uses a simple set-point control that turns down the temperature during the

night and back on during the day. The baseline represents the current practice in most buildings using rule-based control: a fixed set-point pattern used every day. This experiment reflects the actual economic costs of operating the building together with the extra fee when the return temperature is too high. The results demonstrate the emphasis the controller puts on keeping the return temperature below 40 °C while supplying enough heat to comply with the constraints. The actual economic costs associated with each control strategy during the one simulated month are 4522.9 DKK and 4066.6 DKK for the baseline and MPC, respectively. This points toward economic savings of around 10% by using the proposed control strategy. Much of this reduction is explained by the ability of the controller to lower the return temperature and avoid extra penalties, which account for 382.2 DKK and 89.5 DKK, respectively for the two strategies. Especially during the cold periods, where extra heat is needed, the economic savings are high. The total energy use is reduced from 5891.4 kWh to 5742.5 kWh (around 2.5%) by the MPC, which comes from the ability of the MPC to lower the temperature closer to the constraints. This optimisation and the lower return temperature not only benefit the building operators, but also benefits the district heating operators by significantly decreasing the amount of heat loss in the district heating system.

It should be stressed that these results apply only to the current settings and may vary according to different district heating areas and pricing schemes. Also, in a realistic setup with meteorological weather forecasts, building occupants, etc., the control performance may be affected.

## 5 Conclusion

This article introduced a non-linear grey-box model describing the heat dynamics of an old school building. This model enabled us to predict and control the future evolution of temperatures and heating in the building. We presented a NMPC method and used it in a simulation study to cast light on the benefits. The results suggest that smart control of the heat supply unlocks the building's flexibility and supplies economic savings of up to 10% under a particular, but realistic, pricing scheme. The specific savings may vary depending on the district heating area since pricing schemes vary. Also, the controller had access to the actual future weather disturbances, which in a realistic setting must be replaced with weather forecasts potentially decreasing the savings. Future work involves implementation of the NMPC in the building and investigation of how well individual rooms behave under the simplified model [19].

## 6 Acknowledgements

The authors would like to acknowledge the following. *Sustainable plus energy neighbourhoods (syn.ikia)* (H2020 No. 869918), *Centre for IT-Intelligent Energy Systems (CITIES)* (DSF 1305-00027B), *Top-up* (Innovation Fund Denmark 9045-00017B), *SCA+* (Interreg Öresund-Kattegat-Skagerrak) and *Flexibile Energy Denmark (FED)* (IFD 8090-00069B)

## References

[1] J. Drgoňa *et al.*, “All you need to know about model predictive control for buildings,” *Annual Reviews in Control*, vol. 50. Elsevier Ltd, pp. 190–232, Jan. 01, 2020, doi: 10.1016/j.arcontrol.2020.09.001.

[2] H. Madsen *et al.*, “Control of Electricity Loads in Future Electric Energy Systems,” in *Handbook of Clean Energy Systems*, American Cancer Society, 2015, pp. 1–26.

[3] A. Q. Santos *et al.*, “Control strategies and algorithms for obtaining energy flexibility in buildings,” 2019.

[4] C. A. Thilker, H. Madsen, and J. B. Jørgensen, “Model predictive control based on stochastic differential equations,” in *Towards Energy Smart Homes: Algorithms, technologies, and applications*, C. Ghiaus, M. Amayri, and S. Ploix, Eds. Springer, 2021.

[5] F. Oldewurtel *et al.*, “Use of model predictive control and weather forecasts for energy efficient building climate control,” *Energy Build.*, vol. 45, pp. 15–27, Feb. 2012, doi: 10.1016/j.enbuild.2011.09.022.

[6] S. W. Lex, D. Calì, M. Koed Rasmussen, P. Bacher, M. Bachalarz, and H. Madsen, “A cross-disciplinary path to healthy and energy efficient buildings,” *Technol. Forecast. Soc. Change*, vol. 142, pp. 273–284, May 2019, doi: 10.1016/j.techfore.2018.07.023.

[7] P. Bacher and H. Madsen, “Identifying suitable models for the heat dynamics of buildings,” *Energy Build.*, vol. 43, no. 7, pp. 1511–1522, Jul. 2011, doi: 10.1016/j.enbuild.2011.02.005.

[8] K. K. Andersen, H. Madsen, and L. H. Hansen, “Modelling the heat dynamics of a building using stochastic differential equations,” *Energy Build.*, vol. 31, no. 1, pp. 13–24, Jan. 2000, doi: 10.1016/S0378-7788(98)00069-3.

[9] R. Juhl, N. R. Kristensen, P. Bacher, J. Kloppenborg, and H. Madsen, “CTSM-R User Guide,” 2013.

[10] R. Halvgaard *et al.*, “Model predictive control for a smart solar tank based on weather and consumption forecasts,” in *Energy Procedia*, Jan. 2012, vol. 30, pp. 270–278, doi: 10.1016/j.egypro.2012.11.032.

[11] H. A. Schluter, D. Boiroux, N. K. Poulsen, H. Madsen, and J. B. Jorgensen, “Economic Model Predictive Control for Energy Systems in Smart Homes,” *CCTA 2019 - 3rd IEEE Conf. Control Technol. Appl.*, pp. 598–604, 2019, doi: 10.1109/CCTA.2019.8920663.

[12] M. Diehl *et al.*, “Fast Direct Multiple Shooting Algorithms for Optimal Robot Control,” *Fast Motions Biomech. Robot.*, 2009.

[13] C. A. Thilker, R. G. Junker, H. Madsen, D. Cali, and P. Bacher, “Non-Linear Grey-Box Modelling for the Heat Dynamics of Buildings,” *Submitt. to Energy Build.*, 2021.
[14] C. G. Bruun, “Optimization of Building Operation using high-resolution sensor data,” no. February, 2019.
[15] B. Oksendal, *Stochastic differential equations (3rd Ed.): An introduction with applications*. Heidelberg: Springer-Verlag, 1992.
[16] Y. Pawitan, *In all likelihood: statistical modelling and inference using likelihood*. Oxford: Clarendon Press, 2006.
[17] P. Frogerais, J. J. Bellanger, and L. Senhadji, “Various ways to compute the continuous-discrete extended Kalman filter,” *IEEE Trans. Automat. Contr.*, vol. 57, no. 4, pp. 1000–1004, 2012, doi: 10.1109/TAC.2011.2168129.
[18] J. A. E. Andersson, J. Gillis, G. Horn, J. B. Rawlings, and M. Diehl, “CasADi - A software framework for nonlinear optimization,” 2018.
[19] C. A. Thilker, H. Madsen, and J. B. Jørgensen, “Advanced forecasting and disturbance modelling for model predictive control of smart energy systems,” *Submitt. to Appl. Energy*, 2021.

# D Published - Identification of non-linear autoregressive models with exogenous inputs for room air temperature modelling

Energy and AI 9 (2022) 100165

Contents lists available at ScienceDirect

Energy and AI

journal homepage: www.elsevier.com/locate/egyai

# Identification of non-linear autoregressive models with exogenous inputs for room air temperature modelling

Christian Ankerstjerne Thilker *, Peder Bacher, Davide Cali, Henrik Madsen

*Technical University of Denmark, Department of Applied Mathematics and Computer Science, Asmussens Allé, Building 303B, DK-2800 Kgs. Lyngby, Denmark*

ARTICLE INFO

*Keywords:*
Time series analysis
Non-linear models
District heating
Smart energy systems

ABSTRACT

This paper proposes non-linear autoregressive models with exogenous inputs to model the air temperature in each room of a Danish school building connected to the local district heating network. To obtain satisfactory models, the authors find it necessary to estimate the solar radiation effect as a function of the time of the day using a B-spline basis expansion. Furthermore, this paper proposes a method for estimating the valve position of the radiator thermostats in each room using modified Hermite polynomials to ensure monotonicity of the estimated curve. The non-linearities require a modification in the estimation procedure: Some parameters are estimated in an outer optimisation, while the usual regression parameters are estimated in an inner optimisation. The models are able to simulate the temperature 24 h ahead with a root-mean-square-error of the predictions between 0.25 °C and 0.6 °C. The models seem to capture the solar radiation gain in a way aligned with expectations. The estimated thermostatic valve functions also seem to capture the important variations of the individual room heat inputs.

## 1. Introduction

In Denmark, more than 65% of households are heated by district heating [1]. It is standard practice to measure the heat consumption for an individual household — to be able to bill each household for its consumption. But for an individual room in a (large) building, the heat each radiator emits is not known. Hence, room control relies only on temperature measurements. It is an interesting and relevant task to control a single room. Firstly, because rooms have different dynamics due to differences in size and heating capacity and thus require different treatment and control in order to keep them comfortably regulated. Secondly, because occupants perceive the indoor climate individually and therefore want individual settings in the rooms they use [2]. For these reasons, it is desirable to control buildings on room level.

### 1.1. Literature review

Predictive room-level control obviously requires temperature-models of the individual rooms. However, the popular Resistor–Capacitor-based models [3] are not possible to employ due to the missing knowledge of the heat load on room-level. We are left, then, to use models that relate less to physics. AutoRegressive with eXogenous input (ARX) models are a popular class of models for time series modelling [4,5]. ARX models are a variant of AutoRegressive and Moving Average (ARMA) models where the MA-part is left out and input-terms are added [6]. Examples of applications are solar radiation forecasting [7], wind power forecasting [8], and glucose level predictions [9]. For thermal prediction of buildings, popular black-box models include ARX and neural network models. The latter has received much attention recently [10–16]. Standard Artificial Neural Networks (ANNs) are the simplest kind of neural network model and Root Mean Square Error (RMSE) between 0.77 and 0.9 are reported [10,11]. Long short-term memory models, that are suitable neural networks for time series predictions, are also studied intensively with various variations (e.g. in combination with an error correction model or a convolutional neural network) [13,14]. A combination of grey-box models with a neural network to make correct prediction errors have also been done [12]. RMSE between 0.6 and 0.75 was reported. Conclusions regarding the best kind of model is not unanimous, with some studies finding ARX models performing [15] better and vice versa [16]. ARX models are in general much simpler compared to neural networks making them more robust toward overfitting and faster to fit [17,18]. Given time series data of the system, the optimal set of parameters in linear ARX models has a closed-form solution, equivalent to linear regression, which is fast and robust to compute [6]. Sometimes, however, non-linear models are necessary to sufficiently describe input effects due to their richer solution structures compared to linear models [19].

* Corresponding author.
*E-mail addresses:* chant@dtu.dk (C.A. Thilker), pbac@dtu.dk (P. Bacher), dcal@dtu.dk (D. Cali), hmad@dtu.dk (H. Madsen).

https://doi.org/10.1016/j.egyai.2022.100165
Received 19 February 2022; Received in revised form 23 April 2022; Accepted 7 May 2022
Available online 23 May 2022

Neural network models can be thought of as (very high-dimensional) non-linear variants of linear ARX models readily able to model non-linearities. The present approach, however, use the low-dimensional ARX models while including and isolating the non-linear contributions in the model. The heat dynamics between the indoor and outdoor air are well known to be linear [20,21], and therefore there is no need to use non-linear models to capture this effect. However, the solar gain can be very non-linear [22,23]. The proposed method isolates the non-linearities to the solar gain using relatively few parameters compared to neural network models. Thus, the presented approach keeps the robustness and simplicity of the ARX model, while still modelling non-linear effects. The few number of parameters and simple model structure of the proposed ARX models impose and act as regularisation in the model, which ensures robustness of the prediction capabilities. ARX models are also readily used for control purposes.

In the present paper, it is described how important non-linearities that affect the room air temperature can be modelled. The gain from solar radiation is a significant source of heat in rooms. Solar radiation forecasts are typically given as an average effect on a horizontal surface during a time interval, i.e. in the units [W/m$^2$]. However, the solar gain in rooms vary non-linearly throughout the day and is hence a non-linear function of time [24,25]. Another non-linearity arises from the radiator thermostats. A thermostat controls the valve (and mass flow rate in the radiators) as a PI-controller. However, it is well-known that the map from a measured temperature and set point to a valve state is a non-linear function [26,27]. Even chaos in the valve dynamics has been reported [28]. To model the entering non-linearities from the solar gain and the thermostatic valve, functions are fitted to data using B-splines and Hermite polynomials as basis functions.

### 1.2. Main contributions of the paper

This paper describes a method for estimating ARX-models where the estimation problem is non-linear in the parameters. Conventional methods cannot estimate parameters in such models, thus, the proposed method generalises the identification procedure for ARX models. Applying the method for indoor air temperature models enables us to estimate nonlinear effects such as varying solar radiation gain and heat inlet from the heating system in each room. The room air temperature models are able to predict the temperature over a long period with different conditions and may enable smart predictive control on room level. Results indicate that the models perform on par or better compared to the literature in terms of RMSE.

### 1.3. Structure and outline of the paper

Section 2 introduces the building and experimental setup carried out to obtain the data. In Section 3, ARX models are introduced and how to carry out the variable transformation and parameter estimation. Next, Section 4 introduces B-splines and Hermite polynomials for data fitting and explains how to use them for modelling inputs in the ARX models. Section 5 showcases the results from fitting ARX models to the individual room air temperatures of a Danish school building. Lastly, Section 6 concludes and sums up the findings of the paper.

## 2. Case study: A Danish school building

This section presents the building and the experimental setup. Also, it introduces and explains the problems related to operating the indoor climate of the individual rooms and sets the stage for the rest of the paper. It is identified how the following key heat gains of the room air temperature to include in the models:

- **The outdoor air temperature** constantly affects the indoor air temperature through walls and windows. The outer surfaces act as a low-pass filter between the indoor and outdoor air temperature.

**Fig. 1.** A photograph of the building site.


**Fig. 2.** Floor plan of the school building.

- **The solar gain** may deliver significant amounts of energy to the indoor air in short time periods by entering through windows and heating floors, walls, furniture and other materials.
- **The room radiators** are the rooms' main heating sources and are controlled by a thermostatic valve that opens according to a given set-point.

### 2.1. The building and rooms

The building, a school with three floors and a basement, is located in Høje Taastrup, Denmark. The uppermost floor is a partly-refurbished roof attic. A photo of the building is given in Fig. 1. Fig. 2 shows a floor plan of the building. It has 10 classrooms while fewer rooms are hallways, storage rooms, toilets, and teacher's rooms. The following paragraph gives an overview of the basic properties of the building here. For more technical details, the reader is referred to Bruun [29], Lex et al. [30].

The building was built in 1929 and thus is not insulated according to modern standards. The facade and internal walls consist of solid bricks. The windows have wooden frames and double-paned low-E glazings. Floors are made from wood joists and the roof is partly uninsulated and partly insulated slate roof. The building is connected to the local district heating (DH) system. The building uses district heating for domestic hot water and space heating. For this building, the space heating is a separate water-based circuit with dedicated pumps. Radiators of different types (cast-iron, panel convectors, plane conductors) with individual thermostats deliver the heat in the individual rooms. Each radiator has an individual thermostatic valve that automatically and individually

regulates the water flow into the radiator unit to maintain a certain air temperature, and can be remotely controlled by temperature set-points. To measure the room air temperature, each room is equipped with an air temperature sensor, placed somewhere on the inner wall in around 2–3 m height.

### 2.2. Some room modelling problems

Since radiators do not heat up the room in a spacial uniform manner, the measured room air temperature is only representative for the air close to the sensor. There is thus a temperature difference between the air temperature close to the thermostat and measured temperature by the sensor on the wall. Thus, the measured room temperature may react very differently to set-point increases based on room geometry, room size, air circulation, number and placement of radiators and thermostats etc. Such factors support the need for individual room air temperature models. Due to the many complicated physical factors related to modelling the thermostatic behaviour, a data-driven method is proposed using interpolating polynomials to describe the state of the radiator valves as a function of the room air temperature and the room set-point.

Another significant challenge on room level arises from the solar gain. The sun radiates large amounts of energy to rooms in buildings, which leads to a fast increase in the indoor air temperature [31]. It is thus important to model the solar gain in thermal models of buildings [32]. The solar gain pattern is individual for each room due to the individual room and window sizes and different navigational orientations of the windows. Furthermore, the solar gain changes throughout the day as the sun traverses the sky (due to Earth's rotation around itself), which is difficult to describe using regular ARX models. To describe the time-varying solar gain in each room, this paper propose a data-driven approach using B-splines as a basis expansion [33].

### 2.3. The experiment and data

Each room has been equipped with a sensor, which measures the indoor air temperature. The accuracy of the measurements are ±0.2 °C and are taken in resolution of 0.1 °C. All radiators in the rooms are also equipped with smart thermostats, where the operators can read and write set-points in °C. Sensors located in buildings central heating system measure the total heat load of the building and the forward temperature. See Table 1 for an overivew of the experimental data.

The experiment was designed to produce dynamical responses from the rooms to easier learn the thermal dynamics. The experiment lasted from the 1st of March, 2021, through the 27th of March 27, 2021, during which the school was only partly occupied (due to covid-19) but most rooms were used. During the experiment, individual and independent set-points were sent to each room. However, different schedules were used during day- and night time, such that the temperature was more comfortable during occupation times. The measured signals for each room are: the indoor air temperature, $T_{\mathrm{i},t}$, and the thermostatic set-point, $T_{\mathrm{set},t}$. The forward temperature of the space heating water in the building was set constant at 60 °C. The ventilation system was operating at a constant rate with inlet temperature set-point between 20 and 24 °C. The weather data is from a local weather station and is provided by the Danish Meteorological Institute.

## 3. ARX-models for dynamical systems

This section introduces ARX models for modelling dynamical systems. In linear ARX models, the optimal parameters are given by a closed-form solution to a linear regression problem. However, the closed-form solution exists only for models that are linear in the parameters. This section addresses this problem and proposes a method for estimating parameters that appear non-linearly in ARX models.

**Table 1**
Data interpretation.

| Name | Quantity | Unit |
|---|---|---|
| $T_{\mathrm{i},t}^{j}$ | Indoor air temperature in room $j$ | [°C] |
| $T_{t}^{\mathrm{for}}$ | Building supply temperature | [°C] |
| $T_{j,t}^{\mathrm{set}}$ | Temperature set-point in room $j$ | [°C] |
| $I_t$ | Global solar radiation | [W/m$^2$] |
| $T_t^{\mathrm{a}}$ | Outdoor air temperature | [°C] |

### 3.1. Introduction to ARX models

Let $\{Y_t; t \in \mathbb{N}\}$, $Y_t \in \mathbb{Y} \subseteq \mathbb{R}$, be a stochastic process and let the time series $\boldsymbol{y}_N = \left(y_1, y_2, \dots, y_N\right)^\top$ be a realisation of $N$ consecutive observations of $Y_t$. Let $\boldsymbol{X}_N = \left\{\boldsymbol{x}_i\right\}_{i=1}^{N}$, $\boldsymbol{x}_t = (x_{1,t}, \dots, x_{N_x,t})^\top \in \mathbb{X}^{N_x} \subseteq \mathbb{R}^{N_x}$ be a vector time series containing the inputs to the system associated with the realisation. An ARX model of order $M$ has the form

$$\varphi(\mathrm{B})Y_t = \boldsymbol{\beta}(\mathrm{B})^\top \boldsymbol{x}_t + \varepsilon_t\,, \tag{1}$$

where $\varphi(\mathrm{B}) = 1 + \varphi_1\mathrm{B} + \varphi_2\mathrm{B}^2 + \cdots + \varphi_M\mathrm{B}^M$ is a polynomial in the back shift operator B, $\mathrm{B}^k Y_t = Y_{t-k}$. $\boldsymbol{\beta}(\mathrm{B})^\top = (\beta_1(\mathrm{B}), \beta_2(\mathrm{B}), \dots, \beta_{N_x}(\mathrm{B}))$ is a vector with back-shift polynomials where the $i$'th polynomial

$$\beta_i(\mathrm{B}) = \beta_{i,1}\mathrm{B} + \beta_{i,2}\mathrm{B}^2 + \cdots + \beta_{i,M}\mathrm{B}^M, \quad i = 1, \dots, N_x \tag{2}$$

is associated with the $i$'th input. $\{\varepsilon_t; t \in \mathbb{N}\}$ is a white noise process where $\varepsilon_t \sim N(0, \sigma^2)$ is i.i.d. Now, let $\boldsymbol{\beta}_i = \{\beta_{i,m}\}_{m=1}^{M}$ be the set of coefficients in the $i$'th back-shift polynomial. Then $\{\varphi_i\}_{i=1}^{M}$ and $\{\boldsymbol{\beta}_i\}_{i=1}^{N_x}$ are regression coefficients in the ARX model in (1). Isolating $Y_t$,

$$Y_t = \sum_{m=1}^{M} -\varphi_m \mathrm{B}^m Y_t + \sum_{i=1}^{N_x} \beta_i(\mathrm{B}) x_{i,t} + \varepsilon_t \tag{3}$$

we obtain the system on a regression form. Then the optimal set of parameters in Eq. (3) when minimising the sum of squared errors is given by the closed form solution [6]

$$\begin{aligned}(\{\hat{\varphi}_i\}_{i=1}^{M}, \{\hat{\boldsymbol{\beta}}_i\}_{i=1}^{N_x}) = \underset{\varphi_1,\dots,\varphi_M,\boldsymbol{\beta}_1,\dots,\boldsymbol{\beta}_{N_x}}{\arg\min} \sum_{i=1}^{N} \varepsilon_i^2 = \\ (\boldsymbol{X}(\boldsymbol{y}_N, \boldsymbol{X}_N)^\top \boldsymbol{X}(\boldsymbol{y}_N, \boldsymbol{X}_N))^{-1} (\boldsymbol{X}(\boldsymbol{y}_N, \boldsymbol{X}_N)^\top \boldsymbol{y}_N)\,,\end{aligned} \tag{4}$$

where $\boldsymbol{X} : \mathbb{Y}^N \times \mathbb{X}^{N \times N_x} \mapsto \mathbb{R}^{N \times M(N_x+1)}$ is the so-called design matrix of Eq. (1), where each row constitute a time instance of Eq. (3).

### 3.2. Parameter estimation in ARX models

The overall goal of the parameter estimation procedure is to find the set of parameters that minimises the sum of squared residuals (as in Eq. (4)),

$$\sum_{i=1}^{N} (y_i - \hat{y}_i)^2 = \sum_{i=1}^{N} \hat{\varepsilon}_i^2\,. \tag{5}$$

Therefore, the central objective in order to enable us to minimise (5) is to evaluate the squared residuals. Then, a numerical optimisation routine may minimise the squared residuals w.r.t. the model parameters. Since our ARX model includes parameters that are non-linearly coupled (e.g. some regression coefficients may depend non-linearly on some parameters $\boldsymbol{\theta}_{\mathrm{tr}}$, i.e. $\beta_{i,m}(\boldsymbol{\theta}_{\mathrm{tr}})$), the closed-form solution (4) cannot be evaluated directly. Instead, to evaluate the sum of squared residuals (5), the paper propose the following two-stage procedure:

- Transformation stage: Here, transform the regressors such that they appear linearly in the ARX model (given the set of transformation variables).
- Regression stage: Here, insert the transformed regressors into the regression form in (3) to compute the regression coefficients using (4), which afterwards allows us to evaluate the sum of squared residuals.

Performing the two above steps returns the sum of squared residuals, which may be minimised by a numerical optimisation routine to find the optimal set of parameters. This reduces the size of the numerical optimisation to a subset of the model parameters compared to letting all parameters be optimised by numerical means.

#### 3.2.1. Step one: Transformation stage

The regular ARX-model in (1) is linear in the regressor coefficients and does not directly allow terms that are non-linear in the parameters. In order to include non-linear terms in the ARX model, the input variables are *transformed* using a desired non-linear transformation needed in the model. Let $\boldsymbol{U}_t = (\boldsymbol{u}_{1,t}, \dots, \boldsymbol{u}_{N_x,t})^\top \in \mathbb{U}^{N\times N_x}$ be the "raw" input to the model, e.g. horizontal global solar radiation. Then, define the *transformed input variables* by

$$x_{i,t} = h_i(u_{i,t}, y_t, t, \boldsymbol{\theta}_{\text{tr}}), \quad i = 1, \dots, N_x, \tag{6}$$

where $\boldsymbol{\theta}_{\text{tr}} \in \mathbb{P}_{\text{tr}} \subseteq \mathbb{R}^{N_{\text{tr}}}$ are input-specific parameters that may enter into e.g. a basis expansion such as a spline basis, a polynomial basis, a Fourier basis etc., $h_i : \mathbb{U}\times\mathbb{Y}\times\mathbb{R}_+\times\mathbb{P}_{\text{tr}} \mapsto \mathbb{X}_i \subseteq \mathbb{R}$ is the (in general) non-linear transformation for the $i$'th input. Note that the variable $x_{i,t}$ defines a new regressor as a function of the input $u_{i,t}$. But now, a regular ARX model, which is linear in the new regressors, $x_{i,t}$, can be written

$$\begin{aligned} &\varphi(\mathrm{B})Y_t = \boldsymbol{\beta}(\mathrm{B})^\top \boldsymbol{x}_t + \varepsilon_t\,, \\ \implies \quad & Y_t = \sum_{m=1}^{M} -\varphi_m \mathrm{B}^m Y_t + \sum_{i=1}^{N_x} \beta_i(\mathrm{B}) x_{i,t} + \varepsilon_t\,, \\ \implies \quad & Y_t = \sum_{m=1}^{M} -\varphi_m \mathrm{B}^m Y_t + \sum_{i=1}^{N_x}\sum_{m=1}^{M} \beta_{i,m} \mathrm{B}^m x_{i,t} + \varepsilon_t\,. \end{aligned} \tag{7}$$

where $\boldsymbol{x}_t = (x_{1,t}, \dots, x_{N_x,t})^\top$. Note that if $h_i$ does not depend on any parameters, i.e. if $\boldsymbol{\theta}_{\text{tr}} = \emptyset$, the model simplifies to a regular ARX model that is linear in the regression coefficients.

#### 3.2.2. Step two: Parameter estimation in the transformed regression variables

If one writes (7) for all observations, $y_t$, it may be write on the following matrix–vector form

$$\boldsymbol{Y}_N = \boldsymbol{X}(\boldsymbol{\theta}_{\text{tr}}; \boldsymbol{X}_N, \boldsymbol{y}_N)\boldsymbol{\theta}_{\text{reg}} + \boldsymbol{\varepsilon}_N\,, \tag{8}$$

where $\boldsymbol{X} : \mathbb{P}_{\text{tr}}\times\mathbb{X}^{N\times N_x}\times\mathbb{Y}^N \mapsto \mathbb{X}_m^{N\times M(N_x+1)}$, $\boldsymbol{X}_N = (\boldsymbol{x}_1, \boldsymbol{x}_2, \dots, \boldsymbol{x}_N)^\top$, is a function that returns the design matrix of the linear regression problem in (7) as a function of $\boldsymbol{\theta}_{\text{tr}}$. Eq. (8) is now linear in the coefficients $\{\varphi_m\}_{m=1}^M$ and $\{\boldsymbol{\beta}_i\}_{i=1}^{N_x}$. It can then be interpreted as a linear regression problem with $\boldsymbol{\theta}_{\text{reg}} = (-\varphi_1, \dots, -\varphi_M, \beta_{1,1}, \dots, \beta_{N_x,M})^\top \in \mathbb{P}_{\text{reg}} \subseteq \mathbb{R}^{M(N_x+1)}$ as the regression coefficients and $y_i$ and $\boldsymbol{x}_i$ as regressors.

Eq. (8) appears as a linear regression problem w.r.t. $\boldsymbol{\theta}_{\text{reg}}$. It is immediately evident that the design matrix depends on $\boldsymbol{\theta}_{\text{tr}}$. Therefore, consider the case where $\boldsymbol{\theta}_{\text{tr}}$ is given and fixed, then the optimal estimator of $\boldsymbol{\theta}_{\text{reg}}$ when minimising the sum of squared residuals in (4) is

$$\hat{\boldsymbol{\theta}}_{\text{reg}}(\boldsymbol{\theta}_{\text{tr}}) = \left(\boldsymbol{X}(\boldsymbol{\theta}_{\text{tr}})^\top \boldsymbol{X}(\boldsymbol{\theta}_{\text{tr}})\right)^{-1} \left(\boldsymbol{X}(\boldsymbol{\theta}_{\text{tr}})^\top \boldsymbol{Y}\right) \tag{9}$$

where $\boldsymbol{X}(\boldsymbol{\theta}_{\text{tr}}) = \boldsymbol{X}(\boldsymbol{\theta}_{\text{tr}}; \boldsymbol{X}_N, \boldsymbol{y}_N)$ is simply a short-hand notation.

#### 3.2.3. Optimisation of transformation parameters

The above implies that for each given value of $\boldsymbol{\theta}_{\text{tr}}$, the optimal set of $\boldsymbol{\theta}_{\text{reg}}$ is given in a closed form. With $\boldsymbol{\theta}_{\text{tr}}$ and $\boldsymbol{\theta}_{\text{reg}}$ at hand, the sum of squared residuals can be evaluated. Thus, one can write a function alone in $\boldsymbol{\theta}_{\text{tr}}$, which 1) transforms the regressors, 2) solves the arising linear regression problem, and 3) evaluates the sum of squared residuals. The optimisation problem in the transformation variables become:

$$\hat{\boldsymbol{\theta}}_{\text{tr}} = \arg\min_{\boldsymbol{\theta}_{\text{tr}}} \quad \sum_{i=1}^{N} \hat{\varepsilon}(\boldsymbol{\theta}_{\text{tr}})_i^2 \tag{10}$$

where $\varepsilon(\boldsymbol{\theta}_{\text{tr}})_i$ is the $i$'th prediction error as a function of $\boldsymbol{\theta}_{\text{tr}}$. Any numerical optimiser may be used to solve this problem. Practically, is done by defining a function that takes as input $\boldsymbol{\theta}_{\text{tr}}$, computes $\boldsymbol{\theta}_{\text{reg}}$, and in turn computes and returns the sum of squared errors. Algorithm 1 outlines the framework for evaluating (5). The function is fed into a numerical optimiser. The `ipopt` solver through `Python` was used.

**Algorithm 1** Evaluation of sum of squared residuals

**require:** $\boldsymbol{\theta}_{\text{tr}}$, $\boldsymbol{y}_N$, $\boldsymbol{U}_N$

given $\boldsymbol{\theta}_{\text{tr}}$, $\boldsymbol{y}_N$, and $\boldsymbol{U}_N$, compute transformed input variables, $x_{i,t}$, and construct design matrix $\boldsymbol{X} = \boldsymbol{X}(\boldsymbol{\theta}_{\text{tr}}, \boldsymbol{X}_N, \boldsymbol{y}_N)$

compute regression variables $\hat{\boldsymbol{\theta}}_{\text{reg}} = (\boldsymbol{X}^\top\boldsymbol{X})^{-1}(\boldsymbol{X}^\top\boldsymbol{y}_N)$

compute sum of squared residuals, SSE $= \sum_i \varepsilon_i^2 = (\boldsymbol{y}_N - \boldsymbol{X}\hat{\boldsymbol{\theta}}_{\text{reg}})^\top(\boldsymbol{y}_N - \boldsymbol{X}\hat{\boldsymbol{\theta}}_{\text{reg}})$

**return** SSE

## 4. Curve estimation and interpolation using B-splines and Hermite polynomials

This section introduces the modelling techniques applied for modelling non-linear effects to expand inputs and parameters into basis functions. Curve fitting using splines or polynomials is usually a problem of estimating coefficients to *basis functions*. The basis functions typically form a linear function space. The goal of the estimation is to find the element from this space, $\boldsymbol{x}$, that minimises some distance between $\boldsymbol{x}$ and the data points. This section shows how to model the solar radiation and the thermostatic valve function using B-splines and Hermite-polynomials expansion basis functions, respectively [34].

### 4.1. de Boor B-splines

Due to the properties of B-splines, they have proved useful in many data fitting applications [35–37]. de Boor B-splines [38] are defined on a finite interval $[a, b] \subseteq \mathbb{R}$ by a recursion formula via a set of control points $\Delta : a = t_0 \le t_1 \le \cdots \le t_{N_c} = b$ and a polynomial degree $k$. This uniquely defines a set of non-decreasing knot placements $a = z_0 \le z_1 \le \cdots \le z_{N_c+k+1} = b$, where the $i$'th B-spline of order $k$ is given by

$$B_{i,k} = \frac{z - z_i}{z_{i+k} - z_i} B_{i,k-1} + \frac{z_{i+k+1} - z}{z_{i+k+1} - z_{i+1}} B_{i+1,k-1}\,, \tag{11}$$

where $B_{i,0}(z) = \chi_{[z_i, z_{i+1}[}(z)$. Fig. 3(a) shows a set of six fourth order de Boor B-splines with equidistant control points $\Delta = (0, 1, 2, 3)$ on the domain $[0, 3]$. The estimation problem then comes down to estimating the scaling coefficients in a linear combination of basis B-splines to form the estimated function.

#### 4.1.1. Estimation of B-spline knot placements

In addition to the scaling coefficients, it is possible to optimise over the placements of the control points. One strategy to place the control points is to put them according to the quantiles of the data. This way, the control points are put according to the amount of data in the state space. This strategy, however, does not account for the amount of curvature of the true function. By freely optimising the control point placements, splines are able to "move closer" in parts of their domain where more fluctuating and fast-changing dynamics occur. Define the parameters $\boldsymbol{\tau} = \{\tau_k\}_{k=0}^{N_c-2}$ as the distances between interior knots $t_i$ and $t_{i+1}$ for $k = 0, \dots, N_c - 2$ (minus two comes from the last distance being uniquely given by the first $N_c - 1$ distances). Fig. 3(b) shows the de Boor B-splines as in Fig. 3(a), where now the control points are $\Delta = (0, 1/2, 1, 3)$. By moving the two central knots to the left in the domain, the "density" of the spline variation has also moved. This can be useful to capture large curvatures of the data.

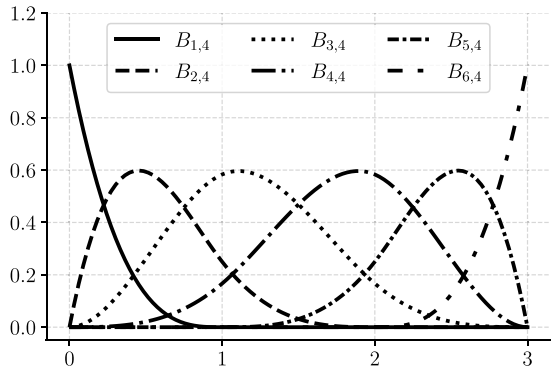


(a) Fourth order de Boor B-splines (that are piece-wise cubic polynomials) with control points $\Delta = (0, 1, 2, 3)$.

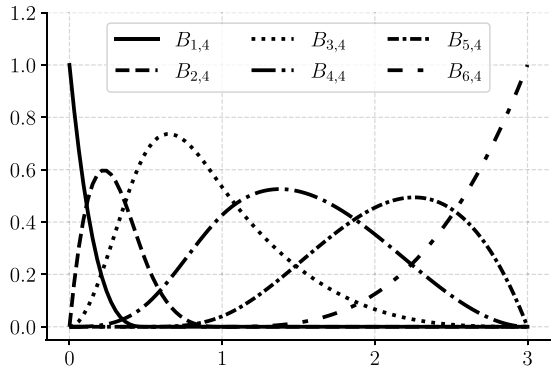


(b) Fourth order de Boor B-splines (that are piece-wise cubic polynomials) where the control points are shifted to $\Delta = (0, 1/2, 1, 3)$. This shifts the variations of the splines to the left.

**Fig. 3.** de Boor's B-splines with uniform and non-uniform knot placements.

### 4.2. Estimation of the solar gain using B-splines

The solar radiation is very fluctuating and is governed by seasonal, diurnal, and hourly variations [39]. It becomes even more complex when estimating the solar gain of a single room of a building since it depends much on the size and orientation of the window(s) of the room. It is very common to estimate models with a constant solar gain parameter e.g. on the form

$$\beta_1(\mathrm{B})I_t = \beta_{1,1}I_{t-1} + \beta_{1,2}I_{t-2} + \cdots + \beta_{1,M}I_{t-M}\,, \tag{12}$$

where $I_t$ is the global solar radiation (typically given by a third party source) at time $t$ and $\{\beta_{1,m}\}_{m=1}^{M}$ are time-independent parameters. As an example, imagine a room with a single window pointing toward east. In that case, solar radiation enters the room in the morning and disappears as the sun travels around south on the sky. The above model formulation (12) is not able to catch such variable gains. Instead, one can expand the coefficients in (12) in a basis formed by a linear combination of B-splines and define a transformed input variable by the expansion

$$x_{I,t} = h_I(I_t, t, \boldsymbol{\alpha}, \boldsymbol{\tau}) = (\alpha_1 B_1^{\boldsymbol{\tau}}(t) + \alpha_2 B_2^{\boldsymbol{\tau}}(t) + \cdots + \alpha_{N_c+k} B_{N_c+k}^{\boldsymbol{\tau}}(t))I_t\,, \tag{13}$$

where $B_n^{\boldsymbol{\tau}}(t)$ is the $n$'th B-spline basis function evaluated at time $t$ with given knot displacements $\boldsymbol{\tau}$. $\boldsymbol{\alpha} = \{\alpha_i\}_{i=1}^{N_c+k}$ is the associated basis spline coefficients. Here, $N_c$ is a tuning paratemeter set by the user. The model in (12) can thus be expanded to

$$\beta_1(\mathrm{B})x_{I,t} = \sum_{m=1}^{M} \beta_{1,m} h_I(I_{t-m}, t-m, \boldsymbol{\alpha}, \boldsymbol{\tau})\,. \tag{14}$$

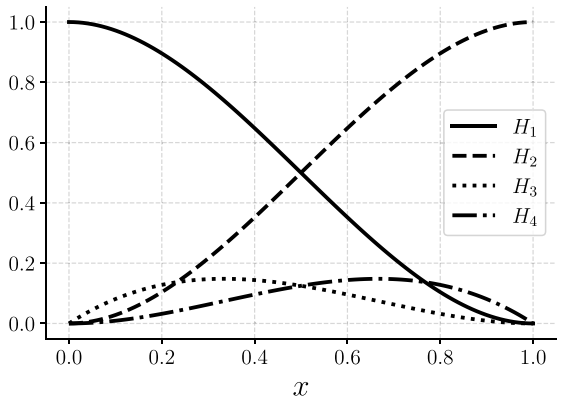


**Fig. 4.** The Hermite basis functions as given in Fritsch and Carlson [40] on the interval $[a, b] = [0, 1]$.

Given $\boldsymbol{\alpha}$ and $\boldsymbol{\tau}$, Eq. (14) is linear in the transformed regressors. Thus, $\boldsymbol{\alpha}$ and $\boldsymbol{\tau}$ belong to the parameters related to the transformed regressors $\boldsymbol{\theta}_{\mathrm{tr}}$, and $\{\beta_{1,m}\}_{m=1}^{M}$ are the regression coefficients.

### 4.3. Estimation of the thermostatic control function using Hermite polynomials

Thilker et al. [41] propose the following function to describe the valve state of a radiator as a function of the measured room temperature and the thermostat set-point $T_t^{\mathrm{set}}$,

$$f_t^{\mathrm{valve}} = \frac{1}{1 + \exp\left(-\alpha(T_t^{\mathrm{set}} + T_{\mathrm{offset}} - T_t^{\mathrm{i}})\right)}\,. \tag{15}$$

This simple model is characterised by two parameters $(\alpha, T_{\mathrm{offset}}) \in ]0, \infty[\times\mathbb{R}$ and has a relatively fixed shape that mimics the intuitive behaviour of thermostats: It acts as a PI-controller, which opens when it is too cold and closes when it is too warm (in a continuous way). The advantage of the model in Eq. (15) is its simplicity and few number of parameters. The disadvantage, however, is that the function's shape might be too restrictive to capture the actual room-specific behaviour. The thermostatic behaviour depends on many parameters such as room size, number of radiators, radiator placements etc. To simplify the complicated thermostatic modelling while keeping the function reasonably constrained, it is proposed to use a Hermite polynomial basis to fit a curve to the valve states as a function of indoor air temperature and the set-point.

In these settings, the estimation problem of the thermostatic valve function comes down to estimating coefficients in a basis expansion. But monotonicity in the solution is also required since it is natural to think that the valve opens monotonically as the relative temperature difference increases.

#### 4.3.1. Cubic interpolation with Hermite polynomials

Let the following be given: an interval $[a, b] \subset \mathbb{R}$, function values at the end points $(a, f(a))$ and $(b, f(b))$, and derivatives at the end points $f'(a)$ and $f'(b)$. Consider then the problem of finding a polynomial, $P$, of degree three with $P(a) = f(a), P'(a) = f'(a), P(b) = f(b), P'(b) = f'(b)$. A solution to this problem has the form [42]

$$P(x) = f(a)H_1(x) + f(b)H_2(x) + f'(a)H_3(x) + f'(b)H_4(x)\,, \tag{16}$$

where $H_i$ are the usual cubic Hermite basis functions (given in e.g. Fritsch and Carlson [40]; see Fig. 4).

Consider now the partition $\Delta : a = x_1 < x_2 < \cdots < x_{N_v} = b$ over the interval $[a, b]$ with associated function values and derivatives for all partition points. This forms an interpolating polynomial between each sub-interval $[x_i, x_{i+1}]$ by using the solution in (16). If one further constrain the function values $\{f_k\}_{k=1}^{N_v}$ to be monotonic increasing, $0 \leq$

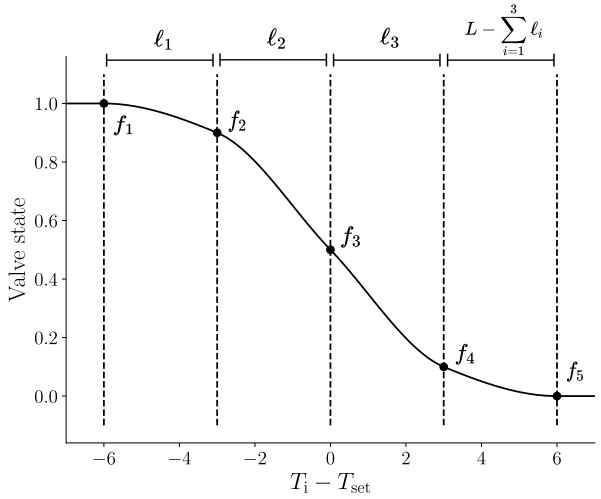


**Fig. 5.** An illustration of the expanded basis formed by piece-wise Hermite interpolations of the valve state function. Each interval of length $\ell_i$, $i = 1, \dots, N_v$, consists of cubic Hermite polynomials that interpolates the interval between function values. The Hermite polynomials have been modified to be monotonic between the function values, which makes the overall function monotonic due to the constraint $f_i \leq f_{i+1}$.

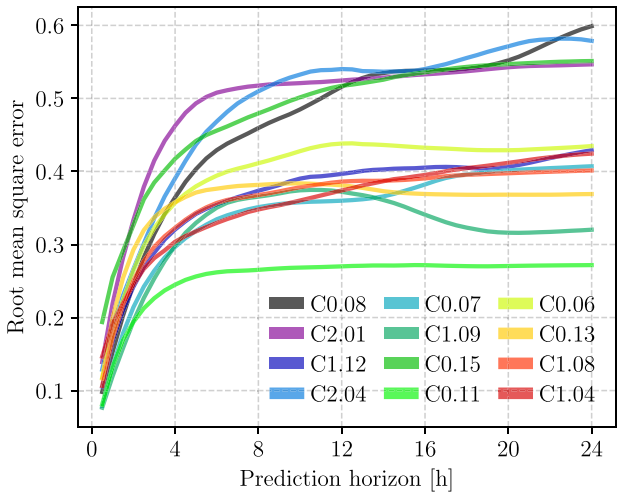


**Fig. 6.** The RMSE of the temperature predictions as a function of the prediction horizon for the rooms. Most rooms reaches a point where the RMSE becomes rather flat after 6–8 h. The performance of the individual model varies a bit: a cluster of rooms whose RMSE is significantly higher compared to the rest that constitute its own cluster.

$f_1 \leq f_2 \leq \cdots \leq f_{N_v} \leq 1$, a monotonic interpolation over the entire interval $[a, b]$ is guaranteed. [40] describes an algorithm for computing interpolating polynomials that are monotonic in each sub-interval. However, data is usually given simply by $(x_i, f(x_i))$, thus a procedure to compute the derivatives at each partition point is also needed. Algorithms for this also exists, see e.g. [40]. We can now optimise over the partition placements and the associated function values to estimate a monotonic increasing curve given by

$$\begin{aligned}\hat{P}(x) =& \hat{f}_i H_1(x) + \hat{f}_{i+1} H_2(x) + \hat{f}'_i H_3(x) + \hat{f}'_{i+1} H_4(x), \\ & x \in [x_i, x_{i+1}[\,.\end{aligned} \tag{17}$$

To perform the piece-wise cubic interpolation, i.e. compute $\hat{P}$ in (17), the authors use `PchipInterpolator` from the `SciPy` library in `Python`. To optimise over the partition points, the lengths of the sub-intervals by $\ell_i = x_{i+1} - x_i$ are defined as parameters. Fig. 5 depicts and illustrates the ideas of this estimation scheme. The parameters related to estimate the thermostatic valve function are $(\ell_1, \dots, \ell_{N_v-2}, f_2, \dots, f_{N_v-1})$ since the end points are fixed to $f_1 = 1$ and $f_{N_v-1} = 0$. The transformed regressors are

$$x_{\text{valve},t} = h_{\text{valve}}(T_{\text{set},t}, y_t, \boldsymbol{\ell}, \boldsymbol{f}) = P_{\boldsymbol{\ell},\boldsymbol{f}}(y_t - T_{\text{set},t})(T_{\text{for}} - y_t), \tag{18}$$

where $P_{\boldsymbol{\ell},\boldsymbol{f}}$ is given by (17), and the subscripts indicates the polynomial's dependence on the parameters. The term $(T_{\text{for}} - y_t)$ is the temperature difference between the supply (forward) water in the heating system of the building and the room air temperature. This term is then multiplied by "how open the valve in the radiator is". The regression model related to the heat input becomes

$$\beta_2(\mathrm{B}) x_{\text{valve},t} = \sum_{m=1}^{M} \beta_{2,m} h_{\text{valve}}(T_{\text{set},t-m}, y_{t-m}, \boldsymbol{\ell}, \boldsymbol{f}). \tag{19}$$

Again, given $\boldsymbol{\ell}$ and $\boldsymbol{f}$, Eq. (19) is linear in the transformed regressors. $\boldsymbol{\ell}$ and $\boldsymbol{f}$ then belongs to $\boldsymbol{\theta}_{\text{tr}}$ and $\{\beta_{2,m}\}_{m=1}^{M}$ are the regression coefficients.

## 5. Modelling results

This section presents and discusses the modelling results and quantifies their performance.

### 5.1. The final non-linear ARX model

Based on the previous section, the following ARX model describes the indoor air temperature, denoted $y_t$, based on inputs from the outdoor air temperature, solar radiation, and radiators

$$\begin{aligned}&\varphi(\mathrm{B}) Y_t = \beta_1(\mathrm{B}) x_{I,t} + \beta_2(\mathrm{B}) x_{\text{valve},t} + \beta_3(\mathrm{B})(T_{a,t} - Y_t) + \varepsilon_t, \\ \implies\ & Y_t = \sum_{m=1}^{M} -\varphi_m \mathrm{B}^m y_t + \sum_{m=1}^{M} \beta_{1,m} \mathrm{B}^m x_{I,t} \\ & \quad + \sum_{m=1}^{M} \beta_{2,m} \mathrm{B}^m x_{\text{valve},t} + \sum_{m=1}^{M} \beta_{3,m} \mathrm{B}^m (T_{a,t} - Y_t) + \varepsilon_t.\end{aligned} \tag{20}$$

The models are estimated using data sampled every 30 min. The authors found that the order $M = 3$ was optimal for almost all rooms based on information criterions such as AIC or BIC (one room model was optimal for $M = 2$).

### 5.2. The estimation problem

We write up the optimisation problem as outlined in Section 3.

$$\min_{\boldsymbol{\theta}_{\text{tr}}} \quad \sum_{i=1}^{N} \hat{\varepsilon}(\boldsymbol{\theta}_{\text{tr}})_i^2 \tag{21a}$$

$$\text{s.t.} \quad \boldsymbol{\theta}_{\text{tr}} = \left[\boldsymbol{\alpha}^\top, \boldsymbol{\tau}^\top, \boldsymbol{f}^\top, \boldsymbol{\ell}^\top\right]^\top \tag{21b}$$

$$\boldsymbol{A}\boldsymbol{\theta}_{\text{tr}} \leq \boldsymbol{b}, \tag{21c}$$

where the sum in (21a) is computed by Algorithm 1. The in-equality constraints $\boldsymbol{A}\boldsymbol{\theta}_{\text{tr}} \leq \boldsymbol{b}$ specifies potential constraints that might be needed on the parameters. For instance, the valve function values are required to be monotonically decreasing, $f_i \geq f_{i+1} \implies \begin{bmatrix}-1 & 1\end{bmatrix} \begin{bmatrix} f_i \\ f_{i+1} \end{bmatrix} \leq 0$. Small minimal distances between knot points in the B-spline and Hermite representations are also formulated as constraints. Keep in mind that the optimisation problem is not necessarily convex and thus a numerical solver may find local optimal solutions. However, the authors did not find that the solution was sensitive to variations in the initial condition.

### 5.3. Room air temperature model validation

Fig. 6 shows the RMSE of the individual room air models for each room as a function of the prediction horizon. For day-ahead predictions,

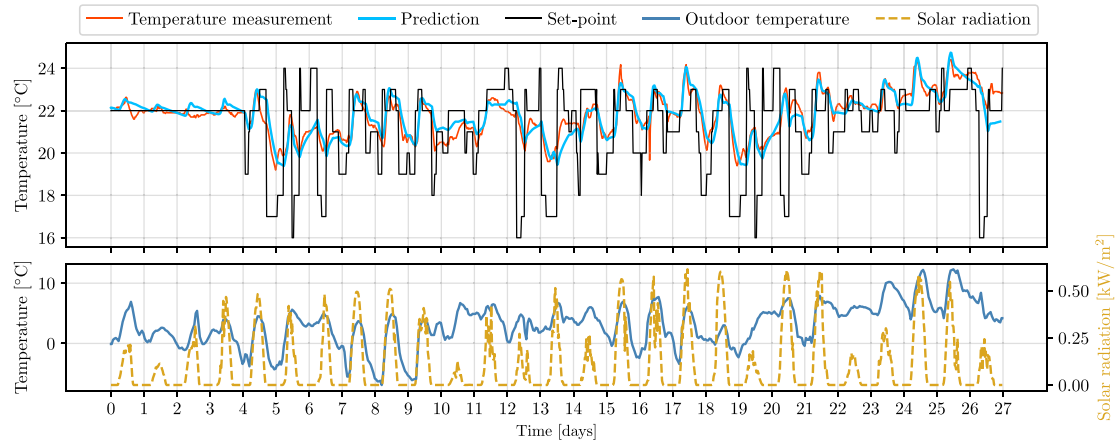


(a) Multi-step prediction given only the initial conditions and the inputs.

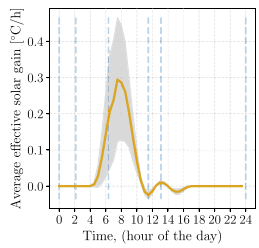


(b) Solar gain throughout the day. The vertical dashed lines indicates the placement of the knots.

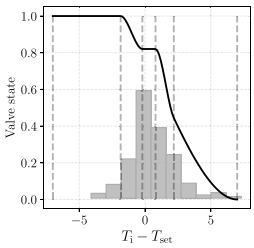


(c) Thermostatic valve function. The vertical dashed lines indicates the placement of the knots. The histogram shows the distribution of the data points.

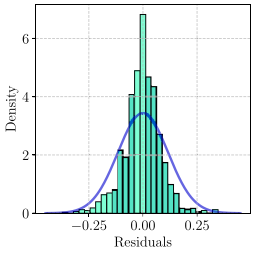


(d) Histogram of residuals and the associated Gaussian distribution.

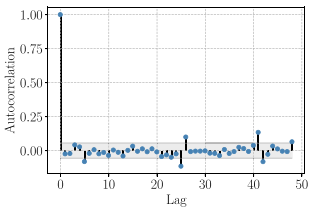


(e) Autocorrelation function of the one-step ahead residuals.

**Fig. 7.** Modelling results of room C0.06.

the rooms deliver an average RMSE of around 0.4° C with the highest being 0.6° C and the lowest being 0.25° C. Most rooms lie in the range of 0.25° C-0.45° C. However, four rooms seem to form a cluster that performs worse compared to the rest. This section investigates the resulting models of three of the rooms. The rest is omitted due to an otherwise large space use.

### 5.3.1. Room C0.06

Fig. 7 shows the results related to the model of room C0.06. To present an example of data and a model simulation to get an intuition of the forecasting abilities, Fig. 7(a) shows a multi-step simulation of the model for the room. Based on the first four days, where the set-point is constant, the model seems to catch the offset of the measured room temperature and the thermostat set-point well. Also, the model does a proper job at catching the exponential decay and increase, when the set-point is lowered or raised. However, there seems to be some more random dynamics where the model struggles; around day 10, the temperature drops much faster than predicted and around day 15/16, the temperature suddenly increases. These random dynamics may be due to occupancy. Lastly, it is also worth noting that the model seems to be ”stable” in time; it does not drift away from the measured trajectory.

Fig. 7(b) displays the estimated average solar gain during a day based on the estimated B-spline representation. The shape of the estimated curve is large during the morning hours and close to zero otherwise. This indicates that the sun has no influence in the afternoon, which is in line with the fact that the windows point toward east and only receives sun during the morning (see Fig. 2).

The estimated thermostatic valve function is displayed in Fig. 7(c). It suggests that the valve is almost fully open at 1°C above the set-point and closes fast below that point. Notice that the knots are centred around the data and where the estimated curvature is high.

Figs. 7(d) and 7(e) show the histogram and autocorrelation of the 1-step prediction residuals. The shape of the histogram is close to a Gaussian distribution, however its tails seem to be too wide. This could be due to a non-constant variance in either time or space. To model spacial variation in the error variance, a transformation might be suitable to mitigate this. For time-varying variance, using e.g. a variant of the generalised autoregressive conditional heteroskedasticity (GARCH) model may be used [43]. The autocorrelation function shows only a few small significant lags. These may be due to e.g. periodic occupant behaviour or some other dynamics that are not captured properly. However, the small magnitude of the significant lags indicates that the model captures the dynamics well overall.

### 5.3.2. Room C0.08

Fig. 8 shows the results related to the model of room C0.08. Fig. 8(a) shows a multi-step prediction of the model for the room. The dynamics for this room have spikes in the measured temperature. Looking at 8(b), it is immediately evident, that the estimated solar gain peaks in the afternoon. This also supports that the room windows point toward west and sees the sun in the evening. After proving the exact placement of the sensor in the room, it is found that the temperature sensor is placed such that it is hit by direct solar radiation. Hence, the measured air temperature does not fully reflect the actual room air temperature during the evening. However, the model still does a good job at catching these spikes. Looking at Fig. 6, C0.08 has a large RMSE which may arise from the difficulty of predicting the spikes. Nevertheless, the model overall seems to catch the temperature offset well together with the exponential decays/increases.

The estimated thermostatic valve function is displayed in Fig. 8(c). It suggests a more linear shape of the valve function compared to room C0.06 with a small flat step around 0. This shape may correspond more to the expected shape the valve state in an ideal thermostat [26]. Again the control points are placed around the largest parts of the density and where the largest estimated curvature is.

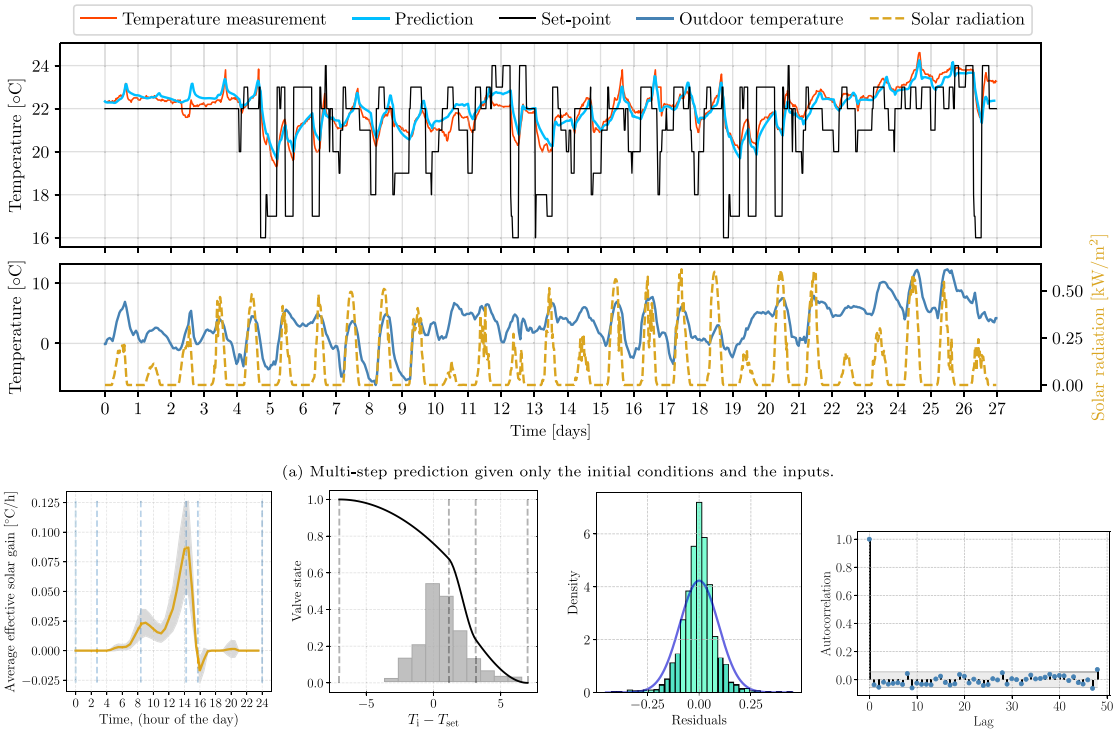


(a) Multi-step prediction given only the initial conditions and the inputs.




(b) Solar gain throughout the day. The vertical dashed lines indicates the placement of the knots.




(c) Thermostatic valve function. The vertical dashed lines indicates the placement of the knots. The histogram shows the distribution of the data points.




(d) Histogram of residuals and the associated Gaussian distribution.




(e) Autocorrelation function of the one-step ahead residuals.

**Fig. 8.** Modelling results of room C0.08.

Figs. 8(d) and 8(e) show the histogram and autocorrelation of the 1-step prediction residuals. Again, the shape of the histogram is close to a Gaussian distribution, but again the tails seem to widen the distribution too much. The autocorrelation function shows essentially no significant lags. The spikes in the temperature due to the solar radiation hitting seems to be captured quite well, since it could have shown in the autocorrelation if it was not the case. This implies that the model captures the dynamics well overall.

#### 5.3.3. Room C1.09

Fig. 9 presents the results from the model of room C1.09. Fig. 9(a) shows a multi-step prediction for the room. Again, based on the first four days, where the set-point is constant, the model seems to catch the offset of the measured room temperature and the thermostat set-point well. Also, the model does a good job at catching the exponential decay and increase, when the set-point is lowered or raised. C1.09 seems to be governed by less random dynamics compared to the other rooms, which makes the fit better (in terms of RMSE, see Fig. 6). The reason hereof is, first, that the room seems not to be occupied. Second, the magnitude of the estimated average solar gain in Fig. 9(b) is small. This small contribution of the solar radiation matches the fact that the room points toward north and less to none solar radiation enters during the day.

The estimated thermostatic valve function is displayed in Fig. 9(c). Its shape is simple and suggests that the valves close completely at 1 °C above the set-point and opens fast below that point. It could indicate that the room temperature reaction to the set-point is consistent.

Figs. 9(d) and 9(e) show the histogram and autocorrelation of the 1-step prediction residuals respectively. The shape of the histogram is more narrow compared to the other rooms (and again too large tails), and the autocorrelation function is insignificant. The good fit may again be due to the few disturbances and few random fluctuations in the room temperature.

### 5.4. Discussion and summary

The overall picture from the results is, that the models are very suitable for temperature predictions for many hours ahead. The RMSE indicates that the performance is on par or better compared to the state-of-the-art in the literature. And at the same time, their consistency in terms of RMSE emphasises the robustness of the identification. The indoor air temperature has significant diurnal variations, which are captured well. The solar radiation effect is successfully isolated by the model and is easily interpreted and is in alignment with physics. The estimated valve functions turned out being significantly different for each room, which confirms the need for room-specific air temperature models in general. A possibly significant effect neglected in the models presented in this paper, is the heat transmission between rooms. However, to model this effect requires all models to be estimated simultaneously, and to identify all neighbouring rooms. This is left for further studies. The flexibility of the valve function is visible from the results and captures what seems to be sudden changes in the dynamics. E.g. for room C1.09 where the valve closes fast when lowering the set-point below the measured temperature.

#### 5.4.1. Potential energy savings in optimal control

The presented ARX models do not have knowledge of the heat load of the individual rooms. This makes direct control of the heat usage infeasible. However, the second regression term in (20) describes the increase in air temperature caused by the radiators, $\sum_m \beta_{2,m} \mathrm{B}^m x_{\mathrm{valve},t}$. Therefore, instead of using the heat load in an objective function in an economic MPC, the air temperature increase as in (20) may be used instead. In such a setup, the room temperatures respond to a price signal instead of the heat load. But this produces the same result under the assumption that the air temperature increase and the heat load are significantly correlated. A possible optimal control problem for each

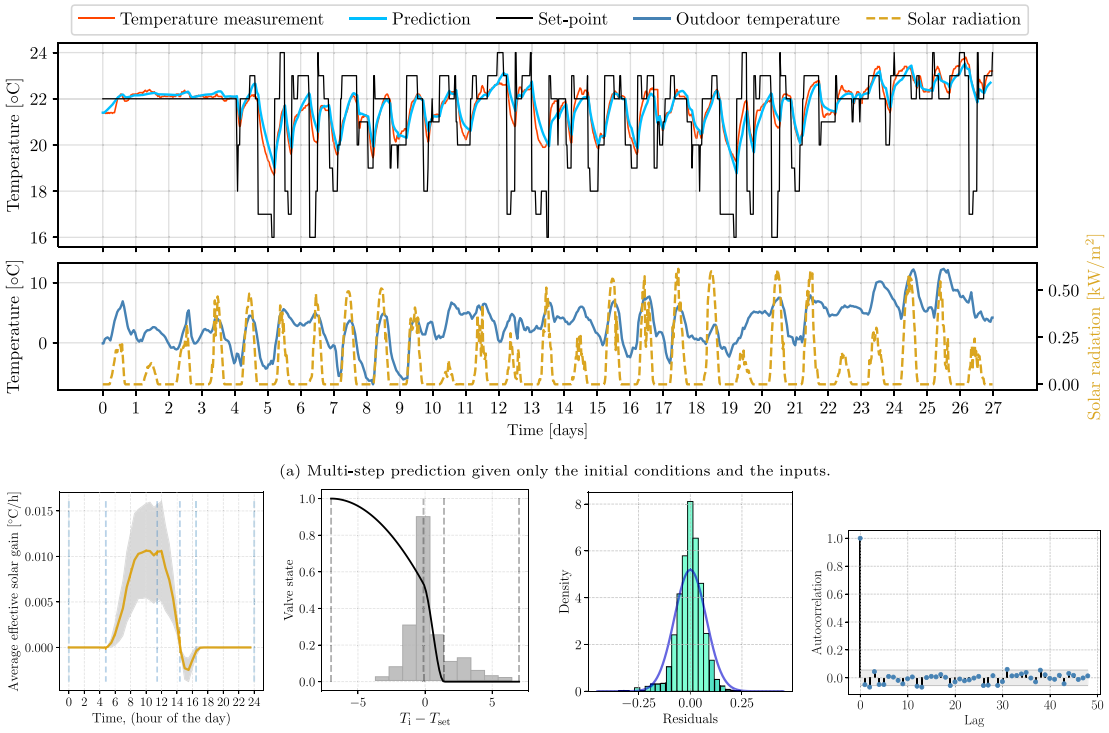


(a) Multi-step prediction given only the initial conditions and the inputs.




(b) Solar gain throughout the day. The vertical dashed lines indicates the placement of the knots.

(c) Thermostatic valve function. The vertical dashed lines indicates the placement of the knots. The histogram shows the distribution of the data points.

(d) Histogram of residuals and the associated Gaussian distribution.

(e) Autocorrelation function of the one-step ahead residuals.

**Fig. 9.** Modelling results of room C1.09.

room could look like the following

$$\min_{T_{\text{set},t+k}} \sum_{k=0}^{N-1} c_k \cdot x_{\text{valve},t+k} \tag{22a}$$

s.t. Eq. (20) (22b)

$$T_{\text{min},t+k+1} \leq \hat{Y}_{t+k+1} \leq T_{\text{max},t+k+1} \tag{22c}$$

where $c_k$ is a time-varying price signal, and $T_{\text{min},t+k+1}$ and $T_{\text{max},t+k+1}$ are upper and lower temperature bounds. In such a control setup, the price in the objective function, $c_k$, is related to the temperature increase in the room at time $t_k$, and not the heat usage. However, due to the presumably high correlation between the two variables, the optimal control sequences of the two problems may be highly correlated. Further work on this control strategy is needed to clarify its potential.

## 6. Conclusion and future work

This paper presented room air temperature models for individual rooms of a Danish school building, and identified non-linearities in the system arising from the time-varying solar gain and the heat input from the radiators. It is proposed to model the varying solar gain by a B-spline basis expansion and the thermostatic valve state using Hermite-polynomials that guarantees monotonicity of the function. The proposed ARX model for each room was consequently non-linear in the parameters, which required us to perform a two-stage identification procedure to estimate these parameters.

However, the individual room temperature models have no knowledge of the their individual heat usage, which is necessary for e.g. peak shaving or load shifting optimisation. To estimate and control the heat consumption, one needs a model of the entire building (since the heat consumption on building level is known). An interesting future work direction could be toward using the individual room models to predict the entire building heat load. With such a model, it is possible to enable flexible control of the building while considering each room's needs.

The individual room temperature models may also be used for fault detection and live diagnostics. For instance, to identify if a room responds slowly or not at all to a set-point increase. They can also be used to identify outliers in operations, to identify e.g. bad occupant behaviour or if a valve breaks etc. In an online monitoring and reporting setup, this may help alert building operators and identify what rooms to pay attention to in order to improve the indoor climate in the building and optimise operations.

## Declaration of competing interest

The authors declare that they have no known competing financial interests or personal relationships that could have appeared to influence the work reported in this paper.

## Acknowledgements

The authors received funding from the following projects; *Sustainable plus energy neighbourhoods (syn.ikia)* (H2020 No. 869918), FME-ZEN (Research Council of Norway - 257660), Top-up (Innovation Fund Denmark 9045-00017B), SCA+ (Interreg Öresund-Kattegat-Skagerrak) and *Flexibile Energy Denmark (FED)* (IFD 8090-00069B).

## References

[1] Fjernvarme D. Fakta om fjernvarme. 2020, URL https://www.danskfjernvarme.dk/presse/fakta-om-fjernvarme.

[2] Cali D, Kindler E, Ebrahimy R, Bacher P, Hu K, Østrup M, et al. climify.org: an online solution for easy control and monitoring of the indoor environment. Vol. 111, E D P Sciences; 2019, p. 05006. http://dx.doi.org/10.1051/e3sconf/201911105006, Clima 2019: 13th REHVA World Congress ; Conference date: 26-05-2019 Through 29-05-2019.

[3] Bacher P, Madsen H. Identifying suitable models for the heat dynamics of buildings. Energy Build 2011;43(7):1511–22. http://dx.doi.org/10.1016/j.enbuild.2011.02.005, URL https://www.sciencedirect.com/science/article/pii/S0378778811000491.

[4] Bacher P, Madsen H, Nielsen HA. Online short-term solar power forecasting. Sol Energy 2009;83(10):1772–83. http://dx.doi.org/10.1016/j.solener.2009.05.016, URL https://www.sciencedirect.com/science/article/pii/S0038092X09001364.

[5] Ríos-Moreno G, Trejo-Perea M, Castañeda-Miranda R, Hernández-Guzmán V, Herrera-Ruiz G. Modelling temperature in intelligent buildings by means of autoregressive models. Autom Constr 2007;16(5):713–22. http://dx.doi.org/10.1016/j.autcon.2006.11.003, URL https://www.sciencedirect.com/science/article/pii/S0926580506001208.

[6] Madsen H. Time series analysis. Chapman & Hall; 2007, http://dx.doi.org/10.1201/9781420059687.

[7] Bacher P, Madsen H, Nielsen H. Online short-term solar power forecasting. Sol Energy 2009;83(10):1772–83. http://dx.doi.org/10.1016/j.solener.2009.05.016.

[8] Durán MJ, Cros D, Riquelme J. Short-term wind power forecast based on ARX models. J Energy Eng 2007;133(3):172–80. http://dx.doi.org/10.1061/(ASCE)0733-9402(2007)133:3(172).

[9] Romero-Ugalde HM, Garnotel M, Doron M, Jallon P, Charpentier G, Franc S, et al. ARX model for interstitial glucose prediction during and after physical activities. Control Eng Pract 2019;90:321–30. http://dx.doi.org/10.1016/j.conengprac.2019.07.013, URL https://www.sciencedirect.com/science/article/pii/S0967066119301121.

[10] Mba L, Meukam P, Kemajou A. Application of artificial neural network for predicting hourly indoor air temperature and relative humidity in modern building in humid region. Energy Build 2016;121:32–42. http://dx.doi.org/10.1016/j.enbuild.2016.03.046, URL https://www.sciencedirect.com/science/article/pii/S0378778816302006.

[11] Thomas B, Soleimani-Mohseni M. Artificial neural network models for indoor temperature prediction: Investigations in two buildings. Neural Comput Appl 2007;16:81–9. http://dx.doi.org/10.1007/s00521-006-0047-9.

[12] Cui B, Fan C, Munk J, Mao N, Xiao F, Dong J, et al. A hybrid building thermal modeling approach for predicting temperatures in typical, detached, two-story houses. Appl Energy 2019;236:101–16. http://dx.doi.org/10.1016/j.apenergy.2018.11.077, URL https://www.sciencedirect.com/science/article/pii/S0306261918317938.

[13] Xu C, Chen H, Wang J, Guo Y, Yuan Y. Improving prediction performance for indoor temperature in public buildings based on a novel deep learning method. Build Environ 2019;148:128–35. http://dx.doi.org/10.1016/j.buildenv.2018.10.062, URL https://www.sciencedirect.com/science/article/pii/S0360132318306875.

[14] Elmaz F, Eyckerman R, Casteels W, Latré S, Hellinckx P. CNN-LSTM architecture for predictive indoor temperature modeling. Build Environ 2021;206:108327. http://dx.doi.org/10.1016/j.buildenv.2021.108327, URL https://www.sciencedirect.com/science/article/pii/S0360132321007241.

[15] Ferracuti F, Fonti A, Ciabattoni L, Pizzuti S, Arteconi A, Helsen L, et al. Data-driven models for short-term thermal behaviour prediction in real buildings. Appl Energy 2017;204:1375–87. http://dx.doi.org/10.1016/j.apenergy.2017.05.015, URL https://www.sciencedirect.com/science/article/pii/S0306261917305032.

[16] Delcroix B, Le Ny J, Bernier M, Azam M, Qu B, Venne J-S. Autoregressive neural networks with exogenous variables for indoor temperature prediction in buildings. Build Simul 2020;14. http://dx.doi.org/10.1007/s12273-019-0597-2.

[17] Sarwar R, Cho H, Cox SJ, Mago PJ, Luck R. Field validation study of a time and temperature indexed autoregressive with exogenous (ARX) model for building thermal load prediction. Energy 2017;119:483–96. http://dx.doi.org/10.1016/j.energy.2016.12.083, URL https://www.sciencedirect.com/science/article/pii/S0360544216318898.

[18] Yun K, Luck R, Mago PJ, Cho H. Building hourly thermal load prediction using an indexed ARX model. Energy Build 2012;54:225–33. http://dx.doi.org/10.1016/j.enbuild.2012.08.007, URL https://www.sciencedirect.com/science/article/pii/S0378778812003933.

[19] Scott A. The nonlinear universe. Berlin, Heidelberg: Springer; 2007.

[20] Andersen KK, Madsen H, Hansen LH. Modelling the heat dynamics of a building using stochastic differential equations. Energy Build 2000;31(1):13–24. http://dx.doi.org/10.1016/S0378-7788(98)00069-3, URL https://www.sciencedirect.com/science/article/pii/S0378778898000693.

[21] Andersen P, Jiménez M, Madsen H, Rode C. Characterization of heat dynamics of an arctic low-energy house with floor heating. Build Simul 2014;7(6):595–614. http://dx.doi.org/10.1007/s12273-014-0185-4.

[22] Zhang X, Ritosa K, Saelens D, Roels S. Comparing statistical modeling techniques for heat loss coefficient estimation using in-situ data. J Phys Conf Ser 2021;2069(1):012101. http://dx.doi.org/10.1088/1742-6596/2069/1/012101.

[23] Hollick FP, Gori V, Elwell CA. Thermal performance of occupied homes: A dynamic grey-box method accounting for solar gains. Energy Build 2020;208:109669. http://dx.doi.org/10.1016/j.enbuild.2019.109669, URL https://www.sciencedirect.com/science/article/pii/S0378778819314999.

[24] Csáky I, Kalmár F. Effects of solar radiation asymmetry on buildings' cooling energy needs. J Build Phys 2016;40(1):35–54. http://dx.doi.org/10.1177/1744259115597444.

[25] Chwieduk D, Bogdanska B. Some recommendations for inclinations and orientations of building elements under solar radiation in Polish conditions. Renew Energy 2004;29(9):1569–81. http://dx.doi.org/10.1016/j.renene.2003.12.018, URL https://www.sciencedirect.com/science/article/pii/S0960148104000096.

[26] Hansen LH. Stochastic modelling of central heating systems. (Ph.D. thesis), Technical University of Denmark; 1997, URL http://www2.imm.dtu.dk/pubdb/pubs/2460-full.html.

[27] Zou X, Jordan J, Shillor M. A dynamic model for a thermostat. J Eng Math 1999;291–310. http://dx.doi.org/10.1023/A:1004587425961.

[28] Hayashi S, Hayase T, Kurahashi T. Chaos in a hydraulic control valve. J Fluids Struct 1997;11(6):693–716. http://dx.doi.org/10.1006/jfls.1997.0096, URL https://www.sciencedirect.com/science/article/pii/S0889974697900967.

[29] Bruun CG. Optimization of building operation using high-resolution sensor data. (Master's thesis), Department of Civil Engineering: Technical University of Denmark; 2019, URL https://findit.dtu.dk/en/catalog/2448777767.

[30] Lex SW, Calí D, Koed Rasmussen M, Bacher P, Bachalarz M, Madsen H. A cross-disciplinary path to healthy and energy efficient buildings. Technol Forecast Soc Change 2019;142:273–84. http://dx.doi.org/10.1016/j.techfore.2018.07.023, URL https://www.sciencedirect.com/science/article/pii/S0040162518301999, Understanding Smart Cities: Innovation ecosystems, technological advancements, and societal challenges.

[31] Thilker CA, Madsen H, Jørgensen JB. Advanced forecasting and disturbance modelling for model predictive control of smart energy systems. Appl Energy 2021;292:116889. http://dx.doi.org/10.1016/j.apenergy.2021.116889, URL https://www.sciencedirect.com/science/article/pii/S0306261921003755.

[32] Li X, Wen J. Review of building energy modeling for control and operation. Renew Sustain Energy Rev 2014;37:517–37. http://dx.doi.org/10.1016/j.rser.2014.05.056, URL https://www.sciencedirect.com/science/article/pii/S1364032114003815.

[33] Rasmussen C, Frölke L, Bacher P, Madsen H, Rode C. Semi-parametric modelling of sun position dependent solar gain using B-splines in grey-box models. Sol Energy 2020;195:249–58. http://dx.doi.org/10.1016/j.solener.2019.11.023, URL https://www.sciencedirect.com/science/article/pii/S0038092X19311235.

[34] Christensen O. Functions, spaces, and expansions. Birkhauser Basel; 2010, http://dx.doi.org/10.1007/978-0-8176-4980-7.

[35] Bruce PD, Kellett MG. Modelling and identification of non-linear aerodynamic functions using B-splines. Proc Inst Mech Eng G 2000;214(1):27–40. http://dx.doi.org/10.1243/0954410001531890.

[36] Meyer K. Random regression analyses using B-splines to model growth of Australian angus cattle. Genet Select Evol 2005;37. http://dx.doi.org/10.1186/1297-9686-37-6-473.

[37] Sekhar Roy S, Roy R, Balas VE. Estimating heating load in buildings using multivariate adaptive regression splines, extreme learning machine, a hybrid model of MARS and ELM. Renew Sustain Energy Rev 2018;82:4256–68. http://dx.doi.org/10.1016/j.rser.2017.05.249, URL https://www.sciencedirect.com/science/article/pii/S1364032117308961.

[38] de Boor C. On calculating with B-splines. J Approx Theory 1972;6(1):50–62. http://dx.doi.org/10.1016/0021-9045(72)90080-9, URL https://www.sciencedirect.com/science/article/pii/0021904572900809.

[39] Thilker CA, Junker RG, Bacher P, Jørgensen JB, Madsen H. Model predictive control based on stochastic grey-box models. In: Ploix S, Amayri M, Bouguila N, editors. Towards energy smart homes: algorithms, technologies, and applications. Cham: Springer International Publishing; 2021, p. 329–80. http://dx.doi.org/10.1007/978-3-030-76477-7_11.

[40] Fritsch FN, Carlson RE. Monotone piecewise cubic interpolation. SIAM J Numer Anal 1980;17(2):238–46, URL http://www.jstor.org/stable/2156610.

[41] Thilker CA, Bacher P, Bergsteinsson HG, Junker RG, Cali D, Madsen H. Non-linear grey-box modelling for heat dynamics of buildings. Energy Build 2021;252:111457. http://dx.doi.org/10.1016/j.enbuild.2021.111457, URL https://www.sciencedirect.com/science/article/pii/S0378778821007416.

[42] Burden RL, Faires JD. Numerical analysis. Boston, USA: Cengage Learning; 1989.

[43] Lamoureux CG, Lastrapes WD. Persistence in variance, structural change, and the GARCH model. J Bus Econom Statist 1990;8(2):225–34. http://dx.doi.org/10.1080/07350015.1990.10509794, URL https://www.tandfonline.com/doi/abs/10.1080/07350015.1990.10509794.

# E Advanced forecasting and disturbance modelling for model predictive control of smart energy systems

Applied Energy 292 (2021) 116889

Contents lists available at ScienceDirect

Applied Energy

journal homepage: www.elsevier.com/locate/apenergy

# Advanced forecasting and disturbance modelling for model predictive control of smart energy systems

Christian Ankerstjerne Thilker *, Henrik Madsen, John Bagterp Jørgensen

*Technical University of Denmark, Department of Applied Mathematics and Computer Science, Asmussens Allé, Building 303B, DK-2800 Kgs. Lyngby, Denmark*

## GRAPHICAL ABSTRACT

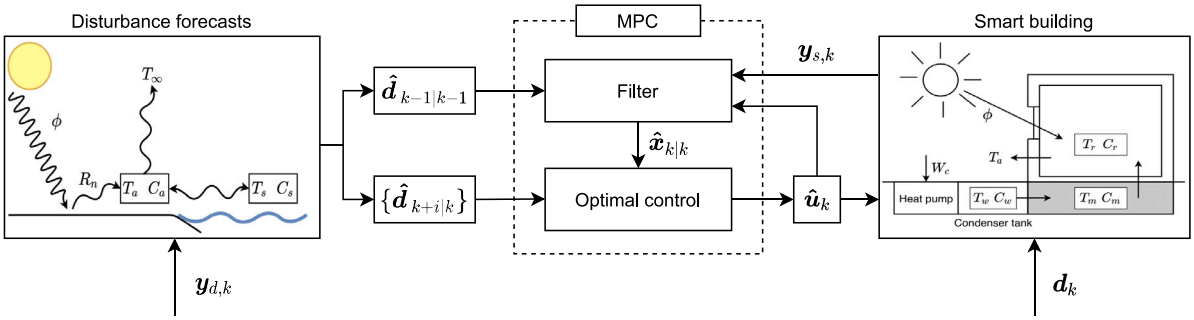


## ARTICLE INFO

*Keywords:*
Model predictive control
Stochastic differential equations
Disturbance models
Smart energy systems

## ABSTRACT

We describe a method for embedding advanced weather disturbance models in model predictive control (MPC) of energy consumption and climate management in buildings. The performance of certainty-equivalent controllers such as conventional MPC for smart energy systems depends critically on accurate disturbance forecasts. Commonly, meteorological forecasts are used to supply weather predictions. However, these are generally not well suited for short-term forecasts. We show that an advanced physical and statistical description of the disturbances can provide useful short-term disturbance forecasts. We investigate the case of controlling the indoor air temperature of a simulated building using stochastic differential equations (SDEs) and certainty-equivalent MPC using the novel short-term forecasting method. A Lamperti transformation of the data and the models is an important contribution in making this SDE-based approach work. Simulation-based studies suggest that significant improvements are available for the performance of certainty-equivalent MPC based on short-term forecasts generated by the advanced disturbance model: Electricity savings of 5%–10% while at the same time improving the indoor climate by reducing comfort violations by up to over 90%.

## 1. Introduction

It is a well known fact that the energy consumption from buildings is high. On a global scale it is estimated that buildings consume more than 30% of the total consumed energy, and in Europe it is estimated to be more than 40% [1]. The high energy consumption creates a significant potential for energy savings by optimising the use of energy for heating and cooling in buildings, without compromising the quality of the indoor climate. Given the many opportunities of model-based control and optimisation of energy consumption in buildings, a vast body of research is available that describes the algorithms [2–5]. MPC has gained much success within many applications due to its simplicity, intuitive use, ability to handle multivariate and constrained systems, and the availability of algorithms and software for embedded as well as cloud computing [6]. However, most of this literature assumes

* Corresponding author.
*E-mail addresses:* chant@dtu.dk (C.A. Thilker), hmad@dtu.dk (H. Madsen), jbjo@dtu.dk (J.B. Jørgensen).

https://doi.org/10.1016/j.apenergy.2021.116889
Received 29 December 2020; Received in revised form 25 March 2021; Accepted 26 March 2021
Available online 8 April 2021

that the system and disturbance models are perfect or use computationally complicated algorithms, e.g. stochastic or robust MPC, to handle uncertainties in these models. The main novelty in the present paper is a nonlinear disturbance model based on stochastic differential equations (SDEs) for embedded short-term forecasting in certainty-equivalent model predictive control (MPC) algorithms for energy and climate control in buildings. The proposed disturbance model is based on SDEs and forecasts the solar radiation and ambient air temperature. The model combines physical description of the climatic processes together with more statistical data-driven models. Beside providing accurate short-term forecasts, the model also has the advantage that it fits naturally into the MPC model framework, which is also based on SDEs.

Much research suggest that SDEs are very competitive models for modelling dynamical and physical phenomena. They also inherently describe the distributions and uncertainties of processes by e.g. solving the Kolmogorov-equations. Knowledge about the uncertainty can be useful for sensitive systems that need extra operational care. SDEs have extensive applications in finance to model e.g. interest rates, security markets and yields [7]. They are also successfully applied in the area of probabilistic power production. Multiple complexity-varying SDE-models for wind power generation forecasts have been introduced and applied [8]. Furthermore, models for forecasting wind speed up to 24 h ahead using SDEs have been proposed [9]. Recent research also indicates that SDEs are well suited for probabilistic solar radiation forecasting [10,11], where first order systems proves to be sufficient. However, such models relies centrally on external long-term forecasts from supplied by external sources. Using the external forecasts, the models in turn supplies probabilistic forecasts. The model proposed here relies purely on local observations and is independent of external parties.

### 1.1. Literature review

The inclusion of weather forecasts for building climate control has been investigated on multiple occasions in the literature [12–18]. In general, the predictive control schemes outperform non-predictive control forms, such as rule-based-and PID-control, due to their ability to consider future disturbances. The solar radiation is an important disturbance in rooms that are considered for temperature control [12]. The fluctuating dynamics of solar radiation and the large amount of energy it delivers, complicates the indoor temperature control in buildings with windows. These complications and uncomfortable overheating can in many cases be avoided or minimised by accounting for the prevalent solar radiation using simple transfer function or regression-based models [12,13]. MPC for buildings using models for weather forecasts reports to significantly reduce energy consumption and increase indoor comfort [14], increase flexibility indicators [15–17] present thorough reviews and recent applications of MPC for building climate control systems based on meteorological weather forecasts. Here, many studies consider perfect forecasts or simple sinusoidal simulations and do not take uncertainties into account. Using stochastic MPC to overcome uncertainties in the weather predictions for temperature regulation in integrated room automation, significant potential energy savings compared to rule-based control are reported [18]. Such simulation results also suggest that stochastic MPC is superior to conventional MPC for this kind of task due to its ability to account for uncertainties in forecasts. However, it remains an open questions whether these differences could be mitigated by tuning or by using better forecasts. In particular, the critical importance of also including local weather measurements for predictive control operations of modern building climate control systems has been noticed [19–22]. An example is to quantify the errors of the supplied meteorological weather forecast. These errors can be used to improve predictions of the heat load and enables better control performance [19]. More complex models based on neural networks has also been developed and applied for building climate control [15,20]. Results suggest that such models offer good accuracy but lacks the ability to generalise to arbitrary prediction lengths or different setups [21]. Comparisons between neural networks and simple time series models have also been carried out. Results are not one-sided as evidence of both linear time series methods and complex neural networks perform better than the other [23,24]. However, it is pointed out the potential performance gain of using such complex methods does not appear to outweigh the additional development and data acquisition efforts [22].

It is also common in the literature to use offset-free control [25–28]. Such approaches have the advantage that they can integrate out a constant unknown contribution of the disturbance and thereby achieve offset-free control [29]. However, the disturbances are not modelled and the integration has poor forecasting abilities for fast-changing disturbances such as the weather.

The conclusion from the literature is that weather predictions in MPC offer significant potential energy savings and comfort improvement. In general, two categories of weather forecasting methods for MPC arise. The first category consists of cases that use meteorological weather forecasts. In the second category, models are developed to forecast disturbances. Here, the dominating standard is to use black-box related models that have no physical relation such as regression-based or neural network models.

### 1.2. Main aim and organisation of the paper

The main aim of this paper is to introduce a general method for embedding forecasts and disturbance models in model-based control. We model the local weather disturbances using advanced models based on SDEs that includes physical descriptions of the climatic processes. Using these advanced forecasts in certainty equivalent MPC simulated for multiple smart building models, this paper suggests that increased performance of building climate control is available. We compare the advanced forecasts to offset-free control, a standard method for dealing with uncertainty in MPC [17,30], and to controllers using perfect forecasts.

In Section 2 we introduce the mathematical notation and system framework. Section 3 proposes the continuous-time stochastic disturbance models. Section 4 introduces the MPC framework and how to incorporate the forecasts. Section 5 analyses the dynamics of the smart buildings considered in this paper. In Section 6 we present and discuss the simulation-based results, while the conclusion are provided in Section 7.

## 2. Stochastic differential equations and the smart building model

In general, we seek a combined model for the smart building that includes a description of the disturbances. That is, we consider stochastic differential equation (SDE) models, sometimes called grey-box models, in the form

$$\mathrm{d}\boldsymbol{x}(t) = f_s(\boldsymbol{x}(t), \boldsymbol{u}(t), \boldsymbol{d}(t))\mathrm{d}t + g_s(\boldsymbol{x}(t), \boldsymbol{u}(t), \boldsymbol{d}(t))\mathrm{d}\boldsymbol{\omega}_s(t)\,, \tag{1a}$$

$$\mathrm{d}\boldsymbol{d}(t) = f_d(\boldsymbol{d}(t))\mathrm{d}t + g_d(\boldsymbol{d}(t))\mathrm{d}\boldsymbol{\omega}_d(t)\,, \tag{1b}$$

$$\boldsymbol{y}_s(t_k) = h_s(\boldsymbol{x}(t_k)) + \boldsymbol{v}_{s,k}\,, \tag{1c}$$

$$\boldsymbol{y}_d(t_k) = h_d(\boldsymbol{d}(t_k)) + \boldsymbol{v}_{d,k}\,, \tag{1d}$$

where $\boldsymbol{x}$, $\boldsymbol{u}$, $\boldsymbol{d}$ are the smart building system states, the input and the disturbances respectively. $f_s$ and $f_d$ are the drift functions and $g_s$ and $g_d$ are the diffusion functions for the smart building system and disturbances. $\boldsymbol{\omega}_s(t)$ and $\boldsymbol{\omega}_d(t)$ are standard Brownian motions and $\boldsymbol{v}_{s,k} \sim N(\boldsymbol{0}, R_s)$ and $\boldsymbol{v}_{d,k} \sim N(\boldsymbol{0}, R_d)$ are the observation noises. Notice the causality between the system model and the disturbance model.

The combined structure in (1) differs from the literature, where the dominating standard is to employ meteorological forecasts as described in Section 1.1 (i.e. no disturbance model). Offset-free control [30,31]

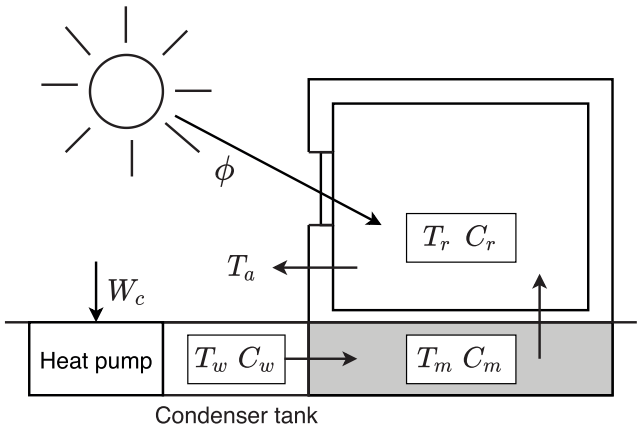


**Fig. 1.** An illustration of the smart building components and their interactions. The arrows indicate the positive direction of the heat flows.

is another method for dealing with non-modelled disturbances, also frequently used in the literature for smart energy systems [25–27]. The idea is to replace (1b) with an integrating state, $\mathrm{d}\boldsymbol{\eta}(t) = B_d \mathrm{d}\boldsymbol{\omega}_\eta(t)$, that integrates and estimates the disturbances. This is limiting in two ways, however. First, the number of integrating states cannot exceed the number of independently observed system states – the system otherwise becomes unobservable. Second, the forecasts supplied by the integrators correspond to persistent forecasts, $\hat{\boldsymbol{d}}(t) = \hat{\boldsymbol{d}}(t_k)$, $t \geq t_k$.

We shall further assume that $f_s$ and $g_s$ in (1a) for the smart buildings are linear, and that $g_s$ is state-independent, i.e. we consider a linear model on the form

$$f_s(\boldsymbol{x}(t), \boldsymbol{u}(t), \boldsymbol{d}(t)) = A_c \boldsymbol{x}(t) + B_c \boldsymbol{u}(t) + E_c \boldsymbol{d}(t)\,, \tag{2a}$$

$$g_s(\boldsymbol{x}(t), \boldsymbol{u}(t), \boldsymbol{d}(t)) = G_c\,, \tag{2b}$$

where $A_c$, $B_c$, $E_c$ and $G_c$ are the continuous-time state evolution, input, disturbance and diffusion matrices.

### 2.1. Smart building model

The rest of this section introduces the components of the smart building model in (1a) and (2a).

#### 2.1.1. System states

This paper considers a model of the heat dynamics of a building based on Andersen et al. [32] and Halvgaard et al. [2]. Fig. 1 shows an illustration of the smart building model components and its heat flows. The smart building model thus considers three system states: the room air temperature, $T_r$, the floor temperature, $T_f$, and the water temperature, $T_w$. The smart building model states thus become

$$\boldsymbol{x}(t) = \left[T_r(t), T_f(t), T_w(t)\right]^T\,. \tag{3}$$

We usually observe only the room air temperature, i.e. the floor and water temperatures are *hidden states*. Furthermore, the observation equation in (1c) is linear, $h_s(\boldsymbol{x}(t_k)) = C\boldsymbol{x}(t_k)$, with $C = [1, 0, 0]^T$.

#### 2.1.2. Inputs

The manipulative variable for the smart building model in [2] is simply the input power (in Watt) given to the compressor of the heat pump, $W_{hp}$, that is

$$u(t) = W_{hp}(t)\,. \tag{4}$$

As we will show, the smart building model equipped with a heat pump is governed by slow heating dynamics. A simpler model that uses electrical heaters where the heat enters the room air directly makes the room air respond to heat inputs much faster. In the results section, we compare smart building models that use different heating strategies where we combine electrical heaters and heat pumps as well as electrical coolers (e.g. an air conditioner). The heat pump, though, is more efficient (a factor 3) compared to the faster heating devices, making it an attractive heating strategy. We shall compare the following heating strategies

$$u_1(t) = W_{eh}(t)\,, \tag{5a}$$

$$u_2(t) = W_{hp}(t)\,, \tag{5b}$$

$$\boldsymbol{u}_3(t) = \left[W_{hp}(t), W_{eh}(t)\right]^T\,, \tag{5c}$$

$$\boldsymbol{u}_4(t) = \left[W_{hp}(t), W_{eh}(t), W_{ec}(t)\right]^T\,, \tag{5d}$$

where $W_{eh}$ is the input to electrical heaters and $W_{ec}$ is the input to the electrical coolers. We assume that the heat from both the electrical heaters and coolers enters the room air directly and that they do not accumulate any heat themselves. We disregard the third system state, $T_w$, for the building model that only considers electrical heaters, $u_1(t) = W_{eh}(t)$.

### 2.2. Disturbances

As extensively reported by the literature [12,18,33], the important disturbances acting on a building are the solar radiation, $\phi$, and the ambient air temperature, $T_a$. The ambient air temperature affects the indoor air temperature through the walls and windows. The solar radiation affects the indoor air temperature by passing through the windows and heating either the room air or floor and furniture. For building climate control, the literature considers the solar radiation the most influential disturbance for short-term purposes. This is due to the large amount of energy it delivers and its considerably fast dynamics. For smart buildings with photo-voltaic cells (PVs), the solar radiation also determines the availability of harvested electricity. We shall not consider this case. Thus, the important weather disturbance states in (1) are

$$\boldsymbol{d}(t) = \left[T_a(t), \phi(t)\right]^T\,. \tag{6}$$

$T_a(t)$ is the ambient air temperature and $\phi(t)$ is the solar radiation on a horizontal surface.

## 3. Disturbance modelling and forecasting

This section establishes the non-linear dynamical model for the disturbances in (1b).

The behaviour of the weather in Denmark varies throughout the year. Hence, in-homogeneous- or regime models for the weather are required in the general case. To model breaks or sudden shifts in the dynamics, often seen in finance [34], jump–diffusion processes can be suitable. See Bemporad et al. [35] for an introduction to a framework for fitting such models. To deal with this, we focus our attention on March and assume that the weather behaviour is constant during this month. In Denmark, March can be both warm and cold and typically with much sun and is therefore an interesting month to consider.

### 3.1. The data

To formulate, identify and validate the statistical weather models used in this paper, we use data from two weather stations located in Værløse and Taastrup in Denmark. [36] thoroughly presents and discusses the data gathering process and setup. The data are gathered every hour for 7 consecutive years from February 1st 1967 through December 31st 1973. Table 1 gives a description of the weather elements of the data, how they are observed, and the observation frequency.

**Table 1**
Facts about the data and how it is measured. The cloud cover unit, okta, is defined according to [37] - okta equal to zero is completely clear skies and okta equal to eight is completely overcast.

| Attribute | Notation | Unit | Measurement method |
|---|---|---|---|
| Cloud cover | $\kappa$ | okta | Measured once every hour |
| Diffuse radiation | $I_D$ | W/m$^2$ | Average of 6 independent observations during an hour |
| Direct radiation | $I_N$ | W/m$^2$ | Average of 6 independent observations during an hour |
| Net radiation | $R_n$ | W/m$^2$ | Average of 6 independent observations during an hour |
| Ambient air temperature | $T_a$ | °C | Average of 6 independent observations during an hour |

### 3.2. Weather model components

The weather disturbance model consists of 4 components:

- Cloud cover
- Global solar radiation
- Net radiation
- Ambient air temperature

The parameters for these model are available in [38] that develops, presents and discusses these models in detail. The rest of the section explains each weather model component and its importance regarding building climate control.

#### 3.2.1. Cloud cover

Important factors governing the energy levels and balances at the surface of the Earth are significantly affected by the amount of cloud cover. Global solar radiation is one such important example. The variations in global solar radiation are primarily due to absorption and reflection of energy by clouds. Other mechanisms such as the amount of water vapour, ozone, dust etc. also play a role. However, it is well known that cloud cover plays the absolute most important role.

Due to the discrete cloud cover data, [39] and [40] show that a discrete state–space Markov model is sufficient for modelling the cloud cover, and furthermore that a homogeneous model could be suitable. However, since we formulate the rest of the disturbance models as continuous state–space models it is mathematically more convenient and consistent to choose an SDE-representation that fits into the framework of (1). We choose a non-linear, mean-reversion process of the form

$$\mathrm{d}\kappa(t) = \overbrace{\theta(\kappa(t))\,(\mu(\kappa(t)) - \kappa(t))\,\mathrm{d}t}^{\text{drift}} + \underbrace{\sigma\kappa(t)(1-\kappa(t))d\omega_\kappa(t)}_{\text{diffusion}}, \tag{7a}$$

where

$$\mu(\kappa(t)) = \frac{\exp(P_n(\kappa(t)))}{1+\exp(P_n(\kappa(t)))}, \tag{7b}$$

$$\theta(\kappa(t)) = \tilde{\theta}\sqrt{\kappa(t)(1-\kappa(t))}. \tag{7c}$$

$\kappa$ is the cloud cover state and $P_n(\cdot)$ is the linear combination of Legendre polynomials till order $n = 7$. The mathematical structure of the drift allows the model to have multiple stationary points.

The term $\sigma\kappa(t)(1-\kappa(t))$ ensures that the diffusion goes to zero in both ends of the support and requires a transformation of the cloud cover state into the state–space $[0, 1]$. Thilker [38] describes how to choose this transformation. The diffusion term $\sigma\kappa(t)(1-\kappa(t))$ is dependent on the system state. Some of the difficulties and problems that are linked with a state-dependent diffusion term are [11,41,42]:

- *Predictions* can be wrong/illegal if they go outside of the domain of the process. This can happen due to the linearisation in the continuous-discrete extended Kalman filter (CDEKF) and the numerical implementation of the differential equation solver. To apply filtering techniques in practice, a state-independent SDE is much more robust.
- *Simulation* of the process has slower convergence rate (e.g. using the Euler–Maruyama scheme) compared to a state-independent diffusion process.

To overcome these problems, the *Lamperti transformation* offers a bijective transformation of the process into a *constant diffusion* process that lives in the domain of the entire real line, $\psi : [0,1] \to \mathbb{R}$. Let $Z_\kappa(t) = \psi(\kappa(t))$, then the Lamperti-transformed process has the simple form

$$\mathrm{d}Z_\kappa(t) = f_\psi(Z_\kappa(t))\mathrm{d}t + \sigma_\psi \mathrm{d}\omega_\kappa(t), \tag{8}$$

where $f_\psi$ is the drift function in the Lamperti domain. For an introduction to the Lamperti transformation, see e.g. [41]. In (8), the noise process is Gaussian, which makes computations such as e.g. confidence intervals easy. Estimation, prediction and simulation take place in the Lamperti domain and are subsequently transformed back into the original cloud cover domain, $\psi^{-1} : \mathbb{R} \to [0,1]$. We estimate the parameters in (7) by means of the maximum likelihood method using the CDEKF [43,44]. The program CTSM-R is used to conduct these computations of the parameter estimates [45]. Also, automatic Lamperti transformation is being integrated into CTSM-R.

#### 3.2.2. Global solar radiation

The term global solar radiation covers all the short-wave radiation coming from the sun and hitting the surface of the Earth. The global radiation is typically split into two contributions; the direct, $I_N$, and diffuse, $I_D$, radiation. The direct radiation is all the short-wave radiation coming from the sun without hitting anything on its way. The diffuse radiation, in contrast, is all the reflected short wave radiation, e.g. from objects like dust, water vapour etc. in the atmosphere. The global solar radiation is simply the total radiation (on a horizontal plane),

$$\phi(t) = I_N(t)\sin\alpha(t) + I_D(t). \tag{9}$$

To model the global solar radiation, $\phi$, this paper performs non-parametric local linear regression as a function of the solar height, $\alpha(t)$, and the cloud cover okta. The estimator is then the solution to the following weighed least squares problem

$$\underset{\phi,\beta}{\operatorname{argmin}} \sum_{i=1}^{N} K_h(\alpha_i, \alpha_0)\left[y_i - \phi - \beta(\alpha_0 - \alpha_i)\right]^2, \tag{10}$$

where $\phi$ is the estimator, $\alpha_0$ is the given solar height and $K_h(\cdot,\cdot)$ is the Gaussian kernel function acting as the weights. We employ leave-one-out cross validation for selection of the band width, $h$. [38] also estimates a variance and auto correlation structure for the model in (10).

#### 3.2.3. Net radiation

It is well known that the so-called net radiation is necessary to predict the ambient air temperature. The net radiation is the net input of both short- and long-wave radiation at Earth's surface and is the main source of thermal energy to the ambient air. [46,47] explains this in more detail and also show that a static model is sufficient. [48] suggests

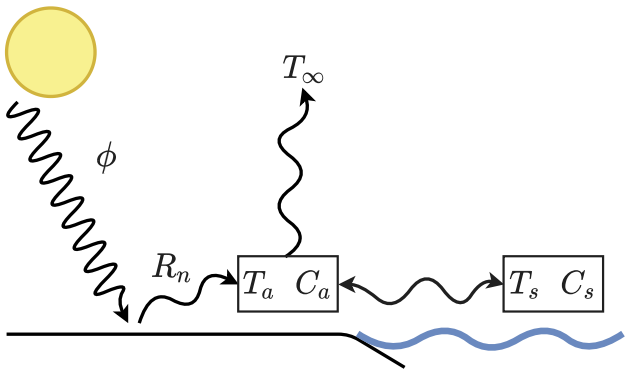


**Fig. 2.** An illustration of the dynamical model in (12). Each box represents a state given by a temperature and heat capacity. The arrows indicate the direction in which the energy is transferred.

a simple linear model that depends on the cloud cover, solar radiation and solar height

$$R_n(\kappa(t), \phi(t), t) = K_\kappa + k_\kappa \phi(t) + k\alpha(t)^2 + \epsilon(t)\,. \tag{11}$$

The subscript $\kappa$ in $K_\kappa$ and $k_\kappa$ indicates the parameters' dependence on the cloud cover. That is one parameter for each cloud cover okta, $\kappa$.

#### 3.2.4. Ambient air temperature

[49] describes and explains the fundamental relationships of surface fluxes and the relationship between the net radiation and the ambient air temperature. Briefly explained, the net radiation heats the surface soil, which in turn heats up the ambient air near the surface. The time lag between the net radiation and the ambient air temperature requires a dynamical model and is well approximated by a simple second-order model Thilker et al. [50]. It is well known that larger annual temperature differences happen in the middle of large continents. However, for countries surrounded by sea, the sea highly regulates the land temperature due to the large heat capacity of water. Fig. 2 illustrates this model that has the mathematical SDE representation [49]

$$C_s \mathrm{d}T_s(t) = \left(\frac{1}{R_{sa}}(T_a(t) - T_s(t))\right)\mathrm{d}t + \sigma_s \mathrm{d}\omega_s(t)\,, \tag{12a}$$

$$C_a \mathrm{d}T_a(t) = \left(\frac{1}{R_{sa}}(T_s(t) - T_a(t)) + \frac{1}{R_{a\infty}}(T_\infty - T_a(t)) + R_n(t)\right)\mathrm{d}t + \sigma_a \mathrm{d}\omega_a(t)\,, \tag{12b}$$

$$d_{T_a}(t_k) = T_a(t_k) + v_{T_a,k}\,. \tag{12c}$$

$T_s(t)$ and $T_a(t)$ are the temperature of the surrounding sea and the land air respectively. $R_{sa}$ and $R_{a\infty}$ are resistances against the heat flow between the states. $C_s$ and $C_a$ are the heat capacities representing the amount of heat the states contain. $R_n$ is the net radiation as in (11) and drives the process, $T_\infty$ is a constant in- or outflow of heat to stabilise the system, $\omega_a$ and $\omega_s$ are standard Brownian motions and $v_{T_a,k}$ is i.i.d. random observation noise. Again, we estimate the parameters in (12) using a maximum likelihood method and use the CDEKF to evaluate the likelihood function.

### 3.3. Combined disturbance model and forecasting scheme

Combining the individual climate models, the combined continuous state–space, stochastic-dynamic disturbance model, (1b) and (1d) in (1), gets the form:

$$\text{Disturbance model} \begin{cases} \mathrm{d}Z_\kappa = f_\psi(Z_\kappa)\mathrm{d}t + \sigma_\psi \mathrm{d}\omega_\kappa \\ \kappa = \psi^{-1}(Z_\kappa) \\ \phi = I_N(\kappa, t) + I_D(\kappa, t) \\ R_n = R_n(\kappa, \phi, t) \\ \mathrm{d}T_s = f_{T_s}(T_a, T_s)\mathrm{d}t + \sigma_s \mathrm{d}\omega_s \\ \mathrm{d}T_a = f_{T_a}(T_a, T_s, R_n)\mathrm{d}t + \sigma_a \mathrm{d}\omega_a \\ \boldsymbol{d} = \left[T_a, \phi\right]^T \end{cases} \tag{13}$$

$$\text{Observation equation} \begin{cases} d_\phi = \phi + v_\phi, \quad v_\phi \sim N_{iid}(0, R_\phi) \\ d_{T_a} = T_a + v_{T_a}, \quad v_{T_a} \sim N_{iid}(0, R_{T_a}) \\ \boldsymbol{y}_d = \left[d_{T_a}, d_\phi\right]^T, \end{cases}$$

The model in (13) returns the important weather elements in $\boldsymbol{d}$ and the corresponding observations in $\boldsymbol{y}_d$. Since (13) is based on (non-linear) SDEs, we need to use e.g. the CDEKF to compute the certainty-equivalent forecasts. This involves numerical solutions to differential equations and requires local weather measurements as the initial conditions preferably from the building site itself. In practice though, the cloud cover is difficult to observe without specialised equipment. Due to the strong correlation between the cloud cover and solar radiation we instead estimate cloud cover at time $t_k$, $\hat{\kappa}_{k|k}$, as the most likely to generate the observed solar radiation, $d_{\phi,k}$. Due to the one-way coupling of the SDEs in (13) between the cloud cover and air temperature models, we split the computations into separate parts described in Algorithm 1. We collect the forecasts in the sequence $\{\hat{\boldsymbol{d}}_{k+i|k}\}_{i=0}^N$, where $N \in \mathbb{N}$ is the prediction horizon. The subscript $k+i|k$ means that $\hat{\boldsymbol{d}}_{k+i|k}$ is an estimate of $\boldsymbol{d}(t_{k+i})$ given information up till time $t_k$.

**Algorithm 1** Disturbance Forecast Algorithm

**require:** $\boldsymbol{y}_{d,k} = \left[d_{T_a,k}, d_{\phi,k}\right]^T$, $\hat{\boldsymbol{d}}_{k-1|k-1}$, $\hat{P}_{T_a,k-1|k-1}$, $t_k$

**Cloud cover predictions:**
Given $d_{\phi,k}$, calculate the cloud cover estimate $\hat{\kappa}_{k|k}$ as the most likely to generate the observation $d_{\phi,k}$.
Compute $\{\hat{\kappa}_{k+i|k}\}_{i=0}^N$ using Eq. (7) with $\hat{\kappa}_{k|k}$ as initial condition.

**Solar radiation predictions:**
For each $i = 0, \ldots, N$ compute the solar radiation $\hat{\phi}_{k+i|k} = \hat{I}_{N,k+i} \sin\alpha(t_{k+i}) + \hat{I}_{D,k+i}$.

**Net radiation predictions:**
For each $i = 0, \ldots, N$ compute the net radiation $\hat{R}_{n,k+i|k}$.

**Ambient air temperature predictions:**
Given $d_{T_a,k}$, calculate the filtered estimate, $\hat{T}_{a,k}$, and its covariance, $\hat{P}_{T_a,k|k}$, using the CDEKF and the model in Eq. (12). Next, compute the Kalman predictions $\hat{T}_{a,k+i|k}$ for $i = 0, \ldots, N$.

Let $\hat{\boldsymbol{d}}_{k+i|k} = [\hat{T}_{a,k+i|k}, \hat{\phi}_{k+i|k}]^T$ be the $i$'th disturbance prediction.

**return** $\{\hat{\boldsymbol{d}}_{k+i|k}\}_{i=0}^N$, $\hat{P}_{T_a,k|k}$

## 4. Model predictive control

This paper uses linear Economic MPC (EMPC) based on SDEs. The overall aim in linear Economic MPC is to mitigate disturbances and control a linear dynamical system to meet operational constraints at minimum cost [30,51]. It minimises the cost according to a *price signal* that reflects the desired behaviour. The desired behaviour could be to

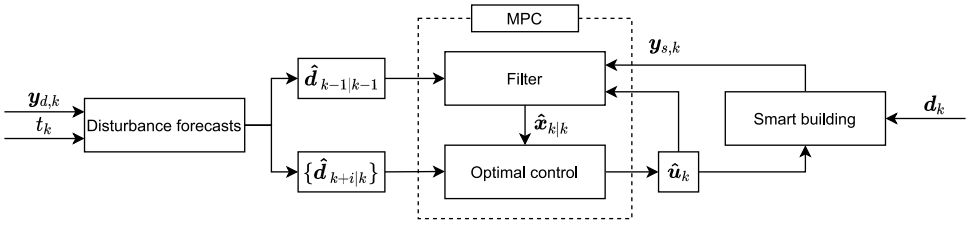


**Fig. 3.** The MPC framework for the smart house control and how the disturbance modelling is incorporated. The "Disturbance forecasts"-box corresponds to Algorithm 1 and the "MPC"-box corresponds to Algorithm 2.

minimise the $CO_2$ emission, the total electricity cost, or the total usage of electricity [52–54]. The MPC algorithm is depicted inside the dashed square in Fig. 3 and consists of a *filter* and an *optimal control problem*. This section provides a short introduction to the general mathematical framework of MPC based on SDEs with a particular emphasis on how to embed disturbance forecasts.

### 4.1. Filtering

For stochastic systems or in cases where we do not observe all states, i.e. a system with hidden states, we need to use a *filter* to estimate the system. Due to the stochasticity, we cannot determine the system states exactly. Instead, we seek an estimate of the present system states, $\hat{\boldsymbol{x}}_{k|k} = \mathrm{E}[\boldsymbol{x}(t_k)|\mathcal{Y}_k]$, and its uncertainty, $\hat{P}_{k|k} = \mathrm{Var}\left[\boldsymbol{x}(t_k)|\mathcal{Y}_k\right]$ where $\mathcal{Y}_k$ is the information up until time $t_k$. Due to the discrete computational nature of computers, it is sometimes advantageous to work with a discrete-time system. For SDEs in the form (2), we perform an exact discretisation with $T_s = t_{k+1} - t_k$ assuming that the input and disturbance are constant within each sampling period, $T_s$; $\boldsymbol{u}(t) = \boldsymbol{u}_k$ and $\boldsymbol{d}(t) = \boldsymbol{d}_k$ for $t \in [t_k, t_{k+1}[$. This is also called *zero-order-hold* discretisation and results in the discrete time linear state space model

$$\boldsymbol{x}_{k+1} = A\boldsymbol{x}_k + B\boldsymbol{u}_k + E\boldsymbol{d}_k + \boldsymbol{w}_k\,, \tag{14a}$$

$$\boldsymbol{y}_{s,k} = C\boldsymbol{x}_k + \boldsymbol{v}_{s,k}\,, \tag{14b}$$

$$\boldsymbol{w}_k \sim N_{iid}(\boldsymbol{0}, Q_s), \quad \boldsymbol{v}_{s,k} \sim N_{iid}(\boldsymbol{0}, R_s)\,, \tag{14c}$$

with $A = \exp(A_c T_s)$, $B = \int_0^{T_s} \exp(A_c s) B_c \mathrm{d}s$, and $E = \int_0^{T_s} \exp(A_c s) E_c \mathrm{d}s$ being matrices governing the discrete-time dynamics. $Q_s = \int_0^{T_s} \exp(A_c s) G_c G_c^T \exp(A_c^T s) \mathrm{d}s$ is the covariance of the process noise and $R_s$ is the covariance of the measurement noise. The discretisation is exact in the sense that at the discrete times $t_k$, $k \in \mathbb{N}$, the discrete- and continuous-time systems are identical, $\boldsymbol{x}_k = \boldsymbol{x}(t_k)$. When the system is linear and the noise is Gaussian as in (14), the Kalman filter provides an optimal estimate of the system states. Given an observation, $\boldsymbol{y}_{s,k}$, and a one-step prediction of the state vector, $\hat{\boldsymbol{x}}_{k|k-1}$, the Kalman filter algorithm computes the optimal filtered state estimate, $\hat{\boldsymbol{x}}_{k|k}$, and the covariance of the filtered state estimate, $\hat{P}_{k|k}$.

### 4.2. Optimal control problem

The optimal control problem of MPC is based on a cost function, $\varphi_k$, that is used to rank the feasible solutions and is formulated such that it promotes a desired behaviour of the system. The optimal control problem determines the optimal input sequence, which we denote with a hat $\{\hat{\boldsymbol{u}}_{k+i|k}\}_{i=0}^{N-1}$, to the system given an estimated initial state, $\hat{\boldsymbol{x}}_{k|k}$, and the disturbance forecast, $\{\hat{\boldsymbol{d}}_{k+i|k}\}_{i=0}^{N}$. By using the disturbance forecast generated by Algorithm 1, $\{\hat{\boldsymbol{d}}_{k+i|k}\}_{i=0}^{N}$, we decouple the disturbance estimation and the system state estimation. From a theoretical point of view, this is a sub-optimal estimate. But the approximation error is small with the given external sensors and it has the advantage that different parties can supply the disturbance forecast and MPC. The general optimal control problem including the disturbances is defined by the following *Bolza problem* [55]

$$J(\hat{\boldsymbol{x}}_{k|k}, \hat{\boldsymbol{u}}_{k-1|k}, \{\hat{\boldsymbol{d}}_{k+i|k}\}_{i=0}^{N}) = \tag{15a}$$

$$\min_{\boldsymbol{u},\boldsymbol{s}} \quad \varphi_k\,, \tag{15b}$$

$$s.t. \quad \boldsymbol{x}(t_k) = \hat{\boldsymbol{x}}_{k|k}\,, \tag{15c}$$

$$\boldsymbol{u}(t) = \boldsymbol{u}_{k+i|k},\ t \in [t_{k+i}, t_{k+i+1}[,\ i \in \mathcal{N}, \tag{15d}$$

$$\boldsymbol{d}(t) = \hat{\boldsymbol{d}}_{k+i|k},\ t \in [t_{k+i}, t_{k+i+1}[,\ i \in \mathcal{N}, \tag{15e}$$

$$\mathrm{d}\boldsymbol{x}(t) = f_s(\boldsymbol{x}(t), \boldsymbol{u}(t), \boldsymbol{d}(t))\mathrm{d}t, \quad t \in \mathcal{T}_k, \tag{15f}$$

$$\boldsymbol{u}_{\min} \le \boldsymbol{u}_{k+i|k} \le \boldsymbol{u}_{\max}, \quad i \in \mathcal{N}, \tag{15g}$$

$$\Delta\boldsymbol{u}_{\min} \le \Delta\boldsymbol{u}_{k+i|k} \le \Delta\boldsymbol{u}_{\max}, \quad i \in \mathcal{N}, \tag{15h}$$

$$c(\boldsymbol{x}(t)) + \boldsymbol{s}(t) \ge \boldsymbol{0}, \quad t \in \mathcal{T}_k, \tag{15i}$$

$$\boldsymbol{s}(t) \ge \boldsymbol{0}, \quad t \in \mathcal{T}_k, \tag{15j}$$

where the cost function is in the form

$$\varphi_k = \int_{t_k}^{t_{k+N}} \ell(\boldsymbol{x}(\tau), \boldsymbol{u}(\tau))\mathrm{d}\tau + \ell_b(\boldsymbol{x}(t_{k+N})) + \int_{t_k}^{t_{k+N}} \ell_s(\boldsymbol{s}(\tau))\mathrm{d}\tau. \tag{16}$$

The stage costs, $\ell(\boldsymbol{x}(t), u(t))$ and $\ell_s(s(t))$, and the cost-to-go, $\ell_b(\boldsymbol{x}(t_{k+N}))$, are

$$\ell(\boldsymbol{x}(t), u(t)) = \boldsymbol{c}(t)^T \boldsymbol{u}(t)\,, \tag{17a}$$

$$\ell_b(\boldsymbol{x}(t_{k+N})) = 0\,, \tag{17b}$$

$$\ell_s(s(t)) = \boldsymbol{\rho}(t)^T \boldsymbol{s}(t)\,, \tag{17c}$$

such that the cost function, $\varphi$, becomes

$$\varphi_k = \int_{t_k}^{t_{k+N}} \left(\boldsymbol{c}(\tau)^T \boldsymbol{u}(\tau) + \boldsymbol{\rho}(\tau)^T \boldsymbol{s}(\tau)\right) \mathrm{d}\tau\,, \tag{18}$$

In the optimal control problem, $\mathcal{T}_k = [t_k, t_{k+N}[$ is both the *control* and the *prediction horizon*. $\mathcal{N} = \{0, 1, \ldots, N-1\}$. $\hat{\boldsymbol{x}}_{k|k}$ is the initial condition of the system estimated by a state estimator. $\{\hat{\boldsymbol{d}}_{k+i|k}\}_{i=0}^{N}$ is the sequence of advanced forecasts obtained from the disturbance model in Section 3. $c(\boldsymbol{x}(t))$ represents the constraint functions. $\boldsymbol{s}(t)$ are slack variables that allow solutions outside of the desired domain and we penalise them with $\ell_s(\boldsymbol{s}(t))$. $\boldsymbol{c}(t)$ is the electricity price signal and $\boldsymbol{\rho}(t)$ is the slack penalty. $\boldsymbol{\rho}(t)$ should be large enough to make the preferred solution satisfy the constraints whenever possible. We assume that the price signal is piece-wise constant in each sampling period, $\boldsymbol{c}(t) = \boldsymbol{c}_k$, $t \in [t_k, t_{k+1}[$. $\ell_b$ is a *cost-to-go* term ranking the end-state, $\boldsymbol{x}(t_{k+N})$. It can be very useful to include for smart buildings with batteries or EVs [3]. However, for long prediction horizons it has negligible effect on the closed-loop performance. Accordingly, we set it equal to zero which makes (15) a *Lagrange problem*. For the optimal control problem, we know the actual input during time $[t_{k-1}, t_k]$, $\hat{\boldsymbol{u}}_{k-1|k}$, should it differ from the control signal $\hat{\boldsymbol{u}}_{k-1|k-1}$. The optimal control, denoted $\hat{\boldsymbol{u}}(t)$, is the $\boldsymbol{u}(t)$ that minimises (15).

#### 4.2.1. Discretisation of the optimal control problem

In the discretisation of the optimal control problem (15), we consider the output constraints (15i)–(15j) as point-wise constraints. The

input, $\boldsymbol{u}_k$, is piece-wise constant. Consequently, the cost function (16) becomes

$$\varphi_k = \sum_{i=0}^{N-1} \boldsymbol{c}_{k+i|k}^T \boldsymbol{u}_{k+i|k} + \sum_{i=0}^{N-1} \boldsymbol{\rho}_{k+i+1|k}^T \boldsymbol{s}_{k+i+1|k} \,. \tag{19}$$

The dynamics are linear and discretised and the soft output constraints are assumed to be linear functions, i.e. $c(\boldsymbol{x}_k) = H\boldsymbol{x}_k + \boldsymbol{b}$. Consequently, the optimal control problem (15) is the linear program

$$J(\hat{\boldsymbol{x}}_{k|k}, \hat{\boldsymbol{u}}_{k-1|k}, \{\hat{\boldsymbol{d}}_{k+i|k}\}_{i=0}^N) = \tag{20a}$$

$$\min_{\boldsymbol{u},\boldsymbol{s}} \quad \varphi_k \,, \tag{20b}$$

$$s.t. \tag{20c}$$

$$\boldsymbol{x}_{k|k} = \hat{\boldsymbol{x}}_{k|k} \,, \tag{20d}$$

$$\boldsymbol{x}_{k+i+1|k} = A\boldsymbol{x}_{k+i|k} + B\boldsymbol{u}_{k+i|k} + E\hat{\boldsymbol{d}}_{k+i|k}, \; i \in \mathcal{N}, \tag{20e}$$

$$\boldsymbol{u}_{\min} \le \boldsymbol{u}_{k+i|k} \le \boldsymbol{u}_{\max}, \qquad i \in \mathcal{N}, \tag{20f}$$

$$\Delta\boldsymbol{u}_{\min} \le \Delta\boldsymbol{u}_{k+i|k} \le \Delta\boldsymbol{u}_{\max}, \qquad i \in \mathcal{N}, \tag{20g}$$

$$H\boldsymbol{x}_{k+i+1|k} + \boldsymbol{b} + \boldsymbol{s}_{k+1+i|k} \ge \boldsymbol{0}, \qquad i \in \mathcal{N}, \tag{20h}$$

$$\boldsymbol{s}_{k+1+i|k} \ge \boldsymbol{0}, \qquad i \in \mathcal{N}. \tag{20i}$$

The solution to the optimal control problem is a sequence of inputs, $\{\hat{\boldsymbol{u}}_{k+i|k}\}_{i=0}^{N-1}$, and slack variables, $\{\hat{\boldsymbol{s}}_{k+i+1|k}\}_{i=0}^{N-1}$, that minimises the cost function, $\varphi_k$.

### 4.3. The economic model predictive control algorithm

Fig. 3 shows the overall MPC setup and the information flow. Algorithm 2 provides a listing of the corresponding computational steps to compute the input (manipulated variable) vector, $\hat{\boldsymbol{u}}_{k|k}$, based on the system measurements, $\boldsymbol{y}_{s,k}$, the previous input $\boldsymbol{u}_k = \hat{\boldsymbol{u}}_{k-1|k}$, the previous filtered state mean–covariance pair, $(\hat{\boldsymbol{x}}_{k-1|k-1}, \hat{P}_{k-1|k-1})$, the previous filtered disturbance, $\hat{\boldsymbol{d}}_{k-1|k-1}$, and the disturbance forecast, $\{\hat{\boldsymbol{d}}_{k+i|k}\}_{i=0}^N$. In this work, Algorithm 1 provides the disturbance forecast. The MPC algorithm (Algorithm 2) consists of (1) a Kalman filter algorithm organised as a one-step prediction and a measurement update; and (2) an optimal control problem, which in this case is a linear program. Solution of the linear program consumes the majority of the computational time to conduct Algorithm 2. Algorithm 2 is conducted each sample time when a new measurement arrives.

## 5. Dynamics of the smart building model

The heating system of the smart building consists of a ground sourced heat pump using a compressor that heats up water that then flows into pipes underneath the floor. This has the advantage of being energy efficient (a COP of 3 is used) due to the thermodynamic processes that extracts heat from some ambient environment, but is disadvantaged by its slow dynamics. When the heat pump is turned on, it takes a long time before the room air temperature responds. This section briefly investigates the dynamics and time/frequency responses of the heat pump model and compares it to that of the disturbances and a standard electrical heater to give an idea and overview of what effects the heat pump delivers in the settings of a smart building.

### 5.1. Pulse- and frequency-response analysis

Fig. 4 shows the pulse response of the smart building model for the first 15 h and 90 days. The disturbances act much faster compared to the heat pump. After 3 h, the disturbance responses have already reverted back to a level of around half of their peak pulse response. The heat pump, however, has not yet heated the room by any significant amount. These large response differences between the heat pump and disturbances indicate that the heat pump might not be sufficient at all times for regulating the indoor air temperature. Fig. 4 shows that

**Algorithm 2** MPC Algorithm

**require:** $\boldsymbol{y}_{s,k}$, $\hat{\boldsymbol{u}}_{k-1|k}$, $\hat{\boldsymbol{x}}_{k-1|k-1}$, $\hat{P}_{k-1|k-1}$, $\hat{\boldsymbol{d}}_{k-1|k-1}$, $\{\hat{\boldsymbol{d}}_{k+i|k}\}_{i=0}^N$

**Filter:**
Compute one-step Kalman predictions
$\hat{\boldsymbol{x}}_{k|k-1} = A\hat{\boldsymbol{x}}_{k-1|k-1} + B\hat{\boldsymbol{u}}_{k-1|k} + E\hat{\boldsymbol{d}}_{k-1|k-1}$
$\hat{P}_{k|k-1} = A\hat{P}_{k-1|k-1}A^T + Q_s$

Compute process noise and Kalman gain
$R_{s,k|k-1} = C\hat{P}_{k|k-1}C^T + R_s$
$K_k = \hat{P}_{k|k-1}C^T R_{s,k|k-1}^{-1}$

Compute filtered estimates
$\hat{\boldsymbol{y}}_{s,k|k-1} = C\hat{\boldsymbol{x}}_{k|k-1}$
$\hat{\boldsymbol{x}}_{k|k} = \hat{\boldsymbol{x}}_{k|k-1} + K_k(\boldsymbol{y}_{s,k} - \hat{\boldsymbol{y}}_{s,k|k-1})$
$\hat{P}_{k|k} = (I - K_kC)\hat{P}_{k|k-1}(I - K_kC)^T + K_kR_sK_k^T$

**Optimal control:**
Given $\hat{\boldsymbol{x}}_{k|k}$, $\hat{\boldsymbol{u}}_{k-1|k}$, and $\{\hat{\boldsymbol{d}}_{k+i|k}\}_{i=0}^N$ solve the optimal control problem in Eq. (20) to obtain $\{\hat{\boldsymbol{u}}_{k+i|k}\}_{i=0}^{N-1}$

**return** $\hat{\boldsymbol{u}}_{k|k}$, $\hat{\boldsymbol{x}}_{k|k}$, $\hat{P}_{k|k}$

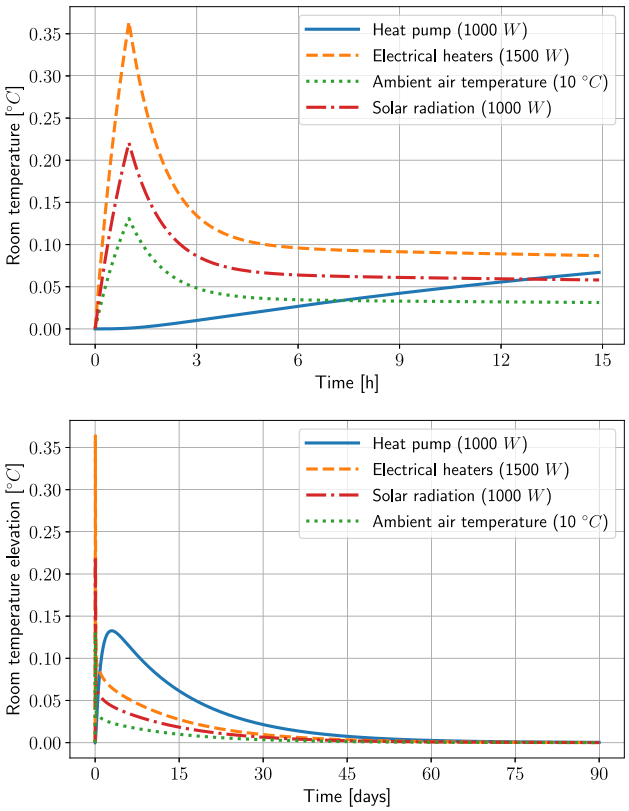


**Fig. 4.** The pulse response for 15 h (top) and 90 days (bottom). The step size of the pulse is given in the legend (all from zero).

electrical heaters heat just as fast as the disturbances, and suggests that the they are much better suited for dealing with fast responses.

Fig. 5 shows a bode plot of the frequency response of the heat pump and the electrical heaters compared to the disturbances. It is again clear, that the heat pump is governed by delayed dynamics for higher

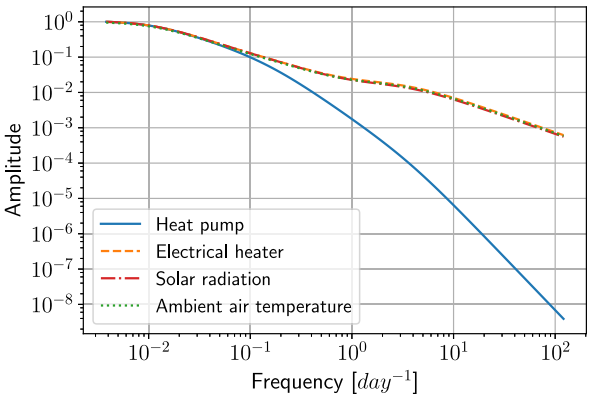


**Fig. 5.** Bode plot showing the frequency responses of the disturbances together with the heat pump and the electrical heaters. The inputs have been normalised in order to make the response have an amplitude equal to 1 for small frequencies.

frequencies. The response signal for the electrical heaters is identical to those of the disturbances due to the direct input of heat into the room.

### 5.2. Summary of the section

The considerations and results of this section suggest that without anything to provide faster heating or cooling, e.g. electrical heaters or electrical coolers, the disturbances act with too high frequencies for the heat pump to deal with. However, as the results will show, if the goal is to keep the room temperature within some relatively large range, say from 20 to 24 °C during cold months where heating is required at almost all times, the heat pump can still be suitable. Electrical heaters (or other faster heating devices) definitely make it easier to obtain good solutions — but they are not as cheap as the heat pump.

## 6. Results and discussion

This section shows simulation-based results of the potential benefits of including the advanced disturbance model (1) in MPC. As the data we use for the true disturbances do not include meteorological forecasts, we cannot directly compare the results to that part of the literature. Instead, we compare the advanced forecasts to offset-free control. We also present control results that use perfect forecasts to give a theoretical upper bound on the performance. We use data for all years during the 7 year period of data.

### 6.1. Visualisation of the advanced disturbance forecasts

As previously discussed, the typical offset-free control schemes in the literature supply *persistent forecasts*, that is

$$\hat{\boldsymbol{d}}_{k+i|k} = \hat{\boldsymbol{d}}_{k|k}, \quad i = 0, \dots, N\,. \tag{21}$$

Fig. 6 shows a visual comparison of the advanced forecasts in (13) and persistent forecasts using a prediction horizon of $N = 96$ hours. The complex dynamics of the advanced forecasts become visible against the zero-order (constant) forecasts.

### 6.2. Simulation-based comparison of the forecasting schemes

As Section 5 shows, the heat pump heats up the smart building in a slow manner. To diversify the results, we therefore also show the use of a smart building with faster heating units such as electrical heaters and/or coolers. The rest of the section describes and presents the control results for each heating strategy based of the smart building in Section 2. As the true disturbances, we use the weather data described in Section 3.1. All results use a slack penalty value of $\rho_k = 5000$, time sample $T_s = 1$ hour, and prediction horizon $N = 96$ hours. We put the electricity price constant and choose it to be the mean price over 7 months of March data from Nordpool, $c_k = 36.5$ [EUR/MWh]. The MPC thus minimises the amount of electricity spend and does not consider varying prices.

For the simulation, we choose the temperature constraints to be $T_{r,min} = 20\,°\text{C}$ and $T_{r,max} = 24\,°\text{C}$. Tables 2 and 3 shows the constraint violation and the total electricity price for all heating strategies respectively. Fig. 7 shows a 15-day sample of the simulations to illustrate the behavioural differences.

#### 6.2.1. Heating strategy 1: Electrical heaters

Due to the faster heating dynamics of the electrical heaters, we expect that the persistent forecasts might perform well, since the MPC can quickly respond to sudden changes of the disturbances. As expected, the differences between the control solutions in Fig. 7, are not very visible. The room air temperatures and the heat inputs from the electrical heaters are almost identical. Table 2 does show a difference in the performance as the solution using the advanced forecasts perform slightly better. The electricity prices are almost identical since the total heat needed over the 7 months is the same for both buildings and the unit price is the same.

#### 6.2.2. Heating strategy 2: Heat pump

The second heating strategy simulation uses the smart building equipped with a heat pump. We recall that the heat pump is 3 times more efficient compared to the faster heating strategies. In contrast to the electrical heaters, the heating pattern from Fig. 7 is very slow, due to the heat pump dynamics. But the solution is also cheaper due to the high efficiency of the heat pump. The difference between the persistent and advanced forecasts becomes very visible here. Due to the slow dynamics, the advanced forecasts of the disturbance dynamics matter much more in this case. Tables 2 and 3 show that the solution using advanced forecasts is both cheaper *and* supplies significantly better indoor climate.

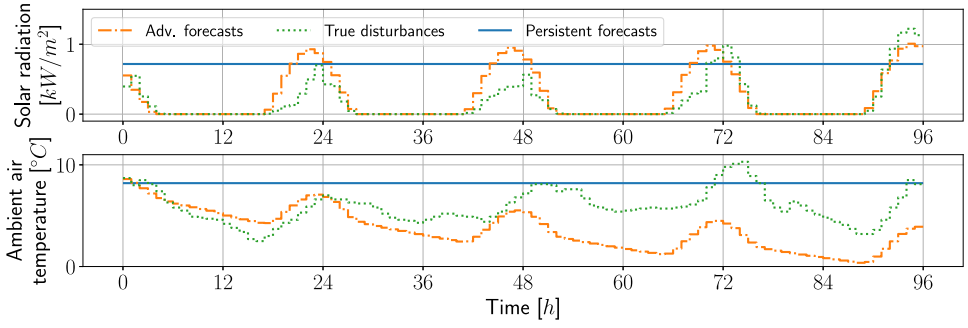


**Fig. 6.** An example of the advanced forecasts from (13) compared to persistent forecasts.

**Table 2**
The constraint violations (the slack variables, $\hat{s}_k$, in the cost function in (19)) for all heating strategies for each forecasting scheme. The number in parenthesis is the $p$-value of a t-test between the advanced- and persistent forecasts.

| Constraint violation of the control simulations | | | |
|---|---|---|---|
| Heating strategy | Persistent | Advanced forecasts | Perfect |
| Electrical heaters, $u_1$ | 48.5 | 39.6 ($p = 0.024$) | 25.1 |
| Heat pump, $u_2$ | 157.9 | 12.3 ($p = 0.008$) | 1.7 |
| Heat pump plus electrical heaters, $\boldsymbol{u}_3$ | 48.0 | 6.7 ($p = 0.023$) | 1.2 |
| Heat pump plus electrical heaters and coolers, $\boldsymbol{u}_4$ | 4.4 | 2.4 ($p = 0.038$) | 0 |

**Table 3**
The electricity price in EUR (the first term in the cost function in (19)) for all heating strategies for each forecasting scheme. The number in parenthesis is the $p$-value of a t-test between the advanced- and persistent forecasts.

| Electricity cost of the simulations | | | |
|---|---|---|---|
| Heating strategy | Persistent | Advanced forecasts | Perfect |
| Electrical heaters, $u_1$ | 303.2 | 302.2 ($p = 0.421$) | 302.0 |
| Heat pump, $u_2$ | 117.3 | 110.4 ($p = 0.198$) | 107.7 |
| Heat pump plus electrical heaters, $\boldsymbol{u}_3$ | 113.0 | 108.2 ($p = 0.248$) | 107.5 |
| Heat pump plus electrical heaters and coolers, $\boldsymbol{u}_4$ | 117.9 | 108.3 ($p = 0.178$) | 107.5 |

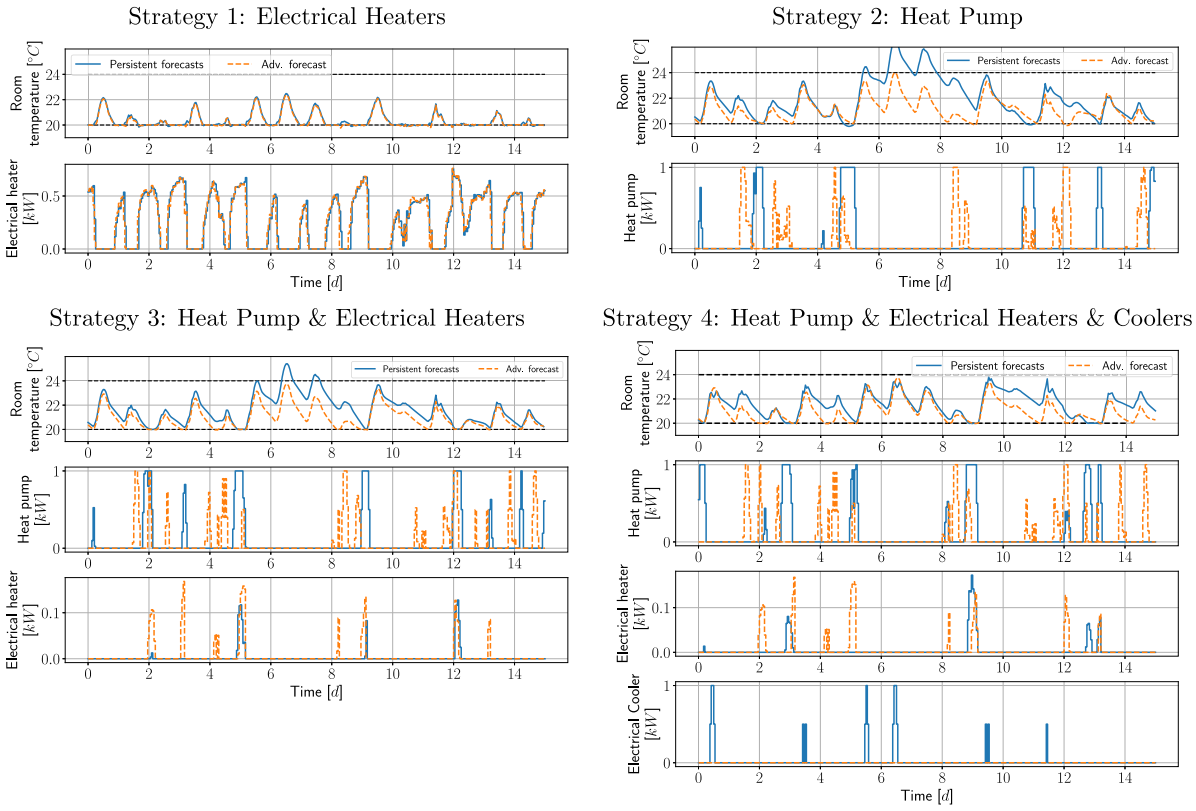


**Fig. 7.** A 15-day sample of the total 7 months of simulation for each heating strategy. The black dashed lines are the constraints. It shows the indoor air temperature as well as the heating inputs at the same point in the time series of disturbances.

### 6.2.3. *Heating strategy 3: Heat pump plus electrical heaters*

Heating strategy 3 combines the (fast but expensive) electrical heaters and the (slow but cheap) heat pump. The input is therefore $\boldsymbol{u} = [W_c, W_{eh}]^T$. The idea is to have cheap heating from the heat pump while being able to quickly adapt using the more expensive electrical heaters. From Table 2 the persistent forecasts show large improvement compared to only using the heat pump. The improvements for the advanced forecasts are around 50% better. It is noteworthy that Table 3 indicates that the advanced forecasts supply results that are very close the perfect forecasts in terms of electricity price and at the same time improves the indoor climate conditions. Fig. 7 also indicates that the controller using the advanced forecasting scheme uses the electrical heater less often.

### 6.2.4. *Heating strategy 4: Heat pump plus electrical heaters and coolers*

An extension to heating strategy 3 is to include an electrical cooling unit beside the electrical heaters to also enable cooling. The input becomes $\boldsymbol{u} = [W_c, W_{eh}, W_{ec}]^T$. This has a great effect on the persistent forecasts as seen in Table 2 compared with the other strategies. It also leads to high electricity costs, which are much higher compared to the other forecasting scheme. The advanced forecasts seem overall superior and by all indications well suited for efficient temperature control while improving the comfort regulation.

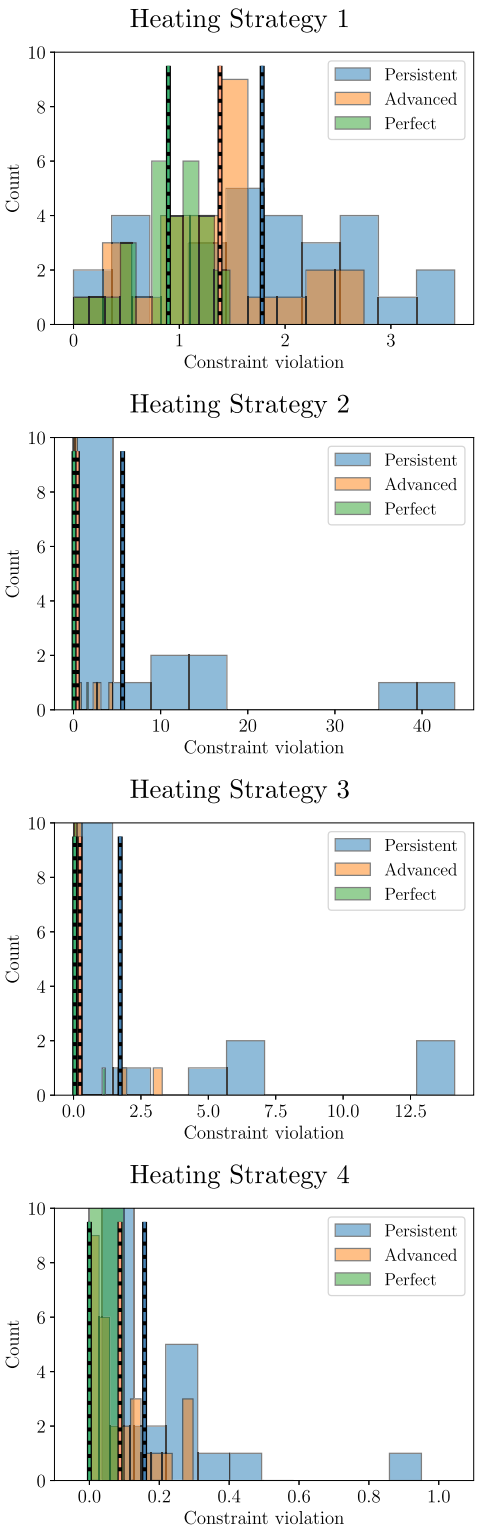


**Fig. 8.** Histogram of the constraint violations for each week of the 7 months of simulations. The vertical lines represents the mean value of the distribution of the forecasting strategies.

### 6.3. Statistical results

To draw statistical conclusions from the results presented in this paper, we carry out a $t$-test based on the following setup. We consider the constraint violation and electricity price of each week of the 7 months of simulation as an observation. This equals $7 \cdot 4 = 28$ observations for each forecasting method for each heating strategy. Fig. 8 shows the histograms of the simulation results where the vertical lines are the mean-value for each forecasting strategy. Similar histograms can be made for the electricity prices. Tables 2 and 3 show the $p$-values of the t-tests between the mean values of the persistent- and advanced forecasts (shown in parenthesis). The constraint violations are all strongly significant below the 95% confidence level. The cost reduction, though, does not appear significant near usual confidence levels. However, the weather is highly correlated over extended time periods, and therefore we do not effectively have 28 observations for the tests. We note that all $p$-values are on the right side of the distribution, which indicates that with more observations, the electricity reduction becomes significant.

### 6.4. Inclusion of meteorological forecasts

It is important to stretch that the advanced forecasts work best for a short future time window. As pointed out by the literature, meteorological forecasts in general provide more accurate predictions beyond 4-10 h ahead compared to short-term forecasts. Assuming that meteorological forecasts are strictly better after 10 h, we can then expect even better results than presented here by using a combined *short*- and *long-term* forecasting scheme. However this needs more work to clarify the specific gains and what forecast setup is optimal.

## 7. Conclusions

This paper proposed a method for incorporating advanced disturbance models into a system model based on stochastic differential equations for model predictive control (MPC). This approach leads to a generic method for embedding forecasting and disturbance modelling for MPC for energy systems. We illustrated the method by statistically modelling the weather and controlling the indoor air temperature for a smart building. But the method itself is much more generally applicable. We mathematically reviewed the disturbance models and even argued that transformations were necessary for some of the disturbance-elements to obtain better accuracy by the dynamical equations.

We compared the advanced embedded forecasts to conventional offset-free control, which suggested significant improvements of the control performance. Results suggest electricity savings between 5%–10% and reduction of constraint violations of up to 90% compared to offset-free MPC. In fact, we were able to achieve results very close to the performance supplied by perfect forecasts. We also illustrated the issues of heat pumps being governed by very slow heat dynamics. Thus, by combining different heating strategies, better control performance was achieved. Nevertheless, the heat pump itself performed very well in combination with the advanced disturbance forecasts and definitely proved useful.

More work is needed on how to combine advanced, short-term forecasts with long-term, meteorological forecasts, since such a setup may improve current forecasting standards. An example is to investigate the best point in time to switch from short-term to long-term predictions.

## CRediT authorship contribution statement

**Christian Ankerstjerne Thilker:** Conceptualization, Methodology, Software, Formal analysis, Writing - original draft. **Henrik Madsen:** Conceptualization, Methodology, Supervision, Writing - review & editing. **John Bagterp Jørgensen:** Conceptualization, Methodology, Supervision, Writing - review & editing.

## Declaration of competing interest

The authors declare that they have no known competing financial interests or personal relationships that could have appeared to influence the work reported in this paper.

## Acknowledgements

The authors obtained funding by *Sustainable plus energy neighbourhoods (syn.ikia)* (H2020 No. 869918), *Centre for IT-Intelligent Energy Systems (CITIES)* (DSF 1305-00027B), *Flexible Energy Denmark (FED)* (IFD 8090-00069B), and EUDP 64017-05136.

## References

[1] Berardi U. A cross-country comparison of the building energy consumptions and their trends. Resour Conserv Recy 2017;123:230–41.
[2] Halvgaard R, Poulsen NK, Madsen H, Jørgensen JB. Economic model predictive control for building climate control in a smart grid. In: 2012 IEEE PES innovative smart grid technologies. 2012. p. 1–6.
[3] Schlüter HA, Boiroux D, Poulsen NK, Madsen H, Jørgensen JB. Economic model predictive control for energy systems in smart homes. In: 2019 IEEE conference on control technology and applications. 2019. p. 598–604.
[4] Salakij S, Yu N, Paolucci S, Antsaklis P. Model-Based Predictive Control for building energy management. I: Energy modeling and optimal control. Energy Build 2016;133:345–58.
[5] Hu M, Xiao F, Jørgensen JB, Li R. Price-responsive model predictive control of floor heating systems for demand response using building thermal mass. Appl Therm Eng 2019;153:316–29.
[6] Lee J. Model predictive control: Review of the three decades of development. Int J Control Autom Syst 2011;9:415–24.
[7] Madsen H, Nielsen J, Lindström E, Baadsgaard M, Holst J. Statistics in finance. Centre for Mathematical Sciences; 2004.
[8] Møller JK, Zugno M, Madsen H. Probabilistic forecasts of wind power generation by stochastic differential equation models. J Forecast 2016;35(3):189–205.
[9] Iversen EB, Morales JM, Møller JK, Madsen H. Short-term probabilistic forecasting of wind speed using stochastic differential equations. Int J Forecast 2016;32(3):981–90.
[10] Badosa J, Gobet E, Grangereau M, Kim D. Day-ahead probabilistic forecast of solar irradiance: A stochastic differential equation approach. In: Drobinski P, Mougeot M, Picard D, Plougonven R, Tankov P, editors. Renewable energy: Forecasting and risk management. Cham: Springer International Publishing; 2018, p. 73–93.
[11] Iversen E, Morales J, Møller J, Madsen H. Probabilistic forecasts of solar irradiance by stochastic differential equations. Environmetrics 2014;25. http://dx.doi.org/10.1002/env.2267.
[12] Candanedo J, Athienitis A. Predictive control of radiant floor heating and transmitted irradiance in a room with high solar gains (ML-11-015). HVAC&R Res 2011;17:235–56.
[13] Gabsi F, Hamelin F, Pannequin R, Chaabane M. Energy efficiency of a multizone office building: MPC-based control and simscape modelling. In: 6th international conference on smart cities and green ICT systems, SMARTGREENS. Porto, Portugal. 2017. http://dx.doi.org/10.5220/0006305002270234.
[14] De Coninck R, Helsen L. Practical implementation and evaluation of model predictive control for an office building in Brussels. Energy Build 2016;111:290–8.
[15] Finck C, Li R, Zeiler W. Economic model predictive control for demand flexibility of a residential building. Energy 2019;176:365–79.
[16] Thieblemont H, Haghighat F, Ooka R, Moreau A. Predictive control strategies based on weather forecast in buildings with energy storage system: A review of the state-of-the art. Energy Build 2017;153:485–500.
[17] Drgoňa J, Arroyo J, Cupeiro Figueroa I, Blum D, Arendt K, Kim D, et al. All you need to know about model predictive control for buildings. Annu Rev Control 2020.
[18] Oldewurtel F, Parisio A, Jones CN, Gyalistras D, Gwerder M, Stauch V, et al. Use of model predictive control and weather forecasts for energy efficient building climate control. Energy Build 2012;45:15–27.
[19] Segarra EL, Du H, Ruiz GR, Bandera CF. Methodology for the quantification of the impact of weather forecasts in predictive simulation models. Energies 2019;12(7):1309.
[20] Pang Z, Niu F, O'Neill Z. Solar radiation prediction using recurrent neural network and artificial neural network: A case study with comparisons. Renew Energy 2020;156:279–89.
[21] Dong B, Lam K. A real-time model predictive control for building heating and cooling systems based on the occupancy behavior pattern detection and local weather forecasting. Build Simul 2014;7:89–106.
[22] Florita AR, Henze GP. Comparison of short-term weather forecasting models for model predictive control. HVAC&R Res 2009;15(5):835–53.
[23] Lago J, De Ridder F, De Schutter B. Forecasting spot electricity prices: Deep learning approaches and empirical comparison of traditional algorithms. Appl Energy 2018;221:386–405.
[24] Hatteland H. Sales forecasting. Technical University of Denmark; 2019.
[25] Vega Lara BG, Castellanos Molina LM, Monteagudo Yanes JP, Rodríguez Borroto MA. Offset-free model predictive control for an energy efficient tropical island hotel. Energy Build 2016;119:283–92.
[26] Taylor C, Leigh P, Price L, Young P, Vranken E, Berckmans D. Proportional-integral-plus (PIP) control of ventilation rate in agricultural buildings. Control Eng Pract 2004;12(2):225–33.
[27] Errouissi R, Al-Durra A, Muyeen SM, Leng S, Blaabjerg F. Offset-free direct power control of DFIG under continuous-time model predictive control. IEEE Trans Power Electron 2017;32(3):2265–77.
[28] Huusom JK, Poulsen NK, Jørgensen SB, Jørgensen JB. Tuning SISO offset-free Model Predictive Control based on ARX models. J Process Control 2012;22(10):1997–2007.
[29] Hagdrup M, Boiroux D, Mahmoudi Z, Madsen H, Poulsen NK, Poulsen B, et al. On the significance of the noise model for the performance of a linear MPC in closed-loop operation. IFAC-PapersOnLine 2016;49(7):171–6.
[30] Rawlings J, Mayne D, Diehl M. Model predictive control: Theory, computation, and design. 2017.
[31] Rossiter JA. Model-based predictive control: a practical approach. Boca Raton, Florida: CRC Press; 2003.
[32] Andersen KK, Madsen H, Hansen LH. Modelling the heat dynamics of a building using stochastic differential equations. Energy Build 2000;31(1):13–24.
[33] Zhang Y, Hanby V. Short-term prediction of weather parameters using online weather forecasts. In: IBPSA 2007 - international building performance simulation association 2007. 2007.
[34] Jung R, Maderitsch R. Structural breaks in volatility spillovers between international financial markets: Contagion or mere interdependence? J Bank Financ 2014;47:331–42.
[35] Bemporad A, Breschi V, Piga D, Boyd SP. Fitting jump models. Automatica 2018;96:11–21. http://dx.doi.org/10.1016/j.automatica.2018.06.022, URL: https://www.sciencedirect.com/science/article/pii/S0005109818303145.
[36] Andersen B, Eidorff S, Perdersen HLE, Rosenørn S, Valbjørn O. Meteorological data for design of building and installation: A reference year, no. 66. Tech. rep., Thermal Insulation Laboratory; 1977, Technical University of Denmark.
[37] WMO. Manual on codes. 3rd ed. World Meteorological Organization; 2019.
[38] Thilker CA. Optimization for smart energy systems [Master's thesis], Technical University of Denmark, Department of Applied Mathematics and Computer Science; 2020.
[39] Madsen H, Thyregod P. Inhomogenous Markov models for the variations in cloud cover. In: International conference on statistical climatology, vol. 3. 1986, p. 71–6, URL: http://imsc.pacificclimate.org/proceedings/3IMSC.pdf.
[40] Madsen H, Spliid H, Thyregod P. Markov models in discrete and continuous time for hourly observations of cloud cover. J. Clim Appl Meteorol 1985;24:629–39.
[41] Møller J, Madsen H. From state dependent diffusion to constant diffusion in stochastic differential equations by the lamperti transform. IMM-Technical report-2010-16, Technical University of Denmark, DTU Informatics, Building 321; 2010.
[42] Breinholt A, Møller JK, Madsen H, Mikkelsen PS. A formal statistical approach to representing uncertainty in rainfall–runoff modelling with focus on residual analysis and probabilistic output evaluation – Distinguishing simulation and prediction. J Hydrol 2012;472–473:36–52.
[43] Kristensen NR, Madsen H, Jørgensen SB. Parameter estimation in stochastic grey-box models. Automatica 2004;40(2):225–37.
[44] Brok NL, Madsen H, Jørgensen JB. Nonlinear model predictive control for stochastic differential equation systems. IFAC-PapersOnLine 2018;51(20):430–5, 6th IFAC Conference on Nonlinear Model Predictive Control NMPC 2018.
[45] Juhl R, Kristensen NR, Bacher P, Kloppenborg J, Madsen H. CTSM-R user guide. Technical University of Denmark; 2013.
[46] Nielsen LB, Prahm LP, Berkowicz R, Conradsen K. Net incoming radiation estimated from hourly global radiation and/or cloud observations. J Climatol 1981;1(3):255–72.
[47] Holtslag B, Ulden A. A simple scheme for daytime estimates of the surface fluxes from routine weather data. J Appl Meteorol 1983;22:517–29.
[48] Andersen LE. Stokastiske modeller af udetemperatur og stråling (Danish) [stochastic models for ambient air temperature and radiation] [Master's thesis], Technical University of Denmark; 1984.
[49] Madsen H. Statistically determined dynamical models for climate processes [Ph.D. thesis], Technical University of Denmark; 1985.
[50] Thilker CA, Junker RG, Bacher P, Jørgensen JB, Madsen H. Model predictive control based on stochastic differential equations. In: Ghiaus C, Amayri M, Ploix S, editors. Towards energy smart homes: algorithms, technologies, and applications. Springer; 2020, Publication expected in 2021.
[51] Maciejowski J. Predictive control with constraints. England: Prentice Hall; 2002.
[52] Junker RG, Kallesøe CS, Real JP, Howard B, Lopes RA, Madsen H. Stochastic nonlinear modelling and application of price-based energy flexibility. Appl Energy 2020;275:115096.
[53] Madsen H, Parvizi J, Halvgaard RF, Sokoler LE, Jørgensen JB, Hansen LH, et al. Control of electricity loads in future electric energy systems. In: Handbook of clean energy systems: intelligent energy systems, vol. 4. Wiley; 2015.
[54] Junker RG, Azar AG, Lopes RA, Lindberg KB, Reynders G, Relan R, et al. Characterizing the energy flexibility of buildings and districts. Appl Energy 2018;225:175–82.
[55] Clarke FH. The generalized problem of bolza. SIAM J Control Optim 1976;14(4):682–99.

# F Linear Quadratic Gaussian Control with Advanced Continuous-Time Disturbance Models for Building Thermal Regulation

Applied Energy 327 (2022) 120086

Contents lists available at ScienceDirect

Applied Energy

journal homepage: www.elsevier.com/locate/apenergy

# Linear quadratic Gaussian control with advanced continuous-time disturbance models for building thermal regulation

Christian Ankerstjerne Thilker *, John Bagterp Jørgensen, Henrik Madsen

*Technical University of Denmark, Department of Applied Mathematics and Computer Science, Asmussens Allé, Building 303B, DK-2800 Kgs. Lyngby, Denmark*

ARTICLE INFO

*Keywords:*
Linear quadratic Gaussian control
Stochastic differential equations
Non-linear disturbance models
Continuous-time
Smart energy systems

ABSTRACT

This paper introduces a linear quadratic control scheme for a continuous-time system with observations taken at discrete times. Particular attention is given to the derivation of the disturbance terms in the model. Control performance may depend critical on accurate disturbance forecasts. This is the case for building climate control, where solar rays pass through e.g. windows and deliver significant amounts of energy and the dynamics can be very fast, fluctuating, and spontaneous. We thus argue that it is critical for control performance to sufficiently describe and include disturbances in the control description to obtain satisfactory control accuracy. We suggest and derive in details a control framework based on continuous-time stochastic differential equations (SDEs) and linear quadratic Gaussian control using an advanced continuous-time disturbance model to supply disturbance forecasts. The numerical simulation results suggest that control with embedded forecasts handles uncertainties well and provides up to 26% performance improvements compared to standard disturbance mitigation techniques. Furthermore, we demonstrate that the quadratic controller has a useful trade-off between variability in the control signal, economic cost, and variability around the reference point.

## 1. Introduction

As the share of renewable energy in the electricity grid continues to grow, related problems become more prominent. Among these problems are misalignments in energy production and consumption, voltage overload, congestion, etc. The traditional solution up to modern times has been to control the production such that the electricity demand is covered. However, in an efficient implementation of future weather-driven energy systems, this is no longer an option. One solution is to focus on demand-response methodologies to unlock and control the flexibility at the consumer side [1,2]. A lot of recent work therefore centre around the concept known as *energy flexibility* [3,4]. The idea is to control the demand to align it with the production by utilising the inherent energy storage in households and buildings (such as thermal mass or stationary batteries), see e.g. [5] for an introduction and specific application examples. A key technology for enabling this solution is sophisticated predictive control of buildings. A well described energy flexibility setup involves a two-level control structure, where the upper-level controller (e.g. for voltage) computes a price signal which shifts the overall energy demand of the lower level controllers (e.g. individual buildings) to times where the CO2-concentration in the electricity mix is lower [2,6].

Linear quadratic regulation (LQR) is a very well studied and applied control scheme due to its optimal linear control law and simplicity [7,8]. The linear quadratic Gaussian (LQG) regulator extends the LQR scheme by also considering Gaussian system noise. Hence, LQG deals with the stochastic case of LQR, which may be closer to reality [9]. Disturbances also constitute an important aspect of control [10]. The literature identifies the solar radiation and ambient air temperature as critical factors dictating the heating and cooling needs for buildings [11,12]. Model-based predictive control (MPC) for smart energy systems is an active research area with many examples of e.g. conventional [13], stochastic [14] and robust MPC [15]. The use of LQG control in the literature is not as widely used for HVAC systems where often the simpler LQR scheme is used instead [16–20]. Furthermore, the common standard for mitigating disturbances in control (such as weather disturbances for buildings) is to apply offset-free regulation, see e.g. Errouissi et al. [21] or Taylor et al. [22] for applications in building climate control. Here, one introduces an additional integrating state that is able to cancel out a constant disturbance. LQG optimal control minimises the *quadratic deviation* of a linear transformation of the states to a set-point. Thus, compared to certainty-equivalent linear control (such as economic MPC with linear costs on constraint violations), LQG control inherently deals with uncertainty in a different manner. The quadratic penalty steers the *mean value* of the system state into the reference signal. Linear cost on the other hand steers the

* Corresponding author.
*E-mail addresses:* chant@dtu.dk (C.A. Thilker), jbjo@dtu.dk (J.B. Jørgensen), hmad@dtu.dk (H. Madsen).

https://doi.org/10.1016/j.apenergy.2022.120086
Received 28 February 2022; Received in revised form 22 September 2022; Accepted 30 September 2022
Available online 18 October 2022

*median* onto the reference point [23]. We discuss the differences and their consequences in more detail later.

For building climate control that uses weather forecasts, one of the dominating standards is to use meteorological forecasts [24]. Such forecasts have the advantage of giving relatively accurate forecasts potentially several days ahead. However, they typically do not include solar radiation forecasts and tend to be less accurate for short-term purposes [25,26]. Many examples of short-term forecasting models exist in the literature, such as linear regression-based models [27], artificial neural networks [28], and more advanced time series techniques [29]. Thilker et al. [10] propose an SDE-based model for predicting key attributes such as the solar radiation and outdoor air temperature. This form has the advantage that it fits naturally in the building model description (which is also formulated using SDEs). This paper shows the benefits of using an embedded model for disturbance forecasts in a LQG control setup for a residential building and highlights possible savings.

### 1.1. Main aim and contribution of the paper

This paper discusses the role of disturbances in dynamical systems in great details and relates it to building thermal control. We derive a zero-order hold discretised system and optimal control problem from the continuous-time system model of a building undergoing disturbances from the ambient air temperature and solar radiation. Furthermore, this paper develops a LQG control framework for a building thermal model with an embedded disturbance model that supplies short-term weather forecasts. We carry out a simulation study suggesting that the proposed LQG controller with embedded disturbance model performs almost as good as a controller that uses perfect disturbance forecasts.

### 1.2. Structure and outline of the paper

This paper has the following structure. Section 2 describes the standard LQG control scheme and derives the optimal control law and state estimate. Section 3 presents, motivates and derives the optimal control problem for the extended multi-step LQG control, which also includes the electricity prices and accounts for the weather disturbances. Section 5 presents the numerical simulation-based results and Section 6 summarises the findings and discusses future work and possibilities.

## 2. Continuous-time LQG control with embedded disturbance forecasts

This section introduces the continuous-time linear quadratic control problem. We start by describing the importance of conditional expectations of the future in predictive control. We also deal with the discretisation in time of the dynamics and the objective function and how to deal with disturbances in such discretisation. Zero-order hold is the dominating discretisation standard. However, such discretisation introduces additional error terms that may affect the performance, and thus are important to characterise. In this section, we discuss errors and their effects on the system.

In this paper, we denote time dependence in subscript $\boldsymbol{x}(t) = \boldsymbol{x}_t$ and we use $\boldsymbol{x}_k$ as short-hand notation for $\boldsymbol{x}_{t_k}$. This paper deals with continuous-discrete time state space models on the following form [30]

$$\mathrm{d}\boldsymbol{x}_t = \left(A_c\boldsymbol{x}_t + B_c\boldsymbol{u}_t + E_c\boldsymbol{d}_t\right)\mathrm{d}t + G_c\mathrm{d}\boldsymbol{\omega}_t \tag{1a}$$

$$\mathrm{d}\boldsymbol{d}_t = f_d(\boldsymbol{d}_t, t)\mathrm{d}t + g_d(\boldsymbol{d}_t, t)\mathrm{d}\boldsymbol{\omega}_t \tag{1b}$$

$$\boldsymbol{z}_t = H\boldsymbol{x}_t \tag{1c}$$

$$\boldsymbol{y}_k = C\boldsymbol{x}_k + \boldsymbol{v}_k\,, \quad \boldsymbol{v}_k \sim N(0, \Sigma) \tag{1d}$$

where $\boldsymbol{x}$, $\boldsymbol{u}$, and $\boldsymbol{d}$ are the system, input, and disturbance states, respectively. $A_c$, $B_c$ and $E_c$ are matrices governing the state evolution, input, and disturbances, respectively. $\boldsymbol{\omega}_t$ is standard Brownian motion, $\boldsymbol{y}_k$ is the observation, $\boldsymbol{v}_k$ is the observation noise, and $\boldsymbol{z}_t$ is the control variable. The disturbance model in (1b) is non-linear and can be used to forecast the disturbance states. Had the disturbances $\boldsymbol{d}_t$ been described by a linear model, we could couple the building and weather states into a single state space model $[\boldsymbol{x}_t^\intercal, \boldsymbol{d}_t^\intercal]^\intercal$. The weather is, however, governed by strong non-linearities and cannot be treated as a linear system, which is why it is necessary to uncouple them. Section 4.2 elaborates on this.

### 2.1. Relation between forecasting and control

In the following, let $\boldsymbol{z}_t$ be a continuous-time stochastic process (not necessarily the same as in Eq. (1)). The following term measures the expected $p$-order moment between $\boldsymbol{z}_t$ and a signal $\boldsymbol{g}_t$

$$\mathbb{E}[\|\boldsymbol{z}_t - \boldsymbol{g}_t\|_p^p \mid \mathcal{Y}_k]\,, \tag{2}$$

where $\|\cdot\|_p$ is the usual $p$-norm of vectors, $p \geq 1$, and $\mathcal{Y}_k = \{y_0, y_1, \dots, y_k\}$ is all historic observations up till time $t_k$. Putting $p = 2$, we obtain the non-central second order moment. Such an objective measures the *variance* of a process. Now, let $\boldsymbol{g}_t$ be controllable in the sense given in [31]. Given information until time $t_k$, we can write the minimum-variance optimal control problem as

$$\min_{\boldsymbol{g}_t} \quad \phi_k = \int_{t_k}^{t_k+T} \mathbb{E}[\|\boldsymbol{z}_t - \boldsymbol{g}_t\|_2^2 | \mathcal{Y}_k]\,\mathrm{d}t\,, \tag{3}$$

The optimal minimiser of the minimum-variance problem (3) can be shown to be the conditional expectation, $\boldsymbol{g}_t = \mathbb{E}[\boldsymbol{z}_t|\mathcal{Y}_k]$:

$$\begin{aligned}
&\mathbb{E}\left[\|\boldsymbol{z}_t - \boldsymbol{g}_t\|_2^2 \mid \mathcal{Y}_k\right] \\
&\quad = \mathbb{E}[\|\boldsymbol{z}_t - \boldsymbol{g}_t + \mathbb{E}\left[\boldsymbol{z}_t|\mathcal{Y}_k\right] - \mathbb{E}\left[\boldsymbol{z}_t|\mathcal{Y}_k\right]\|_2^2 \mid \mathcal{Y}_k] \\
&\quad = \mathbb{V}\left[\boldsymbol{z}_t|\mathcal{Y}_k\right] + \|\mathbb{E}[\boldsymbol{z}_t|\mathcal{Y}_k] - \boldsymbol{g}_t\|_2^2\,,
\end{aligned}$$

where $\mathbb{V}\left[\boldsymbol{z}_t|\mathcal{Y}_k\right]$ denotes the conditional variance with respect to $\mathcal{Y}_k$. The above attains its minimum exactly for $\boldsymbol{g}_t = \mathbb{E}[\boldsymbol{z}_t|\mathcal{Y}_k]$. This implies that we need to use conditional expectations to solve stochastic control problems with a quadratic cost function as in (3). Hence, we need to estimate the following

$$\mathbb{E}[\{\boldsymbol{z}_t : t \geq t_k\} \mid \mathcal{Y}_k] = \{\hat{\boldsymbol{z}}_{t|t_k} : t \geq t_k\}\,. \tag{4}$$

For linear systems with Gaussian noise, the Kalman filter is an optimal estimator of the conditional expectation. In a discrete form (which we derive in Section 2.2), the continuous-time system in Eq. (1) can be written

$$\mathbb{E}[\boldsymbol{x}_{t_{k+1}} \mid \mathcal{Y}_k] = A\hat{\boldsymbol{x}}_{k|k} + B\boldsymbol{u}_k + E\hat{\boldsymbol{d}}_{k|k}\,. \tag{5}$$

Since the conditional expectation of the system state depends on disturbances, $\boldsymbol{d}_t$, we also need forecasts of the conditional expectations of these to do optimal predictive control. That is, we need to supply the following forecasts of the disturbances to the optimal control problem

$$\mathbb{E}[\{\boldsymbol{d}_{k+i}\}_{i=0}^{N-1} \mid \mathcal{Y}_k] = \{\hat{\boldsymbol{d}}_{k+i|k}\}_{i=0}^{N-1}\,. \tag{6}$$

Note that putting $p = 1$ in (2) yields the absolute value, for which the median of $\boldsymbol{z}_t$ is the optimal minimiser. By tilting the absolute value function appropriately, certain quantiles become the minimiser. This knowledge can be very useful in forming the right objective function to mimic the desired behaviour of the system. It might be that one side of the reference trajectory is a very expensive operational area, and thus shaping the objective to make the reference trajectory align with the 99% quantile may be appropriate.

The quadratic objective function thus measures the squared norm of deviation between the conditional expectation of the stochastic process and the signal $\boldsymbol{g}_t$. However, as we shall also do in the present paper, it is

very common to include additional terms in the quadratic cost function in (2) [23] such that the problem becomes

$$\phi_k = \int_{t_k}^{t_k+T} \mathbb{E}[\underbrace{\|\boldsymbol{z}_t - \boldsymbol{r}_t\|_Q^2}_{\text{objective}} + \underbrace{\|\bar{\boldsymbol{u}}_t - \boldsymbol{u}_t\|_R^2}_{\text{regularisation}} + \underbrace{\boldsymbol{c}_t^\mathsf{T}\boldsymbol{u}_t}_{\text{economic cost}} \mid \mathcal{Y}_k] \tag{7}$$

where $\boldsymbol{r}_t$ is a reference trajectory, $\boldsymbol{u}_t$ is the control signal, and $\boldsymbol{c}_t$ is a cost related to the input at time $t$. The subscripts $Q$ and $R$ denotes the weighted 2-norm (with weights $Q$ and $R$). For energy systems, this objective is appropriate for stabilising e.g. voltages in grids, aligning energy consumption of building stocks etc. The first regularisation term reflects the cost of the input deviating too much from a desired reference point. The second term typically reflects some economic costs related to input in time. In the context of building thermal control using a heat pump, the latter can be the electricity price related to the heat pump operations.

### 2.2. Discretisation of the continuous-time dynamics

In this section, we derive a discretisation of the continuous time dynamical system in (1). Due to the discrete nature of the way computers perform numerics, it is necessary to somehow discretise the optimisation problem in (7). For energy systems, the disturbances typically play an important role and are themselves encumbered with uncertainty. We shall therefore put extra attention towards how to handle the disturbance term in (1), $E_c\boldsymbol{d}_t$, in the discretisation.

Let $T_s$ be the sample time between the control points, $T_s = t_{k+1} - t_k$. We assume that the input $\boldsymbol{u}$ is constant during the time intervals $[t_k, t_{k+1}[$ for all $k \in \mathbb{N}$, i.e. zero-order hold. The solution to $\boldsymbol{x}_t$ in (1) gets the form

$$\boldsymbol{x}_{t_{k+1}} = A\boldsymbol{x}_{t_k} + B\boldsymbol{u}_k + \int_{t_k}^{t_{k+1}} \exp\left(A_c(t_{k+1}-\tau)\right) E_c\boldsymbol{d}_\tau \mathrm{d}\tau + \boldsymbol{\xi}_k, \tag{8}$$

where the matrices $A$, $B$ and process noise $\boldsymbol{\xi}_k$ are defined by

$$\begin{aligned} A &= \exp\left(A_c T_s\right), \\ B &= \int_0^{T_s} \exp\left(A_c\tau\right) B_c \mathrm{d}\tau, \\ \boldsymbol{\xi}_k &= \int_{t_k}^{t_{k+1}} \exp\left(A_c(t_{k+1}-\tau)\right) G_c \mathrm{d}\boldsymbol{\omega}(\tau). \end{aligned} \tag{9}$$

$A$ and $B$ in (9) have known closed-form solutions and are easy to compute. However, it is not straightforward how to deal with the integral $\int_{t_k}^{t_{k+1}} \exp\left(A_c(t_{k+1}-\tau)\right) E_c\boldsymbol{d}_\tau \mathrm{d}\tau$ in (8). The rest of this section deals with this integral when disturbance forecasts are supplied as zero-order hold values.

As Section 4 describes, the embedded disturbance model in (1b) estimates the *mean value* of the disturbances between time samples $[t_k, t_{k+1}[$, that is

$$\bar{\boldsymbol{d}}_k = \hat{\boldsymbol{d}}_{k|k} + \boldsymbol{\epsilon}_k, \quad t \in [t_k, t_{k+1}[. \tag{10}$$

$\bar{\boldsymbol{d}}_k$ is the true mean value of the disturbances, $\hat{\boldsymbol{d}}_{k|k} = \mathbb{E}[\bar{\boldsymbol{d}}_k \mid \mathcal{Y}_k]$ is the conditional mean value supplied by the disturbance model given observations up till time $t_k$, and $\boldsymbol{\epsilon}_k$ is *i.i.d.* Gaussian distributed white noise. To rewrite the system in (1) with the weather predictions, we can rewrite the integral in (8) as

$$\int_{t_k}^{t_{k+1}} \exp\left(A_c(t_{k+1}-\tau)\right) E_c\left(\boldsymbol{d}_\tau + \bar{\boldsymbol{d}}_k - \bar{\boldsymbol{d}}_k\right) \mathrm{d}\tau, \tag{11a}$$

$$= E\bar{\boldsymbol{d}}_k + \int_{t_k}^{t_{k+1}} \exp\left(A_c(t_{k+1}-\tau)\right) E_c\left(\boldsymbol{d}_\tau - \bar{\boldsymbol{d}}_k\right) \mathrm{d}\tau, \tag{11b}$$

$$= E\hat{\boldsymbol{d}}_{k|k} + E\boldsymbol{\epsilon}_k + \int_{t_k}^{t_{k+1}} \exp\left(A_c(t_{k+1}-\tau)\right) E_c\left(\boldsymbol{d}_\tau - \bar{\boldsymbol{d}}_k\right) \mathrm{d}\tau, \tag{11c}$$

$$= E\hat{\boldsymbol{d}}_{k|k} + E\boldsymbol{\epsilon}_k + \boldsymbol{\zeta}_k, \tag{11d}$$

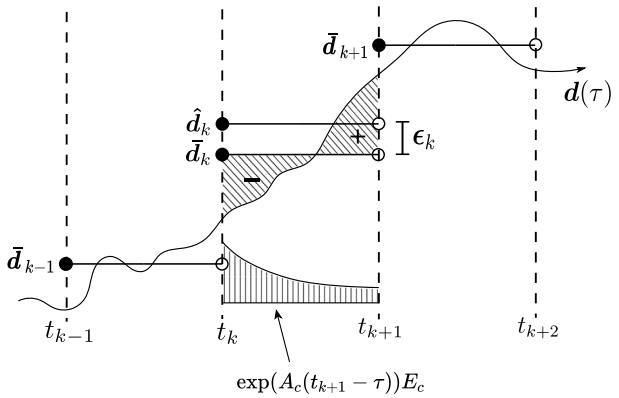


**Fig. 1.** An illustration of the calculations of the model discretisation. The disturbance model estimates the mean value in the time sample $[t_k, t_{k+1}]$. The slanted hatched area indicates the factor $\boldsymbol{d}_t - \bar{\boldsymbol{d}}_k$ and the vertical hatched area shows the exponential factor (in 1 dimension) in the integral in (11c).

$$\approx E\hat{\boldsymbol{d}}_{k|k} + E\boldsymbol{\epsilon}_k + 0, \tag{11e}$$

where $E = \int_0^{T_s} \exp\left(A_c\tau\right) E_c \mathrm{d}\tau$. In (11e), it is assumed (wrongfully) that the disturbances act constantly on the system such that $\boldsymbol{d}_\tau - \bar{\boldsymbol{d}}_k = 0$ and the integral $\boldsymbol{\zeta}_k = \int_{t_k}^{t_{k+1}} \exp\left(A_c(t_{k+1}-\tau)\right) E_c\left(\boldsymbol{d}_\tau - \bar{\boldsymbol{d}}_k\right) \mathrm{d}\tau = 0$ vanishes. The term $\boldsymbol{\zeta}_k$ can be thought of as the error related to the zero-order hold discretisation. Fig. 1 depicts the calculations involved in (11). The hatched areas indicate the two factors in the integral in (11c) between two time samples $t_k$ and $t_{k+1}$. It becomes evident that the integral of the product of the two terms in general is not zero. Unfortunately, the disturbance processes are strongly non-linear and behave indescribably, which implies that $\boldsymbol{d}_\tau - \bar{\boldsymbol{d}}_k$ becomes correlated in time (as Fig. 1 illustrates). For this reason, the easiest solution is to neglect the error as in (11e). Since the uncertainty of the disturbances is described by Brownian motions, it is possible to characterise the uncertainty of the disturbances between time samples using a Brownian bridge. In such a setup, by conditioning the Brownian bridge on attaining the estimated disturbance values at times $\{t_k, t_{k+1}\}$, the disturbance process between the time steps is Gaussian. It is then straight forward to compute uncertainties and densities for the disturbances at all points in time.

Inserting (11e) into (8) gives us the system

$$\boldsymbol{x}_{k+1} = A\boldsymbol{x}_k + B\boldsymbol{u}_k + E\hat{\boldsymbol{d}}_{k|k} + E\boldsymbol{\epsilon}_k + \boldsymbol{\xi}_k, \tag{12}$$

with $\boldsymbol{x}_k = \boldsymbol{x}_{t_k}$ and $\boldsymbol{\epsilon}_k \sim N(0, W_1)$ and $\boldsymbol{\xi}_k \sim N(0, W_2)$. $W_1$ is the covariance of the uncertainty related to the disturbance estimate and $W_2 = \int_0^{T_s} \exp\left(A_c\tau\right) G_c G_c^\mathsf{T} \exp\left(A_c^\mathsf{T}\tau\right) \mathrm{d}\tau$. Aggregating the noise terms, $\boldsymbol{w}_k = E\boldsymbol{\epsilon}_k + \boldsymbol{\xi}_k$, gives the conventional discrete-time stochastic state space system

$$\boldsymbol{x}_{k+1} = A\boldsymbol{x}_k + B\boldsymbol{u}_k + E\hat{\boldsymbol{d}}_{k|k} + \boldsymbol{w}_k. \tag{13}$$

It immediately reveals that the computation of $\mathbb{E}[\boldsymbol{x}_{k+i} \mid \mathcal{Y}_k]$, $i = 1, \ldots, N$ requires conditional mean forecasts of the disturbances.

#### 2.2.1. Error quantification of the discretisation

Since $\boldsymbol{\zeta}_k$ is difficult to determine, the easiest solution is to disregard it. But can we say something about the error we make by this simplification? The discretised system (with all its terms) gets the form:

$$\boldsymbol{x}_{k+1} = A\boldsymbol{x}_k + B\boldsymbol{u}_k + E\hat{\boldsymbol{d}}_{k|k} + E\boldsymbol{\epsilon}_k + \boldsymbol{\xi}_k + \boldsymbol{\zeta}_k, \tag{14}$$

where $\boldsymbol{\zeta}_k = \int_{t_k}^{t_{k+1}} \exp\left(A_c(t_{k+1}-\tau)\right) E_c\left(\boldsymbol{d}_\tau - \bar{\boldsymbol{d}}_k\right) \mathrm{d}\tau$. The error term $\boldsymbol{\zeta}_k$ can be bounded by the following:

$$\|\boldsymbol{\zeta}_k\|_2^2 \leq \int_{t_k}^{t_{k+1}} \|\exp\left(A_c(t_{k+1}-\tau)\right)\|_F^2 \mathrm{d}\tau \cdot \|E\|_F^2$$

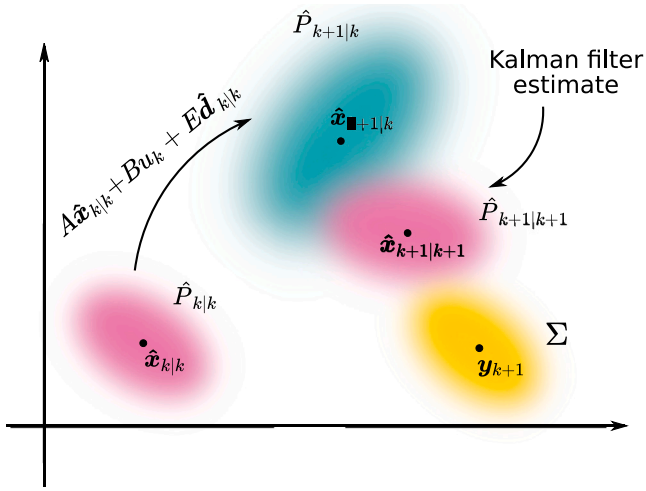


**Fig. 2.** Due to the Gaussian noise acting on the system, we do not know the deterministic position of the system — instead, the position is given by a Gaussian density, centred around $\hat{x}_{k|k}$.

$$\cdot \max_{\tau}\{\|d_\tau - \bar{d}_k\|_2^2\} \tag{15a}$$

$$\leq \Delta t_k \cdot \max_{\tau}\{\|\exp\left(A_c(t_{k+1}-\tau)\right)\|_F^2\} \cdot \|E_c\|_F^2 \cdot \max_{\tau}\{\|d_\tau - \bar{d}_k\|_2^2\} \tag{15b}$$

The first two norms of (15b) are related to the singular values of the dynamics $A$ and $E$—i.e. if the dynamics are fast, the error might be larger (due to the matrix exponential that acts as a weighting factor) and vice versa. The last term relates the error to the maximum quadratic variation between the continuous process $d_\tau$ and its mean value in the interval $[t_k, t_{k+1}[$. Note that the error term $\|\zeta_k\|_2^2$ scales linearly in time, in line with the variance of a standard Brownian motion. Also note that had the weighting factor $\exp\left(A_c(t_{k+1}-\tau)\right)$ not been present, the integral would simply vanish. It is hence the system's dynamical influence that causes the error of the zero order hold.

### 2.3. Discretisation of the continuous-time objective function

The objective function has the purpose of weighting the performance of control solutions to make them comparable. E.g., typically, the purpose of controlling the indoor air temperature of a building is to maintain a comfortable temperature while minimising the electricity consumption and/or price (and perhaps more criteria such as variations in the input signal). It is thus a tuning problem to correctly weight the contributions to mimic desired behaviour.

In the previous subsection, we obtained the system on a discrete-time form using a zero-order hold discretisation scheme. This has the advantage of parameterising the input signal as a set of values $\{\boldsymbol{u}_{k+i}\}_{i=0}^{N-1}$, which is numerically tractable in an optimisation problem. Given information up until time $t_k$, $\mathcal{Y}_k = \{\boldsymbol{y}_0, \boldsymbol{y}_1, \dots, \boldsymbol{y}_k\}$ the finite-horizon continuous-time LQG control objective function from Eq. (7) gets the form

$$\mathbb{E}\left[\int_{t_k}^{t_k+T} \frac{1}{2}(\boldsymbol{z}_t - \boldsymbol{r}_t)^\intercal Q(\boldsymbol{z}_t - \boldsymbol{r}_t) + \frac{1}{2}(\bar{\boldsymbol{u}}_t - \boldsymbol{u}_t)^\intercal R(\bar{\boldsymbol{u}}_t - \boldsymbol{u}_t) + \boldsymbol{c}_t^\intercal \boldsymbol{u}_t \mathrm{d}t \,\middle|\, \mathcal{Y}_k\right], \tag{16}$$

where $\boldsymbol{r}_t$ and $\bar{\boldsymbol{u}}_t$ are reference trajectories. Note that we employ the weighted 2-norm. How to discretise the objective function is not straight forward and can be done in multiple ways. In general, the discretisation is an approximation of the continuous-time objective. However, in the linear-quadratic case, an exact discretisation exists [32]. The derivation is tedious, though, and if the time between samples and control inputs is small, the integral can be approximated well by an Euler discretisation, i.e. evaluating the objective function point-wise. Let

$$t_k \leq t_{k+1} \leq \cdots \leq t_{k+N} = t_k + T \tag{17}$$

be a partition of the future control times of the system. We discretise the objective function point-wise such that the integral in (16) becomes a sum over the values at the time points in (17)

$$\phi = \mathbb{E}\left[\sum_{i=k}^{k+N-1} \underbrace{\frac{1}{2}(\boldsymbol{z}_i - \boldsymbol{r}_i)^\intercal Q(\boldsymbol{z}_i - \boldsymbol{r}_i)}_{\phi_1} + \underbrace{\frac{1}{2}(\bar{\boldsymbol{u}}_i - \boldsymbol{u}_i)^\intercal R(\bar{\boldsymbol{u}}_i - \boldsymbol{u}_i) + \boldsymbol{c}_i^\intercal \boldsymbol{u}_i}_{\phi_2} \,\middle|\, \mathcal{Y}_k\right]. \tag{18}$$

Using that $\boldsymbol{z}_i = H\boldsymbol{x}_i$, the first term in the sum simplifies to

$$\phi_1 = \sum_{i=k}^{k+N-1} \frac{1}{2}\boldsymbol{x}_i^\intercal Q'\boldsymbol{x}_i + \boldsymbol{s}_i^\intercal \boldsymbol{x}_k + \frac{1}{2}\boldsymbol{r}_k^\intercal Q \boldsymbol{r}_k \tag{19}$$

where $Q' = H^\intercal Q H$ and $\boldsymbol{s}_i^\intercal = -\boldsymbol{r}_i^\intercal Q H$. The second part of the objective function equivalently has the form

$$\phi_2 = \sum_{i=k}^{k+N-1} \frac{1}{2}\boldsymbol{u}_i^\intercal R\boldsymbol{u}_i + \bar{\boldsymbol{u}}_i^\intercal R\boldsymbol{u}_i + \frac{1}{2}\bar{\boldsymbol{u}}_i^\intercal R\bar{\boldsymbol{u}}_i \tag{20}$$

The combined discretised objective function (where we omit terms that are independent of the system state or the input signal) is

$$\phi_d = \mathbb{E}\left[\sum_{i=k}^{k+N-1} \frac{1}{2}\boldsymbol{x}_i^\intercal Q'\boldsymbol{x}_i + \boldsymbol{s}_i^\intercal \boldsymbol{x}_i + \frac{1}{2}\boldsymbol{u}_i^\intercal R\boldsymbol{u}_i + \bar{\boldsymbol{u}}_i^\intercal R\boldsymbol{u}_i + \boldsymbol{c}_i^\intercal \boldsymbol{u}_i \,\middle|\, \mathcal{Y}_k\right]. \tag{21}$$

## 3. Solution to the LQG control problem with embedded disturbance model

The previous section presented and derived the discretisation of the system dynamics and objective function to make computations tractable for the computer. There are multiple ways to solve the LQG optimal control problem. Singh and Pal [33] derive an optimal linear feedback law based on the current state and future disturbance input — an extension to the classical LQR feedback law. However, such laws are not able to deal with constraints, which requires (in general) numerical solvers to solve. In this section, we derive solutions to the finite horizon constrained LQG optimal control problem.

When dealing with stochastic systems as in (1) governed by both Gaussian system and observation noise, the LQG control problem can be divided into two sub-problems due to the *separation principle* (under certain conditions) [34]. Given a noisy observation of the system, $\boldsymbol{y}_k$, the steps are

1. Reconstruct the system states, $\boldsymbol{x}_k$, using the regular Kalman filter (which is an optimal state estimator in the linear case with Gaussian noise), i.e. $\hat{\boldsymbol{x}}_{k|k} = \mathbb{E}[\boldsymbol{x}_k|\mathcal{Y}_k]$
2. Solve the LQG optimal control problem using the reconstruction as a certainty-equivalent state estimate.

The LQR and LQG optimal control problems are special cases when it comes to their solutions and ability to separate the estimation and optimal control problems. This section presents and solves both problems.

### 3.1. State estimation (filter)

Due to the Gaussian error term in (13), $\boldsymbol{w}_k = E\boldsymbol{\epsilon}_k + \boldsymbol{\xi}_k$, the system experiences random forces that pushes it away from its deterministic path given by the linear system in Eq. (5). We thus do not know the exact position of the system. To estimate the system state, filters and observers are common choices [30,35]. However, in case of a linear state space model with Gaussian process noise, the Kalman filter provides an *optimal state estimator*. It estimates a distribution of the system state at time $t_k$, $(\boldsymbol{x}_k \mid \mathcal{Y}_k) \sim N(\hat{\boldsymbol{x}}_{k|k}, \hat{P}_{k|k})$ given the past observations. Fig. 2 depicts the distributional development in the Kalman filter update: We start out with an initial state estimate at time $t_k$ given by a distribution $N(\hat{\boldsymbol{x}}_{k|k}, \hat{P}_{k|k})$. The system development gives a predicted estimate of the successive state, $(\boldsymbol{x}_{k+1} \mid \mathcal{Y}_k) \sim N(\hat{\boldsymbol{x}}_{k+1|k}, \hat{P}_{k+1|k})$. When the next observation, $\boldsymbol{y}_{k+1}$, becomes available, the Kalman filter combines the system prediction and the observation at time $t_{k+1}$, to compute the optimal system state estimate, $(\boldsymbol{x}_{k+1} \mid \mathcal{Y}_{k+1}) \sim N(\hat{\boldsymbol{x}}_{k+1|k+1}, \hat{P}_{k+1|k+1})$.

Algorithm 1 lists the necessary computational steps in the Kalman filter to update the system state distribution.

**Algorithm 1** Kalman Filter

**require:** $\boldsymbol{y}_k$, $\hat{\boldsymbol{u}}_{k-1|k-1}$, $\hat{\boldsymbol{d}}_{k-1|k-1}$, $\hat{\boldsymbol{x}}_{k-1|k-1}$, $\hat{P}_{k-1|k-1}$

**Prediction:**
Compute one-step Kalman predictions
$\hat{\boldsymbol{x}}_{k|k-1} = A\hat{\boldsymbol{x}}_{k-1|k-1} + B\hat{\boldsymbol{u}}_{k-1|k-1} + E\hat{\boldsymbol{d}}_{k-1|k-1}$
$\hat{P}_{k|k-1} = A\hat{P}_{k-1|k-1}A^\top + Q$

**Filter:**
Compute estimated process noise and Kalman gain
$\Sigma_{k|k-1} = C\hat{P}_{k|k-1}C^\top + \Sigma$
$K_k = \hat{P}_{k|k-1}C^\top \Sigma^{-1}_{k|k-1}$

Compute filtered estimates
$\hat{\boldsymbol{y}}_{k|k-1} = C\hat{\boldsymbol{x}}_{k|k-1}$
$\hat{\boldsymbol{x}}_{k|k} = \hat{\boldsymbol{x}}_{k|k-1} + K_k(\boldsymbol{y}_k - \hat{\boldsymbol{y}}_{k|k-1})$
$\hat{P}_{k|k} = (I - K_kC)\hat{P}_{k|k-1}(I - K_kC)^\top + K_k\Sigma K_k^\top$

**return** $\hat{\boldsymbol{x}}_{k|k}$, $\hat{P}_{k|k}$

### 3.2. Solution to the LQG optimal control problem

Consider the following finite horizon, inequality constrained optimal control problem given $\hat{\boldsymbol{x}}_{k|k}$ and $\{\hat{\boldsymbol{d}}_{k+j|k}\}_{j=0}^{N-1}$,

$$\boldsymbol{U}_k^* \,\Big|\, \hat{\boldsymbol{x}}_{k|k}, \{\hat{\boldsymbol{d}}_{k+j|k}\}_{j=0}^{N-1} = \underset{\boldsymbol{u}_0,\dots,\boldsymbol{u}_{N-1}}{\arg\min} \quad \phi_k \tag{22a}$$

$$\text{s.t.} \quad \hat{\boldsymbol{x}}_{i+1} = A\hat{\boldsymbol{x}}_i + B\hat{\boldsymbol{u}}_i + E\hat{\boldsymbol{d}}_{k+i|k}, \tag{22b}$$

$$\hat{\boldsymbol{x}}_0 = \hat{\boldsymbol{x}}_{k|k} \tag{22c}$$

$$\boldsymbol{u}_{\min} \le \boldsymbol{u}_i \le \boldsymbol{u}_{\max} \tag{22d}$$

$$\Delta\boldsymbol{u}_{\min} \le \Delta\boldsymbol{u}_i \le \Delta\boldsymbol{u}_{\max} \tag{22e}$$

$$i = 0, \dots, N-1, \tag{22f}$$

with the discrete-time objective function

$$\phi_k = \mathbb{E}\left[\sum_{i=k}^{N-1+k} \frac{1}{2}\hat{\boldsymbol{x}}_i^\top Q'\hat{\boldsymbol{x}}_i + \boldsymbol{s}_i^\top\hat{\boldsymbol{x}}_i + \frac{1}{2}\boldsymbol{u}_i^\top R\boldsymbol{u}_i - \bar{\boldsymbol{u}}_i^\top R\boldsymbol{u}_i + \boldsymbol{c}_i^\top\boldsymbol{u}_i \,\Big|\, \mathcal{Y}_k\right]. \tag{23}$$

We solve the optimal control problem in (22) by introducing a notation for the system for all points in time from $k = 0, \dots, N-1$.

$$\hat{\boldsymbol{X}}_{k+1} = \Phi\hat{\boldsymbol{x}}_{k|k} + \Gamma_u\boldsymbol{U}_k + \Gamma_d\hat{\boldsymbol{D}}_k \tag{24}$$

where the matrices and vectors are

$$\begin{aligned}
\hat{\boldsymbol{X}}_{k+1} &= \left[\hat{\boldsymbol{x}}_{k+1|k}^\top, \dots, \hat{\boldsymbol{x}}_{k+N|k}^\top\right]^\top \\
\boldsymbol{U}_k &= \left[\boldsymbol{u}_{k|k}^\top, \dots, \boldsymbol{u}_{k+N-1|k}^\top\right]^\top \\
\hat{\boldsymbol{D}}_k &= \left[\hat{\boldsymbol{d}}_{k|k}^\top, \dots, \hat{\boldsymbol{d}}_{k+N-1|k}^\top\right]^\top \\
\boldsymbol{S}_k &= \left[\boldsymbol{s}_k^\top, \boldsymbol{s}_{k+1}^\top, \dots, \boldsymbol{s}_{k+N-1}^\top\right]^\top \\
\Phi &= \left[A^\top, (A^2)^\top, \dots, (A^N)^\top\right]^\top \\
\Gamma_u &= \begin{bmatrix} B & 0 & \dots & 0 \\ AB & B & \dots & 0 \\ A^2B & AB & \ddots & \vdots \\ \vdots & \vdots & \ddots & 0 \\ A^{N-1}B & A^{N-2}B & \dots & B \end{bmatrix} \\
\Gamma_d &= \begin{bmatrix} E & 0 & \dots & 0 \\ AE & E & \dots & 0 \\ A^2E & AE & \ddots & \vdots \\ \vdots & \vdots & \ddots & 0 \\ A^{N-1}E & A^{N-2}E & \dots & E \end{bmatrix}
\end{aligned} \tag{25}$$

We also introduce the vector containing the prediction errors $\boldsymbol{\epsilon}_{k+i|k} = \hat{\boldsymbol{x}}_{k+i|k} - \boldsymbol{x}_{k+i}$, $i \in \mathbb{N}$, which are due to the Gaussian error term in (13), $\boldsymbol{w}_k = E\boldsymbol{\epsilon}_k + \boldsymbol{\xi}_k$,

$$\boldsymbol{\epsilon}_k = \left[\boldsymbol{\epsilon}_{k+1|k}^\top, \dots, \boldsymbol{\epsilon}_{k+N|k}^\top\right]^\top \tag{26}$$

Inserting the new notation in to the objective function ultimately isolates the stochasticity to the prediction errors (the predictions and prediction errors are independent under the linear quadratic assumption)

$$\begin{aligned}
\phi_k &= \mathbb{E}\left[\frac{1}{2}\left(\hat{\boldsymbol{X}}_{k+1} + \boldsymbol{\epsilon}\right)^\top\bar{Q}\left(\hat{\boldsymbol{X}}_{k+1} + \boldsymbol{\epsilon}_k\right) + \boldsymbol{S}_k^\top\left(\hat{\boldsymbol{X}}_{k+1} + \boldsymbol{\epsilon}_k\right)\right. \\
&\qquad \left. + \frac{1}{2}\boldsymbol{U}_k^\top\bar{R}\boldsymbol{U}_k - \bar{\boldsymbol{U}}_k^\top\bar{R}\boldsymbol{U}_k + \bar{\boldsymbol{C}}_k^\top\boldsymbol{U}_k \,\Big|\, \mathcal{Y}_k\right] \\
\phi_k &= \frac{1}{2}\hat{\boldsymbol{X}}_{k+1}^\top\bar{Q}\hat{\boldsymbol{X}}_{k+1} + \boldsymbol{S}_k^\top\hat{\boldsymbol{X}}_{k+1} + \frac{1}{2}\boldsymbol{U}_k^\top\bar{R}\boldsymbol{U}_k - \bar{\boldsymbol{U}}_k^\top\bar{R}\boldsymbol{U}_k \\
&\qquad + \bar{\boldsymbol{C}}_k^\top\boldsymbol{U}_k + \mathbb{E}\left[\frac{1}{2}\boldsymbol{\epsilon}_k^\top\bar{Q}\boldsymbol{\epsilon}_k + \boldsymbol{S}_k^\top\boldsymbol{\epsilon}_k \,\Big|\, \mathcal{Y}_k\right],
\end{aligned} \tag{27}$$

where $\bar{Q} = \operatorname{diag}(Q', \dots, Q')$, $\bar{R} = \operatorname{diag}(R, \dots, R)$, and $\bar{\boldsymbol{C}}_k = \left[\boldsymbol{c}_k^\top, \dots, \boldsymbol{c}_{k+N-1}^\top\right]^\top$. Since the last term does not depend on $\boldsymbol{U}$, we can omit it in the optimisation problem. The next step is to insert (24) into the cost function

$$\begin{aligned}
\phi_k &= \frac{1}{2}\left(\Phi\hat{\boldsymbol{x}}_{k|k} + \Gamma_u\boldsymbol{U}_k + \Gamma_d\hat{\boldsymbol{D}}_k\right)^\top\bar{Q}\left(\Phi\hat{\boldsymbol{x}}_{k|k} + \Gamma_u\boldsymbol{U}_k\right. \\
&\quad \left. + \Gamma_d\hat{\boldsymbol{D}}_k\right) + \boldsymbol{S}_k^\top\left(\Phi\hat{\boldsymbol{x}}_{k|k} + \Gamma_u\boldsymbol{U}_k + \Gamma_d\hat{\boldsymbol{D}}_k\right) \\
&\quad + \frac{1}{2}\boldsymbol{U}_k^\top\bar{R}\boldsymbol{U}_k - \bar{\boldsymbol{U}}_k^\top\bar{R}\boldsymbol{U}_k + \bar{\boldsymbol{C}}_k^\top\boldsymbol{U}_k.
\end{aligned} \tag{28}$$

Notice that we eliminated the equality constraints (22b) since they are now embedded in the cost function. We can write the objective, $\phi_k$, as a quadratic function in $\boldsymbol{U}_k$

$$\tilde{\phi}_k = \frac{1}{2}\boldsymbol{U}_k^\top P\boldsymbol{U}_k + \boldsymbol{q}^\top\boldsymbol{U}_k, \tag{29}$$

with the matrix and vector

$$\begin{aligned}
P &= (\Gamma_u^\top\bar{Q}\Gamma_u + \bar{R}) \\
\boldsymbol{q} &= (\Gamma_u^\top\bar{Q}\Phi\hat{\boldsymbol{x}}_{k|k} + \Gamma_u^\top\bar{Q}\Gamma_d\hat{\boldsymbol{D}}_k + \Gamma_u^\top\boldsymbol{S}_k + \bar{\boldsymbol{C}}_k - \bar{R}\bar{\boldsymbol{U}}_k)
\end{aligned}$$

That is, the optimisation problem in (22) is equivalent to the following convex quadratic programme

$$\begin{aligned}
\boldsymbol{U}_k^* \,\Big|\, \hat{\boldsymbol{x}}_{k|k}, \{\hat{\boldsymbol{d}}_{k+j|k}\}_{j=0}^{N-1} &= \underset{\boldsymbol{u}_0,\dots,\boldsymbol{u}_{N-1}}{\arg\min} \quad \tilde{\phi}_k \\
\text{s.t.} \quad & \boldsymbol{u}_{\min} \le \boldsymbol{u}_i \le \boldsymbol{u}_{\max} \\
& \Delta\boldsymbol{u}_{\min} \le \Delta\boldsymbol{u}_i \le \Delta\boldsymbol{u}_{\max} \\
& i = 0, \dots, N-1
\end{aligned} \tag{30}$$

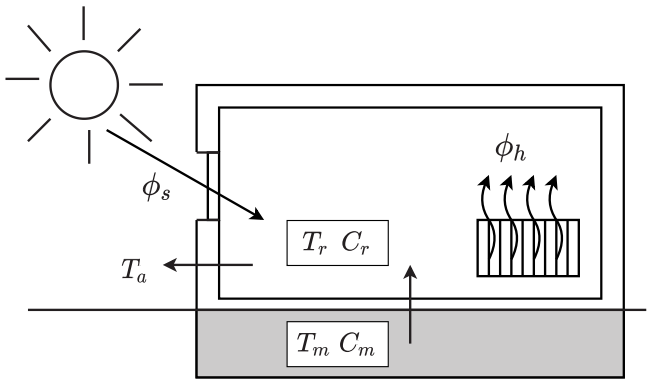


**Fig. 3.** A diagram of the smart building model and the interactions. The room air exchanges heat with the floor and the ambient air and is heated by electrical heaters. The solar radiation enters through the windows and typically delivers significant amounts of heat.

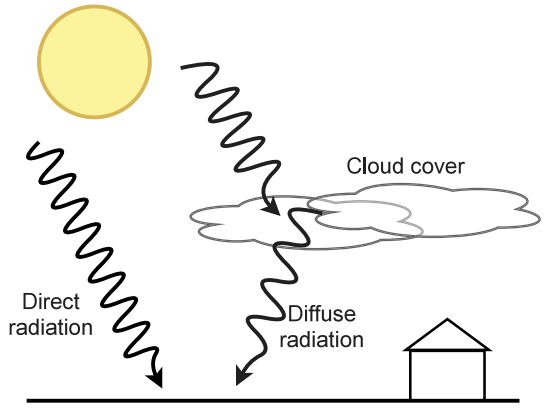


(a) The solar radiation components.

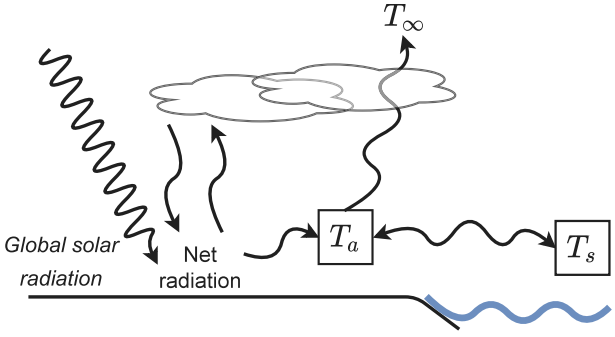


(b) The components related to the air temperature dynamics.

**Fig. 4.** Two illustrations of how the climatic processes interact and how the disturbance model is designed. In 4(a) the two components of the solar radiation is displayed: The global radiation consists of direct- and diffuse radiation where the latter is reflected off from objects in the atmosphere. In 4(b), the interactions of the components near Earth's surface is depicted. The net radiation is the net input of short- and long wave radiation. It plays a crucial role in describing the ambient air temperature. The sea surrounding Denmark highly regulates the air temperature. The heat capacity of water is much larger compared to that of air, and the sea temperature ($T_s$) thus acts as a slow and regulating component in the model. $T_\infty$ represents a constant heat loss of the air.

with $\tilde{\phi}_k$ as in (29). The objective, $\tilde{\phi}_k$, is convex and enables fast numerical solvers such as interior-point methods, see e.g. [36]. Had the problem been unconstrained, the solution to the quadratic optimal control problem would have been given in closed-form [37]. This has the advantages of being fast to evaluate and gives useful insights into how the solution depends on the various parameters.

**Algorithm 2** MPC Algorithm

**require:** $\boldsymbol{y}_{t_k}$, $\hat{\boldsymbol{u}}_{k-1|k-1}$, $\hat{\boldsymbol{x}}_{k-1|k-1}$, $\hat{P}_{k-1|k-1}$, $\hat{\boldsymbol{d}}_{k-1|k-1}$

**Filter:**
Given $\boldsymbol{y}_{t_k}$, $\hat{\boldsymbol{u}}_{k-1|k-1}$, $\hat{\boldsymbol{x}}_{k-1|k-1}$, $\hat{P}_{k-1|k-1}$, $\hat{\boldsymbol{d}}_{k-1|k-1}$, compute the filtered moments of the current system state; $\hat{\boldsymbol{x}}_{k|k}$ and $\hat{P}_{k|k}$

**Disturbance forecasts:**
Given $\hat{\boldsymbol{d}}_{k-1|k-1}$ compute $\{\hat{\boldsymbol{d}}_{k+i|k}\}_{i=0}^{N}$ using the disturbance model in (1b)

**Optimal control:**
Given $\hat{\boldsymbol{x}}_{k|k}$, $\hat{\boldsymbol{u}}_{k-1|k-1}$, and $\{\hat{\boldsymbol{d}}_{k+i|k}\}_{i=0}^{N}$ solve the optimal control problem in (30) to obtain $\{\hat{\boldsymbol{u}}_{k+i|k}\}_{i=0}^{N-1}$

**return** $\hat{\boldsymbol{u}}_{k|k}$, $\hat{\boldsymbol{x}}_{k|k}$, $\hat{P}_{k|k}$

The LQG control framework is now given by a filtering- and an optimisation step. Given an observation, $\boldsymbol{y}_k$, we reconstruct the current state, $\hat{\boldsymbol{x}}_{k|k}$, in the filtering step, and solve the optimal control problem to retrieve the optimal input. In the MPC algorithm, we require an addition computational step to compute the disturbance forecasts. Algorithm 2 lists the LQG control framework.

## 4. The smart building and disturbance model

In the numerical case study (to simulate the performance of controllers using different disturbance forecasting schemes) we consider the heat dynamics of a building given by a model based on SDEs. Furthermore, we use a SDE-based disturbance model to supply forecasts. This section introduces both models briefly.

### 4.1. The smart building model

This paper considers a model based on SDEs with a linear model for the building heat dynamics and a non-linear model for the disturbances. The SDE representation in (1) provides a natural way to express physical systems due to the continuous-time formulation.

This paper uses the continuous-time heat dynamics model of a building identified and estimated by [38]. The authors show that a sufficient model for describing the heat dynamics of the specific building involves two heat accumulating media temperatures: the room air and the floor. We denote the state variable $\boldsymbol{x}(t) = \left[T_r(t), T_f(t)\right]^T$, where $T_r$ and $T_f$ are the room air and floor temperature, respectively. Furthermore, the authors identify how the important disturbances act on the smart building; that is the ambient air temperature, $T_a(t)$, and the solar radiation, $\phi_s(t)$. Lastly the room is equipped with an electrical heater to supply heat. Fig. 3 illustrates the heat dynamics and interactions between the model components. Mathematically, the following matrices govern the continuous-time smart building model on linear form as in (1)

$$
\begin{aligned}
A_c &= \begin{bmatrix} -\frac{1}{r_{fr}C_r} - \frac{1}{r_{ra}C_r} & \frac{1}{r_{fr}C_r} \\ \frac{1}{r_{fr}C_f} & -\frac{1}{r_{fr}C_f} \end{bmatrix}, \quad B_c = \begin{bmatrix} \frac{1}{C_r} \\ 0 \end{bmatrix}, \\
E_c &= \begin{bmatrix} \frac{1}{r_{ra}C_r} & A_w \frac{(1-p)}{C_r} \\ 0 & A_w \frac{p}{C_f} \end{bmatrix}, \quad G_c = \begin{bmatrix} \sigma_1 & 0 \\ 0 & \sigma_2 \end{bmatrix}, \\
C &= \begin{bmatrix} 1 & 0 \end{bmatrix}, \quad H = \begin{bmatrix} 1 & 0 \end{bmatrix}
\end{aligned}
\tag{31}
$$

with the variables $\boldsymbol{x}(t) = \left[T_r(t), T_f(t)\right]^T$, $u(t) = \phi_h(t)$, $\boldsymbol{d}(t) = \left[T_a(t), \phi_s(t)\right]^T$. Table 1 gives the values and descriptions of the parameters in (31). The model in (31) is of course very simple and could be extended to include many effects such as the relative humidity or $CO_2$-levels, both of which impacts the indoor climate [39].

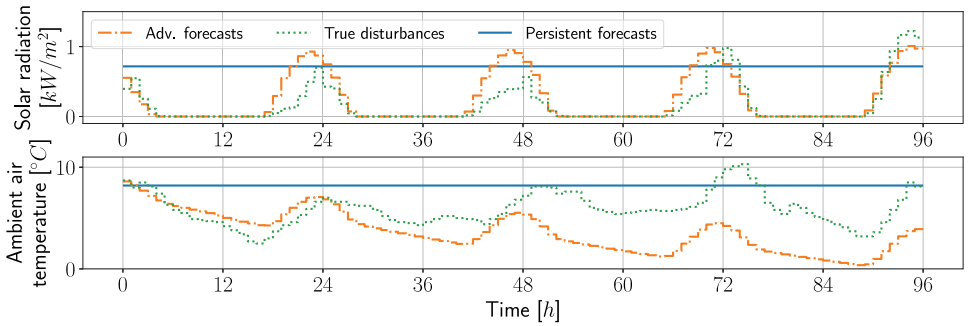


**Fig. 5.** The advanced dynamical disturbance model compared to persistent forecasts and true disturbances.

**Table 1**
The values used in the model for a single smart building in (31).

| Parameter | Value | Unit |
|---|---|---|
| $C_r$ | 810 | kJ/°C |
| $C_f$ | 3315 | kJ/°C |
| $r_{ra}$ | 0.036 | kJ/(°C h) |
| $r_{fr}$ | 0.0016 | kJ/(°C h) |
| $A_w$ | 2.9 | $m^2$ |
| $p$ | 0.1 | |
| $\sigma_1$ | 0.1 | |
| $\sigma_2$ | 0.1 | |

### 4.2. The disturbance model

An important contribution of this paper is to show that disturbance modelling is crucial for control performance. We use the advanced dynamical disturbance model introduced in [6,10]. The disturbance model predicts the mean value of the solar radiation, $\phi_s(t)$, and the ambient air temperature, $T_a(t)$, in the time interval $[t_k, t_{k+1}[$. The model is based on stochastic differential equations and incorporates many climate processes. Fig. 4 gives an overview of the model: It includes models of the following components

- Cloud cover, $\kappa$
- Global solar radiation (based on the direct and diffuse radiation), $\phi_s$
- Net radiation, $R_n$
- Ambient air temperature, $T_a$

Fig. 4 illustrates the way the components are coupled and thoroughly explains the dynamics and interactions. Ultimately, the model predicts the amount of solar radiation hitting a horizontal surface (in Watts) and the ambient air temperature. That is, given an observation of the disturbances at time $t_k$, $\hat{\mathbf{y}}_{d,k}$, the disturbance model returns a sequence of disturbance forecasts

$$\{\hat{\boldsymbol{d}}_{k+i|k}\}_{i=0}^{N-1} \tag{32}$$

where $\hat{\boldsymbol{d}}_{k+i|k} = \left[T_{a,k+i|k}, \phi_{s,k+i|k}\right]^T$ is the prediction of the disturbances in the time interval $\left[t_{k+i}, t_{k+i+1}\right[$, $i \in \mathbb{N}$ and $N$ is the prediction horizon. The building- and disturbance systems in (31) are one-way coupled and the observation of the building system does not contain much additional information about the disturbance state. For this reason, we let separate Kalman filters reconstruct each system for a given time instance. Furthermore, we let the MPC use the weather forecasts as input to the grey-box model for the disturbances to solve the optimal control problem.

Fig. 5 shows a forecasting example with a prediction horizon of four days. The disturbance model forecasts the expected value, which visibly goes to a steady state after some time (after which the forecasts corresponds to a mean value).

**Remark.** The presented model includes only a limited climatic processes for predicting the ambient air temperature and global solar radiation. If relevant for the control objective, other variables could be added to the disturbance model — e.g. humidity factor, $CO_2$, etc.

## 5. Numerical case study

In this section, we carry out a simulation study to quantify the effects of using embedded disturbance forecasts for the continuous-time LQG controller based on the optimal control problem in (30) using the discretised dynamics and objective function in (13) and (21), respectively. We compare the results with a controller that uses perfect forecasts to give an upper bound on the possible control performance. We also compare a controller that uses offset-free control — also known as persistent forecasts. The latter is a standard way of dealing with disturbances in the control literature, see e.g. [40–42] for introductions to the technique.

### 5.1. Simulation setup

To include weather disturbances into the simulations and mimic natural settings, we use actual weather data as the true disturbances acting on the building model. The controllers use weather predictions supplied by the disturbance forecasting schemes (either persistent, advanced, or perfect forecasts). The results in this section (simulation results in Figs. 7 and 8) are based on 7 months of weather data, where observations are separated by 1 h. The data was collected from a weather station located in Taastrup in Denmark in the period from 1971 to 1973. The data include the following variables:

- Cloud cover ([okta])
- Direct radiation ([W/m$^2$])
- Diffuse radiation ([W/m$^2$])
- Net radiation ([W//m$^2$])
- Air temperature ([°C])

For more details on the data, it is thoroughly described in [43].

The controllers use a prediction horizon of 84 h and a time sample of 1 h. The constraints on the input are $u_{\min} = 0$ W, $u_{\max} = 1500$ W, $\Delta u_{\min} = -500$ W, and $\Delta u_{\max} = 500$ W. The electricity price is parameterised as $c_i = c_u \bar{c}_i$, where $\bar{c}_i$ is electricity price data taken from Nordpool and $c_u$ is a constant scalar to weight the electricity price in the optimisation.

To give a visual example of the control solution and better understand the differences of the strategies, Fig. 6 shows the first two weeks of the 7 months of the control simulation. The overall behavioural pattern seems to be more or less the same for all controllers. They tend to buy electricity at the same times. However, the controller using persistent forecasts seems to consistently overheat in periods with significant amounts of sun, compared to the other controllers. Here, the controllers using advanced and perfect forecasts seem to supply more equal control solutions.

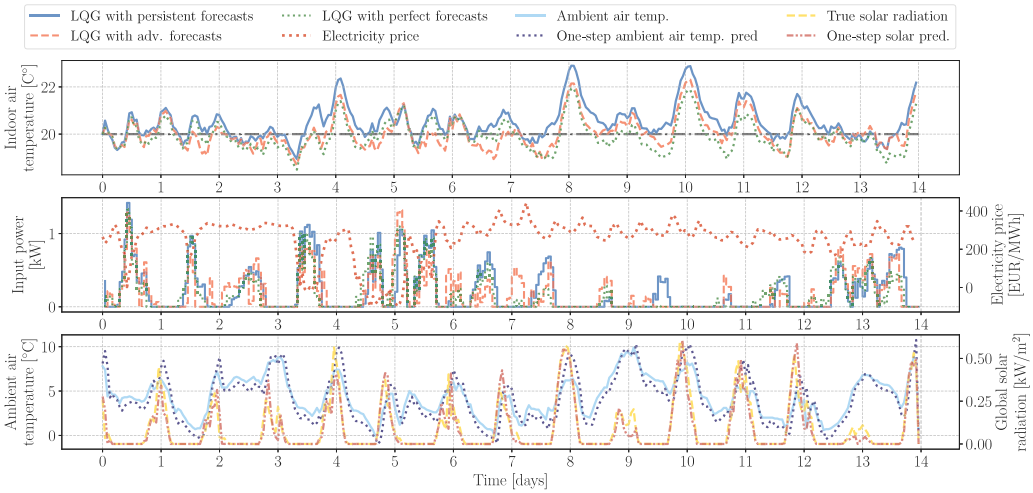


**Fig. 6.** A simulation of a 14 day period with electricity prices taken from Nordpool and weights $c_u = 2.5 \cdot 10^{-5}$, $r_u = 1 \cdot 10^{-6}$.

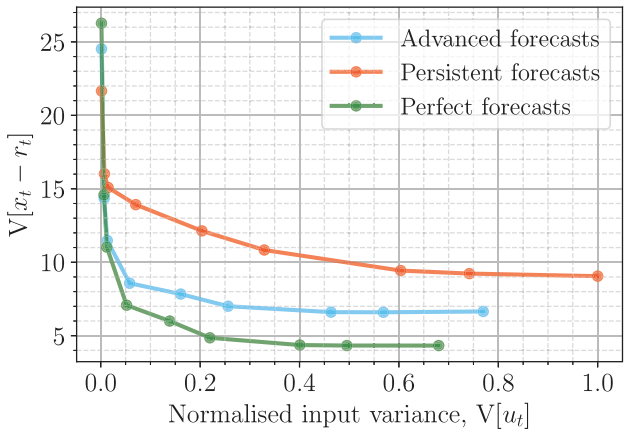


(a) The trade-off between the input variance and the state variance. The electricity cost weight is fixed at $c_u = 1e-5$. The plotted points correspond to the values $r_u \in \{0.0001, 0.000065, 0.00005, 0.000025, 0.000015, 0.000005, 0.000001, 0.0000005, 0.0000001\}$.

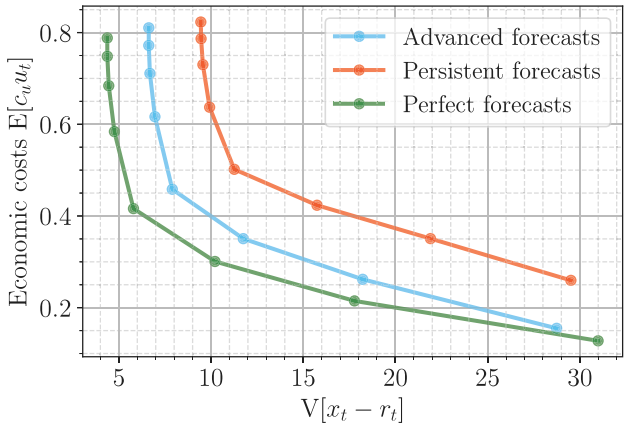


(b) The trade-off between the state variance and the operational costs. The input variance weight is fixed at $r_u = 1e-5$. The plotted points correspond to the values $c_u \in \{0.0004, 0.0002, 0.0001, 0.00005, 0.00002, 0.00001, 0.000005, 0.000002\}$.

**Fig. 7.** Pareto fronts of the variation trade-off of the input and the set-point deviation 7(a) and the set-point deviation and the electricity price 7(b).

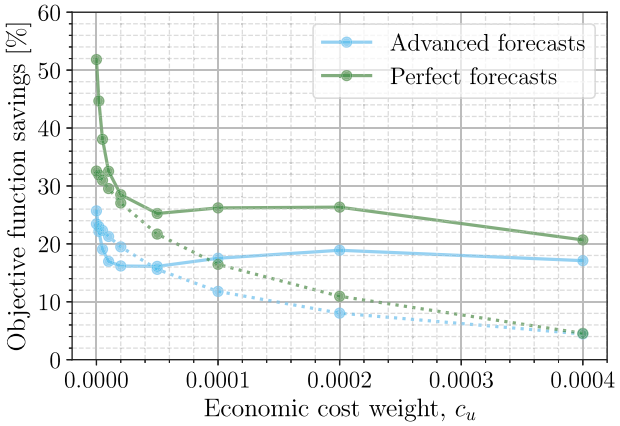


**Fig. 8.** The savings in terms of the objective of the controllers using advanced- and perfect forecasts compared to a controller using persistent forecasts. The solid and dashed lines use $r_u = 0$ and $r_u = 0.5 \cdot 10^{-5}$, respectively. E.g. The dashed lines at the weight $c_u = 0.0002$ shows that the advanced- and persistent forecasts performs around 10% better compared to the persistent forecasts for $r_u = r_u = 0.5 \cdot 10^{-5}$.

### 5.2. Comparison of performances between forecasting schemes

Fig. 7 shows the pareto-fronts displaying the trade-offs between variance in the signals and economic costs. Fig. 7(a) shows the trade-off between the variance of the solution and the control signal: If we require less variance of the process around the reference signal, the variance of the input increases and vice versa. This trade-off is a consequence of the LQG control that weights the variance of solution and the input. The controller using advanced forecasts is able to obtain smaller variation of the solution for a given tolerable input variation compared to persistent forecasts.

Fig. 7(b) shows the trade-off between the variance in the solution and the economic costs. It shows again that it is more expensive to require less variation in the solution. Again, the controller using advanced forecasts is able to obtain a certain variation in the solution for a smaller economic cost.

Overall, the advanced forecasts are able to deliver better solutions in terms of economic costs and variations in the input and solution. The performance is sometimes close to that of using perfect forecasts.

Lastly, Fig. 8 shows the savings of controllers using perfect and advanced forecasts as a function of the economic price weight compared to a controller using persistent forecasts. The objective function savings

are the realised savings:

$$\text{Savings} = 100 \cdot \frac{\phi^{(\text{method})}}{\phi^{(\text{persistent})}}, \quad \text{method} \in \{\text{perfect}, \text{advanced}\} \tag{33}$$

where $\phi^{(\text{method})}$ is the realised objective computed by evaluating the control solution (using either perfect- or advanced forecasts as forecasting scheme) in the objective function and $\phi^{(\text{persistent})}$ is the control solution using persistent forecasts evaluated in the objective function. It shows the savings for two values of $r_u$ (solid and dashed lines) where the results vary from 5% to 26% savings by varying $c_u$ when using advanced forecasts (compared to a controller using persistent forecasts). By including the electricity price in the objective function (with varying electricity price) adds the objective of also using the electricity when it is cheaper. The results thus also give an idea of the strategies' abilities to shift the heat input to beneficial times. This result is in-line with the message from the pareto-fronts — the advanced forecasts supply better forecasts for control compared to persistent forecasts, and for certain choices of parameters the performance is close to that of perfect forecasts. It is also visible that adding more regularisation to the optimal control problem (by increasing the weight $c_u$) the performance between the methods gets smaller.

## 6. Conclusion

This paper introduced and treated in detail the continuous-time linear quadratic Gaussian (LQG) optimal control problem where disturbances are supplied by an embedded disturbance model. We derived a zero-order hold discretisation of the continuous-time dynamics and treated the effects of the disturbances in depth. Next, we introduced the LQG control framework consisting of a filter and an optimal control problem and presented an algorithm to solve the problem. We carried out a numerical case study that involved controlling the indoor climate of a building using the proposed LQG control framework with an embedded disturbance model to supply weather forecasts. We compared the control performance to controllers using persistent forecasts (which is the otherwise dominating standard to supply forecasts). Results suggest control performance improvements up to 26% are available from using an embedded disturbance model. We also showed that the LQG control framework leads to a useful trade-off between variation of the input, variation of the output, and economic costs.

## CRediT authorship contribution statement

**Christian Ankerstjerne Thilker:** Conceptualization, Methodology, Software, Validation, Methodology, Formal analysis, Writing – original draft. **John Bagterp Jørgensen:** Conceptualization, Supervision, Writing – review & editing. **Henrik Madsen:** Conceptualization, Supervision, Writing – review & editing.

## Declaration of competing interest

The authors declare that they have no known competing financial interests or personal relationships that could have appeared to influence the work reported in this paper.

## Data availability

The authors do not have permission to share data.

## Acknowledgements

The authors received funding from the following projects; *Sustainable plus energy neighbourhoods (syn.ikia)* (H2020 No. 869918), *Centre for IT-Intelligent Energy Systems (CITIES)* (DSF 1305-00027B), Top-Up (Innovation Fund Denmark 9045-00017B), SCA+ (Interreg Öresund-Kattegat-Skagerrak), *Research Centre on Zero Emission Neighbourhoods in Smart Cities (FME-ZEN)* (Research Council of Norway, No. 257660), and *Flexible Energy Denmark (FED)* (Innovation Fund Denmark 8090-00069B).

## References

[1] Corradi O, Ochsenfeld HP, Madsen H, Pinson P. Controlling electricity consumption by forecasting its response to varying prices. IEEE Trans Power Syst 2013;28(1):421–30. http://dx.doi.org/10.1109/TPWRS.2012.2197027.

[2] Madsen H, Parvizi J, Halvgaard RF, Sokoler LE, Jørgensen JB, Hansen LH, et al. Control of electricity loads in future electric energy systems. In: Conejo AJ, Dahlquist E, Yan J, editors. Handbook of clean energy systems. Wiley; 2015.

[3] Junker RG, Azar AG, Lopes RA, Lindberg KB, Reynders G, Relan R, et al. Characterizing the energy flexibility of buildings and districts. Appl Energy 2018;225:175–82. http://dx.doi.org/10.1016/j.apenergy.2018.05.037.

[4] Junker RG, Relan R, Madsen H. Designing individual penalty signals for improved energy flexibility utilisation. IFAC-PapersOnLine 2019;52(4):123–8. http://dx.doi.org/10.1016/j.ifacol.2019.08.166.

[5] Jensen SØ, Parker J, Engelmann P, Joanna A. Examples of energy flexibility in buildings. Technical report, 2019.

[6] Thilker C, Junker R, Bacher P, Jørgensen J, Madsen H. Model predictive control based on stochastic grey-box models. In: Towards energy smart homes. Springer; 2021, p. 329–80. http://dx.doi.org/10.1007/978-3-030-76477-7_11.

[7] Schildbach G, Goulart P, Morari M. The linear quadratic regulator with chance constraints. In: 2013 european control conference. 2013, p. 2746–51.

[8] Rawlings J, Mayne DQ, Diehl M. Model predictive control: Theory, computation, and design. Nob Hill Publishing; 2017.

[9] Åström KJ. Introduction to stochastic control theory. Courier Corporation; 2012.

[10] Thilker C, Madsen H, Jørgensen J. Advanced forecasting and disturbance modelling for model predictive control of smart energy systems. Appl Energy 2021;292:116889. http://dx.doi.org/10.1016/j.apenergy.2021.116889.

[11] Chen C, Duan S, Cai T, Liu B, Hu G. Smart energy management system for optimal microgrid economic operation. IET Renew Power Gener 2011;5(3):258–67.

[12] Madsen H, Holst J. Estimation of continuous-time models for the heat dynamics of a building. Energy Build 1995;22:67–79.

[13] Halvgaard R, Poulsen NK, Madsen H, Jørgensen JB. Economic model predictive control for building climate control in a smart grid. In: 2012 IEEE PES innovative smart grid technologies. 2012, p. 1–6.

[14] Oldewurtel F, Parisio A, Jones CN, Gyalistras D, Gwerder M, Stauch V, et al. Use of model predictive control and weather forecasts for energy efficient building climate control. Energy Build 2012;45:15–27. http://dx.doi.org/10.1016/j.enbuild.2011.09.022, URL: http://www.sciencedirect.com/science/article/pii/S0378778811004105.

[15] Wytock M, Moehle N, Boyd S. Dynamic energy management with scenario-based robust MPC. In: 2017 American control conference. 2017, p. 2042–7. http://dx.doi.org/10.23919/ACC.2017.7963253.

[16] Maasoumy M, Vincentelli A. Comparison of control strategies for energy efficient building HVAC systems. 2014, http://dx.doi.org/10.13140/2.1.4813.0560.

[17] Salakij S, Yu N, Paolucci S, Antsaklis P. Model-based predictive control for building energy management. In: Energy modeling and optimal control. Energy Build 2016;133:345–58. http://dx.doi.org/10.1016/j.enbuild.2016.09.044, URL: http://www.sciencedirect.com/science/article/pii/S0378778816308908.

[18] Kang C-S, Park J-I, Park M, Baek J. Novel modeling and control strategies for a HVAC system including carbon dioxide control. Energies 2014;7(6):1–19, URL: https://ideas.repec.org/a/gam/jeners/v7y2014i6p3599-3617d36704.html.

[19] Bayati Poudeh M, Mahdavian M. New adaptive controller in a two area HVAC/HVDC power system. In: 2008 11th International conference on optimization of electrical and electronic equipment. 2008, p. 131–6.

[20] Qi Q, Deng S. Multivariable control of indoor air temperature and humidity in a direct expansion (DX) air conditioning (A/C) system. Build Environ 2009;44(8):1659–67. http://dx.doi.org/10.1016/j.buildenv.2008.11.001, URL: http://www.sciencedirect.com/science/article/pii/S0360132308002679.

[21] Errouissi R, Al-Durra A, Muyeen SM, Leng S, Blaabjerg F. Offset-free direct power control of DFIG under continuous-time model predictive control. IEEE Trans Power Electron 2017;32(3):2265–77.

[22] Taylor CJ, Leigh P, Price L, Young PC, Vranken E, Berckmans D. Proportional-integral-plus (PIP) control of ventilation rate in agricultural buildings. Control Eng Pract 2004;12(2):225–33.

[23] Bagterp Jørgensen J, Frison G, Fog Gade-Nielsen N, Damman B. Numerical methods for solution of the extended linear quadratic control problem. IFAC Proc Vol 2012;45(17):187–93. http://dx.doi.org/10.3182/20120823-5-NL-3013.00092, URL: https://www.sciencedirect.com/science/article/pii/S1474667016314483, 4th IFAC Conference on Nonlinear Model Predictive Control.

[24] Drgoňa J, Arroyo J, Cupeiro Figueroa I, Blum D, Arendt K, Kim D, et al. All you need to know about model predictive control for buildings. Annu Rev Control 2020;50:190–232. http://dx.doi.org/10.1016/j.arcontrol.2020.09.001, URL: https://www.sciencedirect.com/science/article/pii/S1367578820300584.

[25] Bacher P, Madsen H, Nielsen HA. Online short-term solar power forecasting. Sol Energy 2009;83(10):1772–83. http://dx.doi.org/10.1016/j.solener.2009.05.016, URL: https://www.sciencedirect.com/science/article/pii/S0038092X09001364.

[26] Pinson P, Madsen H, Nielsen HA, Papaefthymiou G, Klöckl B. From probabilistic forecasts to statistical scenarios of short-term wind power production. Wind Energy 2009;12(1):51–62. http://dx.doi.org/10.1002/we.284, arXiv:https://onlinelibrary.wiley.com/doi/pdf/10.1002/we.284.

[27] Gabsi F, Hamelin F, Pannequin R, Chaabane M. Energy efficiency of a multizone office building: MPC-based control and simscape modelling. In: 6th international conference on smart cities and green ICT Systems, SMARTGREENS. Porto, Portugal, 2017, http://dx.doi.org/10.5220/0006305002270234.

[28] Lago J, De Ridder F, De Schutter B. Forecasting spot electricity prices: Deep learning approaches and empirical comparison of traditional algorithms. Appl Energy 2018;221:386–405.

[29] Zavala VM, Constantinescu EM, Anitescu M. Economic impacts of advanced weather forecasting on energy system operations. In: 2010 innovative smart grid technologies. 2010, p. 1–7. http://dx.doi.org/10.1109/ISGT.2010.5434772.

[30] Jazwinski A. Stochastic processes and filtering theory. Mathematics in science and engineering, (64). New York, NY [u.a.]: Acad. Press; 1970.

[31] Zabczyk J. Controllability of stochastic linear systems. Systems Control Lett 1981;1(1):25–31. http://dx.doi.org/10.1016/S0167-6911(81)80008-4, URL: https://www.sciencedirect.com/science/article/pii/S0167691181800084.

[32] Jørgensen J. Moving horizon estimation and control (Ph.D. thesis), Technical University of Denmark; 2004.

[33] Singh AK, Pal BC. An extended linear quadratic regulator for LTI systems with exogenous inputs. Automatica 2017;76:10–6. http://dx.doi.org/10.1016/j.automatica.2016.10.014, URL: http://www.sciencedirect.com/science/article/pii/S000510981630406X.

[34] Haussmann UG. Optimal control of partially observed diffusions via the separation principle. In: Stochastic differential systems. Springer; 1982, p. 302–11.

[35] Luenberger D. An introduction to observers. IEEE Trans Automat Control 1971;16(6):596–602.

[36] Boyd S, Vandenberghe L. Convex optimization. Cambridge University Press; 2004, http://dx.doi.org/10.1017/CBO9780511804441.

[37] Nocedal J, Wright SJ. Numerical optimization. 2nd ed. New York, NY, USA: Springer; 2006.

[38] Andersen KK, Madsen H, Hansen LH. Modelling the heat dynamics of a building using stochastic differential equations. Energy Build 2000;31(1):13–24.

[39] Salakij S, Yu N, Paolucci S, Antsaklis P. Model-based predictive control for building energy management. I: Energy modeling and optimal control. Energy Build 2016;133:345–58. http://dx.doi.org/10.1016/j.enbuild.2016.09.044, URL: https://www.sciencedirect.com/science/article/pii/S0378778816308908.

[40] Vega Lara BG, Castellanos Molina LM, Monteagudo Yanes JP, Rodríguez Borroto MA. Offset-free model predictive control for an energy efficient tropical island hotel. Energy Build 2016;119:283–92.

[41] Huusom JK, Poulsen NK, Jørgensen SB, Jørgensen JB. Tuning SISO offset-free model predictive control based on ARX models. J Process Control 2012;22(10):1997–2007.

[42] Hagdrup M, Boiroux D, Mahmoudi Z, Madsen H, Kjølstad Poulsen N, Poulsen B, et al. On the significance of the noise model for the performance of a linear MPC in closed-loop operation. IFAC-PapersOnLine 2016;49(7):171–6. http://dx.doi.org/10.1016/j.ifacol.2016.07.241, URL: https://www.sciencedirect.com/science/article/pii/S2405896316304487, 11th IFAC Symposium on Dynamics and Control of Process SystemsIncluding Biosystems DYCOPS-CAB 2016.

[43] Andersen B, Eidorff S, Perdersen HLE, Rosenørn S, Valbjørn O. Meteorological data for design of building and installation: A reference year. Technical report 66, Thermal Insulation Laboratory; 1977, Technical University of Denmark.

# G Bringing Order to Disorder: A method for stabilising a chaotic system around an arbitrary unstable periodic orbit

# Bringing Order to Disorder: A method for stabilising a chaotic system around an arbitrary unstable periodic orbit

Christian Ankerstjerne Thilker, Mads Peter Sørensen

*Technical University of Denmark, Department of Applied Mathematics and Computer Science, Asmussens Allé, Building 303B, DK-2800 Kgs. Lyngby, Denmark*

**Abstract**

This paper introduces a two-step procedure for stabilising a chaotic system around an arbitrary periodic orbit on a Poincaré map. Chaotic systems lack predictability due to positive Lyapunov exponents. For this reason, predictive control methods tend to perform poorly because the predictable horizon may be short. Current methods for stabilising chaotic systems works by putting them onto already existing unstable periodic orbits, where the dynamics on the Poincaré map disappear. This paper proposes a method for stabilising the system on an arbitrary point on the Poincaré section. The method in this paper consists of two steps. In the first step, we pose an optimisation problem that computes an input signal that, when applied to the system, introduces the desired periodic orbit. In the second step, we use existing methods, such as the method using delay coordinate embedding developed by Ott, Grebogi and Yorke in 1990, to stabilise the system around the newly introduced periodic orbit. As an example, we demonstrate the method on the resistively and capacitively shunted driven Josephson junction.

*Keywords:* chaos, control

## 1. Introduction

In the present paper we suggest a two-step method for controlling a nonlinear dynamical system exhibiting chaotic dynamics such that it follows a predefined periodic path in a Poincaré map of the system. Choosing one point in the Poincaré map corresponds to a simple period one solution intersecting the Poincaré plane in this chosen point. Choosing $n$ points, where $n$ is a positive integer, corresponds to a period-$n$ solution, intersecting the Poincaré plane $n$ times before completing the periodic cycle. The order of these intersections are also chosen arbitrarily.

In the first step we invoke an optimal control problem with an objective function which minimises the distance between the points calculated from the Poincaré map and the arbitrarily chosen points. The objective function only restrains the solution to the chosen points in the plane of intersection of the Poincaré map. The dynamics outside the plane of intersection we do not care about. The optimal control provides a periodic input signal leading to the desired period $n$ solution, which may coexists with other attractors or repellers, including chaotic attractors. If the desired solution is stable we are done. However, if the optimal control leads to an unstable period $n$ solution with the found control signal, we shall apply an additional adaptive control scheme in a second step, such as the ones given in [14] or [4], to stabilise the system around the given unstable fixed points. The method can also constrain the magnitude of the altering periodic signal such that they remain small, that is multiple orders of magnitude smaller than the system dynamics.

The above two-step method is used on the the model of the resistively and capacitively shunted driven Josephson junction. Alternatively the same model arise for the dynamics of a driven and damped fysical pendulum in the gravity field and subject to full rotations around its suspension point.

The paper is organised as follows: Section 2 introduces the model for the driven and damped Josephson junction and provides properties of chaotic dynamical states without control. Section 3 introduces the methods for stabilising the chaotic system using optimal control. Section 4 presents the case study where we apply the introduced stabilisation method on the Josephson junction model. Finally, Section 5 concludes the paper and the findings.

## 2. The driven damped Josephson junction and the pendulum

The Josephson junction is a tunnel diode consisting of two superconductors separated by a thin barrier with a thickness of order 10 Å [7, 2]. The dynamics of a point Josephson junction is governed by the Resistively and Capacitively Shunted Junction (RCSJ) model for the phase

*Email addresses:* chant@dtu.dk (Christian Ankerstjerne Thilker), mpso@dtu.dk (Mads Peter Sørensen)

difference $\phi = \phi(t)$ across the barrier [2].

$$\ddot{\phi} + \alpha\dot{\phi} + \sin(\phi) = \eta + A\sin(\omega t) + u\,. \tag{1}$$

In (1) the time derivative is written shortly as $\dot{\phi} = d\phi/dt$. The term in $\alpha$ is the tunnel resistance due to quasi particles, and $\sin(\phi)$ is the normalized tunnel current of Cooper pairs across the junction barrier. On the right hand side we have added a constant external bias term $\eta$, an external driving signal with amplitude $A$ and frequency $\omega$. Finally, we have added a time dependent control signal $u = u(t)$. The instantaneous voltage $v(t)$ across the junction is proportional to $\dot{\phi}$. Current voltage characteritics are plots of the bias current versus the time average of the voltage.

The model in Eq. (1) also governs a driven and damped pendulum, which is allowed to make full rotations in the gravity field. The variable $\phi$ is the angle of deviation from the vertical hanging pendulum, the term in $\alpha$ models viscous damping and $\sin(\phi)$ is the torque exerted on the pendulum from the gravity force. In the right hand side of Eq. (1) the $\eta$-term is a constant external torque and the sinusoidal term models a time dependant driving torque. Here $u$ denotes a time dependant control torque. In reference [2] a more detailed derivation and comparison is found of the RCSJ Josephson junction model and the pendulum model. The pendulum is a mechanical analog of Jospehson junctions and is used for enhancing the insight into the dynamics of Josephson point juncions.

We can rewrite Eq. (1) as an autonomous system of three coupled ordinary differential equations as follows

$$\dot{x}_1 = x_2\,, \tag{2a}$$
$$\dot{x}_2 = -\alpha x_2 - \sin(x_1) + \eta + A\sin(x_3) + u\,, \tag{2b}$$
$$\dot{x}_3 = \omega\,, \tag{2c}$$

where $x_1(t) = \phi(t)$. This system is used in the numerical implementation, where we applied the Runge-Kutta 4-5 numerical scheme from Matlab [13].

### *2.1. Chaos in the driven Josephson junction*

The driven Josephson junction is well studied [16] and has a rich solution space showing bifurcations, periodic attractors, chaotic dynamics, phase locking and more. In order to illustrate these phenomena we shall follow reference [16] and focus our attention to a small parameter space with $\omega = 1$, $\alpha = 0.2$, $A = 10.198039027$, and a variable bias current $\eta$.

In figure 1 we show the value of $\dot{\phi}(T_n)$ with $T_n = 2\pi n/\omega$, $n \in \mathbb{N}$, as a function of the bias current $\eta$. Here the period of the external sinusoidal drive is $2\pi/\omega$. For each value of $\eta$ we calculate a series of $\dot{\phi}(T_n)$, which are plotted as black dots in the Fig. 1. We can define a Poincaré map from Eq. (1) through the sequence $(x_1(T_n) \bmod 2\pi, x_2(T_n))$ and demanding $x_1(T_n) \bmod 2\pi \in [-\pi; \pi[$. The data points $\dot{\phi}(T_n) = x_2(T_n)$ is then a projection of the Poincaré map onto the $x_2$-axis. Following the reference [16] we recapitulate

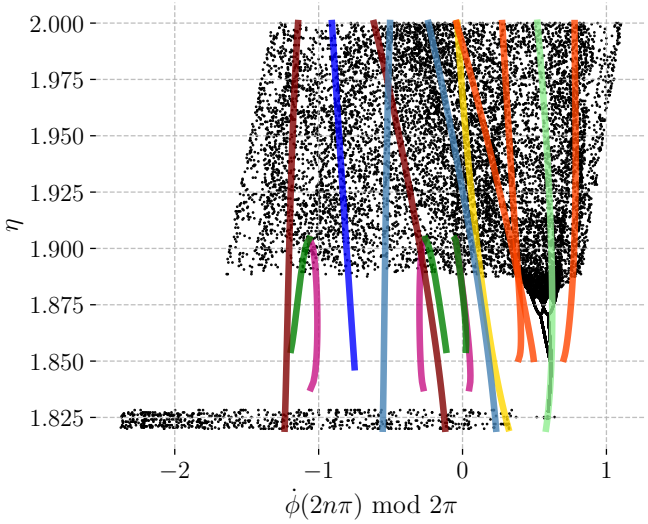


Figure 1: The chaotic attractor as a function of $\eta$. The coloured lines indicate unstable periodic orbits (UPOs); each colour is a distinct UPO. The parameter values are $\omega = 1$, $\alpha = 0.2$, $A = 10.198039027$.

that as $\eta$ increases from $\eta = 1.78$, the chaotic attractor disappears at $\eta = 1.822$ in a boundary crisis as it collides with the unstable period-1 orbit [9]. The system then undergoes a period-doubling sequence as $\eta$ increases further up to around 1.8772 where the system becomes chaotic. The chaotic attractor is rather small or narrow in $\dot{\phi}(T_n)$ until it collides with the unstable period-3 solution, where it suddenly expands at $\eta = 1.888$ in a so-called interior crisis [9, 11, 12]. The unstable period-3 solution appears at $\eta = 1.851$.

In the current study, we have identified a number of new unstable periodic orbits (UPO) in Eq. (1) and they are depicted as the coloured lines in Fig. 1, where each colour is a distinct UPO. As an example the three red lines depict a period-3 fixed point. For $\eta = 1.82$, a chaotic attractor co-exists with a stable period-1 orbit indicated by the black dots to the right in Figure 1.

Chaotic dynamics can be characterised by the Lyapunov exponents of the system [3, 18]. The Lyapunov exponents are the rate of separation of two orbits with an infinitesimal small initial separation. When the Lyapunov exponents become positive for a given system, two initially close orbits separate at an exponential rate. Figure 2 shows the three Lyapunov exponents of the driven Josephson junction model in (2) as a function of $\eta$ with the parameters as previous. For calculating the Lyapunov exponents we have applied the numerical method described in reference [18]. From Fig. 2 we can identify the period-doubling sequence by the points, where the largest Lyapunov exponent, $\lambda_1$, becomes zero, but do not cross $\lambda = 0$. The point at which the system becomes chaotic is the point where the largest Lyapuonv exponent crosses the zero-axis. The internal crisis is also visible by the sudden increase in the positive Lyapunov exponent around $\eta = 1.887$, due to the

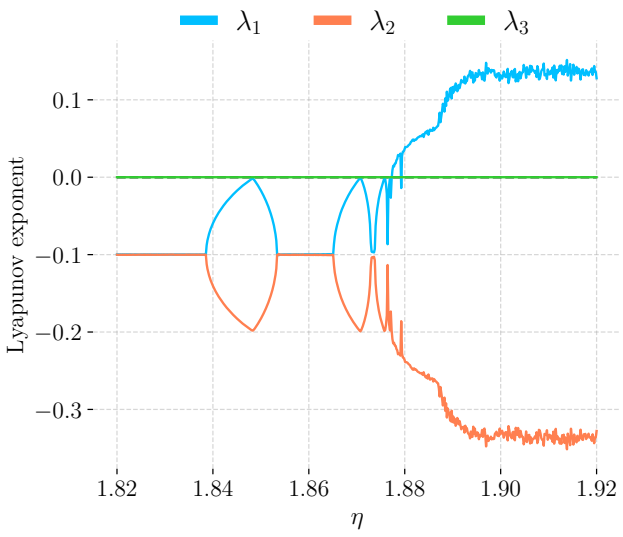


Figure 2: The three Lyapunov exponents as a function of $\eta$. Every time a period doubling happens, the Lyapunov exponents reach zero. At the point of chaos the largest Lyapunov exponent becomes positive and the system goes into a non-predictive state.

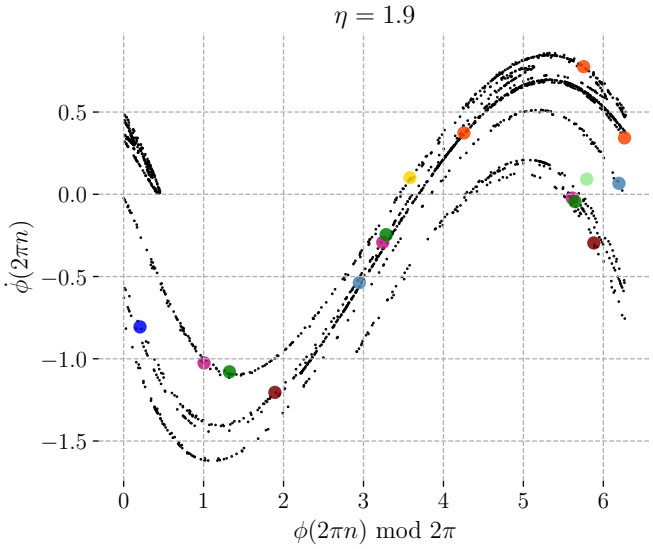


Figure 3: The chaotic attractor in the Poincaré map for the specific value $\eta = 1.9$. The coloured dots indicate the points of the UPOs from figure 1. They all lie within the chaotic attractor.

expansion of the chaotic region. The irregularity of the Lyapunov exponents is also larger after this point with more significant fluctuations. These results comply with those in reference [10].

Figure 3 shows a Poincaré section for $\eta = 1.9$ of the chaotic attractor depicted in Figure 1. An UPO corresponds to an ordered sequence of points in the Poincaré section. The large coloured dots are the locations of the UPOs also depicted in Figure 1.

Figure 4 depicts a current-voltage characteristic, showing the bias current $\eta$ as function of the average voltage $v = <\dot{\phi}>$ across the junction barrier. For $1.825 < \eta < 1.88$ the average voltage is phase locked to the value 10. Increasing the bias current from $\eta = 1.88$ to $\eta = 2$, we observe chaotic dynamics and loss of the phase locked state. As a result the average voltage across the junction decreases and becomes irregular. From an operational point of view, the irregularity may not be desired as the system does not operate in a specified periodic state. Appropriate control is a useful tool for stabilising the system in a state that benefits operations.

### *2.2. Control of UPOs embedded in the chaotic attractor*

Unstable periodic orbits may be embedded within a chaotic attractor. The idea of controlling a chaotic system onto an unstable periodic orbit (UPO) using small perturbations originates from Ott et al. [14]. The goal of the method is to steer the system onto a fixed point in a Poincaré section. That is, the operator first needs to identify an UPO that is desirable to operate the system on. Next, the operator needs knowledge about the local behaviour of the system around the fixed point. The fundamental requirement of the method is the existence of an UPO – but what if we cannot find an existing UPO that suits the needs of the operation we wish do? Figure 3 shows some, there might be more, of the UPOs with period up to 3 of the Josephson junction model in (2). The next section introduces a method for constructing an arbitrary fixed point on the Poincaré section using small perturbations such that the system is not altered too much.

## 3. A method for stabilising an arbitrary unstable periodic orbit

In this section we introduce a method for creating an arbitrary fixed point in the Poincaré section of a chaotic dynamical system (2) and the method for stabilising the system around this fixed point. The idea is to perturb the system using not too large inputs such that a desired sequence of points appear in the Poincaré section, which was not already there. The method consist of two steps: First, we pose an optimal control problem in order to find an input signal that alters the chaotic behaviour such that the desired UPO appears in the Poincaré map of the system. Next, we use existing methods, such as the OGY [14] or the adaptive method [4], to stabilise the system around the newly introduced UPO.

The system is thus altered by two inputs. We therefore consider an input of the form $u(t) = u_1(t)+u_2(t)$, where $u_1$ is the input that alters the system such that the desired UPO appears and $u_2$ is the adaptive control to stabilise the system dynamics onto the UPO. Consequently, the Josephson junction model has the form

$$\ddot{\phi} + \alpha\dot{\phi} + \sin\phi = \eta + A\sin(\omega t) + u_1(t) + u_2(t)\,. \qquad (3)$$

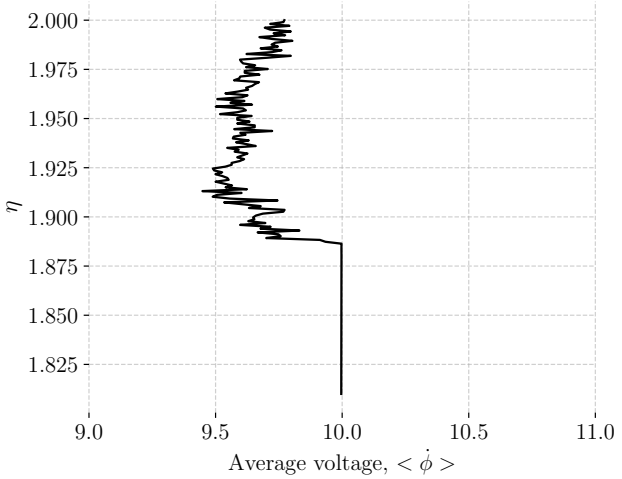


Figure 4: The IV-characteristic of the Josephson junction with the parameters as in Figure 1. $< \cdot >$ is the time average operator. The average voltage is initially locked on step 10. When the system enters the chaotic state around $\eta = 1.8772$, the system leaves the step and the IV-characteristic becomes irregular.

### *3.1. Optimal control problem*

An optimal control problem is the optimisation problem that arises in the search of an optimal control of a system [15]. The problem is based on a cost function, that is used to rank the feasible solutions. The problem should be formulated such that it promotes a desired behaviour of the system. An example is optimal control of the heating system of a building [17]. Here, the problem is to find the optimal times to heat (or cool) the indoor air given the acceptable constraints on the indoor air temperature, the heating prices, and the weather forecasts of outdoor temperature and solar radiation. In many situations, the optimal control problem is based on a Bolza problem [6]

$$\min_{u_1} \quad V(x, u_1) \tag{4a}$$
$$s.t. \quad \dot{x}(t; u_1) = f(x, t; u_1) \tag{4b}$$
$$x(t_0; u_1) = x_0 \tag{4c}$$
$$c_x(x) \geq 0 \tag{4d}$$
$$c_u(u_1) \geq 0 \tag{4e}$$

with

$$V(x, u_1) = \int_{t_0}^{t_0+T} \ell(x(t; u_1), u_1)\mathrm{d}t + \ell_T(x(t_0 + T; u_1)) \,. \tag{5}$$

In (4), $x : \mathbb{R} \to \mathbb{R}^n$ where $n \in \mathbb{N}$ and $c_x$, $c_u$ are functions that constrain the state-space of the system and the input. $V$ is the objective function that the operator wishes to minimise: $\ell$ is the infinitesimal cost that penalises the system for unwanted behaviour while $\ell_T$ is a terminal cost, sometimes called cost-to-go, that penalises the terminal state of the system. In our case, we are interested in planning a path that makes the system travel through specified points in the Poincaré section. We hence do not care about the transient state of the system between these discrete points. This consideration leads us to an attractive formulation of the optimal control problem for planning the desired path described in the following section.

### *3.2. Constructing an arbitrary unstable periodic orbit embedded into the chaotic attractor*

We shall now show how an unstable periodic orbit of our choosing can be constructed as a solution of Eq. (3) by applying an external control function $u_1$ determined from an optimal control problem. Let

$$\mathcal{T}_x \,:\, 0 = t_0^x < t_1^x < \cdots < t_N^x = T_x N \tag{6a}$$
$$\mathcal{T}_u \,:\, 0 = t_0^u < t_1^u < \cdots < t_M^u = T_u M \tag{6b}$$

be sequences of equidistant time points such that $t_k^x = T_x k$, $k = 0, ..., N$ and $t_m^u = T_u m$, $m = 0, ..., M$. $\mathcal{T}_x$ is the collection of time points where the system traverses the Poincaré section while $\mathcal{T}_u$ is the time points where the input signal changes. The operator now chooses a desired ordered sequence of points in the Poincaré section, $\{x_k^*\}_{k=0}^{N-1}$. These points do not necessarily correspond to an already existing UPO. To introduce an UPO traversing these points, $\{x_k^*\}_{k=0}^{N-1}$, we solve the optimal control problem in (4) with a special infinitesimal cost, which is often used in optimal control and parameter estimation of differential equation models [5]. In the optimal control problem, we consider a piecewise constant input signal $u_1(t) = u_{1,m}$, $t \in [t_m^u, t_{m+1}^u[$, $m = 0, \ldots, M-1$. This makes the parameters in the optimal control problem a sequence of values $\{u_{1,m}\}_{m=0}^{M-1}$. Note that $t_N^x = t_M^u$ since the input signal also needs to be $T_x N$-periodic. As described in the preceding section, we care only about the state of the system when it traverses the Poincaré map. Therefore, the following infinitesimal cost reflects this "interest"

$$\ell(x, u_1) = \sum_{k=0}^{N} \delta(t - Tk)\ell_k(x; u_1) \,, \tag{7}$$

where $\delta$ is the Dirac delta function and

$$\ell_k(x, u_1) = \|x_k^* - x(t_k^x; u_1)\|_2^2 \,, \tag{8}$$

penalises the distance between the system at time $t_k^x$ and the desired point. We wish to minimize the distance between $x(t_k^x; u_1)$ and $x_k^*$. As a result, the objective function of the optimal control problem becomes a sum:

$$\int_{t_k}^{t_k+T} \ell(x, u_1)\mathrm{d}t = \sum_{k=0}^{N-1} \ell_k(x, u_1) \,. \tag{9}$$

If we now let $\ell_T(x(t_N^x)) = \|x_0^* - x(t_N^x)\|_2^2$, we can write the objective function for our application as

$$V = \sum_{k=0}^{N-1} \left( \|x_k^* - x(t_k^x; u_1)\|_2^2 \right) + \|x_0^* - x(t_N^x; u_1)\|_2^2 \,. \tag{10}$$

The terms $\left(\|x_k^* - x(t_k^x; u_1)\|_2^2\right)$, $k = 0, \ldots, N-1$, penalises the system $x$ if it does not traverse the points $x_k^*$ in the correct order while the terminal cost, $\|x_0^* - x(t_N^x; u_1)\|_2^2$, makes sure that $x$ arrives at the starting point $x_0^*$ and closes the loop at the end $t = t_N^x$. In practice, it may not be desirable to let $u_1$ be too large. By constraining the magnitude of $u_1$, the optimal control problem finally becomes

$$\min_{\{u_{1,m}\}_{m=0}^{M-1}} \quad V(x, u_1)\,, \tag{11a}$$

$$\text{s.t.} \quad \dot{x}(t; u_1) = f(x(t), t; u_1(t))\,, \tag{11b}$$

$$x(0; u_1) = x_0^*\,, \tag{11c}$$

$$u_1(t) = u_{1,m} \quad \text{for} \quad t \in [t_m^u, t_{m+1}^u[\,, \tag{11d}$$

$$u_{\min} \le u_m \le u_{\max}\,, \quad m = 0, \ldots, M-1\,. \tag{11e}$$

In (11), $u_1(t)$ is piecewise constant and $M$ is the number of piecewise steps it takes on during the time $[t_0^u, t_N^u[$, $u_{\min}$ and $u_{\max}$ are the minimum and maximum admissible values for $u_1$. The optimal control problem minimises the pointwise deviations from the sequence of points in the Poincaré section. That is, we only make specifications or requirements on the system, when it is on the Poincaré section.

*Remark*: We are only interested in solutions where the altered system traverses all fixed points arbitrarily close. That is, given $\epsilon > 0$, we accept a solution $\hat{u}_1(t)$ to (11) if $\hat{u}_1(t)$ implies that $V < \epsilon$. If such a solution exists, the system traverses the points in the Poincaré section sufficiently close. If such a solution does not exist, one can for instance relax the bounds on $u_{1,m}$ in (11) if possible to enlarge the solution space.

The method described above introduces an arbitrary order of fixed points in the Poincaré section. If the optimal perturbations $\hat{u}_1$ are not too large, the system is still chaotic, and we still need to stabilise the system around the UPO somehow. For this, we are able to employ existing methods to stabilise the system onto it. Note that (11) is not necessarily convex, and consequently, we are not guaranteed a unique solution.

### *3.3. The OGY method for stabilising the system around the introduced unstable periodic orbit*

Applying $u_1$ alters the system such that the desired UPO appears. Various methods for stabilising the system around an UPO embedded in a chaotic attractor exists. The OGY method [14] exploits the local dynamics of the fixed points in the Poincaré section to "push" the system onto the stable direction of the UPO whenever the system visits a close neighbourhood of the UPO. By linearising the system around the fixed point in the Poincaré section, it is possible to perturb the system such that it coincides with the stable manifold of the fixed point, provided a stable manifold exists. This method is easy to implement and in fact requires no knowledge about the global dynamics. The local dynamics can typically be learned from experimental data [8]. Boccaletti and Arecchi [4] introduces an alternative method for stabilising the system around an unstable orbit. The method is adaptive in nature and tracks the local rate of variation from the desired UPO. Based on the variation, the method choose the next step size before taking the next observation: If the local variation rate is large, the step size is small and vice versa. The OGY method is chosen in the current study.

Consider here the Josephson junction in (3) where $u_2$ is the perturbations supplied by the OGY method. Using the notation as in Arecchi et al. [1], let $\xi = 0$ be a given fixed point and $\lambda_s$ and $\lambda_u$ be the stable and unstable eigenvalues, respectively. The corresponding eigenvectors are denoted $e_s$ and $e_u$. Here, we assume a stable manifold and an unstable manifold. When we change $u_2$ from $u_2 = 0$ to some small value $u_2 = \bar{u}_2 \ll |1|$, the fixed point $\xi$ changes to some nearby point $\xi(\bar{u}_2)$. In a small neighbourhood around $\xi$, the following linearisation describes the systems dynamics

$$\xi_{n+1} - \xi(u_2) = M \cdot (\xi_n - \xi(u_2)) \tag{12}$$

where $M$ is the Jacobian in the point $\xi = 0$ and $M$ can be determined from experiments by perturbing the system and observing how the fixed point displaces as $u_2$ varies. $\xi_n = x(pTn) \bmod 2\pi$ is the actual sequence of points in the Poincaré map of the controlled system. In a small neighbourhood around $\xi(u_2)$, the linear approximation $\xi(u_2) = Gu_2$ describes the local dynamics of how the fixed point changes as a function of $u_2$, where $G = \frac{\partial}{\partial u_2}\xi$. Inserting $Gu_2 = \xi(u_2)$ into (12), we get

$$\xi_{n+1} = Gu_2 + (\lambda_s e_s f_s + \lambda_u e_u f_u) \cdot (\xi_n - Gu_2) \tag{13}$$

where $f_s$ and $f_u$ are the stable and unstable contravariant basis vectors, respectively. Taking the dot product of the linearised dynamics in Eq.(13) and $f_u$ gives us the feedback $u_n^*$ that puts the system onto the stable manifold of the linear dynamics — or, equivalently, the system is orthogonal to the unstable manifold. The dot product leads to

$$u_2^* = \frac{\lambda_u}{\lambda_u - 1} \frac{f_u \cdot \xi_n}{f_u \cdot G} \tag{14}$$

The contravariant basis vectors $f_s$ and $f_u$ are determined from the relations $f_s \cdot e_s = 1$, $f_s \cdot e_u = 0$, $f_u \cdot e_u = 1$ and $f_u \cdot e_s = 0$ [14].

## 4. Case study: control of the driven and damped Josephson junction

This section implements and demonstrates the method described in Sec. 3 applied to the driven and damped Josephson junction. As described in the previous section, this paper considers the dynamical equation (3), which governs the dynamical behaviour of the Josephson junction. The control $u_1$ is the input signal for altering the

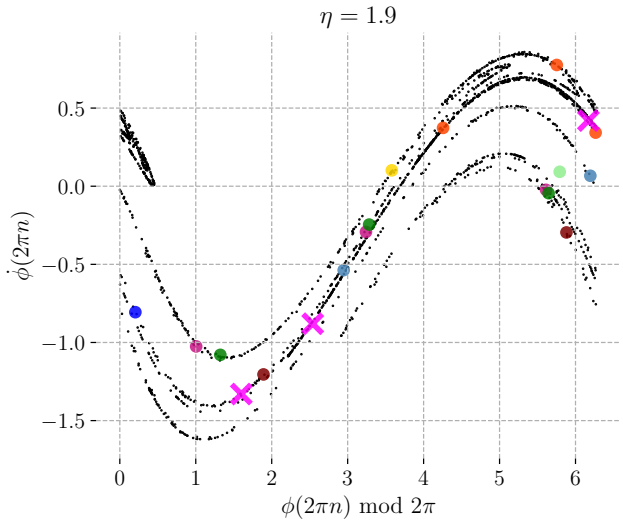


Figure 5: The chaotic attractor of the Josephson junction together with the natural UPOs (circles) and the chosen and desired UPOs (crosses). Each colour is a distinct UPO. Parameter value $\eta = 1.9$ and $u_1(t) = u_2(t) = 0$.

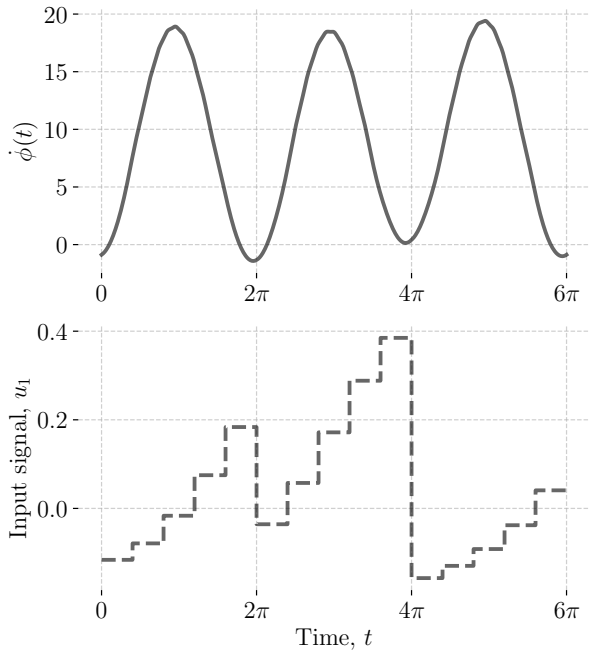


Figure 6: The periodic input signal $u_1$, with $u_2 = 0$, as function of time $t$ (lower graph) we apply to the system in order to create a desired period-3 solution (upper graph). Notice that the magnitude of the signal is 1 to 2 orders smaller in magnitude compared to the magnitude of the dynamical system.

solution such that the desired UPO appears, and $u_2$ is the input signal for stabilising the system around the newly introduced UPO, using e.g. the OGY method. This section demonstrates the presented method for for stabilising the chaotic system around an arbitrary UPO.

### *4.1. Introducing the desired UPO. $u_1(t) \neq 0$ and $u_2(t) = 0$*

Let us for demonstrative purposes choose a period-3 UPO that we wish to stabilise the system around. The placement of the selected UPO in the Pointcaré map is shown in Figure 5 by the purple crosses. The UPO is randomly chosen for the sake of proving the concept but still lying close to the chaotic attractor or at least in its basin of attraction. Solving the optimal control problem in (11) with these points on the Poincaré map, we obtain an input signal that alters the system such that a UPO appears exactly where we want it. Figure 6 shows the input signal obtained from the optimal control problem together with the voltage of the UPO. Notice that the magnitude of the input signal is one and two orders of magnitude smaller than the dynamics of the system.

Figure 7 shows the new chaotic attractor that appears from altering the Josephson junction with the input signal $u_1$, with $u_2(t) = 0$ shown in Fig. 6. The system is still chaotic for $\eta = 1.9$, which the Lyapunov exponents confirm shown in Fig. 8.

Figure 2 shows the estimated Lyapunov exponents for the driven and damped Josephson junction. It clearly shows the period-doubling sequence towards the chaotic region. When we turn on the periodic control signal $u_1$, we of course alter the system. But it is not given that the system remains chaotic after altering it. It could be that the desired periodic solution is stable and no further control is needed. To investigate the behaviour of the altered system, we inspect Figure 8, which shows the altered system's estimated Lyapunov exponents. The system clearly remains chaotic for nearly all values of the bias current—except for a small window around $\eta \in [1.960, 1.981]$ where the Lyapunov exponents suddenly drop and large irregularities appear (see Fig. 9). It indicates that for bias currents in this interval, multiple periodic and quasi-periodic solutions exists.

### *4.2. Stabilising the system around the period-3 UPO. $u_1 \neq 0$ and $u_2(t) \neq 0$*

At this point, the system now embeds a period-3 UPO chosen by the authors. The reason for choosing the exact UPO could be to optimise the operations of the system or minimise some costs/risks related hereto. The next step is to stabilise the system around the chosen UPO. As explained in Sec. 3.3, various methods for stabilising chaotic UPOs exist. Had the system been unstable and non-chaotic, other methods exist. These include feed-forward control, model predictive control, proportional-integral-derivative control etc.

Figure 10 shows a time series of the Josephson junction where we apply the two types of control. The first black arrow from the left shows the point in time, where we alter the system with the periodic signal $u_1$ and with $u_2(t) = 0$. The behavioural difference of the new altered system is quite clear after this point. The second black arrow indicates the point in time where the altered system gets close to the desired orbit and where the adaptive control

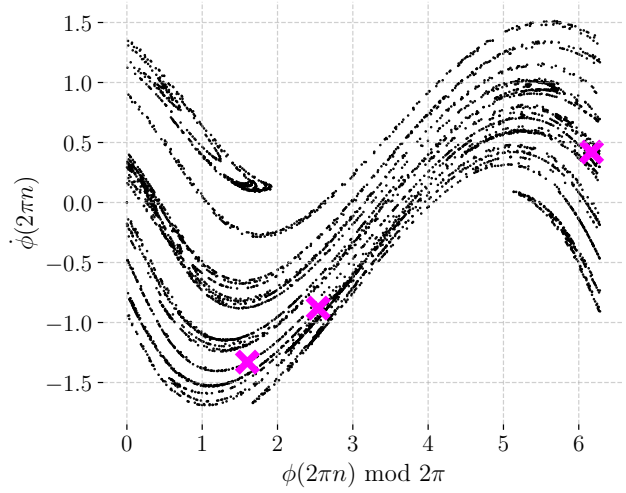


Figure 7: The chaotic attractor of the altered Josephson junction. The purple crosses indicate the unstable period-3 solution on the Poincaré map, embedded in the attractor. Parameter values are $\eta = 1.9$ and $u_1$ is taken from Fig. 6 and $u_2(t) = 0$.

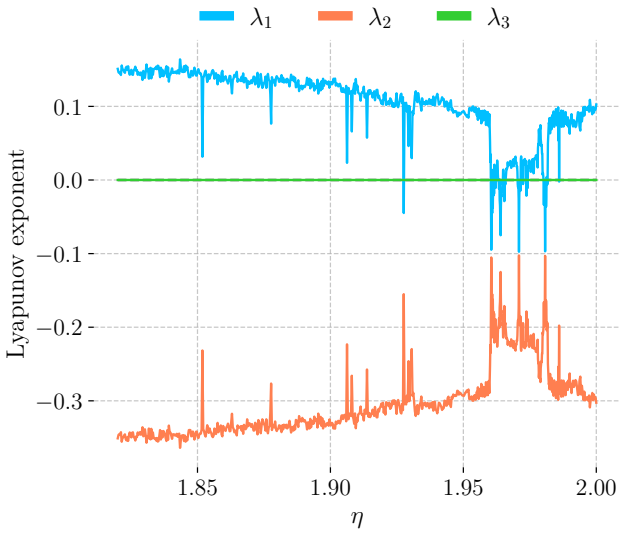


Figure 8: The Lyapunov exponents of the controlled system as a function of $\eta$. No patterns from the original system is visible here. The system appears to be chaotic for almost all values of the bias current, with exceptions of a few points or narrow intervals, where the system might be non-chaotic or even be quasi-periodic. The control $u_1$ is taken from Fig. 6 and $u_2(t) = 0$.

$u_2$ is turned on. From this point onwards, the system is stabilised around the period-3 UPO until we choose to turn off either the periodic signal or the adaptive control.

## 5. Conclusion

This paper presented a two-step method for stabilising a chaotic system around any, even initially non-existing, UPO inside a chaotic attractor. The method is inspired by optimal control problems and uses this for introducing the desired UPO. Existing methods is then used for stabilising the system around this UPO. In order to demonstrate this approach, we have chosen a random set of points in the Poincaré map of the driven and damped Josephson junction and then force the dynamics to pass through the Poincaré plane at the chosen points. The method is generally applicable to chaotic systems.

## References


[1] Arecchi, F.T., Boccaletti, S., Ciofini, M., Meucci, R., Grebogi, C., 1998. The control of chaos: Theoretical schemes and experimental realizations. International Journal of Bifurcation and Chaos 08, 1643–1655. URL: https://doi.org/10.1142/S0218127498001315, doi:10.1142/S0218127498001315, arXiv:https://doi.org/10.1142/S0218127498001315.

[2] Barone, A., Paterno, G., 1982. Physics and applications of the Josephson effect. volume 1. Wiley Online Library.

[3] Benettin, G., Galgani, L., Giorgilli, A., Strelcyn, J.M., 1980. Lyapunov characteristic exponents for smooth dynamical systems and for hamiltonian systems; a method for computing all of them. part 1: Theory. Meccanica 15, 9–20.

[4] Boccaletti, S., Arecchi, F.T., 1995. Adaptive control of chaos. Europhysics Letters (EPL) 31, 127–132. URL: https://doi.org/10.1209/0295-5075/31/3/001, doi:10.1209/0295-5075/31/3/001.

[5] Büskens, C., Maurer, H., 2000. Sqp-methods for solving optimal control problems with control and state constraints: adjoint variables, sensitivity analysis and real-time control. Journal of Computational and Applied Mathematics 120, 85–108. URL: https://www.sciencedirect.com/science/article/pii/S0377042700003058, doi:https://doi.org/10.1016/S0377-0427(00)00305-8.

[6] Clarke, F.H., 1976. The generalized problem of bolza. SIAM Journal on Control and Optimization 14, 682–699. URL: https://doi.org/10.1137/0314044, doi:10.1137/0314044, arXiv:https://doi.org/10.1137/0314044.

[7] Dauxois, T., Peyrard, M., 2006. Physics of solitons. Cambridge University Press.

[8] Dressler, U., Nitsche, G., 1992. Controlling chaos using time delay coordinates. Phys. Rev. Lett. 68, 1–4. URL: https://link.aps.org/doi/10.1103/PhysRevLett.68.1, doi:10.1103/PhysRevLett.68.1.

[9] Grebogi, C., Ott, E., Yorke, J.A., 1983. Crises, sudden changes in chaotic attractors, and transient chaos. Physica D: Nonlinear Phenomena 7, 181–200.

[10] Kautz, R., 1983. Chaos in josephson circuits. IEEE Transactions on Magnetics 19, 465–474.

[11] Kautz, R.L., 1981. Chaotic states of rf-biased josephson junctions. Journal of Applied Physics 52, 6241–6246.

[12] Kautz, R.L., 1989. Global stability of the chaotic state near an interior crisis, in: Structure, coherence and chaos in dynamical systems, Manchester University Press, 1989. Eds. Christiansen, Peter L and Parmentier, Robert D.

[13] Online, 2022. Mathworks matlab. https://se.mathworks.com/products/matlab.html. MathWorks, Matlab.

[14] Ott, E., Grebogi, C., Yorke, J.A., 1990. Controlling chaos. Phys. Rev. Lett. 64, 1196–1199. URL: https://link.aps.org/doi/10.1103/PhysRevLett.64.1196, doi:10.1103/PhysRevLett.64.1196.

[15] Rawlings, J.B., Mayne, D.Q., Diehl, M.M., 2019. Model Predictive Control: Theory, Computation, and Design. volume 1. Nob Hill Publishing, LCC.

[16] Sørensen, M., Davidson, A., Pedersen, N., Pagano, S., 1988. Crises in a driven josephson junction studied by cell mapping. Physical Review A (Atomic, Molecular and Optical Physics) 38, 5384–5390. doi:10.1103/PhysRevA.38.5384. copyright (1988) by the American Physical Society.

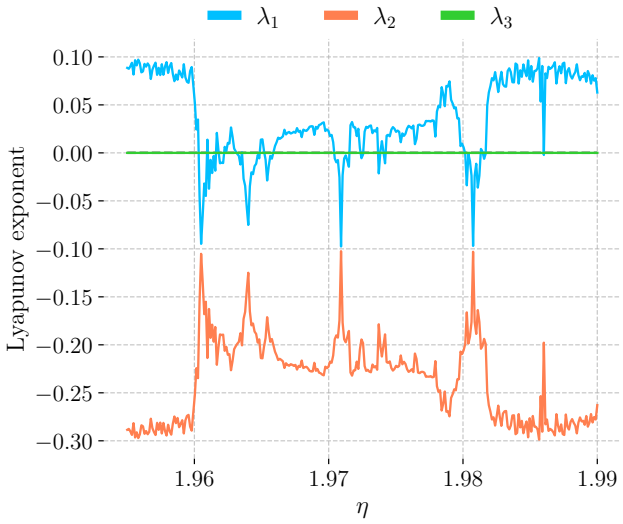


Figure 9: The Lyapunov-exponents of the controlled system as a function of $\eta$, using $u_1$ shown in Fig. 6 and with $u_2 = 0$. No patterns from the original system is visible here. The system appears to be chaotic for almost all values of the bias current, with exceptions of a number of narrow intervals where the system is non-chaotic or even quasi-periodic.


[17] Thilker, C., Bergsteinsson, H., Bacher, P., Madsen, H., Cali, D., Junker, R., 2021. Non-linear model predictive control for smart heating of buildings, in: Proceedings of Cold Climate HVAC & Energy 2021. URL: `http://hvac2021.org`. cold Climate HVAC; Energy 2021 ; Conference date: 20-04-2021 Through 21-04-2021.

[18] Wolf, A., Swift, J.B., Swinney, H.L., Vastano, J.A., 1985. Determining lyapunov exponents from a time series. Physica D: nonlinear phenomena 16, 285–317.


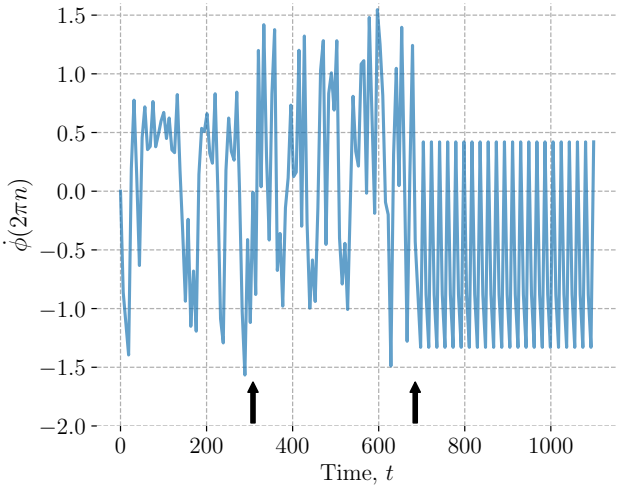


Figure 10: Adaptive control of the period-3 UPO of the Josephson junction. From time $t = 0$ until the first arrow from the left ($t \approx 300$) we have set $u_1(t) = u_2(t) = 0$. In the interval between the two arrows we have set $u_1$ equal to the optimal control shown in Fig. 6 and $u_2(t) = 0$. The second arrow shows where the control $u_2$ is applied leading to a period-3 solution.

Technical
University of
Denmark

Asmussens Allé, Building 303b
2800 Kgs. Lyngby
Tlf. 4525 1700

www.compute.dtu.dk